University of Nottingham
UK | CHINA | MALAYSIA

Nanoscale Characterisation of Soot Particulates from Gasoline Direct Injection Engines

Sebastian A. Pfau

Thesis submitted to the University of Nottingham
for the degree of Doctor of Philosophy

July 2021

Abstract

Understanding the intricacies of particulate emissions from internal combustion engines is important due to their harmful impact on human health and the environment, as well as their contribution to engine wear and performance. Particulate emissions were historically associated with diesel engines which are predominantly using direct-injection systems. Thus, diesel soot is widely covered in the literature. However, the increasing market share of vehicles with gasoline direct-injection (GDI) engines over recent years raises the question of how GDI soot compares to diesel soot and if existing knowledge can be applied. The aim of this work was to close this gap in knowledge between GDI and diesel engine soot.

Fringe analysis was assessed as a tool for quantifying graphitic nanostructures from transmission electron microscopy (TEM) images. A considerable influence of the processing parameters on the produced metrics was demonstrated, and optimised parameters were proposed. Moreover, the importance of the TEM focus point and the role of image quality was outlined. Subsequent thermogravimetric analysis of soot-in-oil samples suggested that the soot deposition rate into the lubricating oil is similar for GDI engines compared to diesel engines, even though their exhaust particulate emissions are generally considered to be one order of magnitude lower. Direct comparison of GDI and diesel engine soot samples and a carbon black identified primary particles with similar core-shell nanostructures in TEM images. However, for the GDI samples, also particles with surrounding amorphous layer were observed along with entirely amorphous particulates and traces of wear and oil chemistry. Fringe analysis revealed that fringes of GDI soot were distinctly shorter compared to the other soot types. This finding was confirmed by Raman spectroscopy, indicating that GDI soot is more disordered.

Electrical mobility measurements of particulate emissions were acquired for a GDI engine with a differential mobility spectrometer (DMS). As additional processing is required to compare the detailed particle size distributions to the regulatory solid particle number (SPN), different methods were assessed. While lognormal function fitting can be sufficient for SPN23 measurements, modelling of counting efficiencies by applying digital filtering functions is required for measurements below 23 nm. A new function was designed to match the proposed counting efficiencies for SPN10 of upcoming regulations. Measurements with the DMS combined with a catalytic stripper showed an increase of up to 11.2 % using this new function compared to the closest previous sub-23 nm function. However, the results are highly dependent on the shape of the particle size distribution. For a matrix of test conditions, the shift from SPN23 to SPN10 was observed to result in increases of 27 % to 390 %.

Furthermore, soot particulates were sampled from the exhaust gas on TEM grids for three operating conditions. Core-shell primary particles were observed for all conditions. In addition, some particles at 1500 rpm fast-idle exhibited a surrounding amorphous layer. For 1500 rpm with 40 Nm brake torque, crystalline features within agglomerates and entirely amorphous/crystalline particulates could be found. Fringe analysis of the graphitic primary particle nanostructures did not find significant differences between the operating conditions; however, longer fringes than for the soot-in-oil samples were identified. An additional feature observed in all samples were separate sub-10 nm particulates of non-volatile nature. The average diameter of these particulates was below the lower detection size limit of the DMS.

List of Publications

The following publications resulted from work carried out over the course of the PhD project. For all of these, I was the primary contributor.

S.A. Pfau, A. La Rocca, E. Haffner-Staton, et al. Comparative nanostructure analysis of gasoline turbocharged direct injection and diesel soot-in-oil with carbon black. Carbon, 139:342—352, 2018, DOI 10.1016/j.carbon.2018.06.050.

S.A. Pfau, A. La Rocca, E. Haffner-Staton, et al. Soot in the lubricating oil: An overlooked concern for the gasoline direct injection engine? SAE Technical Paper 2019-01-0301, 2019, DOI 10.4271/2019-01-0301.

S.A. Pfau, A. La Rocca, and M.W. Fay. Quantifying soot nanostructures: Importance of image processing parameters for lattice fringe analysis. Combustion and Flame, 211:430—444, 2020, DOI 10.1016/j.combustflame.2019.10.020.

S.A. Pfau, E. Haffner-Staton, and A. La Rocca. Measurement of sub-23 nm particulate emissions from GDI engines: A comparison of processing methods. SAE Technical Paper 2021-01-0626, 2021, DOI 10.4271/2021-01-0626.

S.A. Pfau, E. Haffner-Staton, A. La Rocca, and M.W. Fay. Investigating the effect of volatiles on sub-23 nm particle number measurements for a downsized GDI engine with a catalytic stripper and digital filtering. Manuscript submitted for publication, 2021.

S.A. Pfau, A. La Rocca, E. Haffner-Staton, and M.W. Fay. TEM investigation of soot from a GDI engine: Influence of operating conditions on nanostructure and morphology. Manuscript submitted for publication, 2021.

Acknowledgements

First and foremost, I thank my supervisor Dr Antonino La Rocca for his guidance, advice, and constant feedback throughout this project. I am grateful for the various opportunities, rewarding experiences, and unwavering support in what has been a formative time, both professionally and personally.

I would also like to thank my co-supervisor Prof Andrei Khlobystov for the insightful conversations and the access to his laboratory. My thanks go to Dr Michael Fay for numerous hours on the electron microscope and to Dr Graham Rance for the Raman spectroscopy and NTA investigations.

Among the technical staff, special thanks go to John Lane, Nigel Sykes, and Paul Bramman for their help maintaining the engine rig, setting up new equipment, and for introducing me to the Nottingham dialect(s).

I would like to thank Dave Spivey and Keith Howard at Lubrizol for supporting the engine tests and the helpful discussions. My thanks also go to Andy Barron at Cambustion for his technical support with the DMS.

I am deeply grateful for my colleagues and friends that supported me along this journey. With special thanks to Ephraim, for all the discussions on soot, politics, and British/German culture. To Annalisa and Felix, for sharing the ups and downs. To Luca, for being mates since Broadgate Park. To Alex, for all the defining features. To Lisa and Matthias, for being there since day one in Wörth. And to Jan, for countless hours on the telephone (even if the hydrogen internal combustion engine might never take off).

Last but certainly not least, I am forever grateful to my family: My parents Andrea and Dirk, my brother Constantin, and my grandparents Erika and the late Albert. I would not be the person I am today without their support, love, and encouragement.

Contents

List of Tables

List of Figures

List of Abbreviations

AFR	air-fuel ratio
AHE	adaptive histogram equalisation
AM	accumulation mode
BDC	bottom dead centre
BMEP	brake mean effective pressure
CAI	controlled auto-ignition
CA	crank angle
CF	conformity factor
CI	compression-ignition
CMD	count median diameter
CNHR	cumulative net heat released
CLAHE	contrast limited adaptive histogram equalisation
CMA	cumulative moving average
CoV	coefficient of variation
CPC	condensation particle counter
CS	catalytic stripper
CVS	constant volume sampling
DAQ	data acquisition
DI	direct-injection
DLS	dynamic light scattering
DMA	differential mobility analyser
DMS	differential mobility spectrometer
DPF	diesel particulate filter
DVPE	dry vapour pressure equivalent
ECU	engine control unit
EDC	European driving cycle
EDX	energy-dispersive X-ray spectroscopy
EEA	European Environment Agency
EELS	electron energy loss spectroscopy
EEPS	engine exhaust particle sizer
EGR	exhaust gas recirculation

EMS	electrical mobility spectrometer
EOC	end of combustion
EOI	end of injection
EVC	exhaust valve closing
EVO	exhaust valve opening
FBP	final boiling point
FFT	fast Fourier transformation
FMEP	friction mean effective pressure
FTP	federal test procedure
GDI	gasoline direct-injection
GHRR	gross heat release rate
GMD	geometric mean diameter
GPF	gasoline particulate filter
GSD	geometric standard deviation
HC	hydrocarbon
HCCI	homogeneous charge compression-ignition
HEPA	high-efficiency particle air
HRR	heat release rate
HRTEM	high-resolution transmission electron microscopy
IMEP	indicated mean effective pressure
IVC	intake valve closing
IVO	intake valve opening
JRC	Joint Research Council
LHV	lower heating value
LNV	lowest normalised value
LRM	linear regression models
MBT	maximum brake torque
MEP	mean effective pressure
MFB	mass fraction burned
MON	motor octane number
NEDC	new European driving cycle
NHRR	net heat release rate
NM	nucleation mode
nmRC	Nanoscale and Microscale Research Centre
NTA	nanoparticle tracking analysis
NTE	not-to-exceed
PAH	polyaromatic hydrocarbons
PEMS	portable emissions measurement system
PFI	port fuel injection
PI	positive-ignition
PM	particulate matter
PMEP	pumping mean effective pressure
PMP	particle measurement programme
PN	particulate number

PNC	particle number counter
PSD	particle size distribution
RDE	real driving emission
ROI	region of interest
RON	research octane number
RP	reference point
SACI	spark-assisted compression-ignition
SD	standard deviation
SI	spark-ignition
SMPS	scanning mobility particle sizer
SOC	start of combustion
SOI	start of injection
SPN	solid particle number
TBD	to be determined
TC	test condition
TDC	top dead centre
TEM	transmission electron microscopy
TGA	thermogravimetric analysis
THC	total unburned hydrocarbon
TPN	total particle number
UNECE	Economic Commission for Europe of the United Nations
TWC	three-way catalyst
VPR	volatile particle remover
WHO	World Health Organization
WLTC	worldwide harmonized light vehicles test cycles
WLTP	worldwide harmonized light vehicles test procedure
XRD	X-ray diffraction

List of Symbols

A	instrument transfer function matrix
a_i	vehicle acceleration at the time i (km/h^2)
A_c	cylinder chamber surface area (m^2)
c_p	specific heat coefficient at constant pressure (J/(kg K))
c_v	specific heat coefficient at constant volume (J/(kg K))
C_1	first constant of Hohenberg's equation
C_2	second constant of Hohenberg's equation
d_i	cut-off size for i % detection or filtration efficiency (nm)
d_p	particle size (nm)
$\overline{d}_{p,g}$	particle geometric mean diameter
e	error term
f_0	constant road load coefficient (N)
f_1	first-order road load coefficient (N)
f_2	second-order road load coefficient (N)
f_e	counting efficiency function
F_c	road load force (N)
h_c	heat transfer coefficient (W/(m^2 K))
h_v	vehicle height (m)
i	electrometer ring current vector
k_{lm}	number of modes
k_r	correction factor for inertial resistance of the drive train during acceleration
k_{sc}	number of size classes
l	lognormal function
LHV	lower heating value of gasoline (MJ/kg)
m	mass (kg)
m_v	vehicle kerb weight (kg)
n_p	particle size concentration (#/cm^3)
N	engine speed (rpm)
N_c	revolutions per complete engine cycle
N_{cyl}	number of cylinders
N_p	total particle number (#/cm^3)

p	in-cylinder pressure (Pa)
p_{max}	in-cylinder peak pressure (Pa)
p_{me}	mean effective pressure (Pa)
$p_{me,b}$	brake mean effective pressure (Pa)
$p_{me,f}$	friction mean effective pressure (Pa)
$p_{me,i}$	indicated mean effective pressure (Pa)
$p_{me,i,g}$	gross indicated mean effective pressure (Pa)
$p_{me,i,n}$	net indicated mean effective pressure (Pa)
$p_{me,p}$	pumping mean effective pressure (Pa)
p_r	in-cylinder pressure at reference CA θ_r (Pa)
$P_{req,i}$	required power at the time i (kW)
PM_i	particulate matter, comprising particles with diameters $\leq$ i µm
Q_g	gross energy released by the combustion (J)
Q_{ht}	energy conveyed by heat transfer (J)
Q_n	net energy released by the combustion (J)
Q_{tot}	total energy released per hour (MJ/h)
R_s	specific gas constant (J/(kg K))
s	particle size spectrum vector
t_{inj}	fuel injection duration (µs)
T	temperature (K)
T_b	brake torque (Nm)
$T_{in,r}$	intake-air temperature at reference CA θ_r (K)
T_w	cylinder wall temperature (K)
U_s	sensible energy of the charge (J)
v_i	vehicle speed at the time i (km/h)
$\overline{v}_p$	mean piston speed (m/s)
V	volume (m^3)
V_r	cylinder volume at reference CA θ_r (m^3)
V_s	swept volume (m^3)
w_v	vehicle width excluding mirrors (m)
W	work (J)
W_b	brake work (J)
W_i	indicated work (J)
W_p	work done by the piston (J)
γ	heat capacity ratio or isentropic coefficient
θ	crank angle (°)
μ_d	count median diameter
σ_g	geometric standard deviation

1 Introduction

Parts of this chapter have previously been published in the journal Carbon and as an SAE Technical Paper that was presented at the SAE 2019 WCX World Congress Experience in Detroit:

S.A. Pfau, A. La Rocca, E. Haffner-Staton, et al. Comparative nanostructure analysis of gasoline turbocharged direct injection and diesel soot-in-oil with carbon black. Carbon, 139:342–352, 2018, DOI 10.1016/j.carbon.2018.06.050.

S.A. Pfau, A. La Rocca, E. Haffner-Staton, et al. Soot in the lubricating oil: An overlooked concern for the gasoline direct injection engine? SAE Technical Paper 2019-01-0301, 2019, DOI 10.4271/2019-01-0301.

1.1 Particulate Emissions of Gasoline Engines

Particulate emissions were historically associated with compression-ignition (CI) diesel engines which are predominantly using direct-injection (DI) systems. Due to the injection directly into the combustion chamber during the compression stroke, the air-fuel mixture is inherently heterogeneous to some degree. During the combustion process, particles form in fuel-rich zones of the cylinder. In the case of gasoline engines, also referred to as spark-ignition (SI) or positive-ignition (PI) engines, DI systems offer significant improvements in terms of fuel efficiency over port fuel injection (PFI) systems [1]. The technology is not new but was already used in the 1950s for some automotive applications. The Goliath GP700 and Gutbrod Superior 600 were powered by two-stroke DI gasoline engines and were shortly

followed by the well-known Mercedes 300SL with the first automotive four-stroke DI gasoline engine [2]. The new technology was implemented to increase performance. Fuel evaporation upon high-pressure injection into the combustion chamber provides a charge cooling effect. The cooling effect enables higher compression ratios and thus increased volumetric efficiency. The injection timing was initially placed early, during the intake stroke, to achieve a homogeneous air-fuel mixture. Further potential of the DI technology can be realised by operating the engine without restricting the air intake. Therewith, throttling losses that are inherent to PFI systems can be eliminated. However, stratified fuel injection late in the compression stroke is required for good combustion performance [1]. The stratification achieves a rich air-fuel mixture around the spark plug within a generally lean combustion chamber environment. Limitations of mechanical fuel injection systems at the time meant that the available range for injection timing variations was restricted [3]. The results were performance penalties at higher loads and increased soot emission. As NO_X emissions were an additional concern, PFI engines with three-way catalysts (TWCs) were more cost-effective [2].

A distinctive change in this preference could be observed over the last two to three decades. Due to increasingly stricter emission regulations and targets to reduce CO_2 emissions, manufacturers had to seek ways to improve the efficiency of internal combustion engines. Advances in electronic control systems enabled circumventing the previous obstacles of DI systems for gasoline engines [2]. Wider ranges for injection timing variations meant that throttling loss reductions could be realised with stratified lean-burn at low loads, while a transition to homogeneous injection at higher loads provides the required performance. In combination with developments in turbocharger technology, engine downsizing becomes feasible and enables further performance improvements [4, 5]. The sum of these changes led to a fundamental change in market trends.

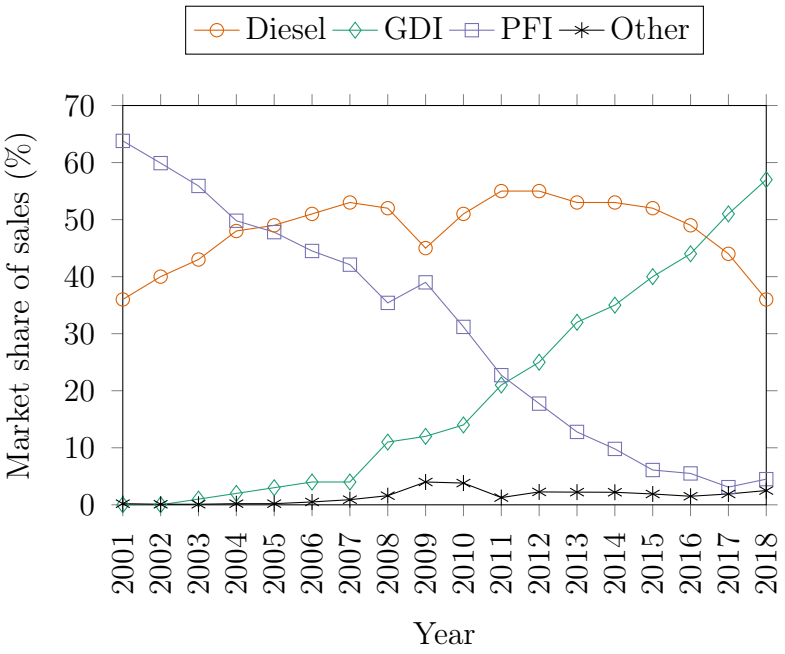

Figure 1.1: Market share of passenger vehicle sales by engine technology. Average of all vehicle sales in the European Union (EU-27). 'Other' includes natural gas and battery electric vehicles. Data from [6].

To illustrate the resulting dynamic situation in the automotive sector, the market share of sales in the European Union by different engine technologies is presented in Figure 1.1. The data set from 2001 to 2018 shows a drastic restructuring in terms of prevalent engine types. In 2001, PFI engines were dominant with almost 64 % of sales. Over the following 17 years, their share decreased to below 5 %. In contrast, the share of gasoline direct-injection (GDI) engines increased from virtually non-existent to 57 % during the same period. A different observation can be made for diesel engines. Their share of sales initially increased with the decline of PFI engines, from 36 % in 2001 up to a maximum of 55 % in 2011/2012. Beyond 2012 the share of diesel engines declined. The pronounced decrease after 2015, down to 36 % in 2018, can likely be attributed to the Dieselgate scandal that broke in late 2015 and the subsequent loss of trust in diesel engines [6].

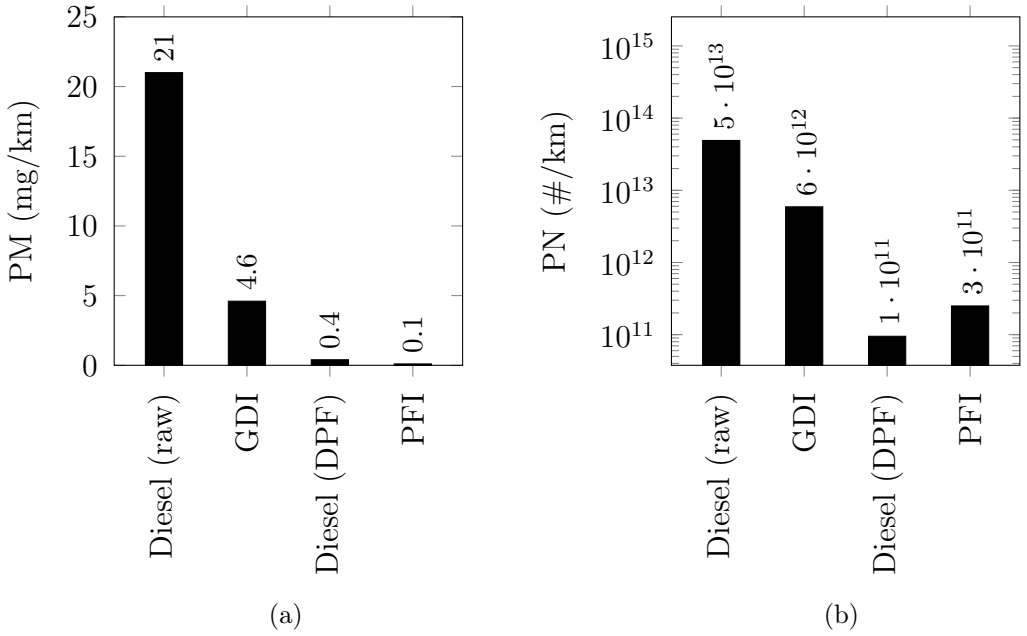

Figure 1.2: Particulate mass (a) and number (b) emission levels for different engine types over the NEDC. Data from [7].

Despite the significant improvements that enabled the rise of GDI engines, the inherent challenge of particulate emissions for this engine type remains. A comparative study by Braisher et al. [7] investigated the difference in particulate emission levels between diesel engines with and without diesel particulate filter (DPF), PFI engines, and GDI engines (see Figure 1.2). The highest levels could be observed for diesel engines without DPF, both in terms of mass and number. On the other end of the spectrum are diesel engines with DPF and PFI engines. Their emission levels were similar and two orders of magnitude lower than those of diesel engines without DPF. GDI engines fall in the middle, with emission levels that are one order of magnitude higher than PFI engines but lower than diesel engines without DPF.

With ongoing efforts to reduce emissions and to decarbonise transport, the question arises as to what the role of GDI engines could be in the future. Even for heavily hybridised powertrains which can facilitate engine operation

at more steady and optimised conditions, the efficiency advantage of GDI systems over PFI concepts applies, i.e. higher compression ratios as a result of charge cooling effects. Borghi et al. [8] noted that the GDI technology could also be beneficial for smaller range extender engines in electric vehicles. While electrification is advancing in many developed countries, the resulting changes are not as readily possible in developing countries. Consequently, traditional engine technologies and the associated emissions remain relevant challenges in these markets. Biofuels such as ethanol could potentially penetrate a wider range of different markets. However, recent studies suggest that the resulting particulate emissions can differ greatly for various fuel blends [9–11]. In the following, the necessary terminology for the description of particulate emissions is detailed. Moreover, the implications of elevated particulate emission levels are outlined regarding human health, the environment, and engine components.

1.2 Terminology and Nomenclature

A range of terms is used to describe particulate emissions from vehicles and other sources. 'Particulate matter' is an umbrella term to describe aerosols from various sources such as power plants, wood fires or even household cooking. In the context of internal combustion engines, particulate matter (PM) comprises a range of species such as soot, ash, volatile components, and other air-borne species such as particles derived from sulphates (SO_X) and nitrates (NO_X) [12]. The acronym 'PM' is often used in conjunction with a size range indication; PM_i includes particles with a diameter of i µm and smaller, e.g. particles 10 µm and smaller for PM_{10}. Specifically, $PM_{2.5}$ and $PM_{0.1}$ are often referred to as fine and ultrafine particles, respectively. PM emission levels are commonly expressed as mass concentration, e.g. the World Health Organization (WHO) guideline of $PM_{2.5}$ below 10 µg/m^3 as annual mean [13]. Recent regulations for engine emissions include limits on both the

total mass of particles and the particulate number (PN). With this additional metric, the acronym 'PM' is often used to describe particulate mass.

Likewise, a range of terms is used for the qualitative description of the particle types. Soot specifically refers to carbonaceous particles from the incomplete combustion of hydrocarbons. Studies on atmospheric aerosols often use the term 'black carbon' to refer to both soot and other combustion-derived chars, with a high potential for light absorption [14]. Despite similar in name, 'carbon black' refers to commercially generated soot from processes such as combustion or pyrolysis of hydrocarbons, with applications in printer inks, tyres, and others [15]. Moreover, carbon black is considered to be a more affordable and reproducible substitute for engine soot in studies on engine wear due to the high costs, long run-times, and strong dependency on operating conditions associated with generating genuine engine-soot [16].

An additional dimension to the description of samples is their chemical composition. The ratio of elemental carbon to organic carbon is often used in studies to characterise carbon-based aerosols [17]. 'Elemental carbon' refers to materials that are predominantly composed of carbon ($> 80\,\%$), such as pyrolysis-derived carbon black or flame-derived soot. 'Organic carbon' comprises a range of other molecular hydrocarbon species with a—in comparison—lower concentration of carbon.

Particulates emitted from engines are often classified in three size groups that are based on commonly observed modes in the particle size distributions (PSDs) [18] and further relate to steps of the formation process: nucleation mode (5 nm to 50 nm diameter range), accumulation mode (100 nm to 300 nm diameter range), and coarse mode (> 1000 nm diameter range). The formation process of soot is described in detail in Section 2.2.1.

1.3 Impact on Health and Environment

Ambient air pollution was identified to be the biggest environmental risk to human health by the WHO in 2016 [19]. One in nine deaths was found to be attributable to ambient air pollution. Likewise, the European Environment Agency (EEA) noted that "fine particulate matter ($\leq$ 2.5 µm, $PM_{2.5}$) is responsible for around 400 000 premature deaths in Europe every year with the largest relative impacts observed in central and eastern European countries" [20]. In light of increasing urbanisation, it is concerning that the EEA observed in a 2020 report that almost 74 % of the urban population in Europe is exposed to $PM_{2.5}$ levels above the WHO limits [21]. To combat this issue, guidelines on particulate emission levels have been published by the WHO already in 2005 [13]: annual average emission levels of 10 µg/m^3 and 20 µg/m^3 for $PM_{2.5}$ and PM_{10}, respectively. These guidelines are typically implemented on a national level, e.g. by the national air quality objectives as part of the Air Quality Strategy in the UK [22]. The strategy paper lists targeted annual emission levels for the UK (except Scotland) of 25 µg/m^3 and 40 µg/m^3 for $PM_{2.5}$ and PM_{10}, respectively. These targets are roughly double the limits of the WHO guidelines.

A range of adverse health effects is associated with the exposure to particulate emissions, such as contribution to cardiovascular diseases [23], elevated levels of inflammation [24], and increased risk of cancer [25]. The detrimental effect can be partly attributed to the particles themselves and further to adsorbed species such as polyaromatic hydrocarbons (PAH) on the surface of the particles [26]. The health impact appears to be highly dependent on particle size. The inflammatory response was previously observed to correlate better with the particle surface area rather than the total mass [27]. Smaller particles were found to penetrate deeper into the respiratory tract [24]. While the specific location of deposition along the respiratory tract varies, the total deposition fraction generally increases with decreasing particle size [28]. Further studies observed that ultrafine particles could

translocate from the lungs into the bloodstream and could potentially even disrupt the blood-brain barrier [23, 29].

An additional dimension of particulate emissions is their climate impact. Suspended in the atmosphere, black carbon particulates absorb more light than they reflect and contribute to global warming [30]. The residence time in the atmosphere is again dependent on the particle size. Nucleation mode particles are likely to coagulate, while coarse mode particles are removed quickly from the atmosphere due to gravitational sedimentation. The longest residence time can be observed for accumulation mode particles [28]. Bond et al. [30] noted that particles are typically removed within days to weeks via precipitation as well as contact with surfaces. Due to the shorter atmospheric lifetime compared to CO_2, benefits of particulate emission reductions could be more quickly realised [31].

1.4 Impact on Engine Components

The fitting of particulate filters to diesel vehicles has become a widely adopted approach to lowering particulate emission levels. Soot, ash, and other particles are trapped in layers of mesh grid. The accumulating soot-cake is periodically oxidised, commonly referred to as regeneration. For optimal efficiency, the combination of regeneration frequency and selected filter mesh grade has to be adjusted for the properties of the emitted soot. Specifically, the size of the soot particulates determines the available surface area and affects the build-up of deposits [32, 33]. The filter regeneration highly depends on the material's reactivity. In addition to the surface area, the reactivity of soot is influenced by its composition and nanostructure [34, 35]. Song et al. [32] observed a correlation between better DPF regeneration and a higher concentration of oxygen-containing functional groups on the surface of soot structures. This was attributed to an increased oxidation efficiency. Lapuerta et al. [33] noted that while biodiesel soot possessed a more ordered and graphitic—i.e. theoretically less reactive—structure than

diesel soot, it was more efficiently oxidised in the particulate filter due to smaller primary particles increasing the available surface area.

While the generated PM predominantly escapes the cylinder with the exhaust gas, a small proportion of particles transfers into the lubricating oil via blow-by gases and thermophoretic processes upon impingement on the combustion chamber walls [36]. The accumulation of soot in the lubricating oil has long been understood to cause a variety of issues. Gautam et al. [37] observed a proportional relation between the soot concentration in the oil and the wear of lubricated engine components. The correlation was confirmed in studies by Sato et al. [38] and Green et al. [36], further reporting that the wear is more pronounced for components with thinner films of lubricating oil. One such part is the engine valve train. Wear of the incorporated valve train manifests as surface degradation and a reduction in cam diameter, leading in turn to increased friction and reduced valve lift, respectively. Consequently, the cylinder gas exchange is impeded and the engine efficiency is reduced.

Li et al. [39] suggested that three-body abrasive wear occurs for lubricant films thinner than the soot particle size. This theory was supported by observed wear scar widths closely matching the size of primary particles. Several studies into the wear behaviour of soot in the lubricating oil can be found in the literature; many of these used carbon black as a substitute for engine-generated soot. Despite some differences in surface chemistry and aggregate size, Clague et al. [16] suggested that nanostructure similarities enable the surrogacy of carbon black for diesel soot. The motivation for the replacement can be found in the long run-times and high costs associated with generating genuine engine-soot, as well as the influence of operating conditions on the soot properties. In contrast, commercial processes provide a more affordable product with easily reproducible characteristics. Berbezier et al. [40] investigated the effect of the primary particle size of different carbon blacks on the component wear. With increasing particle size, the wear rate increased and the anti-wear properties of the oil were reduced.

This finding was confirmed by Mainwaring [41], observing more aggressive wear behaviour for soot with larger primary particle sizes.

However, Growney et al. [42] found that the ability to substitute engine soot with carbon black is highly dependent on the lubricating oil formulation. Likewise, investigations by Antusch et al. [43] showed distinctive differences between engine wear tests conducted with engine soot and carbon black in the lubricating oil. The authors established that the wear rate is not exclusively influenced by the concentration of soot or carbon black but also by the interaction of oil additives and particles, i.e. affected by morphology, chemical composition, and reactivity of the particles. Esangbedo et al. [44] found that the effectiveness of oil additives, such as dispersants, depends on the nanostructure and the surface oxygen content. Unsuitable oil formulations can lead to agglomeration of particles and, in turn, a change of the oil effective viscosity, i.e. oil thickening. The implications of oil thickening can be pumpability issues [45], oil starvation, and consequently wear due to metal-metal contact.

Only a few studies are available on the direct comparison of soot generated by diesel and GDI engines. Barone et al. [46], as well as Gaddam and Vander Wal [47], identified similarities in the nanostructure of GDI and diesel soots, although larger primary particles were observed for GDI. In a study by Uy et al. [48], GDI soot was found to be less homogeneous than diesel soot. While some GDI particles appeared to be similar in morphology to diesel soot, some particles with an amorphous structure were detected, and other regions seemed “sludge-like”. The latter exhibited higher concentrations of trace elements linked to wear metals and oil additives. A later study by Liati et al. [49] found GDI soot nanostructure to be less ordered than diesel soot, indicating that the former may contain organic compounds that prevent crystallisation.

1.5 Aims and Objectives

The overall aim of this project is to obtain detailed characteristics of soot from GDI engines and to progress towards understanding the effect of operating conditions on the emitted particulates, closing the gap in knowledge to diesel engine soot. The following objectives were defined to achieve this:

- Enable meaningful nanostructure quantification by assessing the influence of processing parameters on fringe analysis metrics, identifying an optimal set of parameters, and outlining considerations for image acquisition.
- Compare soot samples from GDI engines with diesel engine soot and carbon black, using a broad range of techniques to cover both agglomerate and primary particle sizes but also nanostructure properties and the chemical composition.
- Compare existing data processing methods for electrical mobility measurements of particulate emissions with a focus on sub-23 nm regulatory size limits. Update the data filtering function for proposed counting efficiencies of future regulations.
- Assess the effect of a catalytic stripper on particulate measurements and the potential impact of upcoming regulatory changes. Further, investigate the effect of operating conditions on particulate emissions.
- Acquire transmission electron microscopy (TEM) images in addition to electrical mobility measurements to enable detailed particle measurements, nanostructure quantification, and confirmation of sub-23 nm particulates.

1.6 Thesis Layout

This thesis comprises a total of nine chapters. After this introductory first chapter, a literature review is presented in Chapter 2, and the experi-

mental methods are described in Chapter 3. The main working chapters are Chapters 4 to 8. The findings of each of these main chapters led to at least one publication or submitted manuscript. The final chapter comprises the conclusions and an outline of the contribution to knowledge and opportunities for future work.

The literature review in Chapter 2 covers the fundamental characteristics of soot and the background of both ex-situ and in-situ soot analysis techniques. Moreover, the regulatory framework of vehicle emission limits is described and existing knowledge on the effect of engine operating conditions on particulate emissions is summarised, with a focus on GDI engines.

The experimental description in Chapter 3 includes details of engine equipment, measurement instruments, and relevant calculations, and analytical techniques. Furthermore, a test matrix of relevant operating conditions is derived from driving cycles that are used for regulatory checks of vehicles. A defined procedure is further outlined for conditioning the engine and to assess the repeatability using key metrics. Moreover, the analysis of these metrics for the conducted engine tests is included to improve the flow of subsequent chapters.

The focus of Chapter 4 lies on fringe analysis as a tool for the quantitative assessment of graphitic nanostructure. The influence of the image processing parameters on the obtained metrics is investigated, and optimised parameters are suggested. Moreover, the importance of the TEM image quality and focus point is demonstrated.

Soot-in-oil samples from GDI and diesel engines as well as a carbon black are compared in Chapter 5 using a range of analysis techniques. The deposition rate of soot into the lubricating oil for a GDI is determined and compared to values in the literature for diesel engines. TEM images of soot particulates are used to qualitatively describe their morphology and further to determine the size of aggregates, primary particle diameters, and nanostructure properties. For the latter, fringe analysis was were employed.

In Chapter 6, different approaches to data processing of exhaust soot measurements are compared, with the underlying goal of obtaining regulatory metrics from more detailed size distributions. An updated digital filtering function for differential mobility spectrometer (DMS) data is proposed, based on the counting efficiencies under discussion for upcoming regulations of sub-23 nm measurements.

The presence of volatiles and their impact on exhaust soot size measurements is investigated in Chapter 7. Measurements acquired with and without catalytic stripper are compared to determine the fraction of volatile species—that are removable by the catalytic stripper—in the exhaust gas. By applying filtering functions based on the current and newly proposed regulatory counting efficiencies to the respective data sets, the effect of the new regulations on the total particulate number is assessed.

The previous two chapters are complemented by a TEM analysis of exhaust-sampled soot particulates in Chapter 8. Aggregates and primary particles are characterised both qualitatively and quantitatively. The findings are compared to the analysis of the soot-in-oil samples in Chapter 5.

The thesis is concluded in Chapter 9 by summarising the findings of the main chapters, outlining the contribution to existing knowledge, and providing an outlook on opportunities for future work.

2 Literature Review

As established in Chapter 1, the characteristics of particulate matter are diverse. Likewise, a broad range of analysis techniques is available with various underlying measurement principles and specific strengths. In general, two areas can be differentiated: measurement of soot as it is emitted from an engine (i.e. in-situ, on-line, simultaneously to engine testing) and analysis of soot after collection with potential further sample preparation (i.e. ex-situ, off-line, after completed engine testing). The former is commonly used for legislative purposes and enables characterisation of particulate emissions from vehicles on rolling road test stands or in real-world environments. Off-line analysis techniques can provide more in-depth characteristics of soot particles. As such, characterisation is not only limited to exhaust emissions but can also extend to soot that transferred into the lubricating oil. However, these techniques often involve dedicated sample preparation and additional equipment with associated time requirements and expenses. This chapter sets out to provide a comprehensive overview of both areas.

First, the underlying coverage of GDI soot is assessed through a systematised literature search. Next, general information on soot nanoparticles is provided, covering the formation process, particulate modes, and details on more detailed characteristics. As much of this description is based on ex-situ techniques, a selection of analysis methods is outlined next. Subsequently, considerations for in-situ analysis of soot are outlined, covering methods for sampling and conditioning of exhaust gas, and different measurement devices. The challenging aspect of measurement variability is outlined before describing the legal dimension to emissions measurements. Lastly, a

summary of previous research studies is presented, including findings on the effect of engine operating conditions (i.e. speed and load) and parameters (e.g. injection timing and pressure, valve timing, and spark timing) on the particulate emissions.

Parts of this chapter have previously been published in the journal Carbon, as an SAE Technical Paper that was presented at the SAE 2019 WCX World Congress Experience in Detroit, in the journal Combustion and Flame, as an SAE Technical Paper that was presented at the SAE 2021 WCX Digital Summit, and also included in a manuscript that was submitted for publication:

S.A. Pfau, A. La Rocca, E. Haffner-Staton, et al. Comparative nanostructure analysis of gasoline turbocharged direct injection and diesel soot-in-oil with carbon black. Carbon, 139:342-–352, 2018, DOI 10.1016/j.carbon.2018.06.050.

S.A. Pfau, A. La Rocca, E. Haffner-Staton, et al. Soot in the lubricating oil: An overlooked concern for the gasoline direct injection engine? SAE Technical Paper 2019-01-0301, 2019, DOI 10.4271/2019-01-0301.

S.A. Pfau, A. La Rocca, and M.W. Fay. Quantifying soot nanostructures: Importance of image processing parameters for lattice fringe analysis. Combustion and Flame, 211:430-–444, 2020, DOI 10.1016/j.combustflame.2019.10.020.

S.A. Pfau, E. Haffner-Staton, and A. La Rocca. Measurement of sub-23 nm particulate emissions from GDI engines: A comparison of processing methods. SAE Technical Paper 2021-01-0626, 2021, DOI 10.4271/2021-01-0626.

S.A. Pfau, E. Haffner-Staton, A. La Rocca, and M.W. Fay. Investigating the effect of volatiles on sub-23 nm particle number measurements for a downsized GDI engine with a catalytic stripper and digital filtering. Manuscript submitted for publication, 2021.

2.1 Coverage in the Literature

Despite the publication of a number of studies that investigated the intricacies of particulate matter emitted by GDI engines, the literature on this subject is still sparse compared to the vast quantity of articles on diesel particulate matter. A brief systematised literature search was conducted to quantify this perceived situation. The accessed platforms were Web of Science [50] with all available databases, and SAE Mobilus [51]. The search was conducted on 23 February 2021 to include documents published up to and including 2020. Only documents of type 'article' were included from Web of Science, and the results from SAE Mobilus were filtered for journal articles and technical papers. The general field of interest was first specified with three relevant search terms:

```
(soot OR particulate matter OR partic* emission*)
```

These terms were assumed to cover a range of the used terminology. Furthermore, the three technology types—diesel, GDI, and PFI—were covered by the following search terms, respectively:

```
(diesel OR compression ign* OR ci engine*)

(gasoline direct inject* OR gdi OR gtdi OR disi OR
   sidi OR direct injection spark ign*)

(port fuel inject* OR pfi)
```

The search for each technology type was then conducted by combining its search term with the general field search term (i.e. by using `AND`).

The earliest articles found for GDI and PFI engines using these criteria were published in 1999. In the same year, the literature on diesel engines in this thematic area counted already 573 articles. From there, the number of publications on diesel particulate matter continued to grow at increasing rates (see Figure 2.1a). The rate of published studies with GDI engines

remained low until 2009. In the following year—virtually coinciding with the increase in sales of vehicles with GDI engines—a surge of new articles could be observed that continues until today (see Figure 2.1b). However, the total number of publications on GDI engine particulate matter in 2020 is still below the number of studies with diesel engines in 1999. While almost 50 % of papers on diesel particulate matter and soot were published before 2010, nearly 95 % of papers on GDI particulate matter and soot were published after 2010. Interestingly, articles focusing on particulate emissions from PFI engines increased only after 2013. However, their number remains low with less than 50 articles.

As an additional point, the search was also conducted only with the initial terms specifying the field, without applying further terms for the engine technologies. This search resulted in a total of 24 807 articles that have been published up to and including 2020. The studies cover a range of areas, including health impacts, implications for the environment, and laboratory works on flame-generated soot. The latter being conducted to investigate the underlying principles of soot formation.

2.2 Soot Nanoparticles

Despite the relatively scarce literature on GDI engine soot, knowledge on underlying principles of soot formation and characteristics can be found. The general tendency of soot to form in fuel-rich zones within the engine cylinder during combustion was mentioned in Section 1.1. The following discussion covers a more detailed outline of the chemical pathways of soot formation, differentiating the individual stages and resulting structural properties. Subsequently, further information is provided, ranging from the size of primary particles and their nanostructure to aggregate morphology and chemical features.

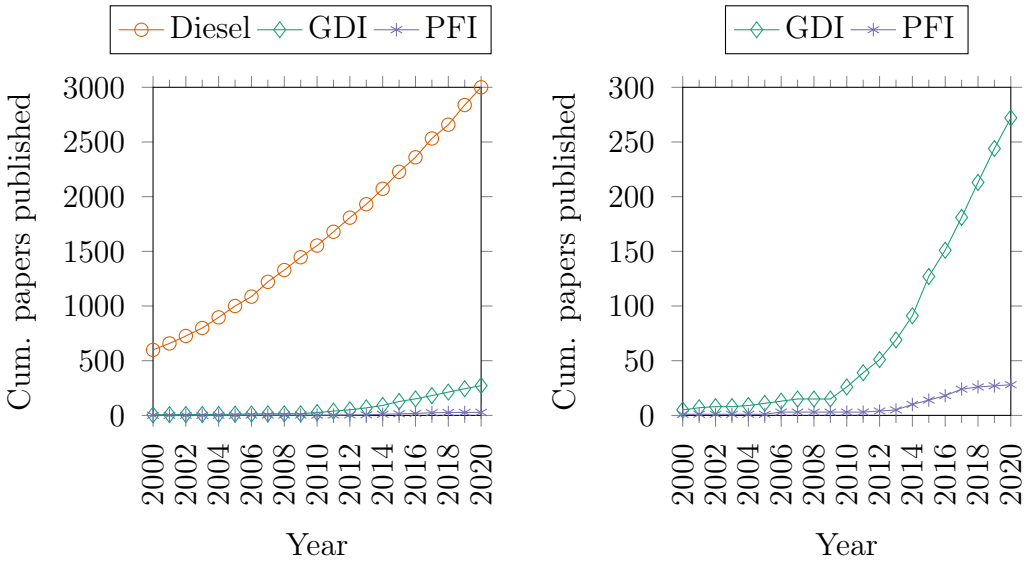

Figure 2.1: Cumulative number of publications on particulate emissions from diesel, GDI, and PFI engines (a). Enlarged section for publications on GDI and PFI engines (b). Data from systematised literature search on Web of Science [50] and SAE Mobilus [51], dated 23 February 2021.

2.2.1 Formation Process and Particulate Modes

A considerable amount of research has been conducted on the fundamental principles of soot formation. The general phases of this process have been understood to consist of: creation of vapour-phase precursor molecules, nucleation of solid particles, surface growth by addition of vapour-phase molecules, coagulation due to particle-particle collisions, and lastly, carbonisation and oxidation processes [52].

In non-stoichiometric conditions, fuel is broken down into unsaturated and radical species rather than reacting with oxygen. Acetylene is often thought of as an initial species, leading to the formation of small aromatic species such as benzene and naphthalene through polymerisation reactions. However, the

extent of acetylene's role is under debate and considered to vary depending on the specific fuel [52]. For aliphatic fuels, the first aromatic ring must be formed by elemental reactions of other species first, while the breakdown of aromatic fuels provides such species in higher concentration directly [53].

Radical reactions continue to form extended polyaromatic species—i.e. PAH—with a mass range of ca. 500 u to 1000 u (atomic mass units). The nucleation of incipient or 'nascent' soot particles occurs at effective diameters of around 1.5 nm with a particle mass of around 2000 u. Theoretical models have been proposed for the specific chemical pathways, but the incipient particles and even more so the vapour-phase species are challenging to identify experimentally. Gas-chromatography can be used for chemical analysis; however, the technique is usually limited to species up to 300 u [52]. On the other hand, imaging by high-resolution transmission electron microscopy (HRTEM) can only identify solid particles larger than 1.5 nm [52]. Only in a recent study by Commodo et al. [54], aromatic species—assumed to originate from the early stage of particle formation—were imaged by atomic force microscopy, covering a mass range of 200 u to 700 u.

The growth of particles continues by the addition of vapour-phase species to the surface of the solid particulates. This step is considered to be the predominant source of mass increase, with higher growth rates for smaller particles due to more available reactive radical sites [55]. Moreover, coalescence (or coagulation) of particles occurs due to particle-particle collisions. In this case, two roughly spherical particles collide and form another, also spherical particle [55]. Consequently, the average particle size increases while the particle number decreases. The overall particle mass remains constant during this process. The resulting particulates are often referred to as 'primary particles', typically in the range of 10 nm to 50 nm in diameter [34]. Subsequent collisions of primary particles lead to agglomeration or aggregation, forming fractal-like structures typically associated with soot particulates [56] (see Figure 2.2a).

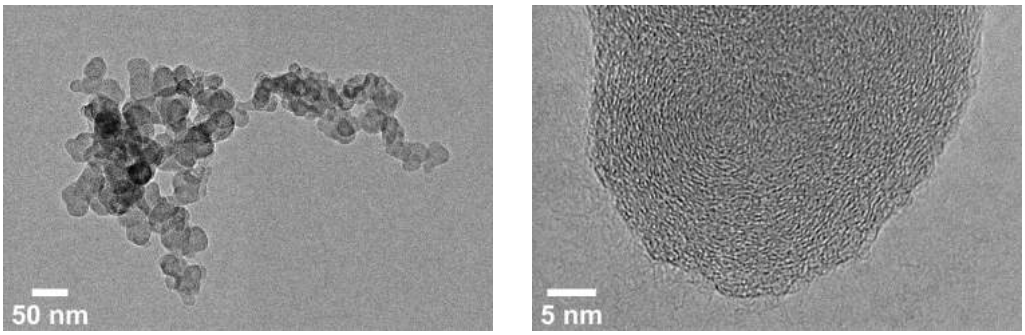

(a) (b)

Figure 2.2: TEM images of a typical soot agglomerate (a) and the nanostructure of a primary particle (b).

In the high-temperature environment of the cylinder during combustion, the particles further undergo restructuring processes and are increasingly carbonised. This process—also referred to as dehydrogenation—effectively shifts the carbon-to-hydrogen ratio from initial values of up to 1:1 to more carbon-dominant ratios of 8:1 by eliminating functional groups [57]. Concurrently, the initially amorphous particles become increasingly graphitic [52], resulting in the typical nanostructure of primary particles with an amorphous core and a surrounding graphitic shell (see Figure 2.2b). This transition is often used as a criterion of soot 'maturity', i.e. distinguishing between nascent and carbonised soot primary particles [58].

In addition to restructuring, exposure of the carbonaceous particles to oxygen in a high-temperature environment also leads to oxidation reactions. Despite the description of the formation process as an ordered sequence, the individual steps take place in parallel. Consequently, the oxidation step can eliminate soot nuclei entirely or reduce the size of larger particles [36].

In practical terms, size measurements of exhaust particulates commonly exhibit three distinct size modes: nucleation mode, accumulation mode, and coarse mode. Typical particle size distributions in terms of number and mass weighting are displayed in Figure 2.3 as reported by Kittelson [18].

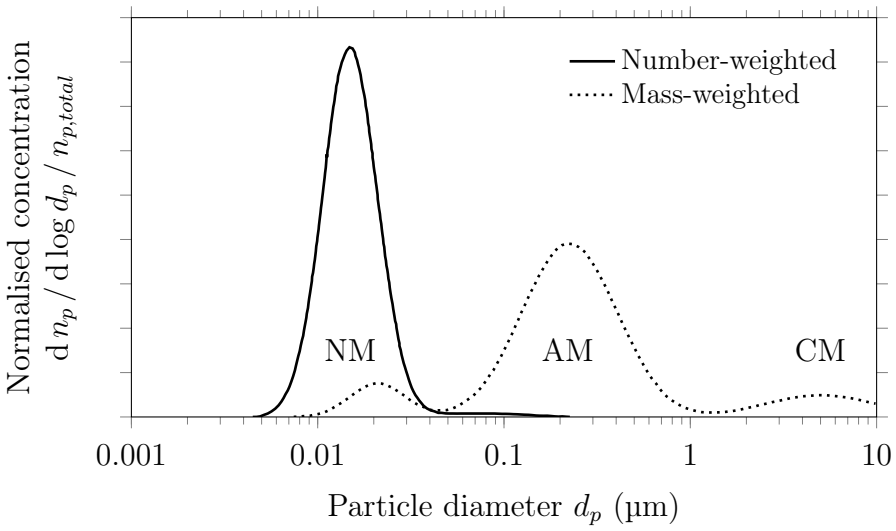

Figure 2.3: Typical size distribution for engine particulate emissions, both number-weighted and mass-weighted. NM: nucleation mode, AM: accumulation mode, CM: coarse mode. Adapted from [18].

It should be noted that particle distributions reported in several studies, since the publication by Kittelson, show a predominance of particulates around 100 nm. The nucleation mode is thought to comprise (semi-)volatile species, i.e. soot precursors and solid primary particles. More mature soot agglomerates are included in the accumulation mode. The third size mode, the coarse mode, is considered to stem from soot that deposited on exhaust surfaces or the cylinder surface itself, and later re-entered the exhaust gas [18]. However, the mode can also include particulates other than soot, such as from engine wear and rust [59, p. 53]. The coarse mode does not significantly contribute to the total PN and is often excluded from PN measurements [60]. However, coarse particles have to be considered in PM measurements.

2.2.2 Primary Particles and Nanostructure

Primary particles are usually integrated within larger agglomerates. Thus, in-situ analysis is generally not feasible, but rather ex-situ measurement upon

the sampling of particulates is required. TEM imaging is a commonly used technique for this purpose, further described in Section 2.3.1. A simple metric that can be obtained from the acquired images is the primary particle size. An overview of some reported findings is presented in Table 2.1. Information on the overall range, mean, and mode of the measurement statistics are not always reported consistently; however, general trends can still be identified.

Lee et al. [61] collected soot from the exhaust gas of a light duty diesel engine. The primary particle diameters ranged 10 nm to 60 nm, with mean diameters of 28 nm to 34 nm depending on the operating conditions. In a subsequent study of Zhu et al. [62] with a different engine, the same diameter range and similar mean diameters of 19 nm to 33 nm were observed. Similarly, Neer and Köylü [63] observed primary particles of mean diameter 20 nm to 35 nm for exhaust soot from a medium duty diesel engine at different operating conditions. Such findings are further supported by a study of Lapuerta et al. [64], reporting a mean primary particle diameter of 25 nm for a light duty diesel. However, the diameters only ranged from 10 nm to 45 nm. In contrast, a study by Liati et al. [65] found a mean primary particle diameter of 13.7 nm, with 60 % of particles measuring below 13 nm.

Barone et al. [46] assessed primary particles of exhaust soot from a GDI engine. The particle diameters ranged 7 nm to 60 nm with a mode between 20 nm and 25 nm. Liati et al. [49] observed a similar range of 5 nm to 50 nm but with a lower mode between 10 nm and 15 nm. Gaddam and Vander Wal [47] further reported a diameter range of 7 nm to 65 nm and mean diameters of 16 nm to 25 nm for GDI soot particles, depending on engine operating conditions. Thus, GDI exhaust soot primary particles appear to be similar to those of diesel engines.

Fewer studies are available on the properties of soot that has transferred into the lubricating oil ('soot-in-oil'). For soot in the lubricating oil of a diesel engine, La Rocca et al. [34] observed the mean primary particle diameter to be 20.2 nm, similar to exhaust soot. However, the range of diameters was narrower with a span from 10 nm to 35 nm. A study by

Table 2.1: Reported primary particle diameter ranges, means, and mode as measured from TEM images for diesel and GDI soot obtained from the exhaust gas stream and lubricating oil of the engines. (* bimodal distribution observed)

Reference	Fuel	Origin	Range (nm)	Mean (nm)	Mode (nm)
Lee et al. [61]	Diesel	Exhaust	10–60	28–34	20–40
Zhu et al. [62]	Diesel	Exhaust	10–60	19–33	15–25
Neer and Köylü [63]	Diesel	Exhaust	—	20–35	—
Lapuerta et al. [64]	Diesel	Exhaust	10–45	25	20–25
Liati et al. [65]	Diesel	Exhaust	4–36	13.7	10
La Rocca et al. [34]	Diesel	Oil	10–35	20.2	20
Ferraro et al. [66]	Diesel	Oil	—	25 / 48*	—
Barone et al. [46]	GDI	Exhaust	7–60	—	10–15
Liati et al. [49]	GDI	Exhaust	5–50	—	10–15
Gaddam and Vander Wal [47]	GDI	Exhaust	7–65	16–25	14–22
La Rocca et al. [67]	GDI	Oil	20–90	36	32

Ferraro et al. [66] reported a mean particle diameter of 25 nm; however, a second distribution around 48 nm was also observed, accounting for almost 9 % of particles. Research on GDI soot-in-oil is even more scarce. An initial study by La Rocca et al. [67] showed an extended diameter range of 20 nm to 90 nm, with a mean diameter of 36 nm.

A qualitative assessment of primary particles by Antusch et al. [43] identified more disorder in GDI soot compared to diesel soot. Likewise, Liati et al. [49] found the GDI soot nanostructure to be less ordered than diesel soot. In contrast, Barone et al. [46] identified similarities in the nanostructure of GDI and diesel soot with comparable structures, i.e. amorphous core and graphitic shell. These findings were confirmed by Uy et al. [48]; however, entirely amorphous particles were observed in addition to traditional primary particles. A study by La Rocca et al. [67] identified an additional amorphous layer surrounding the segment of graphitic layers for GDI soot primary particles.

Carbon nanostructures can further be quantified by analysing the graphitic segments, so-called 'fringes', in the HRTEM images. The relevant background of such image processing algorithms is described in Section 2.3.2. Individual methods and scripts have generally been developed using carbon blacks and flame-generated soot as samples [68–70]. Few studies are available on diesel soot [71–75] and just as is the case for soot-in-oil, only few publications focus on GDI soot [47, 76, 77]. A detailed discussion is included in Section 5.3.1, with findings indicating that GDI soot exhibits a more disordered nanostructure. However, prior to the publication of the findings in Chapter 5, no study had been based on an integrated approach of comparing diesel and GDI soot samples within a single study. The challenge of comparing quantitative results across studies lies in the inherent variability of the TEM imaging process and the potential influence of previously underreported parameters of the fringe analysis algorithms (cf. Section 2.3.2).

2.2.3 Soot Aggregates and Morphology

The measurement of aggregates can be facilitated in-situ, enabling particulate measurements during transient and steady-state engine tests. Several techniques are available for this purpose; however, obtaining reliable and repeatable results presents a particular challenge. Depending on the specific measurement method, a simplified total number of particles or a more detailed size distribution of equivalence diameters can be obtained. The technical background and efforts towards standardisation are described in Section 2.4. Findings of previous studies are further discussed in Section 2.6.

As shown in Figure 2.2a, aggregates are not simplistic spheres but rather complex, fractal structures consisting of several spherical particles. Consequently, equivalence diameters can describe a general size distribution but cannot capture the intricacies of specific particle shapes. More information can be obtained from TEM imaging. Qualitatively, an early comparative study by Uy et al. [48] observed structural similarities between diesel and GDI soot from both exhaust and lubricating oil. However, GDI soot also exhibited "sludge-like" regions with less distinctive particle borders and amorphous carbon. Similar observations were reported by An et al. [78]. These observations could indicate differences in the soot formation process for GDI engines, affecting the carbonisation of particles.

Measurements of soot particles as imaged by TEM promise further insight into their properties. Different approaches have been used across studies, mostly relying on the two-dimensional projections of agglomerates as visible in a single TEM image. Common parameters include the radius of gyration [62, 79] as well as skeleton width and length [67, 80]. Although these methods enable the quantitative description of agglomerates, they do not represent the whole three-dimensional, fractal shape of the particulates and tend to overestimate the size [81]. In contrast, electron tomography can reconstruct the actual shape and volume of particles [82, 83]. The caveat of this technique is that TEM imaging itself is relatively time- and

cost-intensive. To combat this limitation, Haffner-Staton [84] developed a methodology for high-throughput tomography. The comparison of two- and three-dimensional measurements revealed size differences of 20 % to 35 % between the techniques.

2.3 Ex-Situ Analysis

As apparent by the previous section, TEM and fringe nanostructure analysis are powerful tools for the investigation of soot properties. In the following, background information on both techniques is provided. Subsequently, additional methods for soot characterisation are outlined: Raman spectroscopy, nanoparticle tracking analysis (NTA), and thermogravimetric analysis (TGA).

2.3.1 Transmission Electron Microscopy

TEM analysis is a widely adopted technique to characterise soot, as addressed in the description of soot nanoparticles in Section 2.2. The term "TEM image" in this context commonly refers to bright-field images. In this operating mode of the TEM, the images are acquired using the "direct beam", i.e. electrons that are transmitted directly through the sample without interacting with any of its atoms. Consequently, areas of the TEM grid that are covered with a thicker or denser layer of sample particles—i.e. more atoms and thus more chances for interaction with the incident beam—appear darker, while areas that are less densely covered—i.e. fewer atoms—appear brighter.

The process of acquiring HRTEM images at higher spatial resolutions is considerably more complicated. This technique facilitates both the direct beam and elastically scattered electrons. The image is produced by so-called phase contrast, an intricate pattern of constructive and destructive interference between the two beams. The underlying theory and methodological background are extensive, and in full, these are beyond the scope of this

thesis. In simple terms, the phase contrast approach provides a representation of the arrangement of atoms and molecules within the sample. HRTEM images of highly ordered, crystalline materials will exhibit a series of ordered lines or points, while images of amorphous materials will appear random and "noisy" [84]. An extensive source of information on both TEM and HRTEM can be found in the textbook by Williams and Carter [85].

In addition to elastic scattering, electrons are also scattered inelastically as they exchange energy with the atoms in the specimen. As a consequence, photons are released which provide valuable information on the chemical composition of the sample. The measurement technique based on this phenomenon is known as energy-dispersive X-ray spectroscopy (EDX) and the required sensor can often be found on TEM instruments. The underpinning physical principle is briefly outlined in the following: Upon interaction, the high energy electrons of the incident beam can ionise atoms in the specimen. Electrons are elevated to a higher energy level, leaving so-called "holes" in the core energy levels below. As this state is highly unstable, electrons of said higher energy levels will relax to fill these holes to regain stability. The excess energy of the electrons must be emitted to match the core energy level. This can occur in the form of emitting photons. The energy or wavelength of these photons corresponds to the energy difference of the energy levels between the relaxation occurred, thus providing a "fingerprint" of the atoms in the sample. [84]

TEM has been used to characterise soot from both the exhaust gas [44, 46–49] and lubricating oil [34, 43, 44, 48] of internal combustion engines, as well as soot from diffusion flames [86–88]. Depending on the soot origin, the methods of sample collection differ significantly. A variety of techniques have been used previously to obtain soot from the exhaust gas of internal combustion engines. Gaddam and Vander Wal [47] sampled soot directly from the exhaust gas on TEM grids. However, high soot concentration in the exhaust gas can oversaturate the grids. To prevent oversaturation and reduce overlapping of agglomerates, the collection time can be reduced

[89]. Alternatively, the exhaust gas can be diluted with clean air [46] or an inert gas, e.g. nitrogen [90], enabling longer collection times. Barone et al. [46] as well as Liati et al. [49] diluted the exhaust gas by a factor of 30 and 13.5, respectively, prior to deposition on TEM grids. To image soot-in-oil samples, the soot agglomerates need to be separated from the lubricating oil. Esangbedo et al. [44] diluted oil samples in *n*-heptane and transferred small amounts onto TEM grid after ultrasonic bathing. La Rocca et al. [34] separated soot from the used lubricating oil by multiple cycles of centrifugation and replacing the liquid oil-phase with *n*-heptane. Despite altering the observed size distribution of the agglomerates, this procedure enabled observation of the primary particle nanostructure. A similar procedure was used by Uy et al. [48] using hexane as the solvent. Soot generated from diffusion flames, also known as carbon black, can be collected directly from the flame by thermophoresis on TEM grids, as done by Bhowmick et al. [87] and Schenk et al. [88]. Alfè et al. [86] collected soot from the flame on probes in bulk and subsequently transferred it onto TEM grids by ultrasonic agitation in methanol.

Established techniques for nanostructure characterisation can be found in Raman spectroscopy and X-ray diffraction (XRD). The former can identify nanostructure types, such as ordered graphitic, disordered graphitic, and amorphous carbon domains. However, due to differences in the experimental parameters (i.e. laser wavelength, laser intensity, and spectra collection time) and the band fitting (i.e. the number of bands for deconvolution), only relative comparisons within studies are made. Further background on Raman spectroscopy is discussed in Section 2.3.3. By using XRD, the lattice spacing numbers of the sample structure can be determined. Both techniques provide general information on the sample by assessing larger sample regions in comparison to the size of individual particles. In contrast, TEM enables the imaging of individual soot agglomerates and primary particles using various magnifications up to the atomic level. Thus, the technique can provide a wide range of different properties and more nuanced information. Particular

areas and specific regions can be easily differentiated. Therewith, detailed information on both morphology and nanostructure can be obtained.

The observable soot morphology provides initial information about the general appearance and type of soot. This can range from larger particles in clusters of several hundred nanometers as commonly observed for carbon blacks, to small and "sludge-like" particulates as observed for some GDI soot samples [48]. Moreover, simple measurements of primary particle size and two-dimensional agglomerate dimensions can be carried out without extensive software or image acquisition procedures. However, two-dimensional images cannot fully capture the fractal, three-dimensional nature of soot agglomerates. Recent advances towards electron tomography [82] and its automation [91] could provide a feasible way to close this gap.

2.3.2 Fringe Analysis

In addition to morphological imaging at low resolution, higher resolutions can be utilised to capture the particle nanostructure. Early attempts of manual measurements from electron microscopy images have been performed as early as 1971 [68]. The individual segments of graphitic layers, commonly referred to as fringes, can be assessed for their geometric parameters (referred to as metrics in the following). The metrics comprise the length, tortuosity, and separation of the fringes. The length of the fringe is defined as the distance between its endpoints along the fringe, i.e. geodesic length. The shape of fringes can be quantified as tortuosity by obtaining the ratio of the respective geodesic length and the direct endpoint distance, i.e. the Euclidean length. The separation of a fringe pair can be determined by averaging the perpendicular distance between the two fringes along their geodesic lengths. Several years after the initial advances, various researchers moved towards the automated analysis of HRTEM images [69, 92–94]. More recently, a comprehensive methodology was developed by Yehliu et al. [70] and was implemented using the commercial software MATLAB. Their

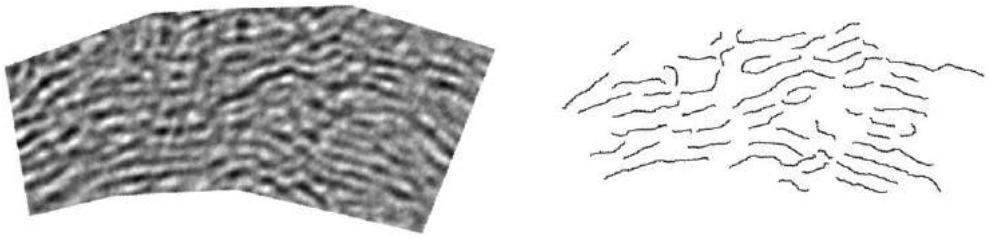

(a) (b)

Figure 2.4: Nanostructure-section of primary particle (a) shown in Figure 2.2b and extracted fringes (b).

approach extracted fringes with improved quality and was subsequently widely adopted in the literature [75–77, 95]. However, other approaches of fringe analysis can be found in the existing literature [96–101]. An example nanostructure section of the primary particle shown in Figure 2.2b is displayed in Figure 2.4 along with the extracted fringes (using the method and settings outlined in Section 3.6.2).

Despite differences between the specific methods, some recurring elements can be identified across the techniques. Initially, histogram equalisation is employed to expand the distribution of intensities over the full greyscale. Thus, the contrast of fringes to the background is enhanced. To reduce both residual noise and noise from the histogram equalisation, low-pass filters are applied. While initial approaches employed ideal filters [69], Gaussian filters in the frequency domain have been used in later studies to avoid resulting ringing effects [102]. Despite the correction for uneven illumination of the TEM before the acquisition of images [103], white top-hat transformation is often included to filter any artefacts from remaining illumination variations [70]. Subsequently, fringes can be extracted from the prepared image by threshold filtering. However, the obtained fringes require further processing to allow for automated calculations. As such, raw fringes have to be reduced to a single line of a single-pixel width by skeletonisation. Moreover, branched fringes have to be resolved by splitting and subsequent

connecting of similarly orientated branches. Upon completion of these steps, the length and tortuosity can be obtained for each fringe. While not all of the described steps are included in every methodology, some features of specific approaches can be noted. The method by Toth et al. [97, 98, 102] pays particular attention to the low-pass filter selection and subsequently the fringe separation. Botero et al. [104] focused on different radial regions of entire primary particles. In contrast to other analysis approaches that are limited to the graphitic shell of a particle, this method enabled the identification of differences within particles as well as changes with soot maturity. Another advanced approach was developed by Pré et al. [101]. Their algorithm is based on the assessment of parallelism between fringes. Thus, it allows for fringe stacks and continuous domains to be identified as well as quantified in terms of size and separation spacing. Consequently, information on the density of the nanostructure can be obtained. This approach was subsequently employed to assess changes in nanostructure for soot of different heights above flame burners [105] as well as laser-induced heating effects [106]. Wang et al. [99, 100] employed a similar method with a focus on fringe orientation, and characterisation of branched and self-intersecting fringes.

Using the algorithm of Yehliu et al. [70, 107], Jaramillo et al. [73] observed the fringe length and tortuosity for soot from a diesel-powered industrial forklift to be 1 nm and 1.17 respectively, while fringe separation was not analysed. For soot sampled directly from a diesel spray flame, Sakai et al. [71] obtained similar values of fringe length, separation and tortuosity as 0.98 nm, 0.42 nm and 1.23, respectively. Gaddam et al. [47] characterised soot from a GDI engine run under various operating conditions. The fringe length was found to be between 0.72 nm to 0.82 nm, while the tortuosity ranged from 1.176 to 1.21. These values differ from the previous measurements of diesel soot; however, the study did not focus on the differences between the two soot types. Values obtained by fringe analysis were compared to XRD and Raman spectroscopy measurements by Yehliu et al. [107]. Samples

with various degrees of oxidation were compared. The trends in fringe separation as obtained from fringe analysis and XRD were reported to be in good agreement. Similarly, a linear correlation was observed between fringe length and band intensity ratio I_G/I_D as obtained from fringe analysis and Raman spectroscopy, respectively. However, the laser wavelength can affect the observed spectra and prevent comparison of results between studies [108]. Moreover, the obtained data from Raman spectra strongly depends on the method of band deconvolution [109] as well as the method of measuring peaks, e.g. peak maximum or full width at half maximum [110]. While such restrictions are known for Raman spectroscopy, only little work has been carried out for respective constraints of fringe analysis. Gaddam et al. [35] conducted a study using three parameter-cases of three different binarisation threshold values. The remaining processing parameters remained constant; however, for one case, the contrast enhancement was skipped. Thus, the direct impact of the threshold value could effectively only be compared between two cases. The baseline threshold value was determined by Otsu's method. This algorithm was proposed by Otsu [111] and calculates the ideal threshold value to maximise inter-class variance and minimise intra-class variance. This approach has been implemented in the fringe analysis methodology of Yehliu et al. [70]. However, alternative methods have been used to determine suitable threshold values in other works. Palotas et al. [92] suggested that the optimal threshold value maximises the number of obtained fringes. In addition, Sharma et al. [69] and Shim et al. [93] used fixed threshold values in combination with further algorithms for correction of broken or merged fringes. In contrast, Gaddam et al. [35] did not observe a statistically significant effect of different threshold values on obtained fringe lengths. This was based on two parameter-cases without variation of parameters, neither Gaussian low-pass filter nor white top-hat transformation. However, both variables could be of importance as the threshold value is only calculated after those processing steps.

Similarly to processing parameters, the variation associated with TEM imaging is only scarcely covered in the literature. Wan et al. [112] assessed the imaging process by both TEM analysis of nascent soot samples and simulated computational studies. The findings suggested that observed fringe properties could be affected by the focusing of the microscope. However, the impact of the degree of defocus on the fringe dimensions has not been studied prior to the publication of the findings in Chapter 4. In addition to setting the focus, the TEM operator also has to correct the instrument for uneven image illumination prior to image acquisition [103]. The operator's experience can greatly affect the results of TEM imaging, as observed by Kondo et al. [113] for the imaging of primary particles. Moreover, the respective camera equipment could play a role in this process. Maximum spatial resolution as well as image acquisition time and subsequently signal-to-noise ratio could affect how clearly fringes can be imaged.

2.3.3 Raman Spectroscopy

Quantitative analysis of the structure of soot and related nanocarbons can be readily obtained by Raman spectroscopy. This optical technique relies on the inelastic scattering of a monochromatic laser beam, with the resultant shift of the incident photon energy corresponding to specific vibrational modes present in the material under examination. As soot principally comprises carbon, structured at the nanoscale, but often highly disordered at the molecular level, the first-order Raman spectrum is dominated by two broad and strongly overlapping bands within the region 900/cm to 1800/cm, corresponding to the so-called 'D' (a breathing mode of six-atom rings of A_{1g} symmetry, requiring a defect for its activation, found in defective and nanocrystalline graphitic carbons at 1350/cm) and 'G' bands (a carbon-carbon stretching vibration of E_{2g} symmetry ubiquitously present in graphitised nanostructures at 1580/cm). For carbon black, the intensity ratio of these two bands (I_D:I_G) has been directly related to the fringe length

of the nanostructure [107, 114]. However, this strategy is not necessarily applicable across all studies as the 'D' band is dispersive in nature, with its position and intensity sensitive to the wavelength of the excitation laser [109]. For example, Uy et al. [48] observed that spectra acquired using a 244 nm ultraviolet laser exhibited no defective 'D' peaks, and therefore, important information could not be extracted. Moreover, it is now widely recognised that the observed bands in the D/G region more likely represent a superposition of up to five different vibrational modes, deconvolution of which permits quantification of the extent of ordered graphitic ('G' mode), disordered graphitic ('D1', 'D2' and 'D4' mode), and amorphous domains ('D3' mode) within the primary particles [109]. However, it is interesting to note that for highly disordered carbons, the 'D2' mode can be indistinguishable from the 'G' mode [115]. Furthermore, no universal approach for the analysis of the Raman spectra of soot has yet to be established, as the method used for the determination of the band intensities varies across different studies. While some reports use maximum peak values, i.e. peak height [48, 114], others determine the intensity by measuring the broadness of the peak, as defined by the full width at half maximum [109, 110]. Moreover, the quality of the obtained spectra is often dependent on the conditions used for the preparation of the sample for analysis, as fluorescence, likely due to contamination from PAH and other substances from the lubricating oil and engine wear, can significantly impact the attainable signal to noise ratio in the resultant spectrum. Uy et al. [48] noted the exhibition of fluorescence, particularly for soot-in-oil samples, despite attempts to purify the sample by dilution in *n*-heptane and centrifugation. The procedure was first employed by Clague et al. [16] and recently used in studies by La Rocca et al. [34, 67]. However, sample dilution and its impact on the quality of the measurements was not investigated further.

2.3.4 Nanoparticle Tracking Analysis

The measurement of agglomerates represents a complex challenge due to their fractal geometrical nature. Different approaches have been used across studies, mostly relying on two-dimensional projections in the form of TEM images. Common parameters include the radius of gyration [62, 79] as well as skeleton width and length [67, 80]. Although these methods enable the quantitative description of agglomerates, they do not represent the whole three-dimensional, fractal shape of the agglomerates and tend to overestimate the size [81]. In contrast, electron tomography can be used to reconstruct the actual volume of particles [82, 83]. However, despite recent progress towards throughput optimisation [91], such procedure is still relatively time and cost intensive. Analysis of soot-in-oil samples adds further complexity, usually requiring the removal of the particles from the lubricating oil. However, NTA has been shown to be an effective alternative [116]. To enable the particle analysis, the soot-laden oil has only to be diluted with a suitable agent, such as *n*-heptane. Thus, reducing both the particle density and the viscosity of the dilution. By diluting the oil sample rather than centrifugally removing the soot particulates, the agglomerate size is not altered and can be measured. The initial study by La Rocca et al. [116] was conducted on diesel soot-in-oil samples; however, no comparable studies using GDI soot-in-oil could be found prior to the publication of the findings in Chapter 5.

For the size measurement of soot particles, NTA utilises the principle of Brownian motion. The particles are exposed to a laser beam and the scattered light is recorded by a camera aligned with the beam axis (see Figure 2.5). Particles are identified separately, and their centres subsequently traced for as long as they are visible within the frame and are in focus. The movement of the particle, or translation diffusion coefficient D, is measured on a frame-by-frame basis. The hydrodynamic diameter of the particle d_h can subsequently be obtained from the Stokes-Einstein equation:

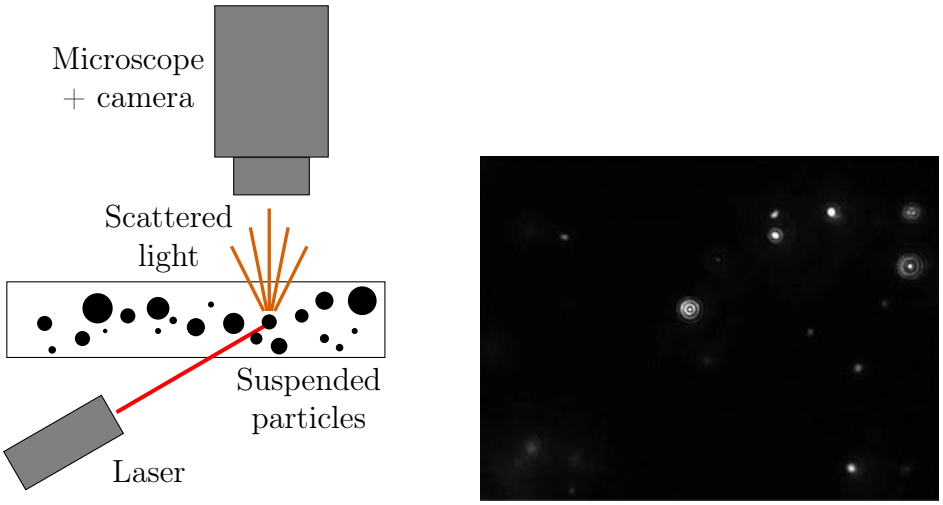

(a) (b)

Figure 2.5: Schematic of the NTA operating principle (a) and example picture of light scattered by particles as observed in an NTA instrument (b).

$$d_h = \frac{k_B \cdot T}{3 \cdot \pi \cdot \eta \cdot D} \tag{2.1}$$

where:

- d_h is the hydrodynamic particle diameter;
- k_B is the Boltzmann constant;
- T is the sample temperature in Kelvin;
- η is the sample viscosity;
- D is the translation diffusion coefficient.

2.3.5 Thermogravimetric Analysis

A commonly used technique to assess the content of soot in used lubricating oil samples is TGA. This analysis method is based on deconvoluting the

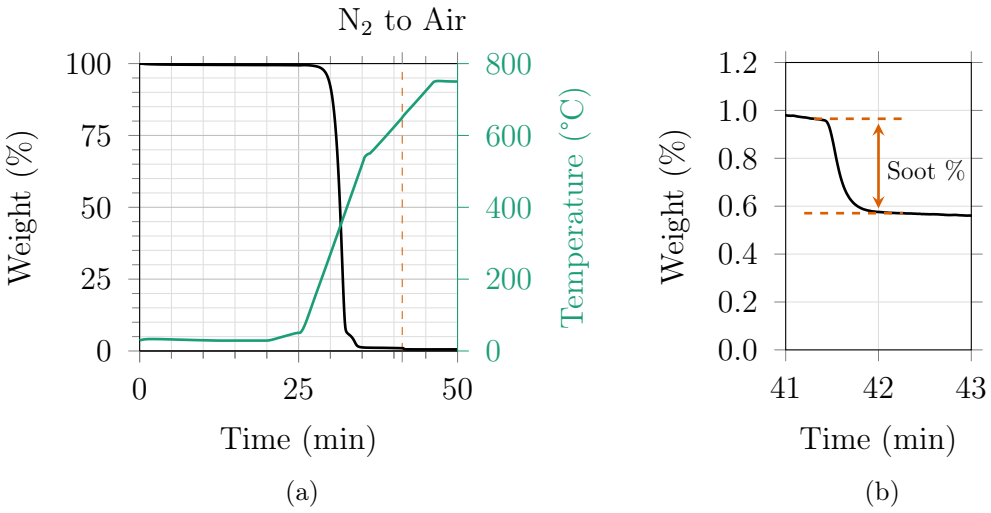

Figure 2.6: Example of TGA data with plotted weight fraction (—) and temperature (—) over time (a) and enlarged plot-section (b) to visualise measurable soot fraction after switch from inert gas to air. The specimen used was the 6733 km oil drain sample from a GDI vehicle, as described in Section 3.5.

individual components of the sample: organic volatiles, combustible matter (i.e. soot), and non-reactive ash [16, 48, 117]. This process is facilitated by measuring the change in mass while altering both the temperature and the gas environment in the chamber. While the specific protocols that are used vary, two underlying principles remain consistent. Initial heating of the sample in an inert gas environment, such as nitrogen, enables desorption of volatile components from the sample while preventing any simultaneous oxidation [118]. Subsequent use of air or oxygen allows for controlled oxidation of the combustible compounds, i.e. residual soot. An example of such analysis is shown in Figure 2.6.

Clague et al. [16] compared exhaust soot samples with soot extracted from lubricating oil of the same engines. The samples were heated to 650 °C in a nitrogen environment and then further to 750 °C in oxygen. The results showed differences between carbon-ash-volatile contents for the same

source, indicating a change from exhaust soot to soot-in-oil. However, the extraction process appeared to alter the observed results. Yehliu et al. [119] assessed the impact of fuel formulations on the properties of exhaust soot from diesel engines. The study showed differences in the fraction of volatiles as well as oxidation rates. To reflect the conditions of in-vehicle applications, i.e. regeneration of particulate filters, different parameters for the TGA were used: The samples were oxidised at 550 °C after preheating in a nitrogen environment 500 °C. Such protocol is in line with works of Mullins and Truhan [120] as well as Bredin et al. [118], reducing the maximum temperature for the initial stage to avoid oxidation due to oxygen traces. Aside from compositional details, information on soot concentration is important for automotive applications as the amount of soot in the lubricating oil is linked to the extent of wear [36–38]. Thus, the rate of deposition for engines is fundamental for recommendations of oil change intervals. Lockwood et al. [121] collected samples from three diesel engines operated under on-road conditions of five tracks. The authors observed a linear correlation between oil mileage and soot content with $R^2 = 0.8$. However, no deposition rates were derived and no information on the TGA protocol included. Di Liberto et al. [122] analysed 15 soot-in-oil samples from 10 vehicles with diesel engines. The oil mileage of the samples ranged from 3320 km to 23 386 km, and a modified version of the ASTM D5967 test method was employed. The engines exhibited an overall deposition rate of 1 wt% per 15 000 km with a standard deviation of 0.4 wt%. Sharma et al. [123] also assessed diesel soot-in-oil with the ASTM D5967 method. The sample contained 1.78 wt% soot after 12 798 miles, equivalent of a rate of 1.3 wt% per 15 000 km and thus within the model of Di Liberto et al. [122]. Uy et al. [48] measured soot-in-oil samples of both diesel and GDI engines. The TGA protocol involved heating to 650 °C in nitrogen before switching to air for an isothermal hold at the same temperature. The diesel sample showed higher soot content; however, no information on mileage was provided and thus no correlation was possible.

2.4 In-Situ Analysis

The above-described ex-situ techniques enable in-depth characterisation of soot and can provide great insight. However, these analysis approaches are also time-consuming and not feasible for the assessment of particulate emissions from vehicles. Instead, in-situ measurements are commonly used. In the following, different methods of sampling and conditioning exhaust gas are described, and different techniques for subsequent particulate measurements are outlined. Moreover, considerations of measurement variability are discussed.

2.4.1 Sampling Methods

Sampling and measuring particles directly from the raw exhaust gas stream is possible, but some challenges may arise. First and foremost, water vapour in the exhaust gas and volatile species can condensate in the connected sampling lines. This issue can be mitigated to some extent by using heated sampling lines. However, dilution of the exhaust gas can be more effective at preventing condensation and can help reduce contamination in the form of deposits and residue on the walls of the sampling line. Consequently, the dilution mitigates test-to-test artefacts due to contamination and improves overall accuracy [124]. Another consideration might be continued reactions between gaseous and particulate species and their transformation in terms of composition and shape. Reducing the relative concentration of such species in the sample gas can effectively help "freeze" their state to minimise changes on the way from the sampling point to measurement instrument [124]. Lastly, an aspect that is particularly relevant for measurement in diesel engine-out exhaust gas, i.e. pre DPF, is the total concentration of particles. The concentration of particles in the raw exhaust gas can often exceed the measurement instruments' available range. Thus, dilution of the exhaust gas is necessary to bring the concentration down to within the measurement range.

In the following, four dilution methods are described that are either at the core of legislative regulations or used in this work: full flow diluter, porous tube diluter, ejector diluter, and rotating disk diluter. More systems are available, such as partial flow diluter or bifurcated flow diluter. However, these are not covered here. Further information can be found elsewhere in the literature, e.g. [124].

2.4.1.1 Constant Volume Sampling

A full flow dilution system mixes the entirety of the exhaust gas with preconditioned ambient air in a dilution tunnel (see Figure 2.7) to achieve a constant flow of diluted aerosol across the testing cycle. The dilution of the exhaust gas reduces the risk of water condensation in instrument sampling lines. Moreover, the effect of pressure and temperature fluctuations is diminished. Such constant volume sampling (CVS) systems enable the accurate measurement of the total output flow rate of the diluted gas. The total gas flow rate, in turn, allows the precise scaling of subsequent measurement results by using the ratio of the instrument flow rate to the CVS flow rate [124]. However, as the diluter's output flow rate is fixed, the dilution ratio inherently varies with engine speed changes, as the exhaust flow rate varies. While an isothermal increase of the dilution ratio can reduce the PM due to a lower contribution of the volatile fraction [125], higher dilution ratios with reduced temperatures can increase PM [126].

Similarly, the PN size distribution and concentration can be susceptible to measurement variability [124]. Varying the dilution ratio and temperature can result in differences in the observed nucleation mode [127]. Consequently, close control of these parameters is required to ensure reliable and comparable results. High-efficiency particle air (HEPA) and hydrocarbon filters are commonly used to condition the dilution air to minimise any background artefacts. Due to these considerations and the very high operating

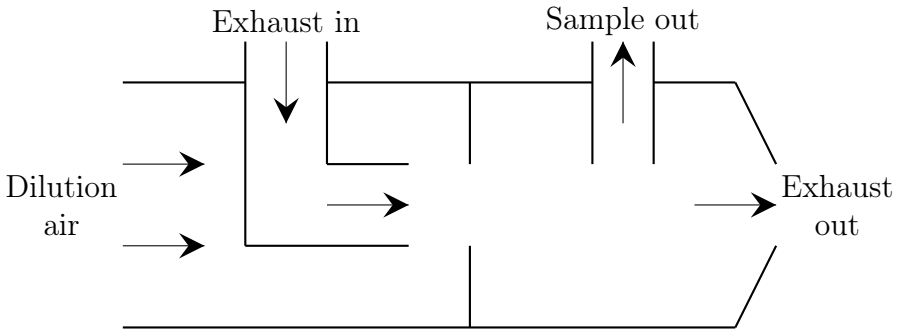

Figure 2.7: Schematic of a constant volume sampling system.

flow rates, particularly for larger engines, full flow dilution systems are costly and bulky [124].

2.4.1.2 Porous Tube Diluter

As the name of this diluter type suggests, the exhaust gas fraction is guided through an encased porous tube (see Figure 2.8). The dilution gas is introduced in the encasing and enters through the tube's pores, acting as sheath gas. Therewith, aerosol dilution is facilitated with minimised particle wall-losses [128]. While the dilution gas can be heated in most dilution methods, an advantage of the porous tube diluter is that the dilution gas can also be cooled [124]. Thermophoretic losses, generally associated with cooling in diluters, are here counteracted by the sheath gas effect. The dilution ratio can be controlled via the flow rate of the dilution gas. However, it should be noted that pressure fluctuations in the tailpipe can cause backflow of a fraction of the diluted aerosol into the tailpipe [129]. Consequently, it can be more reliable to determine the effective dilution ratio by comparing raw and diluted CO_2 concentrations instead of direct calculations from the flow rates [129].

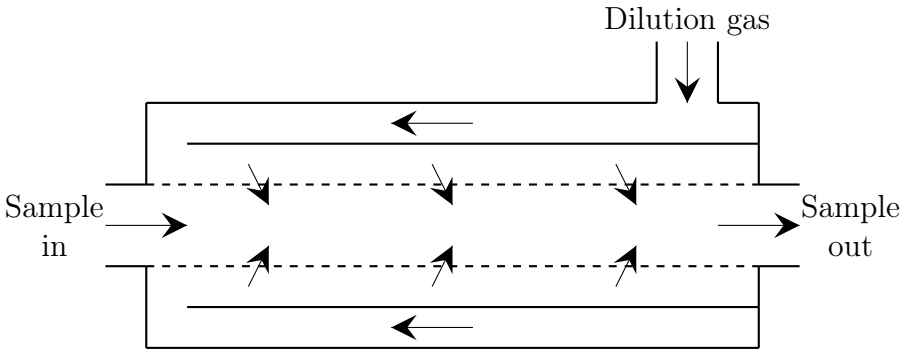

Figure 2.8: Schematic of a porous tube diluter.

2.4.1.3 Ejector Diluter

Ejector diluters are designed based on Bernoulli's principle. For an incompressible flow, pressure decreases as the speed increases. In an ejector diluter, a low-pressure region is created by the flow of dilution gas through a ring orifice. The low-pressure draws in the sample gas through the nearby inlet nozzle (see Figure 2.9). The dilution ratio is therefore influenced by the geometry of the ejector diluter itself. The composition, temperature, and pressure of both the dilution gas and the sample gas can further affect the dilution ratio [130]. Consequently, this dilution method is susceptible to pressure and temperature variations of the exhaust gas. However, particle losses were found to be low, with minimal influence of particle size for diameters larger 15 nm [131].

2.4.1.4 Rotating Disk Diluter

In contrast to porous tube and ejector diluters, this dilution method involves a moving part in the system. A rotating disk diluter consists of two fixed body plates with two openings each and a rotating disk with a number of cavities (see Figure 2.10). One side of the body plate is utilised for the sample flow, while the other side is used for the dilution flow. As the cavities move past the opening on the sample flow side, some of the sample gas

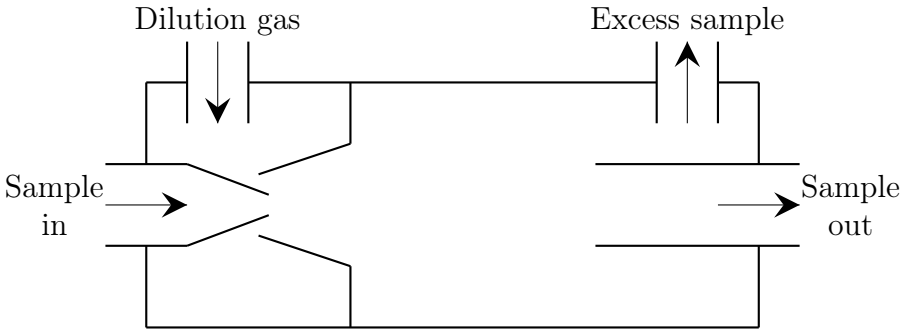

Figure 2.9: Schematic of an ejector diluter.

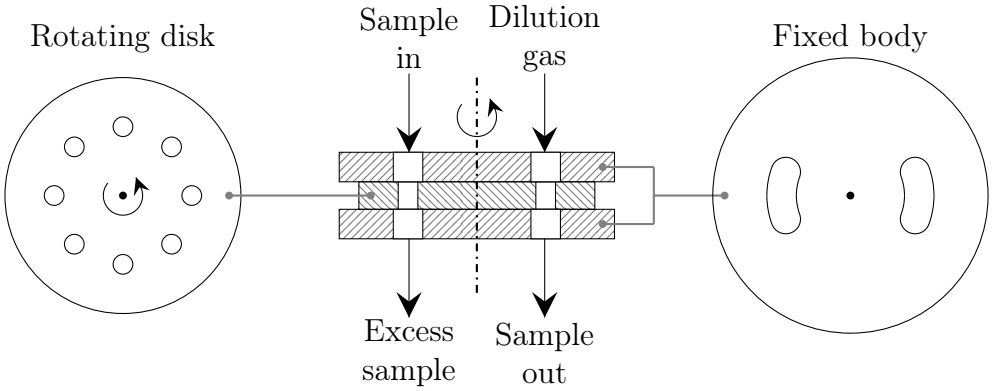

Figure 2.10: Schematic of a rotating disk diluter. Adapted from [124].

is retained and subsequently transported to the opening on the dilution flow side. Therewith, the sample gas portion is mixed with the dilution gas. The dilution ratio depends on a series of properties: the dimensions and the number of the cavities in the rotating disk, the dimensions of the fixed body openings, the temperature of the diluter and gases, the gas flow rates, and the rotational speed of the disk [60]. The latter is typically adjusted during operation to facilitate a dilution range of over one order of magnitude, e.g. from 1:10 to 1:100. The rotary diluter's advantages are its low sensitivity to contamination and stability against both pressure and temperature fluctuations [124]. However, the drawbacks are higher particle losses and necessary maintenance due to the moving parts [124].

2.4.2 Conditioning Methods

The composition of exhaust gas can be diverse with a dynamic shape with constituents ranging from solid particles to gaseous hydrocarbons. Volatile and semi-volatile species occur as gaseous molecules, liquid droplets, and adsorbed on solid soot particles. The specific state is determined by factors such as their concentration, the temperature, and the vapour pressure [124]. Differentiating between the individual components is therefore difficult and has an adverse effect on repeatability. Hence, a common approach is to remove all volatile species and focus only on non-volatile particle emissions. The exhaust gas must be conditioned by a volatile particle remover (VPR) to enable such a methodology. In the following, three methods of volatile removal are explained: evaporation, adsorption, and oxidation. In practice, these are implemented as VPR by evaporation tubes, thermodenuders, and catalytic strippers, respectively.

2.4.2.1 Evaporation Tube

This method involves a relatively simple setup of only a heated chamber (see Figure 2.11a). The aim is to evaporate any volatiles or semi-volatiles to the point that they fall below the detection limit or imposed threshold of the measurement procedure [132]. To enable evaporation of semi-volatiles, i.e. nucleation mode species, temperatures of more than 250 °C are required [133]. The efficiency of this process is primarily influenced by the concentration of the (semi-)volatiles and the residence time in the evaporation tube [124]. Hence, dilution of the exhaust gas prior to this conditioning step is beneficial to the evaporation efficiency and prevention of re-condensation.

2.4.2.2 Thermodenuder

The design of a thermodenuder builds upon an evaporation tube. A heated section is placed first in line to evaporate all (semi-)volatiles in the exhaust

gas by increasing its temperature. Subsequently, the gas passes through an unheated section that contains an adsorbing material (see Figure 2.11b). Activated carbon is commonly used for this purpose. The adsorbent actively removes the evaporated (semi-)volatiles from the sample gas. Due to the faster diffusion velocity of volatiles compared to solid particles, these gaseous species are preferentially removed [124]. Most of the observed particle size distribution remains unaffected. However, some artefacts can occur for the smallest particles, i.e. nucleation mode particles on the verge of becoming solid particles. While the removal of volatiles can enable lower dilution ratios without adverse effects on the equipment used, particle deposition in the thermodenuder can become an issue. Particle losses occur due to thermophoresis in the unheated section and are considered to be on the order of 25 % to 30 % [124]. With increasing usage time, the amount of deposited particles increases and, in turn, the adsorption efficiency of the activated carbon decreases [134]. Hence, the lifetime of thermodenuders is limited and regular maintenance is necessary.

2.4.2.3 Catalytic Stripper

The concept of a catalytic stripper attempts to mitigate the drawbacks of the two previous systems. The device is heated throughout to incorporate the principle of evaporation. Instead of adsorbing hydrocarbons, volatile species are removed by oxidation upon evaporation. The removal is facilitated by an embedded oxidative catalyst (see Figure 2.11c). It was noted that catalytic strippers could handle higher concentrations of (semi-)volatiles more effectively than the other two conditioning systems; however, this is only possible at the expense of higher particle losses [124]. The complete removal of any volatiles prevents the subsequent condensation and re-nucleation entirely, therewith also minimising artefacts in the nucleation mode of the distribution [135]. Thus, the use of catalytic strippers is particularly advantageous for the investigation of smaller particle sizes. Further details of such a use-case for catalytic strippers is discussed in Section 2.5.3.

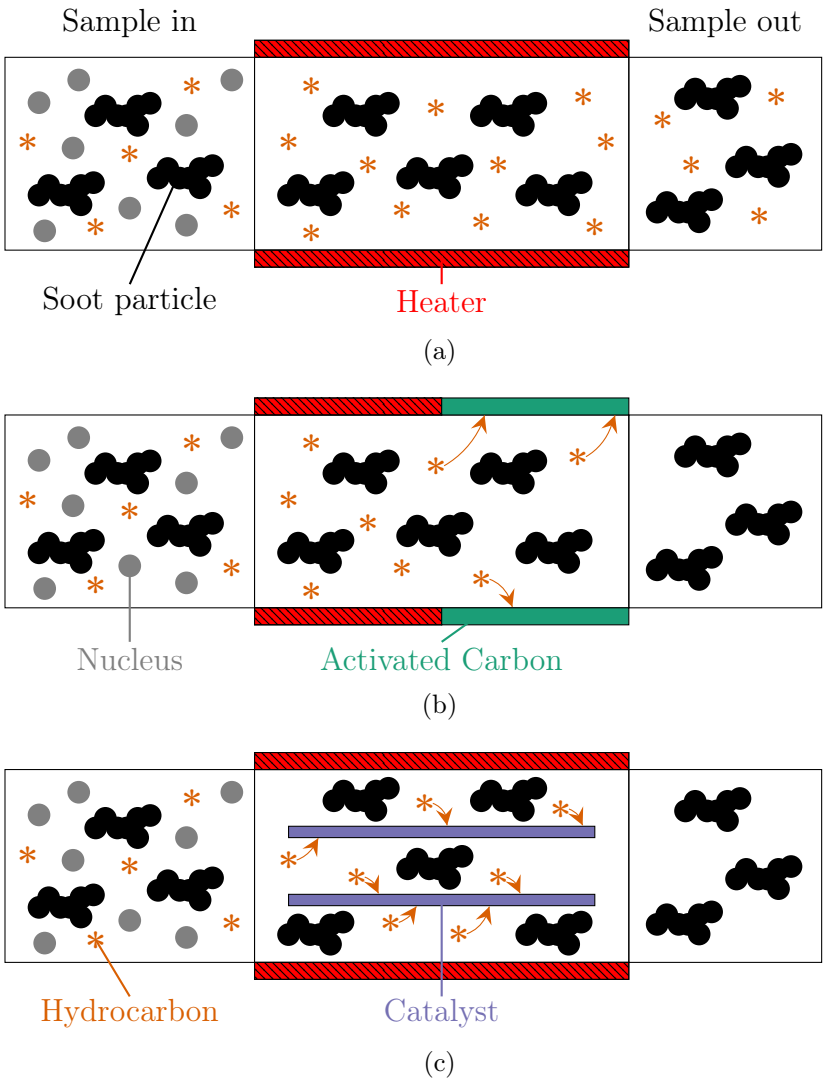

Figure 2.11: Schematics of sample conditioning methods: evaporation (a), adsorption (b), and oxidation (c). For simplicity, all nuclei are assumed to be liquid droplets and all hydrocarbons to be gaseous. Adapted from [124].

2.4.3 Measurement Devices

Detection and measurement of airborne particles can be facilitated by a broad range of methods. One group of techniques utilises optical phenomena such as scattering, absorption, and extinction of laser beams. A further group uses electrical charges transferred to particles, which are subsequently measured. In the following, one application of each group of techniques is described: condensation particle counters (CPCs) and electrometers. These methods are commonly used in available particle sizing instruments; however, these do not provide a comprehensive PSD on their own. Consequently, the detectors are used in combination with classification devices to appreciate different particle sizes in polydisperse samples. Two instrument types for this purpose are also described: differential mobility analysers (DMAs) and electrical mobility spectrometers (EMSs). Details on alternative means of particle characterisation can be found elsewhere in the literature [59, 136, 137].

2.4.3.1 Condensation Particle Counter

An optical method of detecting and measuring particles can be found in CPCs. At their core, CPCs facilitate the principle of light scattering with optical particle counters, comprising a laser source and a suitable detector for the respective laser wavelength. During operation, the aerosol of interest is pumped to the particle counter with a controlled flow rate. Particles in the aerosol cross the laser beam as they pass through the counter. In doing so, the particles scatter and absorb the photons of the beam, thus affecting the detected beam intensity at the detector. From the change in the detector signal, a light-scattering equivalent diameter can be obtained. The lower sizing limit of commercially available instruments is around 50 nm [137]. While the upper limit can reach as high as several hundred microns, the dynamic range of an instrument is highly dependent on the required lower limit [137].

The optical particle counter can subsequently be extended to form a CPC by adding a condensation stage to enlarge the particles artificially. By increasing the particle size at the measurement point, the detection limit is effectively lowered. The first section of the device is a heated, porous tube that saturates the aerosol with a working fluid (see Figure 2.12). Subsequently, the aerosol passes through a condenser section in which the temperature is lowered. Thus, the aerosol enriched with the working fluid becomes supersaturated and fluid traces condensate onto the particles. This method commonly enlarges nanometric particle to the micrometric scale [124]. The final element of a CPC is an optical particle counter, as described above. The lower detection limit is primarily determined by the properties of the chosen working fluid and the temperatures of the saturator and condenser. As the smallest detectable particle size can be increased from mere nanometres to micrometres, a more extensive dynamic range can be achieved within a single instrument [137]. For the working fluid, *n*-butanol is commonly used. Water-based CPC have been developed; however, these are problematic for engine applications as soot is hydrophobic [138].

While stand-alone CPCs provide some sizing ability, they cannot fully differentiate polydisperse samples. To obtain full PSDs of such samples such as engine exhaust particulate emissions, additional equipment is required (cf. Sections 2.4.3.3 and 2.4.3.4).

2.4.3.2 Electrometer

An alternative to optical measuring techniques is the size determination via electrical charge using electrometers. An electrometer comprises electrodes with a defined charge. If charged particles impact the measurement electrode, a current can be observed at the electrode. This current is proportional to the particles' active surface area and the total number of particles [124]. This effect can be exploited by imposing a controlled charge distribution onto the particles prior to the measurement with electrometers. Different approaches

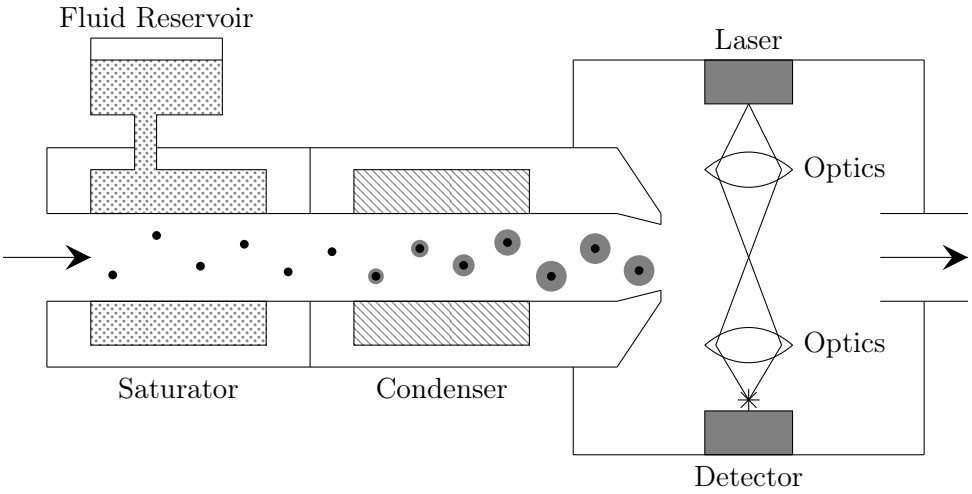

Figure 2.12: Schematic of a continuous-flow condensation particle counter.

to particle charging have been implemented over time, e.g. unipolar or bipolar charging. The former uses a high voltage corona discharge from a needle or wire electrode, while the latter facilitates ions generated from radioactive decay [136, p. 354]. The specific advantages are related to the particle size range of interest and desired charge distributions, among other factors. A comprehensive history of instrument development and respective considerations can be found in [139].

With the knowledge of the achieved charge distribution, the particles' acquired charge can be directly related to its active surface area [140]. However, the shape of the particles can affect the particle charge. Fractal combustion generated particles were observed to have a significantly different charging efficiency compared to spherical reference aerosols [141, 142]. The measurement can further be influenced by any pre-existing charge of the aerosol [143]. For engine exhaust particles, a large fraction was found to be charged; however, the samples exhibited equal numbers of positively and negatively charged particles [144]. The impact of this observation was tested by inverting the charging polarity [145]. The authors of that study concluded that the behaviour did not differ from neutral particles, and

as such, the pre-existing charge does not affect the measurement. As for CPCs, additional equipment is required to assess the PSD of polydisperse samples (cf. Sections 2.4.3.3 and 2.4.3.4).

2.4.3.3 Differential Mobility Analyser

For the analysis of polydisperse samples, DMAs can be used. Such devices contain a centrally mounted high voltage electrode (see Figure 2.13a). The sample aerosol with charged particles enters the device in the outer section. Sheath gas is channelled into the device close to the electrode, initially separating the particles from the electrode. As particles move along the device coaxially to the high voltage electrode, they experience a radial force depending on their charge. This force translates into a radial movement depending on the electrical mobility that also includes the particle mass. Only particles with certain electrical mobility for a given electrode voltage are deflected the right amount to pass through the sample outlet of the DMA [136, p. 343]. Particles with higher or lower electrical mobility are either deposited on the electrode or pass through the device exhaust, respectively (see Figure 2.13a). Thus, a monodisperse extract of a polydisperse aerosol can be obtained [59, pp. 185–186]. The number of particles in the sample stream from the outlet can subsequently be measured using instruments such as CPCs or electrometers.

A range of electrical mobilities must be assessed by changing the electrode voltage to cover the entire size spectrum of polydisperse samples. The instruments for this purpose, commonly known as scanning mobility particle sizer (SMPS), vary the voltage either in discrete steps or a continuous sweep [137]. The PSD can subsequently be obtained from the measurements for the electrical mobility bins using various algorithms [146]. The challenge in this lies in the possibility of particles possessing multiple charges [59, p. 186]. Furthermore, the measurement requires a relatively stable aerosol source as scans can require 2 min to 3 min [59, p. 186]. Faster scans risk distorting

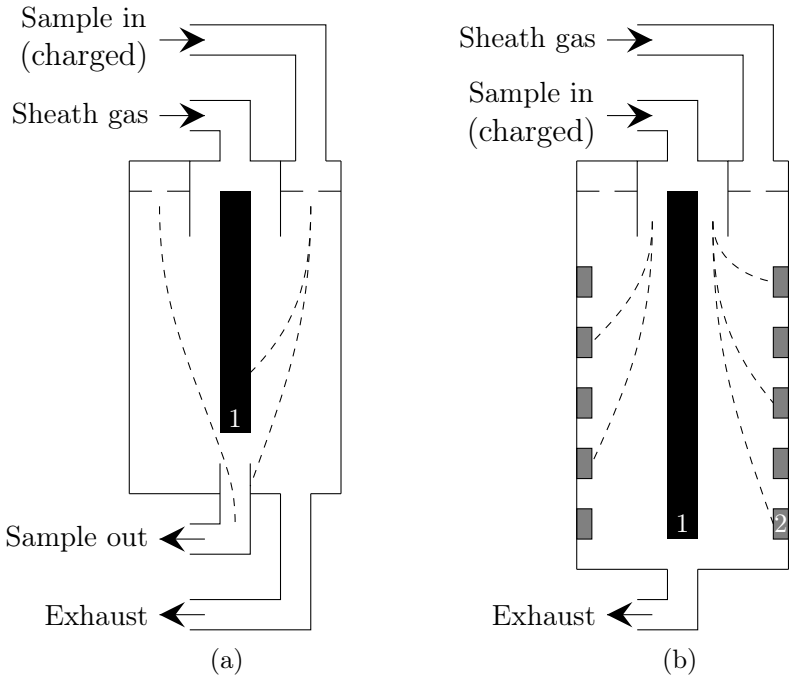

Figure 2.13: Schematics of a differential mobility analyser (a) and a differential mobility spectrometer (b). The former is adapted from [150]. Annotations: 1 High voltage electrode, 2 Collection ring with connected electrometer.

the observed size distribution [147]. Fast-response CPCs can help reduce the minimum scan times [148]. However, the number of measured particles must be sufficient to provide reliable counting statistics [124]. This problem mainly arises for modern combustion engines with relatively low particulate emissions (e.g. after particulate filters). Further uncertainties arise from CPC counting efficiencies, particle losses, and differences in charging distributions between instruments [149]. Despite all these restrictions, SMPSs are considered highly accurate for relevant measurement ranges of exhaust aerosols and are consequently widely used for vehicle exhaust studies [124].

2.4.3.4 Electrical Mobility Spectrometer

An alternative approach to SMPSs for characterising polydisperse samples are EMSs. Instead of sequentially analysing monodisperse extracts, differently sized particles of polydisperse samples are detected simultaneously. As for DMAs, a known distribution is imposed on the aerosol stream. The particles are subsequently detected in a classification column with a series of ring electrodes. Based on their electrical mobility, the particles experience different radial velocities while travelling along the column with the sheath gas (see Figure 2.13b). Consequently, particles with higher electrical mobility (i.e. lighter, smaller, or more charged) impact electrodes closer to the start of the column, while those with lower electrical mobility impact electrodes towards the end of the column. The resulting currents are detected by a series of electrometers that are connected to the respective electrodes. This operating principle enables measurements as fast as 10 Hz [136, p. 404]. Such short intervals are beneficial for the characterisation of engine exhaust gas in transient testing conditions.

Corona diffusion chargers are often used for EMSs to impose a unipolar charge distribution on the aerosol. These chargers further enable a higher charge to be transferred. The increased charge level is required due to a lower sensitivity of electrometers as compared to CPCs but also lowers the minimum detectable concentration [124]. However, multiple charging of particles becomes more prevalent as well. This complicates the derivation of the mobility size distribution from the electrometer readings [136, p. 404]. Resulting differences between EMSs and SMPSs can be as high as 30 % [151].

Two commonly used instrument types are DMSs and engine exhaust particle sizers (EEPSs), commercially available, for example, as DMS500 from Cambustion and EEPS 3090 from TSI, respectively. While the EEPS uses an initial negative charger followed by a positive charger, the DMS only uses a single positive charger. The additional negative charger minimises the likelihood of high positive charges before imposing a defined charge level [136,

p. 402]. Hence, different derivation algorithms are required for the respective instruments. Notably, the DMS provides an extended measurement range of 5 nm to 1000 nm—compared to 5.6 nm to 560 nm of the EEPS—due to the sub-atmospheric system pressure of 250 mbar [152].

2.4.4 Measurement Variability

Uncertainties in the measurement of particles can be described in two dimensions: repeatability and reproducibility. The former describes the variability of repeated measurements with the same instrumentation and test setup. Contributing factors to poor repeatability can originate from the particle source, i.e. the engine itself. The observed concentrations and distributions of particles can, for example, be affected by cold start conditions or the regeneration state of the particulate filter [153]. Hence, engine conditioning plays a vital role in achieving consistent results. Furthermore, volatile artefacts can lead to increased uncertainty. The exhaust gas can contain varying fractions of unburned hydrocarbons (HCs) and volatile species depending on the operating conditions and exhaust after-treatment devices installed. These species can condensate onto existing soot particles or form separate nucleation mode particles, thus affecting the PSD [154]. The resulting repeatability uncertainty can be as high as 40 %, as observed in an inter-laboratory study across nine different laboratories [155].

The aspect of reproducibility entails the variability across facilities with different instruments and varying setup. One reason for differences can be the algorithms that are required to obtain PSDs from the measurement signals of DMA and DMS systems [136, p. 411]. Furthermore, the calibration of PN measurement instruments and drift over time remain issues that can lead to high uncertainties of 30 % and higher [153]. In the aforementioned inter-laboratory study with different instruments but a similar test setup, the variability between the laboratories was found to be ca. 25 % [155]. Further variability might be introduced by changes in the test setup, such

as the measuring position. Differences in PN concentrations were observed by Giechaskiel et al. [156] between sampling directly from the tailpipe and sampling after dilution in a CVS dilution tunnel. While the uncertainty for sampling at the same location was 5 %, the difference between locations could be as high as 20 %. Thermophoretic losses in a heated line at 150 °C with exhaust gas at 300 °C were found to be ca. 10 %. A later study by some of the same authors [154] found lower PN concentrations for CVS sampling, which was primarily attributed to particle agglomeration in the heated sampling line from engine tailpipe to the CVS. However, the differences in PN concentration between tailpipe and CVS sampling were considered to be within an acceptable range (below 15 %) when particle losses are taken into account. The study used the same instrumentation for the measurements in both positions and observed similar uncertainty levels.

Particle losses in the sampling setup must be considered for accurate results, as mentioned in Sections 2.4.1 and 2.4.2. These can be described by two main mechanisms [156]: sampling effects and transport effects. The former describes anisoaxial and anisokinetic sample extraction, i.e. sample extraction at flow directions and flow rates, respectively, different from the exhaust gas flow. To prevent high particle losses, bends in the sample line should be avoided as much as possible and flow rates should be matched. However, bends in the flow path do not necessarily have to lead to appreciable particle losses. Giechaskiel et al. [131] compared gas samples from the axial outlet of an ejector diluter (sample outlet, see Figure 2.9) with gas samples from its perpendicular outlet (exhaust outlet, see Figure 2.9). Differences in their PSDs were considered to be negligible for particles with sizes of 10 nm to 300 nm.

Transport effects comprise internal processes within the sample—such as agglomeration—and external processes between the sample gas and the device—such as diffusion and thermophoresis. High particle losses due to thermophoresis can usually be avoided by heating the equipment. Thus, preventing particle condensation onto the sampling line walls. However,

interactions between sample gas components can still occur. The extent of the resulting changes depends on the residence time in the sampling line from the sampling position to the measurement instrument or conditioning device. A study by Isella et al. [157] confirmed this assumption, as the length of the sample transfer tube from vehicle exhaust to dilution tunnel affected the observed PSD. While the geometric mean diameter (GMD) of the observed particle distribution increased by 16 nm to 17 nm over a 6 m transfer tube, a shift of 22 nm to 23 nm was observed for a 9 m tube.

Furthermore, the particle measurements can vary significantly with the settings of the sampling devices. For dilution tunnels, e.g. CVSs, the obtained results can be influenced by the dilution air temperature, dilution ratio, total gas flow rate, and subsequently, the residence time [158]. Similarly, the dilution factor of an ejector diluter depends on the pressure, temperature, and composition of both sample and dilution gas [130, 159]. The aforementioned study by Giechaskiel et al. [131] also investigated whether diluting the sample gas in an ejector diluter could affect the observed PSD. As for the sampling orientation, particle losses across the diluter were considered negligible (below 5 %) for accumulation mode particles in the size range of 15 nm to 300 nm. The same was reported for nucleation mode particles larger than 10 nm. The observed PSD was neither significantly affected by the removal of volatiles in a thermodenuder nor by changes in dilution ratio through altering the dilution gas pressure. Hence, ejector diluters are assumed to be relatively robust tools for diluting exhaust gas samples without changing the particle distribution.

2.5 Legislative Regulations and Technical Limits

As highlighted in Section 1.1, particulate emissions from internal combustion engines are not a fundamentally new issue. In the following, the regulatory

efforts of more than 50 years since the first regulation on vehicle emissions are summarised. The scope for this is limited to passenger vehicles and focuses regionally on Europe. Increasingly stricter limits give greater importance to measurement variability, as outlined in Section 2.4.4. Thus, standardisation of measurement procedures and the involved technical solutions are outlined, linking the in-situ analysis techniques to real-world applications. Lastly, the progress towards the measurement of sub-23 nm to date and proposed regulatory changes for the future are discussed.

2.5.1 History of Vehicle Emission Legislation

In the European region, the first regulation of vehicle emissions was introduced by the European Council in 1970 with Directive 70/220/EEC [160]. This document focused on the total quantity of emitted CO and HCs over a defined test procedure. Reductions of the emission levels were considered feasible by using catalysts as after-treatment solutions. However, several challenges remained: durability of the catalyst in harsh exhaust conditions, interaction with anti-knock lead additives in the fuel, and selection of the catalytic material itself [161]. The move towards unleaded fuels throughout the 1980s and simultaneous improvements in fuel quality enabled stricter regulations to push for the widespread adoption of catalysts as exhaust after-treatment solution [162]. A new emissions standard was introduced with Directive 91/441/EEC [163] and became later known as 'Euro 1'. In addition to a limit for emitted CO and a combined limit for emitted NO_X and HCs, a maximum level of PM emissions was set for CI engines (see Table 2.2). The subsequent 'Euro 2' emissions standard was introduced with Directive 94/12/EC [164], reducing the existing limits. Both Euro 1 and Euro 2 prescribed a defined test cycle known as European driving cycle (EDC). Directive 98/69/EC [165] introduced a two-staged reduction in allowed emission levels ('Euro 3' and 'Euro 4'). With Euro 3, the initial warm-up phase of the EDC was directly included in the measurement to

simulate cold-start conditions. The modified test cycle was labelled as new European driving cycle (NEDC). Another aspect of Directive 98/69/EC is the altered structure of emission limits. Dedicated limits for emitted NO_X were introduced and while a dedicated HCs limit was also set for PI engines, the combined NO_X plus HCs limit was maintained for CI engines.

Limitations of PM emissions from PI engines were only introduced with the Euro 5 and Euro 6 standards in Regulation 715/2007 [166]. This can be attributed to the increasing market share growth of PI engines with DI systems around this time, as outlined in Section 1.1. Both standards were subsequently amended by Regulation 692/2008 [167]. The previous standards became classified as Euro 5a and Euro 6a, followed by the amended versions, Euro 5b and Euro 6b, with altered timelines. The modified emissions standards introduced an additional PN limit of $6 \cdot 10^{11}$ #/km for CI engines and lowered the PM limit to 4.5 mg/km for both engine types. The introduction of PN limits was considered to assist in pushing for particulate filters to be used for diesel vehicles [153], i.e. for DPFs to be commonly employed. Measurements with the lower particulate emission levels proved challenging with the established PM method. The issues were high variability and poor reproducibility of background levels from dilution tunnels [168]. It became evident that large numbers of fine particulates were present; however, these could not effectively be detected as they contribute significantly less to the PM [153]. Therefore, the additional measurement of particulate numbers was required. However, the measurement of PN presents itself challenging with various factors involved [155]. The challenges were addressed with the development of the particle measurement programme (PMP). Further details on this matter are discussed in Section 2.5.2. The newly introduced particulate emission limits were subject to the implementation of the PMP. The subsequent Regulation 459/2012 [169] further added a preliminary PN limit of $6 \cdot 10^{12}$ #/km for PI engines to Euro 6b (as displayed in Table 2.2). Moreover, a three year transition period was introduced with Euro 6c to allow time for research and development required to comply with the same

Table 2.2: Euro emissions standards by the European Union for passenger cars (vehicle category M). Implementation dates are indicated for new types (NT) and new vehicles (NV). PI: positive-ignition (i.e. gasoline). CI: compression-ignition (i.e. diesel). The PM and PN limits only apply to PI engines with direct-injection systems (i.e. GDI). *(g/km) **(mg/km) ***(#/km)

Euro Tier	NT	NV	Drive-cycle	CO*		HC**		NO_X**		HC+NO_X**		PM**		PN***	
				PI	CI	PI	CI	PI	CI	PI	CI	PI	CI	PI	CI
1	’92	’93	EDC	2.72	2.72	—	—	—	—	970	970	—	140	—	—
2	’96	’97	EDC	2.20	1.00	—	—	—	—	500	700	—	80	—	—
3	’00	’01	NEDC	2.30	0.66	200	—	150	500	—	560	—	50	—	—
4	’05	’06	NEDC	1.00	0.50	100	—	80	250	—	300	—	25	—	—
5a	’09	’11	NEDC	1.00	0.50	100	—	60	180	—	230	5.0	5.0	—	—
5b	’11	’13	NEDC	1.00	0.50	100	—	60	180	—	230	4.5	4.5	—	$6 \cdot 10^{11}$
6a	’14	’15	NEDC	1.00	0.50	100	—	60	80	—	170	5.0	5.0	—	—
6b	’14	’15	NEDC	1.00	0.50	100	—	60	80	—	170	4.5	4.5	$6 \cdot 10^{12}$	$6 \cdot 10^{11}$
6c	—	’18	WLTC	1.00	0.50	100	—	60	80	—	170	4.5	4.5	$6 \cdot 10^{11}$	$6 \cdot 10^{11}$
6d-TEMP	’17	’19	WLTC	1.00	0.50	100	—	60	80	—	170	4.5	4.5	$6 \cdot 10^{11}$	$6 \cdot 10^{11}$
6d	’20	’21	WLTC	1.00	0.50	100	—	60	80	—	170	4.5	4.5	$6 \cdot 10^{11}$	$6 \cdot 10^{11}$

lower PN limit of $6 \cdot 10^{11}$ #/km for PI as for CI engines (i.e. full Euro 6 requirements) [162].

The latest Euro 6d emissions standard was introduced with Regulation 2016/646 [170]. The new standard extends the previous Euro 6c by real driving emission (RDE) testing against conformity factors, as outlined in the preceding Regulation 2016/427 [171]. Regulation 2016/427 and Regulation 2016/646 are also referred to as RDE Act 1 and RDE Act 2, respectively. The RDE protocol is intended to better reflect the real engine performance on roads by using portable emissions measurement systems (PEMSs) as well as not-to-exceed (NTE) limits. As the name suggests, these limits must be adhered to consistently throughout the test. This type of limits contrasts with the previous standards, which only required the average emissions to remain below the threshold. NTE limits are based on the previous thresholds for laboratory tests plus an additional margin to account for the increased uncertainty associated with the PEMS instrumentation. In practice, this is achieved by using a so-called conformity factor (CF) that is applied to the respective limit:

$$\text{limit}_{\text{NTE}} = \text{CF} \cdot \text{limit} = (1 + \text{margin}) \cdot \text{limit} \tag{2.2}$$

Conformity factors are only intended for NO_X and PN emission measurements. In 2016 these were initially marked as to be determined (TBD) in RDE Act 1 [171]. However, in the same year RDE Act 2 defined a margin for NO_X with 0.5 (i.e. CF = 1.5) [170]. Moreover, a temporary CF of 2.1 was added also for NO_X as part of Euro 6d-TEMP. Euro 6d-TEMP was introduced alongside the Euro 6d as a transitional phase for the introduction of PEMSs measurements. The regulations further defined that these margins are to be reviewed annually.

Two regulations were published in 2017. First, Regulation 2017/1151 [172] outlined the implementation of the new worldwide harmonized light vehicles test procedure (WLTP) with the Euro 6c and Euro 6d(-TEMP) standards.

Further detail on the protocol and the included worldwide harmonized light vehicles test cycless is provided in Section 3.4.1. Second, further specifications of the PEMS were defined in Regulation 2017/1154 [173], i.e. RDE Act 3. The margin for PN measurements was defined as 0.5 (i.e. CF = 1.5). The same margin was included for both Euro 6d and Euro 6d-TEMP. In a study by Giechaskiel et al. [174], published 2018, a possible framework for this review was proposed and reasonable margins for a given uncertainty level were experimentally investigated. A margin range of 0.24 to 0.43 for NO_X measurements was calculated. The worst-case scenario, i.e. a margin of 0.43, was adopted in RDE Act 4 with Regulation 2018/1832 [175] the same year. However, the temporary margin was left unchanged. An overview of the current resulting conformity factors is presented in Table 2.3. Moreover, a timeline of the emissions standards with the respective legal acts is presented in Table 2.4.

It should be mentioned that the addition of conformity factors for NO_X measurements in the regulations was found to be impermissible by the General Court of the European Union in late 2018 [176]. The court found "that even if it had to be accepted that technical constraints may justify a certain adjustment, a difference such as that stemming from the contested regulation means that it is impossible to know whether the Euro 6 standard is complied with during those tests" [177]. The passages regarding the NO_X conformity factors were consequently annulled. However, previously granted vehicle approvals were not retrospectively annulled and allowed to remain effective for 12 months to allow sufficient time to amend the legislation.

2.5.2 Standardisation of Particulate Measurements

The measurement of size-resolved particle concentrations is a challenging process due to the nature of the exhaust gas and the complexity of the required methods (cf. Section 2.4). The PMP was developed by the Joint Research Council (JRC) of the European Commission to enable comparable

Table 2.3: Conformity factor (CF) for measurements of NO_X and PN with PEMS instruments by RDE Acts.

RDE Act	NO_X		PN	
	CF	CF-TEMP	CF	CF-TEMP
1	TBD	—	TBD	—
2	1.5	2.1	TBD	TBD
3	1.5	2.1	1.5	1.5
4	1.43	2.1	1.5	1.5

Table 2.4: Timeline of European emissions standards for passenger vehicle with respective legal acts.

Year	Emissions Standard	European Legal Act
1970	First Emission Limits	Directive 70/220/EEC [160]
1991	Euro 1	Directive 91/441/EEC [163]
1994	Euro 2	Directive 94/12/EC [164]
1998	Euro 3+4	Directive 98/69/EC [165]
2007	Euro 5a+6a	Regulation 715/2007 [166]
2008	Euro 5b+6b	Regulation 692/2008 [167]
2012	Euro 6c	Regulation 459/2012 [169]
2016	RDE Act 1	Regulation 2016/427 [171]
2016	Euro 6d(-TEMP), RDE Act 2	Regulation 2016/646 [170]
2017	WLTP	Regulation 2017/1151 [172]
2017	RDE Act 3	Regulation 2017/1154 [173]
2018	RDE Act 4	Regulation 2018/1832 [175]

results for legislation purposes. The key target was to establish a robust measurement protocol with good repeatability and reproducibility. The non-gaseous fraction of the exhaust gas contains solid particles (i.e. soot and ash) and volatile species. The latter proved to be especially sensitive to the sampling method [178]. Volatiles can condensate onto existing particles [124] or form a separate nucleation mode of particles below 23 nm [155]. Moreover, volatiles can deposit onto the walls of transfer lines and re-enter the sample gas stream at later times [179]. The combination of these processes results in high variability of measurements. Moreover, the question remains whether the recorded data represents real particles or is distorted by volatile artefacts. Thus, a defined conditioning protocol is required to achieve a defined sample state.

The adopted approach was to remove all volatiles from the measurement so that only solid (i.e. non-volatile) particles remain. Therefore, in the legislation, the PN limit is expressed in terms of solid particle number (SPN). The proposed method was formally adopted in 2012 with Regulation 83 of the Economic Commission for Europe of the United Nations (UNECE) [180]. It comprises a sampling design from a CVS tunnel and requires a VPR before particles are detected in a particle number counter (PNC). Additionally, a pre-classifier is recommended to be placed before the VPR. The connecting tube between the vehicle and VPR must be designed to minimise heat-loss and requires heat insulation for lengths above 3.6 m. Regulation 2017/1151 [172] later added that the tube could optionally be heated to above the dew point, for which 70 °C could be assumed to be sufficient. The specifications for the pre-classifier state that the d_{50} cut-off size should be between 2.5 µm to 10 µm and d_{99} at 1 µm, i.e. 50 % and 99 % of particles below the respective size must pass through the classifier (i.e. low-pass filtering). This step is considered to protect the downstream components from excessive particulate contamination and provide a defined upper size limit [155].

The VPR must comprise a heated first dilution, an evaporation tube, and a second 'cold' dilution stage. The first diluter should be capable of diluting

the sample by a factor of 10 to 200 with HEPA filtered air and should be operated at a constant temperature of 150 °C to 400 °C. The evaporation tube should be at or above the temperature of the first diluter but between 300 °C and 400 °C. The second diluter should dilute the gas further by factor 10 to 15 to produce an acceptable particle concentration for the PNC and achieve a sample temperature of below 35 °C. As both the device and the HEPA filtered dilution air are not heated, this stage is described as 'cold' dilution. The VPR unit must be capable of vaporising at least 99 % of 30 nm tetracontane particles at an inlet concentration of 10 000 #/cm^3. For engine testing, this VPR setup was found to achieve removal efficiencies of 50 % to 90 % for the volatile fraction in the accumulation mode of 50 nm to 500 nm [181].

For particle detection with the PNC, detection efficiency cut-off points are defined with d_{50} at 23 nm and d_{90} at 41 nm. In contrast to the above-mentioned cut-off points of the pre-classifier (low-pass), these values describe the fraction of particles detected above the cut-off (high-pass). This limitation is intended to provide an additional safeguard against nucleation mode particles of low volatility compounds [155]. The size of 23 nm is considered a compromise between reliable measurements and the importance of the health risks arising from ultra-fine particles [178]. Moreover, the issue of solid particles below 23 nm was not considered essential, as the underlying intention was to use the method to assess filtration efficiencies of DPFs. Furthermore, research at the time suggested that these were also effectively removed by the particulate filters [153]. The emission level measured with this approach is described as SPN23.

Commercially available systems generally use CPCs as PNC [153]. These devices have been established for several years with d_{50} detection efficiencies as low as 3 nm already reported in 1991 [182]. The d_{50} and d_{90} cut-off points of the individual device can be adjusted to meet the requirements by setting the temperatures of condenser and evaporator elements (cf. Section 2.4.3.1). Accurate calibration requires a source of particles with defined properties. This can be facilitated, for example, by using an electrospray

aerosol generator in combination with a DMA [183]. An electric field is established in the generator between a conductive liquid solution and the containing structure. The electric force evaporates the liquid, generating an aerosol with a distinct particle size peak. The subsequent DMA filters the selected peak further to produce a highly-monodisperse aerosol. The size can be modified by adjusting the voltage of the applied electric field in the generator and corresponding settings of the DMA.

As mentioned in Section 2.5.1, Euro 6d is intended to focus on assessing vehicle emissions in more realistic environments. Rather than testing vehicles in laboratories on chassis dynamometers ('rolling road'), the RDE protocol was introduced with the PEMS. This system can be installed in the vehicle and enables the measurement of emissions while driving on-road. The analysers cover both gaseous and particulate (PN) emissions. Due to the installation of the measurement system on-board the test vehicle, different technical restrictions apply. Consequently, altered regulations apply for the PEMS compared to the PMP system. Instead of a sizeable CVS dilution tunnel, the sample gas is directly collected from the tailpipe. The connecting sample line must always be heated to a minimum of 60 °C for measurement of gaseous emissions, 100 °C for particulate measurements (until the first point of dilution or particle detector), and 190 °C if HCs are measured. Moreover, all parts of the system must be kept at a temperature to avoid condensation. The suggested methods for this are heating, dilution, and oxidation of (semi-)volatile species.

The measurement of PN again requires a VPR and a PNC. The VPR should include a heated section with a temperature above 300 °C and must achieve the same volatility removal efficiency as outlined in the PMP. No further detailed requirements regarding the sample dilution are made; however, a similar VPR setup with two dilution stages—as in the PMP—is depicted in the regulation. The PNC only has a single detection efficiency requirement of d_{50} at "approximately 23 nm" [173]. The $d_{90} = 41$ nm is not included and not prescribed for validation testing. However, additional efficiency

Table 2.5: Required PEMS system detection efficiencies (including sampling line). Adapted from [173].

Mobility Diameter (nm)	System detection efficiency
Sub-23	to be determined
23	0.2–0.6
30	0.3–1.2
50	0.6–1.3
70	0.7–1.3
100	0.7–1.3
200	0.5–2.0

requirements were established for the overall system particle detection (see Table 2.5). The detection efficiency is established as the ratio of the particle concentration readings of the PN analyser system and a reference CPC with $d_{50} = 10\,\text{nm}$ or lower. For the efficiency test, the two systems must be operated in parallel while analysing monodisperse aerosols of the described mobility diameters. As can be observed in Table 2.5, the issue of sub-23 nm solid particles has been introduced on this level with Regulation 2017/1154 [173]. The document states that this area is being investigated to ensure that the real-world PN emissions are adequately reflected in the measurement methods [173]. The aspect of particles below the current size threshold is further discussed in Section 2.5.3.

The gap between measurements from PEMSs and PMP systems remains an ongoing challenge. Uncertainties can be attributed to several reasons. Firstly, the calculation of the exhaust mass flow rate from the tailpipe sampling is higher compared to the CVS sampling [174]. While the uncertainty is below 4 % for higher flow rates—such as during urban driving—variation as high as 10 % can be observed for low flow rates—such as during idling. Moreover, particle losses can differ between the systems due to the different system designs. Thermophoretic losses in the heated line were found to be

around 10 % [156]. Furthermore, agglomeration in the line was found to be the main reason for the difference between CVS and tailpipe measurements [154]. However, the same study suggested that the difference could be reduced to an acceptable level (< 15 %) by accounting for particle losses in the data processing.

The issue of measurement uncertainty was addressed in the legislation by implementing conformity factors, as described in Section 2.5.1. These relax the required emission limits by an additional margin. An annual review is included to ensure continuous improvements towards comparable measurement limits. The initial CF for NO_X was reduced for the first time in with Regulation 2018/1832 [175]; however, the CF for PN remains the same at 1.5 to date. This level appears to be in line with recent research findings. A study by Giechaskiel et al. [184], published the same year as Regulation 2018/1832, found that the technical uncertainty associated with the PEMS is 50 % to 60 % of which 30 % are due to sampling method, i.e. sampling raw exhaust gas from the tailpipe.

2.5.3 Measurement of Sub-23 nm Particles

After the initial exclusion of sub-23 nm particles in the PMP, these particles have moved to the centre of attention in recent years. An early comprehensive literature review by Giechaskiel et al. [28] from 2014 identified several studies that observed solid core particles in the nucleation mode of diesel engines and gasoline engines with both PFI and GDI technology. The review study further included experiments of the JRC that found the fraction of particles excluded with the PMP to be 30 % to 40 %. Despite confirming the presence of such particles, the results were deemed insufficient to support a change of the legislation due to other sources of error and variability, and the overall low PN emission level. However, it was suggested that sub-23 nm particles should be monitored for existing and new technologies.

The implementation of a lower detection threshold presents several challenges. For robust measurements, the volatile fraction of the sample gas must be removed. This reduces the measurement variability associated with these species and enables the measurement of sub-23 nm solid particles. The PMP includes an evaporation tube that is considered to eliminate the nucleation mode and evaporate species that had condensed onto accumulation mode particles. However, as the volatiles are not removed from the sample gas, there is still a risk of re-nucleation for high concentrations of volatile species. This was demonstrated by Otsuki et al. [185] using H_2SO_4 and $(NH_4)_2SO_4$ mists. For inlet concentrations above $1 \cdot 10^6$ #/cm^3, the PMP VPR could not achieve the required 99 % removal efficiency. The same study investigated an alternative to the evaporation tube: removal of volatiles by a catalytic stripper. This approach also delivered compliant removal efficiencies up to inlet concentrations of $1 \cdot 10^7$ #/cm^3. Other studies suggested that by using high dilution ratios for the PMP of up to 1500:1, re-nucleation of volatile species could be sufficiently suppressed without the need of a catalytic stripper [186, 187]. Both options were suggested in a feasibility study by Giechaskiel et al. [188] that was published alongside the 2014 literature review mentioned above. However, it was pointed out that despite preventing volatile artefacts to some extent, high dilution ratios resulted in poor signal to noise ratios and sub-23 nm artefacts could still be observed in some conditions. For either solution, measurements below 10 nm were considered infeasible due to extreme particle losses below this point and a higher risk of artefacts.

As part of the Horizon 2020 research framework programme of the European Union, several projects were funded to investigate sub-23 nm particle emissions and suitable measurement procedures: *Down To Ten*, *SUREAL-23*, and *PEMs4Nano*. As part of the projects, an optimised CPC calibration protocol was developed with detection efficiencies of $d_{50} = 10$ nm and $d_{90} = 23$ nm [189]. The use of catalytic strippers for engine exhaust measurements was once more shown to be effective [190]. Moreover, the projects developed

an improved catalytic stripper with sufficient volatile removal efficiency of 99 % and a penetration rate of 50 % at 10 nm [191, 192]. Meanwhile, work to include the particle range below 23 nm in the legislation had progressed. During the 52nd PMP session in January 2020, new CPC efficiencies of $d_{65} = 10\,\text{nm}$ and $d_{90} = 15\,\text{nm}$ were discussed [193]. Emission levels with this lowered detection threshold are referred to as SPN10. The minutes of a following web conference in May 2020 state a limit of $d_{50} = 10\,\text{nm}$ and the intention to submit a regulation draft in June 2020 to the relevant working body [194]. This was followed up on with a technical report on the development of such a regulatory amendment published in the informal document GRPE-81-15 [195]. In the report, the detection efficiencies of the 52nd PMP session are included.

A larger-scale study was published in 2020 [196], comparing different measurement approaches. Vehicles were tested on roller dynamometers following the NEDC and worldwide harmonized light vehicles test cycles (WLTC) procedures, depending on the applicable regulation for the respective engine and vehicle. Various engine types were included: The majority of vehicles had a GDI engine with gasoline particulate filter (GPF), but also some PFI engines, GDI engines without GPF, and diesel engines with DPF were included. Tests were conducted on two dynamometers with different dilution tunnel systems. For both of these systems, two sets of kits were used for particulate measurements in parallel. The first PN system was equipped with an evaporation tube and a CPC for SPN23. The second PN system used a catalytic stripper and two CPC, one for SPN10 and SPN23 each. The study observed good agreement for SPN23 between both systems, as indicated by a linear correlation with coefficient 0.9429 and a corresponding coefficient of determination $R^2 = 0.9979$. This suggests that the changes in the measurement setup are effective in maintaining consistency for the previously regulated range above 23 nm while enabling measurements down to 10 nm. The sub-23 nm fraction (i.e. particles sized

10 nm to 23 nm) was found to range mostly between 25 % to 50 %, without correcting for particle losses in this range.

A review paper from 2019 by Giechaskiel et al. [162], identified a general tendency of high sub-23 nm particulate emissions for otherwise low PN emission level conditions. The paper cites studies such as the investigation by Zheng et al. [186]; in their work, particles in the exhaust gas were analysed with several CPCs, calibrated for d_{50} of 23 nm, 10 nm, and 3 nm. The measurements of the three detectors were in better agreement when the accumulation mode in the sample was more pronounced. Consequently, the nucleation mode was considered to be suppressed by preferential adsorption onto the larger accumulation mode particles.

A subsequent literature review was published in 2020, comparing catalytic strippers and evaporation tube use-cases [197]. Two dimensions were differentiated in this comparison: residual levels of unburned hydrocarbons and concentrations of sulfuric compounds (i.e. sulfuric acid H_2SO_4 and sulfur dioxide SO_2). Evaporation tubes removed artefacts above 10 nm up to hydrocarbon concentrations of 2 mg/m^3. Artefacts above 23 nm were removed even for higher concentrations; however, an upper limit for effective operation was identified at 15 mg/m^3. The implementation of catalytic strippers removed any artefacts up to significantly higher concentrations of 13 g/m^3; however, some sub-10 nm particles could be observed even at low hydrocarbon concentrations of below 2 mg/m^3. Regarding H_2SO_4, the review summarised that artefacts below 10 nm could always be observed with evaporation tubes. Even for low concentrations of 0.1 mg/m^3, artefacts in the 10 nm to 23 nm range remained. In contrast, catalytic strippers removed all particles originating from sulfuric acid for concentrations as high as 9.3 mg/m^3. Measurements at higher concentrations were generally considered feasible by using catalytic strippers combined with additional sulfur traps.

2.6 Engine Conditions and Parameters

2.6.1 Air-Fuel Ratio

He et al. [198] observed the air-fuel ratio (AFR) to be the parameter with the greatest influence on particulate emissions, with an order of magnitude higher PN emissions for rich mixtures compared to stoichiometric mixtures. Particularly for high-load conditions, fuel-rich combustion modes ought to be avoided, if possible, to prevent high particulate emissions. This observation can easily be explained by the lack of sufficient oxygen for complete combustion of the fuel [199]. In addition to PN reductions of up to 90% for lean mixtures, Pei et al. [200] also observed that the distribution of emitted particles primarily consisted of nucleation mode particles. Likewise, Park et al. [201] observed high concentrations of ultra-fine particles and found significant increases in particulate emissions for very lean mixtures. High excess-air ratios can deteriorate combustion quality and lead to incomplete combustion [199]. Kayes et al. [202] observed increases in PM by two to three orders of magnitude and in PN by around one order of magnitude, for deviations in either direction from the stoichiometric equivalence ratio. Similarly, Price et al. [203] observed PN increases for mixtures leaner than stoichiometric. These were attributed to lower combustion temperatures and thus limited oxidation.

2.6.2 Engine Speed and Load

Particulate emissions from diesel engines generally increase as higher loads are applied. This effect is primarily due to the change in AFR associated with the load variation [204]. In contrast, GDI engines mainly operate with stoichiometric AFR in homogeneous injection mode. Exceptions are rich mixtures in high load-speed conditions for enhanced charge cooling [205] or lean mixtures at part-load conditions in stratified injection operation [2]. In both cases, localised rich AFRs can promote soot formation. Moreover, the

injection of larger fuel quantities at higher loads can result in increased spray impingement on piston or cylinder wall and thus also contribute to elevated particulate emissions [206]. Implications of different injection modes are further discussed in Section 2.6.3.

The effect of engine speed on particulate emissions appears to be similarly linked to the fuel injection. Increased speeds are considered to contribute to the formation of soot due to reduced time available for fuel evaporation and mixing [207]. A study by Hageman and Rothamer [206] conducted tests on an engine in premixed pre-vaporised operation to isolate the effects of reduced time for soot formation and oxidation from the effects of the injection event. A kinetic limitation in the formation process was observed, leading to increased particulate emissions at lower speeds. However, comparisons runs on the same engine with a DI setup revealed the opposite trend, i.e. elevated particulate emissions with increased engine speeds. Thus, indicating that the reduced time for fuel mixing is the predominant factor.

Zhang et al. [208] observed a threefold increase in emitted PN as the engine speed was increased in steps from 1000 rpm to 3000 rpm at 40 Nm, i.e. 3.6 bar brake mean effective pressure (BMEP). The measurements were taken with a Cambustion DMS500. The PSD was observed to be distinctly bimodal at 1000 rpm with a nucleation mode around 10 nm to 30 nm and accumulation mode peak at just above 100 nm. At 1400 rpm and 2000 rpm the nucleation mode manifested itself as a shoulder of the accumulation mode rather than a distinct mode. Moreover, the peak position dropped to 80 nm to 90 nm. At 3000 rpm, the PSD became monomodal with a broad peak between ca. 20 nm to 80 nm. For an engine load sweep at 2000 rpm through 20 Nm, 40 Nm, 80 Nm, and 110 Nm (i.e. 1.8 bar, 3.6 bar, 7.2 bar, and 9.9 bar BMEP), the PN level increased up to 80 Nm before decreasing again. Likewise, the accumulation mode peak became more pronounced towards 80 Nm.

Bonatesta et al. [209] conducted speed and load sweeps while also acquiring measurements with a DMS500. The test matrix ranged from 1600 rpm to 3700 rpm and 30 Nm to 120 Nm (i.e. 2.36 bar to 9.42 bar BMEP), in

four equal steps each. Three areas with high particulate emissions were identified: low-speed high-load ($<$ 2000 rpm, $>$ 6 bar BMEP), medium-speed medium-load (2800 rpm to 3200 rpm, 3.5 bar to 5 bar BMEP) and high-speed high-load ($>$ 3400 rpm, $>$ 8 bar BMEP). The latter exhibited the highest total PN with up to $1 \cdot 10^7$ #/cm^3 compared to $6 \cdot 10^6$ #/cm^3 at the other two areas and low levels outside the three areas of down to $1 \cdot 10^6$ #/cm^3. The PSD plots were not reported directly but in the form of GMDs. Up to ca. 3000 rpm, the GMD increased with load up to 6.75 bar BMEP, beyond which point GMD decreased with further load increases. The largest GMD of 50 nm to 60 nm were observed for high-load low-speed ($<$ 2000 rpm, 4 bar to 8.5 bar BMEP). The lowest GMD of below 23 nm was found for the highest load-speed condition (3700 rpm, 9.42 bar BMEP). This is somewhat surprising as it is otherwise understood that the accumulation mode generally increases with engine load and speed [162], i.e. the highest GMD would have been expected in this area.

Among a series of test conditions, Leach et al. [210] conducted a load sweep from 3 bar to 32 bar BMEP in nine steps at 2000 rpm. Up to ca. 10 bar BMEP the engine was naturally aspirated. Beyond this point, an external charging system simulated supercharging and turbocharging. Particulate measurements were acquired with a Cambustion DMS500 with two processing methods: SPN23 digital filtering for total PN and mean diameter from accumulation mode lognormal fitting for particle sizing. The individual processing methods are further explained in Section 6.2. PN emissions showed a linear increase with load in the naturally aspirated region, from $0.8 \cdot 10^7$ #/cm^3 to $2.2 \cdot 10^7$ #/cm^3 (for 3 bar to 10 bar BMEP). The PN level dropped to $0.2 \cdot 10^7$ #/cm^3 at 15 bar BMEP with the move into the boosted region and slowly increased to ca. $1.5 \cdot 10^7$ #/cm^3 at 28 bar BMEP, before jumping to around $4 \cdot 10^7$ #/cm^3 at 32 bar BMEP. The mean diameter of the accumulation mode increased with load in the naturally aspirated region, from 100 nm to above 200 nm. In contrast, the mean diameter remained

just below 50 nm for the boosted region, even decreasing by few nanometres as the load increases to the maximum.

A study by Bock et al. [211] covered the impact of speed and load on sub-23 nm particulate emissions. A TSI EEPS was used after a double-stage dilution and a catalytic stripper. Moreover, a TSI SMPS was included to verify the measurements. Four conditions were assessed: 1400 rpm with 2 bar BMEP, 2000 rpm with 4 bar BMEP, 2000 rpm with 7 bar BMEP, and 2400 rpm with 7 bar BMEP. Under stoichiometric operation, the PN level gradually increased from $3 \cdot 10^{13}$ #/kWh to $6 \cdot 10^{13}$ #/kWh from the lowest to the highest speed-load point for SPN10. The fraction of sub-23 nm particulates, i.e. (SPN10 − SPN23)/SPN10, decreased from 70 % to 40 %, indicating that the PN increase is predominantly due to accumulation mode particulates. This can also be identified in the PSD plots. At 1400 rpm with 2 bar BMEP, a distinct peak just above 10 nm can be observed, with particle concentrations steadily decreasing towards larger particle sizes. In contrast, the other conditions exhibit less of a nucleation mode peak but rather a plateau between 10 nm and ca. 60 nm.

2.6.3 Fuel Injection Pressure and Timing

The main variable parameters of engine fuel injection systems are injection timing, duration, and pressure. While all three parameters can have a substantial effect on the particulate emissions [212], the highest sensitivity can be identified for changes to the injection timing [213]. Injection of the fuel too early can lead to fuel impingement on the cylinder walls and piston head, and thus the occurrence of pool fires [198, 214]. However, if the fuel is injected too late, the available time for air-fuel mixing can be insufficient and thus result in fuel pockets [200, 203, 214]. Consequently, an optimal injection timing for minimal particulate emissions can be identified for any combustion system [199].

Two distinct combustion modes can be identified by their range of fuel injection timings which lead to different fuel mixing modes: homogeneous and stratified combustion. For homogeneous mixing with air, the fuel is injected early during the intake stroke [57]. This is commonly used for stoichiometric AFRs to avoid incomplete combustion. The early injection of the fuel helps with charge cooling and thus reductions of fuel consumption and CO_2 emissions [199]. To minimise particulate emissions, Kim et al. [212] employed a start of injection (SOI) timing of 330 °CA bTDC, while Ming et al. [215] recommended an SOI range of 250 °CA bTDC to 280 °CA bTDC. He et al. [198] suggested SOI timings later 270 °CA bTDC to avoid fuel impingement.

Stratified injection strategies are often used to facilitate lean combustion [57], i.e. sub-stoichiometric air-fuel-ratios. Lean-burn combustion can increase efficiency by eliminating throttling losses at sub-maximal load conditions [216]. However, large increases in both PM and the accumulation mode of PN emissions by 2x and 5x, respectively, have been observed by Di Iorio et al. [217]. The SOI was set for best combustion stability with 308 °CA bTDC and 73 °CA bTDC for homogeneous and stratified combustion mode, respectively. Johansson et al. [218] observed an overall increase in PN by one to two orders of magnitude for stratified combustion. However, the authors also observed a shift towards accumulation mode, compared to a more pronounced nucleation mode for homogeneous combustion.

In addition to the timing of the fuel injection, splitting the total volume into partial injections can reduce particulate emissions by preventing fuel impingement [199]. Using multiple injections, the individual fuel pulses terminate before they can advance too far into the combustion chamber, i.e. the fuel jet length is reduced. Thus, liquid impingement on the cylinder wall and piston head can be avoided. He et al. [198] observed potential reductions of more than 50% for high-load conditions. However, only little potential of multiple injections was identified at low-load conditions. Su et al. [219] reported a reduction by 60% and 80% for double- and triple-injection strategies, respectively, as mixture preparation was improved

and fuel impingement avoided. Similarly, Ming et al. [215] found that triple-injection strategies can reduce particulate emissions by one order of magnitude compared to single-injection strategies.

The fuel injection duration can be influenced not only by injection splitting but also by the fuel pressure itself. Moreover, higher injection pressures can aid the mixing process by dispersing the fuel in smaller droplets [57]. Better dispersion combined with higher injection speeds could avoid locally rich air-fuel mixtures. Berndorfer et al. [220] observed that finer atomisation leads to more homogeneous mixtures and thus less intense flame radiation. However, while enhancing atomisation, higher fuel pressures can also increase penetration length as the inertia of the fuel pulse increases [221]. Thus, fuel impingement can become an issue if the duration is not limited sufficiently. He et al. [198] recommended fuel injection pressures near the available maximum for minimum particulate emissions, provided that no pump durability or fuel economy penalties apply. However, beyond a certain threshold, additional fuel pressure increases did not improve particulate emissions any further.

2.6.4 Spark Timing

While the SOI commences the fuel mixing process, the ignition spark initiates the combustion process and thus concludes the fuel mixing. The spark timing for maximum brake torque (MBT) appears to be a universal reference point [199]; however, it is not used consistently in the literature. Consequently, the terminology of advanced and delayed spark timings is not necessarily comparable between different studies. Generally, advancing the spark timing extends the time available for combustion and subsequently particulate oxidation, resulting in reduced PM emissions [199]. However, several studies also observed higher PN emissions for advanced spark timings and attributed these to higher peak in-cylinder temperatures and pressures [207, 222, 223]. Pei et al. [200] observed PN increases, especially in the nucleation mode of

the PSD by up to 65%. Kayes et al. [224] had outlined in 1999 that increased temperatures could enhance the mechanisms of both soot nucleation and oxidation. In a more recent study of 2019, Hageman and Rothamer [206] noted that the peak temperatures are above the typical range of soot formation and instead suggested incomplete mixing as the primary reason for the increased number of particulates. Qian et al. [57] added that the high-temperature duration is reduced with advanced spark timings, despite elevated peak temperatures. Thus, the oxidation of particulates would be restricted. De Francquevilla and Pilla [225] observed reduced particulate emissions and improved air-fuel mixing with delayed spark timing due to compression-induced turbulence and longer mixing time. Moreover, elevated in-cylinder and exhaust temperatures were suggested to promote post-flame oxidation and thus reduce particulate emissions [199]. Despite reducing PN emissions [226] and improving anti-knock properties, early spark timings are also associated with engine efficiency and fuel consumption penalties [57]. Therefore, He et al. [198] did not recommend using spark timing as a mean to control particulate emissions but rather to optimise efficiency and other emissions.

2.6.5 Valve Timing

The setting of intake and exhaust valve timing can significantly affect the gas exchange processes. Specifically, the overlap between intake valve opening (IVO) and exhaust valve closing (EVC) is of interest. The optimum timing configuration is highly dependent on the engine speed [227, pp. 293–303]. At low engine speeds, the inlet manifold pressure is low and can thus lead to the backflow of exhaust for large valve overlap. In contrast, the gas exchange can be improved by utilising the exhaust gas pulse, effectively flushing the cylinder for large valve overlaps. Consequently, Chen et al. [228] observed a direct impact of valve timings on the internal exhaust gas recirculation (EGR). Increased EGR levels would result in higher in-cylinder

temperatures and thus better fuel spray evaporation, reducing particulate emissions. However, combustion stability can be compromised at high levels of EGR. Rodriguez and Cheng [229] identified an opportunity for modified valve timings to reduce emissions during cold-start cranking. Late opening of the intake valve was observed to reduce unburned HCs and PN emissions by 25 % and 28 %, respectively. The delayed opening was considered to improve charge mixing by creating a higher initial pressure difference across the valve, increasing intake air velocity and ultimately turbulence. A comprehensive study by He et al. [198] investigated the impact of various valve timings, among other parameters. The impact of intake and exhaust valve timings on PN level was observed to be minor compared to other variables, such as fuel injection settings. However, the impact on NO_X was more pronounced, suggesting that valve timings should be optimised for low NO_X levels rather than control particulate emissions. Similarly, an investigation by Tan et al. [230] observed little effect of different valve timings on particulate emissions for transient condition investigations.

2.6.6 Intake Air Temperature

The temperature of the intake air can have profound implications on the efficiency of the engine and its emissions. Cooler intake air can improve volumetric efficiency as its density is higher, thus enabling more mass to be taken into the same cylinder volume. However, the particulate emissions are inversely related to the air temperature. Elevated intake air temperature leads to higher in-cylinder temperatures and is therefore considered to optimise fuel evaporation and thus improve mixing. Leach et al. [210] found clear reductions in PN with an intake air temperature increase from 20 °C to 40 °C at steady-state tests at 1250 rpm with 3.77 bar BMEP. Moreover, a reduction in mean particle size was observed. Similar findings were previously reported by Chan et al. [231]. Particulate measurements were taken from a GDI vehicle over the FTP-75 driving cycle, as defined by the US Environmental

Protection Agency. Hot- and cold-start tests at ambient temperatures of −18 °C, −7 °C, and 22 °C were compared. Measured PN levels increased by 43 % for the hot-start test when the coldest temperature was compared to the highest temperature. For cold-start tests, the increase was higher with 60 %. The observed size distribution was shifted towards smaller particle sizes for higher ambient air temperatures. A study by Giechaskiel et al. [28] reported on research activity by the JRC from late 2013: The PN emissions of a GDI engine over the WLTC increased threefold for an ambient air temperature of −7 °C compared to 23 °C. The fraction of sub-23 nm particles was observed to increase by up to 100 %, but at least 30 %. Unfortunately, no further information on the experimental setup was included.

2.6.7 Advanced Engine Technologies

One approach in combating elevated vehicle emissions has been the increasing electrification of powertrains in recent years. A variety of different systems can be found on the market, ranging from mild hybrid vehicles with an electric motor assisting the combustion engine to full hybrid vehicles in which the electric motor can be the sole power source [232]. In the case of mild hybrid powertrains, functions such as start-stop modes or the mentioned assisting power by the electric motor during high acceleration can help reduce particulate emissions of the combustion engine, primarily by avoiding these adverse operating conditions for the engine [232]. Specifically, engine idling is associated with high hydrocarbon and PN emissions [233], and elevated PN levels have been linked to stronger acceleration phases [234].

In other efforts, modified operating modes are considered for the design of engines to reduce emissions. One such operating mode is homogeneous charge compression-ignition (HCCI), which offers the potential of reduced NO_X emissions by means of burning "ultra-lean" air-fuel mixtures and achieving reduced combustion temperatures [235]. While this technology can be implemented with PFI engines, the use of GDI systems enables additional

control over the mixture formation through timing and splitting of injections [236]. Two distinct ignition mechanisms can be differentiated in design approaches: controlled auto-ignition (CAI) and spark-assisted compression-ignition (SACI). For the latter, a fraction of the charge is ignited by the spark, and the remaining fraction is subsequently driven into autoignition by the compression of the flame combustion [237]. Consequently, the low and high load capabilities can be extended without the issue of knock. Regarding particulate emissions, it was suggested that production of soot could be avoided if the air-fuel mixture is sufficiently lean [55]. Ojapah et al. [236] observed that particulate emissions of a GDI engine were predominantly below 5 nm when in SI mode, while the distribution was shifted to around 20 nm in CAI mode. The authors hypothesised that reduced combustion temperatures negatively influence soot oxidation. However, literature on the details of particulate emissions behaviour of HCCI engines is scarce.

A limitation of ultra-lean engine designs can be poor ignitability of the air-fuel mixture [238]. For stable engine operation under such conditions, a higher energy ignition source is considered to be required [239]. This problem can be solved, for instance, by using a combustion pre-chamber. An initial combustion event is produced by injecting fuel into the pre-chamber and igniting the mixture with a conventional spark plug. Subsequently, the main chamber combustion is initiated "through chemical, thermal, and turbulent effects" [240], as the pre-chamber contents are forced into the main chamber by the pressure increase of the pre-combustion. This technology was demonstrated to enable considerably leaner air-fuel mixtures compared to traditional SI engines [241], and more recent progress was made towards better stability under low load conditions [238], such as idling and catalyst light-off. Concerns were reported regarding the possibility of elevated particulate emissions due to fuel wall impingement in the pre-chamber [242]; however, the full implications on particulate emissions have yet to be investigated in more detail as the literature is scarce to date, similar to the situation for HCCI engine systems.

2.7 Summary

This literature review provided background information on soot nanoparticles, discussed various techniques for both ex-situ and in-situ measurements, and covered the legislative dimensions with emissions limits and technical requirements. Despite this breadth of existing knowledge, the initial systematised literature search highlighted the relatively sparse coverage of GDI soot, compared to the considerable market share of this engine type.

While some investigations of GDI soot properties exist, further work is required to understand the similarities and differences to other types of soot. For this purpose, robust analysis techniques are required to obtain meaningful and comparable results. Special attention has to be placed on sub-23 nm, as these will be included in PN measurements of future regulations but have been investigated to an even lesser extent.

3 Experimental Methods

Details on the engine equipment and analysis instruments are provided in this chapter. Relevant calculations are presented, and additional soot sampling procedures and preparation methods are outlined. Furthermore, engine test conditions are derived from an in-vehicle driving cycle simulation, and the repeatability of conducted engine tests is assessed through reference points.

Parts of this chapter have previously been published in the journal Carbon, as an SAE Technical Paper that was presented at the SAE 2019 WCX World Congress Experience in Detroit, in the journal Combustion and Flame, as an SAE Technical Paper that was presented at the SAE 2021 WCX Digital Summit, and also included in a manuscript that was submitted for publication:

S.A. Pfau, A. La Rocca, E. Haffner-Staton, et al. Comparative nanostructure analysis of gasoline turbocharged direct injection and diesel soot-in-oil with carbon black. Carbon, 139:342-–352, 2018, DOI 10.1016/j.carbon.2018.06.050.

S.A. Pfau, A. La Rocca, E. Haffner-Staton, et al. Soot in the lubricating oil: An overlooked concern for the gasoline direct injection engine? SAE Technical Paper 2019-01-0301, 2019, DOI 10.4271/2019-01-0301.

S.A. Pfau, A. La Rocca, and M.W. Fay. Quantifying soot nanostructures: Importance of image processing parameters for lattice fringe analysis. Combustion and Flame, 211:430—444, 2020, DOI 10.1016/j.combustflame.2019.10.020.

S.A. Pfau, E. Haffner-Staton, and A. La Rocca. Measurement of sub-23 nm particulate emissions from GDI engines: A comparison of processing methods. SAE Technical Paper 2021-01-0626, 2021, DOI 10.4271/2021-01-0626.

S.A. Pfau, E. Haffner-Staton, A. La Rocca, and M.W. Fay. Investigating the effect of volatiles on sub-23 nm particle number measurements for a downsized GDI engine with a catalytic stripper and digital filtering. Manuscript submitted for publication, 2021.

3.1 Engine Test Setup

3.1.1 Engine Description

For the experiments, a three-cylinder 1.0 l turbocharged GDI Ford EcoBoost engine was used. The maximum torque of ca. 170 Nm—i.e. BMEP of ca. 21.4 bar—is available in the speed range of 1400 rpm to 4500 rpm. The maximum power of 92 kW is produced at 6000 rpm. The full load curve is presented in Figure 3.1. The valve train incorporates a lost-motion type system on the rocker arms of cylinder one for its deactivation. However, the engine was operated conventionally—without cylinder-deactivation—for this study. The spark plugs were not indexed. As this spray-guided GDI engine was operated homogeneously in sub-maximal conditions, the effects from differences in spark plug orientation were considered negligible. The complete specifications of the engine are presented in Table 3.1. The engine control unit (ECU) was accessed via the software ATI Vision, enabling the monitoring and controlling of operating parameters. The test runs were conducted using the default mapping as per the manufacturer settings. Section 3.4.2 in the following includes further detail on these parameters.

The engine is equipped with a Hohner Automation optical shaft encoder with a resolution of 0.5 °CA. The encoder transmits 720 pulses per revolution plus an additional pulse at top dead centre (TDC), thus enabling data acquisition in crank angle (CA) resolution. An accurate setup of the crankshaft encoder is the basis for any CA-resolved measurements. Here, cylinder one is used as a reference point for the calibration. The cylinders are numbered in descending order from the flywheel, i.e. cylinder one is the furthest from the

Table 3.1: Specifications of the 1.0 l Ford EcoBoost engine.

Parameter	Value
Powertrain control module (PCM)	Bosch MED17
Maximum engine speed	6450 rpm (continuous)
Maximum power	125 PS (92 kW) @ 6000 rpm
Maximum torque	170 Nm @ 1400 rpm to 4500 rpm
Idle speed	860 rpm
Bore	71.9 mm
Stroke	82.0 mm
Total engine capacity	999 cm^3
Capacity of each cylinder	333 cm^3
Con rod length	137.0 mm
Nominal compression ratio	10.5:1 ($\pm$0.1)
Firing order	1-2-3
Injector	5-hole solenoid, commonrail
Max. fuel injection pressure	200 bar
Spark plug gap	0.7 mm (+0 –0.1)
Crank offset	8 mm
Piston offset	0.5 mm
Total offset	7.5 mm
Intake valve diameter	23.8 mm
Exhaust valve diameter	19.3 mm
Intake valve opening (IVO)	with lock-pin: 20 °CA aTDC with VVT: up to 40 °CA bTDC
Exhaust valve closing (EVC)	with lock-pin: 0 °CA TDC with VVT: up to 50 °CA aTDC
Intake/exhaust duration	240 °CA / 248 °CA
Tappet clearance intake/exhaust	hydraulic roller finger follower
Turbocharger	fixed geometry with wastegate

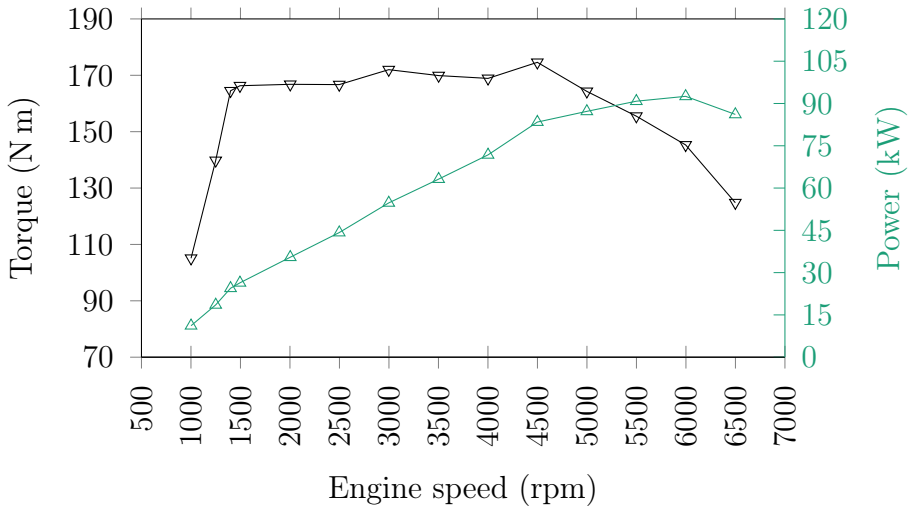

Figure 3.1: Full-load curve of torque (–▽–) and power (–△–) for the 1.0 l Ford EcoBoost engine.

flywheel. The engine's crankshaft can be mechanically locked in place with a pin so that cylinder one is at TDC. The crankshaft encoder is manually rotated, and the TDC signal pulse monitored via the LabVIEW script. This way, a rough positioning of the encoder is facilitated. Subsequently, the locking pin is removed and the crankshaft is rotated. The position of the piston is identified using a TDC probe and the signal is recorded simultaneously with the crankshaft position. Direct comparison of these two data sets enables the accurate calibration of the encoder.

The engine is installed on an engine test stand and the power take-off shaft is connected to a Froude Consine EC38 TA Eddy-Current dynamometer with a rated capacity of 165 kW at 3280 rev/min, maximum speed of 8000 rev/min, and maximum torque of 480 Nm. The dynamometer is regulated by a Froude Texcel V4 controller and is operated in engine speed mode. In other words, the engine speed is regulated to a set speed by varying the applied brake torque. If the engine is below the speed setpoint, the dynamometer remains passive. However, if the engine speed exceeds the set value, the dynamometer applies adequate torque to achieve the desired speed. This closed-loop system

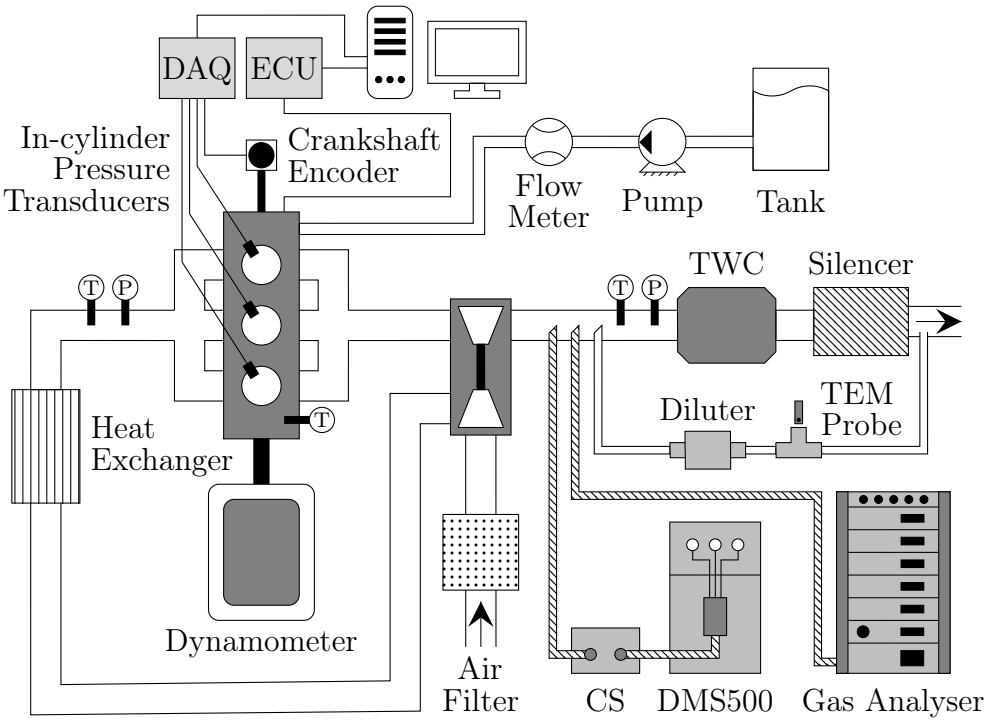

Figure 3.2: Schematic of the measurement and sampling equipment in the engine test stand setup. Thermocouples and additional pressure transducers are marked by Ⓣ and Ⓟ, respectively.

enables operating the engine at specific speed-load conditions; however, motoring of the engine is not possible. Thus, only steady-state conditions are used in this thesis.

3.1.2 Fuel Properties

The fuel for the tests was a RON98 gasoline. The blend does not contain ethanol (0 %V/V), different to commonly available pump gasoline which contains 5 %V/V to 10 %V/V. This fuel was selected due to project constraints for the test schedule into which the tests for this thesis are embedded.

Noteworthy in the context of this thesis, the fuel contains a relatively low concentration of sulfur with 3.4 mg/kg. As sulfur compounds have been

Table 3.2: Fuel specifications as per the supplier data sheet.

Parameter	Value
Density @ 15 °C (kg/m^3)	747.7
LHV (MJ/kg)	42.8
RON	98.4
MON	87.1
DVPE (kPa)	62.7
FBP (°C)	198.3
Ethanol (%V/V)	0
Aromatics (%V/V)	34.5
Oxygenates (%V/V)	<0.8
C:H ratio (H=1)	6.62
Sulfur (mg/kg)	3.4

associated with sub-23 nm particle emissions (cf. Section 2.5.3), the low concentration in the used fuel removes one possible aspect of the formation process. The full specifications as per the data sheet of the supplier are presented in Table 3.2.

3.1.3 Data Acquisition and Sensors

The data acquisition (DAQ) system used for the experiments was a National Instruments cDAQ-9178 with eight module slots. It was equipped with three thermocouple modules, one high-speed analogue voltage input module for in-cylinder pressure transducers. Furthermore, two low-speed analogue voltage input modules for oil pressure, emissions, and fuel flow meter. Lastly, one analogue voltage output module was installed for the engine throttle. The DAQ enables the connection to the computer and LabVIEW script. Two separate scripts are employed; one script for the time-resolved and one for the CA-resolved measurement. The former records measurement

points every 0.25 s, while the latter records the data of 200 continuous cycles with the resolution of the crankshaft encoder (i.e. 0.5 °CA). Moreover, the accelerator pedal signal was emulated by an additional LabVIEW script and controlled through the DAQ.

Piezoelectric Kistler 6045 pressure transducers were installed in the three cylinders to measure the in-cylinder pressures over the combustion cycle (i.e. CA-resolved). Kistler Type 5018 charge amplifiers amplified the signals of the transducers. These amplifiers were set to a maximum pressure of 100 bar and drift compensation measuring mode for engine applications. The advantage of these piezoelectric transducers is their high-frequency response and relatively small size [243]. However, the quality of the signal is affected by thermal shock during the combustion cycle. The effect of thermal load on piezoelectric pressure transducers has two components [244]. Temperature changes can lead to (temporary) deformation of the transducer, pressing on the piezo element, thus altering the baseline signal. Moreover, the sensitivity of the transducer can be affected and thus change the output signal. For this study, it was assumed that the measurements remain reliable throughout one combustion cycle and that any thermal drift over the measurement window of 200 cycles is negligible. Any changes in pressure are thus only attributed to the combustion itself. Prior to the first engine test run, the pressure transducers were calibrated with a dead weight tester up to a maximum pressure of 100 bar.

A secondary source of variability is the referencing procedure. For the subsequent thermodynamic calculations, it is necessary to reference the relative measurements of the pressure transducers. The referencing is ideally done in a portion of the cycle with low thermal drift. Here, the in-cylinder pressure was referenced at bottom dead centre (BDC) of the intake stroke to the intake manifold pressure for each cycle. This method is favourable over referencing to the exhaust manifold pressure during the exhaust stroke [243]. The pressure at the intake and exhaust manifold was measured CA-resolved by piezoresistive Kulite pressure transducers suitable for up to 3 bar and 7 bar,

respectively. In contrast to piezoelectric transducers, these do not suffer from thermal shock issues and thus no risk of drifts in the measurements.

Several K-type thermocouple sensors were installed across the engine, e.g. in the air stream of the intake and exhaust manifold, the coolant lines of the cylinder head, and the oil feed from the oil sump. The thermocouples have a nominal accuracy of ±0.5 °C and include a built-in cold junction compensation. The temperature reference for the signal input is controlled via the settings of the DAQ thermocouple module. Temperature measurements were acquired time-resolved.

The flow of gasoline to the engine was measured time-resolved with a Micro Motion CMFS010M mass flow sensor paired with a Micro Motion 2700 transmitter. The zero stability of the Coriolis mass flow sensor, i.e. the minimum flow rate for accurate measurements, is 0.0045 l/h. The maximum flow rate is 110 l/h and the nominal flow rate is 97 l/h. With an average density of gasoline of 0.75 kg/l, flow rates from 0.0034 kg/h to 82.5 kg/h can be measured. The maximum fuel flow rate for this engine is 30.09 kg/h at 6000 rpm under full load. As the engine plan focuses on low-medium loads and low-medium speeds (see Section 3.4.1), the output range of the transmitter was set to 0 kg/h to 20 kg/h. The obtained mass flow rate reading was compared to fuel injection quantities from the ECU and released energy calculations at the end of Section 3.2.3.

The fuel injection signal was measured CA-resolved with a Fluke i30s current clamp to monitor injection timing and duration. The measuring range of ±30 A covers the current delivered to the peak-and-hold solenoid injectors. The response time is indicated to be better than 1 µs and thus sufficient for measuring injection durations down to a fraction of a microsecond.

3.1.4 Emissions Analyser

The engine-out exhaust gas was analysed for the unburned HCs concentration. A sample gas stream was extracted from a sampling port between the

turbocharger and the catalyst (see Figure 3.2). A heated sampling line was used to avoid condensation of the water fraction and any volatile species. The temperature of the line was set to 190 °C. The sample gas initially passed through a Signal Pre Filter module 352. The module was included to remove particulates from the sample gas to protect the subsequent instruments from damage and contamination.

The HC concentration was measured by a flame ionisation detector in a Signal 3000HM analyser. The instrument mixes the sample gas with a fuel—here hydrogen was used—which is subsequently combusted and ionised. On subsequent collector plates, a small current can be observed from the impacting ions. Changes in this current can be related to the fraction of ionised carbonaceous particles. From this fraction, the equivalent methane fraction in the sample gas can be evaluated.

3.1.5 Differential Mobility Spectrometer

Particulate emissions were measured with a Cambustion DMS500. The general operating principle of a DMS is outlined in Section 2.4.3.4. The sampling block for initial gas conditioning was mounted to the exhaust pipe after the turbocharger to measure engine-out emissions directly. The instrument itself was connected to the sampling block via a 5 m sampling line. Both the sampling line and block were heated to 191 °C to avoid condensation of water and volatile species. The sampling block contained a first dilution stage and a cyclone. The sample gas was diluted 5:1 with compressed air that was HEPA filtered in the DMS500 and then delivered through a separate tube in the heated line. The cyclone was included to remove particles larger than 1000 nm. This prevents excessive contamination that can occur by deposition of large particles which are not included in the measurement range. Moreover, this exclusion of large particles prevents errors due to overlapping electrical mobility. The electrical mobility is high for small particles and then decreases with increasing particle size as the

mechanical drag increases. However, this trend reverses at around 600 nm (see Figure 3.3). Beyond this point, the mobility increases again due to larger increases in electrical charge as compared to mechanical drag [245]. By reducing the operating pressure to 250 mbar (ca. 0.25 atm), the inversion point can be shifted to above 1000 nm. The pressure drop was facilitated by a flow restrictor in the form of a disk with a small hole in it as the last element of the sampling block. Upon entering the DMS500, the sample gas passes through a rotary diluter that provides a second dilution in the range of 12:1 to 500:1. Alternatively, the diluter can be bypassed for direct measurements (1:1). The dilution ratio was selected based on the particulate emission level of the respective operating condition. Measurements were acquired over a window of 180 s. For transient testing conditions, a sampling frequency of 10 Hz is recommended. However, as steady-state conditions are to be investigated here, a longer averaging window—with a sampling frequency of 0.5 Hz—can be facilitated to reduce noise.

For some measurements, a catalytic stripper (CS) from Cambustion was used. The device provides a nominal volatile particle removal efficiency of $> 99\,\%$ for 30 nm tetracontane aerosol. The catalyst heater temperature was set to 410 °C and the cooler temperature was set to 80 °C.

To account for particle losses in the heated sampling line, a penetration efficiency model was applied (see Figure 3.4). This model was provided by Cambustion and is based on the work of Kumar et al. [246]. Specifically, the presented figure includes two models: one for the particle losses in the heated sampling line only and an additional model that also considers additional particle losses of the catalytic stripper.

3.1.6 Exhaust Soot Collection for TEM Analysis

DMS measurements are an effective method for obtaining size distributions of particulates in the exhaust gas during engine tests. However, the technique is also limited by the particle charge model that is used to extract the electrical

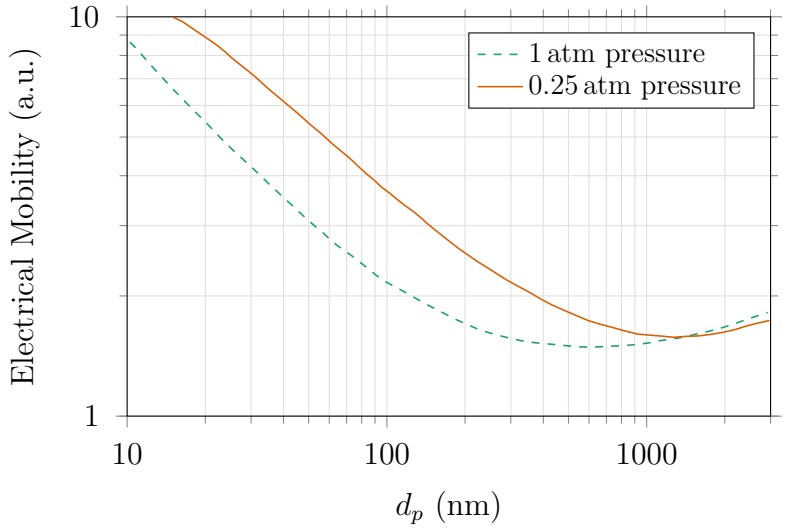

Figure 3.3: Electrical mobility for particle sizes at 1 atm and 0.25 atm operating pressure. Adapted from [245].

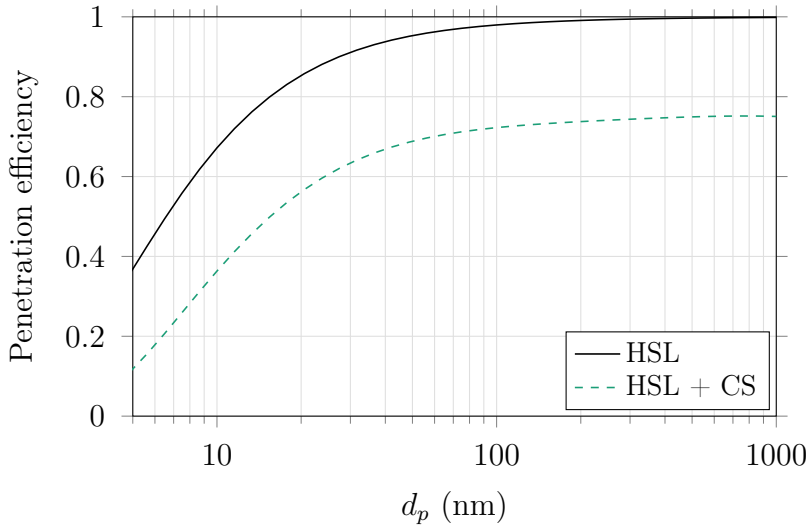

Figure 3.4: Correction model for penetration efficiencies of particles to the DMS after transfer through the heated sampling line (HSL) and after combined HSL plus catalytic stripper (CS). Model provided by Cambustion.

mobility diameters from the recorded electrometer currents. Additional information on morphological and nanostructure properties of soot particles can be obtained by TEM analysis. To facilitate such investigations, soot was captured on TEM grids. This process proved to be challenging due to the two-fold character of the requirements. On the one hand, the exhaust gas presents a hostile environment with high temperatures for the carbon-based grids. Specifically, the TEM grids used consisted of a copper mesh substrate with lacey amorphous carbon and were coated with a graphene-oxide layer. These carbon materials can easily oxidise in the harsh environment of the exhaust pipe, thus limiting the maximum sampling duration. On the other hand, a sufficient concentration of soot particulates must be achieved on the grid to enable meaningful results. While an oversaturation of the grid would be expected especially for engine-out sampling of diesel engines with high particulate emission levels, the experience for the present GDI engine suggested the opposite issue. Consequently, the sampling duration has to be sufficiently long for enough particles to be captured but not too long so that the grid integrity is maintained.

Two sampling setups were used to collect the samples. First, a Dekati ejector diluter was employed as depicted in the schematic of Figure 3.2. The diluter provided a dilution ratio of 1:12 with compressed air. The compressed air was filtered, dried, and heated to 180 °C before entering the ejector diluter. Likewise, the ejector diluter was heated to 180 °C with a covering heating jacket. The TEM grids were placed in an in-house manufactured sampling probe, which in turn was exposed to the diluted gas stream via a T-piece in the tubing. The probe design was based on the concept of Kook et al. [247]. The sampling probe not only provided a practical way of handling the delicate TEM grids but also offered a higher thermal capacity to enable longer sampling durations. To achieve acceptable concentrations of soot on the grids, sampling durations of 40 min had to be used. Even with such extended spans, the particle concentrations on the grid remained relatively low; however, no decomposition of the grid materials could be observed.

The second approach was to place the sampling probe directly into the exhaust gas stream. An in-house manufactured mechanical valve was used to facilitate access into the exhaust pipe with the engine running. The valve was designed to be mountable using the same fitting as for the pipe that connected the ejector diluter so that the two systems can be swapped and can sample at the same location along the exhaust pipe. Initial investigations were carried out with the engine operated at 1750 rpm with 20 Nm brake torque and a resulting exhaust gas temperature of just under 400 °C. Incipient grid decomposition could be observed for a sampling duration of 5 min, with further distinct breakdown at 10 min. The feasible maximum duration was found to be approximately 3 min.

3.2 Analysis of Cylinder Pressure Data

Simple means to monitor the engine operation include load and speed as observed from the dynamometer and properties available from the ECU. A variety of additional metrics can be obtained from the in-cylinder pressure traces. These can provide additional insight into aspects such as engine health in the form of the condition of the valves (pumping losses), liners and bearings (friction losses), and combustion chamber seals (isentropic coefficients). Furthermore, properties relating to the specifics of the combustion process can be extracted.

In the following, the definitions and calculation of these metrics are detailed. To help visualise the properties, the pressure trace of cylinder one over an entire combustion cycle of operation at 2000 rpm with 8 Nm is used as an example (see Figure 3.5).

3.2.1 Mean Effective Pressures

Output brake torque T_b and in-cylinder peak pressure p_{max} are helpful metrics to examine the performance of engines. However, both properties

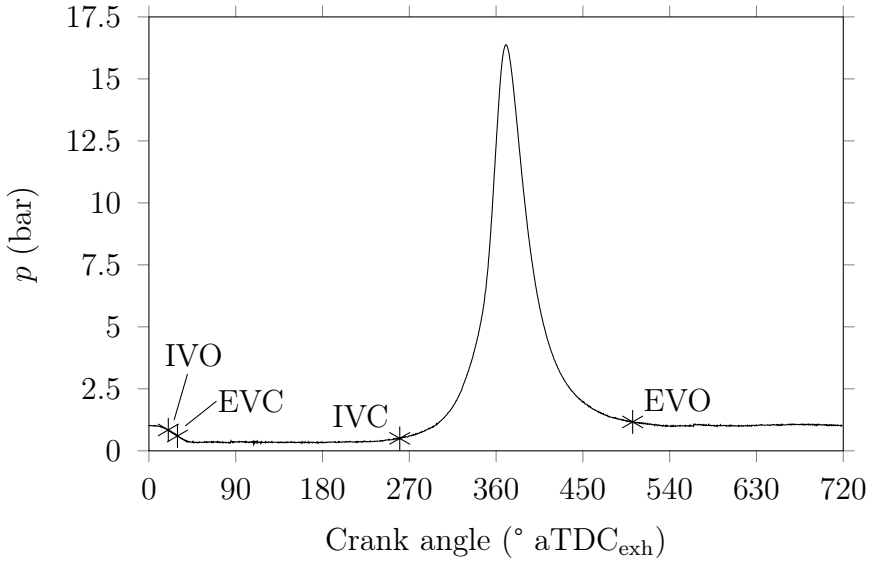

Figure 3.5: In-cylinder pressure trace over an entire cycle. Data from the EcoBoost engine operated at 2000 rpm with 8 Nm. Valve timings as per ECU readings.

depend on the size of the respective engines [248, p. 50]. Dividing the work by the swept volume provides a more suitable parameter: the mean effective pressure (MEP).

$$p_{me} = \frac{W}{V_s} \tag{3.1}$$

where:

p_{me} is the mean effective pressure (Pa);

W is the work (J);

V_s is the swept volume (m^3).

There are several MEPs that can be differentiated. The BMEP can be calculated from the dynamometer brake torque measurement T_b. First, the brake work W_b is calculated by:

$$W_b = 2\pi T_b N_c \tag{3.2}$$

where:

W_b is the brake work (J);

T_b is the brake torque (Nm);

N_c is the revolutions per complete engine cycle.

With the obtained W_b and $N_c = 2$ (for a four-stroke engine), the BMEP $p_{me,b}$ can be obtained:

$$p_{me,b} = \frac{4\pi T_b}{V_s} \tag{3.3}$$

where:

$p_{me,b}$ is the brake mean effective pressure (Pa).

The indicated mean effective pressure (IMEP) relates to the pressure generated by the combustion and can be calculated from the measured in-cylinder pressure p. Initially, the indicated work W_i is obtained by integrating the pressure over the volume change of the cycle:

$$W_i = \int p \, \mathrm{d}V \tag{3.4}$$

where:

W_i is the indicated work (J),

p is the in-cylinder pressure (Pa);

V is the volume (m^3).

With W_i in Equation 3.1, the IMEP $p_{me,i}$ follows:

$$p_{me,i} = \frac{\int p \, \mathrm{d}V}{V_s} \tag{3.5}$$

where:

$p_{me,i}$ is the indicated mean effective pressure (Pa).

The intake and exhaust strokes of four-stroke engines contain periods of negative work due to the pumping of gas in and out of the cylinder. If these pumping losses are included, and the pressure is integrated over the entire cycle, the net IMEP $p_{me,i,n}$ is obtained. However, if the pressure is only integrated over the compression and power stroke, i.e. the pumping losses are excluded, the gross IMEP $p_{me,i,g}$ is calculated. Consequently, the pumping mean effective pressure (PMEP) $p_{me,p}$ is the difference between these two metrics:

$$p_{me,p} = p_{me,i,g} - p_{me,i,n} \tag{3.6}$$

where:

$p_{me,p}$ is the pumping mean effective pressure (Pa);

$p_{me,i,g}$ is the gross indicated mean effective pressure (Pa);

$p_{me,i,n}$ is the net indicated mean effective pressure (Pa).

Lastly, the difference between the net IMEP and the BMEP describes the friction of the engine, i.e. the friction mean effective pressure (FMEP) $p_{me,f}$:

$$p_{me,f} = p_{me,i,n} - p_{me,b} \tag{3.7}$$

where:

$p_{me,f}$ is the friction mean effective pressure (Pa).

3.2.2 Isentropic Coefficient

An additional consideration of engine health is the condition of the components sealing the combustion chamber, such as piston seals, head gasket, and valves. Only if these parts are intact, the combustion chamber is properly closed-off, and the nominal compression ratio can be achieved. One approach to monitoring this aspect is the isentropic coefficient. Any process that is both reversible and occurring without heat or mass exchange with the system's surroundings can be described as isentropic. For such a process, the heat capacity ratio γ—also known as the isentropic coefficient—of an ideal gas is constant:

$$p \cdot V^{\gamma} = const. \tag{3.8}$$

where:

γ is the heat capacity ratio or isentropic coefficient.

In the case of internal combustion engines, this can be assumed as approximation for the compression stroke from intake valve closing (IVC) to start of combustion (SOC) and the power stroke from end of combustion (EOC) to exhaust valve opening (EVO). The calculation of the SOC and EOC is outlined in Section 3.2.3. The isentropic nature of these two cycle-segments can be observed as linear behaviour in the logarithmically scaled pV-diagram (see Figure 3.6b). The isentropic coefficient for the process between two points can be calculated by:

$$\gamma = \frac{log\left(\frac{p_2}{p_1}\right)}{log\left(\frac{V_1}{V_2}\right)} \tag{3.9}$$

To account for signal noise near the end and the start of the valve movements, a 10 °CA offset from IVC and EVO was added, respectively. Further, a

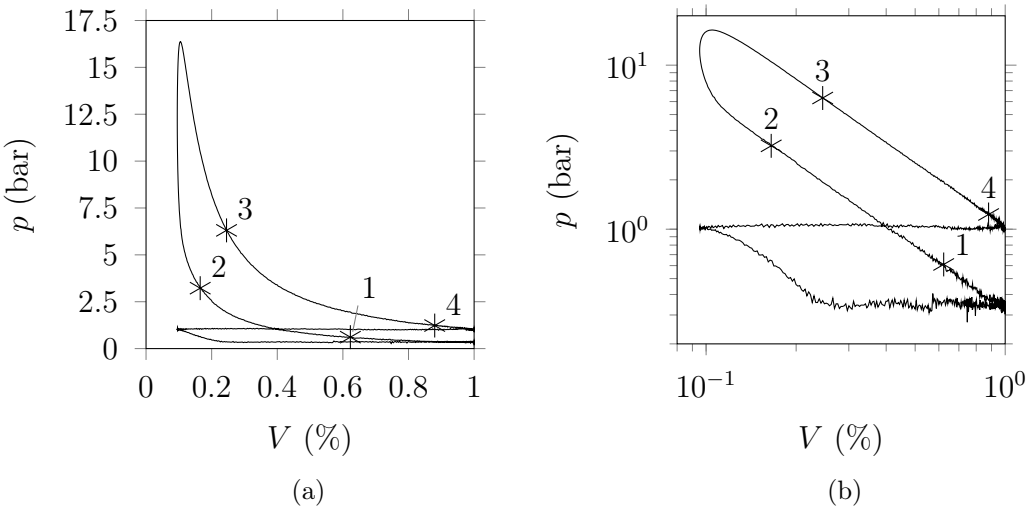

Figure 3.6: pV-diagram on a linear (a) and logarithmic (b) scale. 1: 10 °CA after IVC, 2: 20 °CA before SOC, 3: 20 °CA after EOC, 4: 10 °CA before EVO. Data from the EcoBoost engine operated at 2000 rpm with 8 Nm.

20 °CA offset from the cycle-averaged SOC and EOC was added to account for pressure changes outside the 1.5 J/°CA threshold window. It should be noted that this approach neglects the effect of blow-by gases, heat transfer to the cylinder walls, and losses due to friction.

3.2.3 Heat Release Rate

Further insight into the combustion process can be gathered from analysis of the heat release rate (HRR). This property can be obtained from the in-cylinder pressure using equations based on a simplified form of the first law of thermodynamics [227, p. 547]. This simplification requires the following underlying assumptions. First, the properties of the initial reactants and resulting combustion products are considered not to change. Secondly, the temperature and composition are assumed not to vary within the cylinder, i.e. that only a single zone exists within the cylinder. Lastly, the mass

flow across the system boundary is neglected. The latter comprises blow-by gases through the space between piston and cylinder wall, as well as crevice volumes in threads of the spark plug and fuel injector [248, p. 361]. The equation for the total energy released follows as:

$$\delta Q_g = \mathrm{d}U_s + \delta W_p + \delta Q_{ht} \tag{3.10}$$

where:

Q_g is the gross energy released by the combustion (J);

U_s is the sensible energy of the charge (J);

W_p is the work done by the piston (J);

Q_{ht} is the energy conveyed by heat transfer (J).

Further:

$$U_s = c_v m T \tag{3.11}$$

where:

c_v is the specific heat coefficient at constant volume (J/(kg K));

m is the mass (kg);

T is the in-cylinder temperature (K).

Considering the ideal gas equation:

$$pV = mR_sT \tag{3.12}$$

where:

R_s is the specific gas constant (J/(kg K)).

It follows for U_s:

$$U_s = \frac{c_v}{R_s} \cdot pV \tag{3.13}$$

The two properties c_v and R_s are further related by:

$$R_s = c_p - c_v \tag{3.14}$$

$$\gamma = \frac{c_p}{c_v} \tag{3.15}$$

where:

c_p is the specific heat coefficient at constant pressure ($\mathrm{J/(kg\,K)}$).

Therewith Equation 3.13 can be rewritten as:

$$U_s = \frac{1}{\gamma - 1} \cdot pV \tag{3.16}$$

The properties of the charge gas vary with its temperature. Thus, γ changes as the gas is compressed, as the combustion occurs, and as the gas expands. Two approaches can be distinguished for calculating γ: constant value approximation and instantaneous value modelling. The former uses a constant value across the combustion window. This approximation neglects the changes to the gas properties; however, it reduces the computational complexity. For the instantaneous value modelling, γ is calculated individually for every point in the combustion window. Various models are available for this estimation. Here, the model by Brunt et al. [249] is used:

$$\gamma = 1.338 - 6 \cdot 10^{-5} \cdot T + 1 \cdot 10^{-8} \cdot T^2 \tag{3.17}$$

The in-cylinder temperature can be obtained using the ideal gas equation (see Equation 3.12) combined with the intake air temperature and pressure at a reference CA position θ_r:

$$T = T_{in,r} \cdot \frac{p \cdot V}{p_r \cdot V_r} \tag{3.18}$$

where:

$T_{in,r}$ is the intake-air temperature at reference θ_r (K);

p_r is the in-cylinder pressure at reference θ_r (Pa);

V_r is the cylinder volume at reference θ_r (m^3).

For this study, the condition at IVC is used as reference CA position, i.e. $\theta_r = \theta_{IVC}$. As γ changes with the crank angle position as well as p and V, the derivative of U_s from Equation 3.16 is:

$$\mathrm{d}U_s = \frac{1}{\gamma - 1} \cdot (\mathrm{d}pV + p\,\mathrm{d}V) - \frac{1}{(\gamma - 1)^2} \cdot pV\,\mathrm{d}\gamma \tag{3.19}$$

With $\delta W_p = p\,\mathrm{d}V$ and Equation 3.19, the net heat release rate (NHRR) per CA can be obtained from Equation 3.10 as:

$$\begin{aligned} \frac{\mathrm{d}Q_n}{\mathrm{d}\theta} &= \frac{\mathrm{d}Q_g}{\mathrm{d}\theta} - \frac{\mathrm{d}Q_{ht}}{\mathrm{d}\theta} \\ &= \frac{1}{\gamma - 1} \cdot V\frac{\mathrm{d}p}{\mathrm{d}\theta} + \frac{\gamma}{\gamma - 1} \cdot p\frac{\mathrm{d}V}{\mathrm{d}\theta} - \frac{1}{(\gamma - 1)^2} \cdot pV\frac{\mathrm{d}\gamma}{\mathrm{d}\theta} \end{aligned} \tag{3.20}$$

where:

Q_n is the net energy released by the combustion (J);

θ is the crank angle position (°).

In the obtained NHRR, a noticeable level of high-frequency noise can be observed (see Figure 3.7). Consequently, filtering the raw signal is advisable to remove the background noise and to increase the quality of the subsequent processing. Here, this is facilitated by envelope averaging. The upper and lower peak envelopes are obtained by spline interpolation over local extrema with minimum separations of at least four measurement intervals (i.e. 2 °CA. This minimum separation value was found to provide sufficient smoothing with only minimal alteration of the signal shape. The mean of these two envelope functions is used as the input for the subsequent analysis (see Figure 3.8).

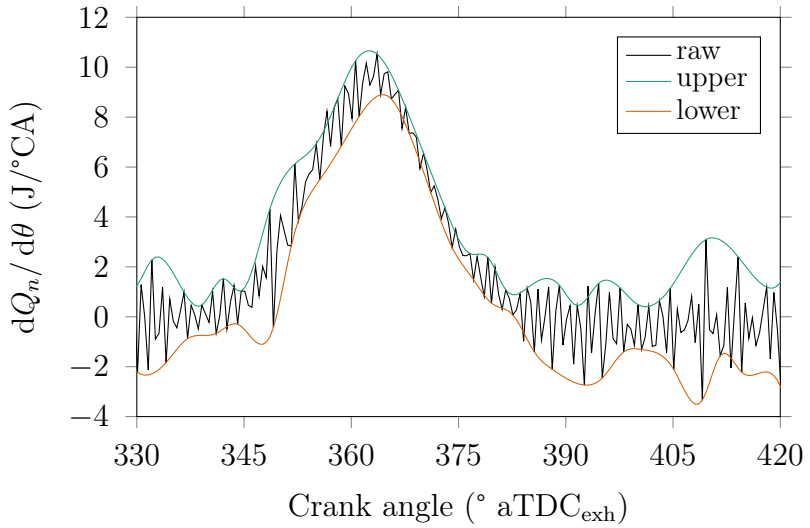

Figure 3.7: Raw NHRR with upper and lower envelope, obtained by spline interpolation over local extrema separated by at least 4 samples. Data from the EcoBoost engine operated at 2000 rpm with 8 Nm.

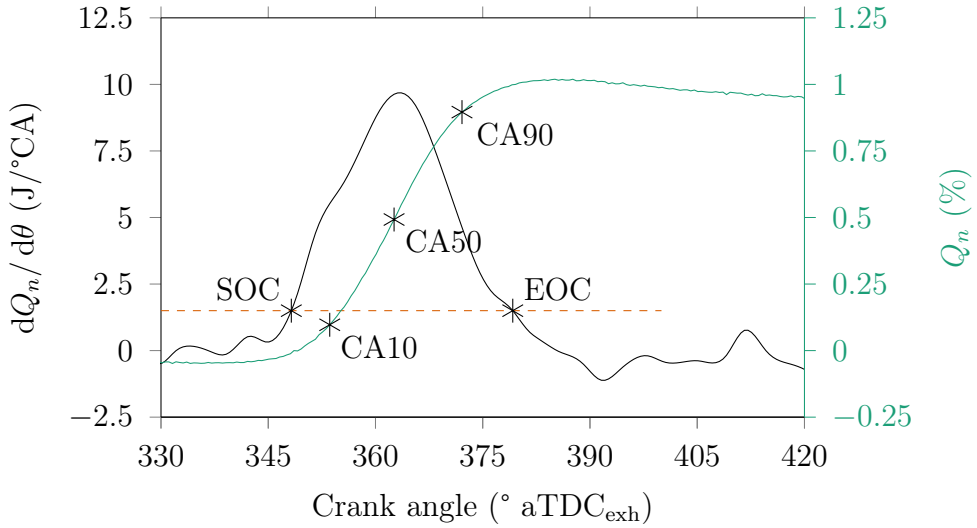

Figure 3.8: Smoothed NHRR (——) and CNHR (——) with annotated SOC, EOC, MFB positions, and the critical HRR threshold (- - -). Data from the EcoBoost engine operated at 2000 rpm with 8 Nm.

To determine the start and end point of the combustion window, a critical HRR threshold of 1.5 J/°CA is employed. The SOC is defined as the first CA position where the NHRR exceeds this threshold (see Figure 3.8). Likewise, the EOC is the first CA position after SOC where the NHRR drops below the threshold. Subsequently, the cumulative net heat released (CNHR) can be obtained by integrating the calculated NHRR curve from SOC to EOC. For better visualisation, the CNHR has also been plotted beyond this combustion window, maintaining $\mathrm{CNHR}_{\mathrm{SOC}} = 0$. Once the CNHR is normalised to its value at EOC, the mass fraction burned (MFB) can easily be identified (see Figure 3.8). The typically reported positions are 10 %, 50 %, and 90 % MFB. These are also depicted in Figure 3.8 as CA10, CA50, and CA90, respectively. The combustion duration is generally understood as the span between 10 % and 90 % MFB (i.e. CA10 and CA90).

The gross heat release rate (GHRR) can be calculated by considering the heat transfer to the cylinder walls. Heat losses typically account for 10 % to 15 % of the heat release from the fuel energy [248, p. 387]. The transfer occurs predominantly via convection near the cylinder walls. Thus, the heat transfer rate can be calculated as:

$$\frac{\mathrm{d}Q_{ht}}{\mathrm{d}t} = A_c \cdot h_c \cdot (T - T_w) \tag{3.21}$$

where:

- A_c is the cylinder chamber surface area (m^2);
- h_c is the heat transfer coefficient ($\mathrm{W/(m^2\,K)}$);
- T_w is the cylinder wall temperature (K).

This time-resolved heat transfer equation can be converted to the CA domain using the following term (units included in the equation for clarification):

$$\frac{\mathrm{d}t}{\mathrm{d}\theta} = \frac{60\,\mathrm{s/min}}{N\,\mathrm{rev/min} \cdot 360\,\mathrm{CA/rev}} = \frac{1}{6N}\ \mathrm{s/CA} \tag{3.22}$$

where:

N is the engine speed (rpm).

Thus:

$$\frac{\mathrm{d}Q_{ht}}{\mathrm{d}\theta} = \frac{A_c \cdot h_c \cdot (T - T_w)}{6N} \tag{3.23}$$

The cylinder wall temperature can be assumed to be constant throughout a single engine-cycle. For the engine used here, temperature measurements of the crankcase block near the cylinder liners are available. Temperatures in the range of 90 °C to 100 °C were previously observed for operation in low to medium load/speed conditions. Hence, 95 °C (i.e. 368.15 K) is used here as an estimate of T_w.

For the surface area, the cylinder chamber is simplified to a simple cylindrical shape. Thus, an equivalence surface area can be obtained for the respective instantaneous volume. However, this approach omits the contour of the cylinder head with valves, spark plug, fuel injector, and the piston head's shape. The effect of these is neglected.

Commonly used models for the heat transfer coefficient were previously developed by Woschni [250]—universally for all engines—and by Hohenberg [251]—for Diesel engines in particular. However, Huegel et al. [252] found that Hohenberg's equation is also better suitable for gasoline engines, compared to Woschni's model. The equation is as follows:

$$h_c = \frac{C_1 \cdot p^{0.8}}{V_s^{0.06} \cdot T^{0.4}} \cdot (\overline{v}_p + C_2)^{0.8} \tag{3.24}$$

where:

C_1 is the first constant of Hohenberg's equation;

C_2 is the second constant of Hohenberg's equation;

$\overline{v}_p$ is the mean piston speed (m/s).

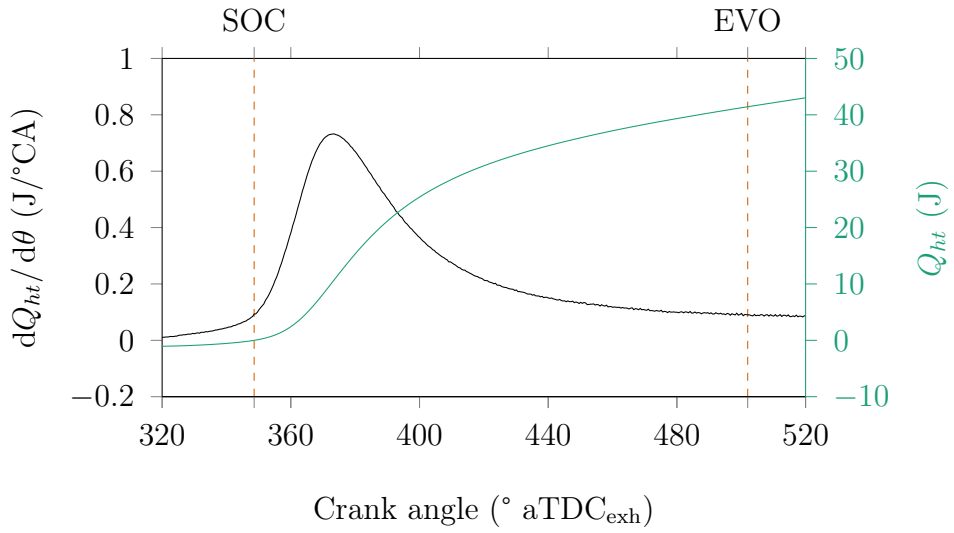

Figure 3.9: Rate of heat transfer (——) and cumulative heat transferred (——). Additionally the SOC and EVO positions are marked (- - -). Data from the EcoBoost engine operated at 2000 rpm with 8 Nm.

The constants for this equation as established by Hohenberg [251] are $C_1 = 130$ and $C_2 = 1.4$. The former is based on the input of pressure values in bar. However, for consistency of units, here $C_1 = 1.3 \cdot 10^{-2}$ is chosen to facilitate a pressure input in Pa. The second constant is used as per Hohenberg.

Heat transfer to the cylinder walls becomes noticeable as heat is increasingly generated by the combustion (i.e. SOC) and continues until the exhaust gas is removed from the cylinder. While some heat transfer still occurs after the exhaust valve is opened (i.e. EVO), the in-cylinder temperature cannot be accurately determined beyond this point as the underlying condition for the ideal gas equation—that of an enclosed system—is no longer satisfied. Thus, the cumulative heat transferred to the cylinder walls is obtained here by integrating from SOC to EVO (see Figure 3.9).

Q_g can now be calculated as:

$$Q_g = Q_n(\theta_{EOC}) + Q_{ht}(\theta_{EVO}) \tag{3.25}$$

To determine the hourly fuel consumption, i.e. $\dot{m}_f$, the total energy released across all cylinders per hour is required. This value can be calculated from the Q_g, i.e. the energy released per cylinder per cycle:

$$Q_{tot} = \frac{60 N_{cyl} N}{N_c \cdot 10^{-6}} \cdot Q_g \tag{3.26}$$

where:

Q_{tot} is the total energy released per hour (MJ/h);

N_{cyl} is the number of cylinders.

With the lower heating value (LHV) of the used gasoline, 42.8 MJ/kg (see Table 3.2), the fuel mass flow rate $\dot{m}_f$ follows as:

$$\dot{m}_f = \frac{Q_{tot}}{LHV} \tag{3.27}$$

where:

LHV is the lower heating value (MJ/kg).

For the example case of the EcoBoost operating at 2000 rpm and 8 Nm, the total energy released across all cylinders was 38.3 MJ/h (SD 3.25). Thus, the fuel consumption follows as 0.89 kg/h (SD 0.075). This value can be checked against the two other methods: the fuel flow as recorded by the mass flow meter and the fuel injection as controlled by the ECU. The mass flow meter recorded a fuel flow of 1.00 kg/h with a standard deviation (SD) of 0.14. The average amount of fuel per injection was $1.2 \cdot 10^{-5}$ lb. This equates to a fuel consumption of ca. 0.98 kg/h. The reading was constant over the recording period at the available resolution level of the ECU, $1 \cdot 10^{-6}$ lb. Consequently, the SD is assumed to be smaller than $0.5 \cdot 10^{-6}$ lb, or 0.04 kg/h

for this operating condition. The ECU-derived fuel consumption is closely matched by the reading of the fuel flow meter. The HRR-derived value is ca. 10 % below the ECU equivalent; however, the range of one SD overlaps with its counterpart from the flow meter. The SD of the HRR-derived fuel consumption is half that of the flow meter equivalent; however, some variation between the cylinders should be considered. The individual values are 0.93 kg/h (SD 0.03), 0.83 kg/h (SD 0.1), and 0.89 kg/h (SD 0.03) as extrapolated for the engine from cylinder one, two, and three, respectively.

3.3 Analysis of Fuel Injector Signal

The fuel injection signal was recorded with a single Fluke i30s for all three cylinders. Over two revolutions, i.e. 720 °CA, one injection is triggered per cylinder. Thus, a window of 240 °CA is available for each cylinder. As the current clamp signal is recorded CA-resolved and referenced to the TDC of cylinder one, the order of injection signals matches the engine's firing order. The SOI is here defined as the CA position with the maximum current in the respective window (see Figure 3.10). It should be noted that the current threshold for the peak-and-hold injectors is likely reached slightly before the maximum current. As the threshold value for the used injectors is not specifically known, the simplified approach of using the maximum current position as SOI is used. However, the main purpose of observing the injection signals is to monitor the injection duration t_{inj}. Thus, the minor offset is neglected as it remains constant for different conditions. The end of injection (EOI) is here defined as the drop in the current after the hold-phase of the signal pulse. The current average over the entire 720 °CA window is used as a threshold for establishing the EOI. By averaging over the entirety of two revolutions the background noise is taken into account. This approach further elevates the threshold slightly above the noise level due to the signal pulses' contribution (see Figure 3.10). The EOI is defined as the CA position where the current first drops below this threshold.

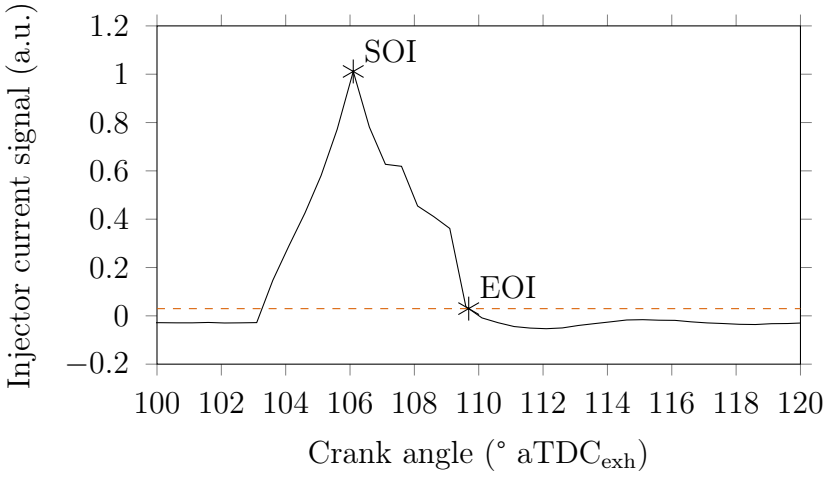

Figure 3.10: Injector current signal (——) with annotated SOI, EOI, and EOI signal threshold (- - -). Data from the EcoBoost engine operated at 2000 rpm with 8 Nm.

3.4 Engine Test Schedule

3.4.1 Test Matrix from WLTC

Fundamentally, engine tests can be performed under either constant load conditions or transient load cycles. The latter are commonly established as driving cycles for the standardised testing of engines for in-vehicle applications on chassis dynamometers. Early driving cycles were established in Europe and the USA with the NEDC in 1970 and the federal test procedure (FTP) in 1978, respectively. Furthermore, the 10-mode driving cycle was introduced in Japan in 1983. All of the mentioned driving cycles have been updated or extended since their introduction; however, they remained limited to specific regions. The WLTP was introduced in 2015 as the successor to the NEDC, to be the first globally uniform protocol. The WLTP comprises a series of driving cycles, i.e. the WLTC. As these are among the most recent driving cycles and incorporate a broad range of load conditions, the WLTC are here used as the basis for the testing layout. Transient driving

cycles are suitable for assessing engine behaviour in terms of performance and emissions in real-world driving applications. However, steady-state tests are necessary as these allow for isolated assessment of individual engine parameters and facilitate repeatability. In the following, steady-state conditions are derived from the WLTC to ensure meaningful tests.

The WLTC comprise three vehicle classes based on the ratio of rated power to mass in running order minus 75 kg (see Annex 1 of [253]): class 1 for low power vehicles of under or equal 22 W/kg, class 2 for vehicles of up to 34 W/kg, and class 3 for vehicles over 34 W/kg. As the engine is mounted on an engine test stand for this study, a reference vehicle application must be defined to derive corresponding engine conditions. The available Ford EcoBoost engine is widely used in the third generation Ford Focus. For this study, a four-door sedan with manual transmission is selected as a reference vehicle. Further specifications are listed in Table 3.3. Based on a vehicle kerb weight of 1306 kg and a maximum engine power of 92 kW, the power to weight ratio is 74.7 W/kg. Thus, WLTC class 3 has to be used for the test. This class is further differentiated based on the maximum vehicle speed, i.e. class 3a and 3b for maximum speeds of under and over 135 km/h, respectively. With a top speed of 195 km/h, the reference vehicle falls within WLTC class 3b. The prescribed vehicle speed profile with four distinct speed phases is presented in Figure 3.11. The phases of the driving cycle are labelled as low, medium, high, and extra-high. These are intended to correspond to driving conditions in urban, suburban, main roads and motorway environments, respectively. The combination of both the low and medium phase is also known as the city cycles and included in the testing of electric and hybrid-electric vehicles.

The WLTC are designed for vehicle testing on chassis dynamometers, as pointed out above. Consequently, the testing protocols are described as vehicle speed in km/h. For tests on an engine dynamometer, these values have to be converted to engine speeds and loads. The engine speed at given vehicle speeds and gears can be directly obtained using the wheel

Table 3.3: Specifications of the reference vehicle (Ford Focus).

Parameter	Value
Type	Ford Focus, 3rd generation
Model	Sedan, four-door
Width with/without mirrors	2010 mm / 1823 mm
Height	1484 mm
Aerodynamic coefficient	0.274
Kerb weight	1306 kg
Gross vehicle mass	1900 kg
Gross train mass	3100 kg
Engine	1.0 l EcoBoost, 125 PS (92 kW)
Maximum speed	195 km/h
Transmission	Durashift 6-speed manual
	6th 0.690
	5th 0.821
	4th 1.032
	3rd 1.357
	2nd 2.048
	1st 3.727
	Reverse 3.820
	Final drive 4.070
Wheels (standard)	16 in x 6.5 in
Tyres (standard)	205/55-R16

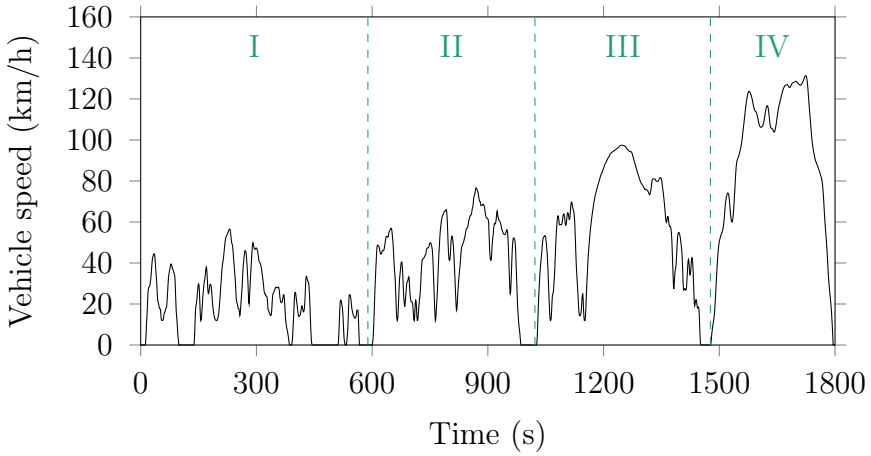

Figure 3.11: Vehicle speed over the complete WLTC class 3b driving cycle with annotated cycle phases. I: low-speed phase, II: medium-speed phase, III: high-speed phase, IV: extra-high-speed phase.

and tyre size, and final drive ratio. To establish the required gear for every point of the driving cycle, the required power has to be determined. The required power can be obtained as:

$$P_{req,i} = \frac{(v_i * (F_c + k_r \cdot a_i \cdot m_v))}{3600} \tag{3.28}$$

where:

$P_{req,i}$ is the required power at the time i (kW);

v_i is the vehicle speed at the time i (km/h);

F_c is the road load force (N);

k_r is the correction factor for inertial resistance of the drive train during acceleration;

a_i is the vehicle acceleration at the time i (km/h^2);

m_v is the vehicle kerb weight (kg).

The formula comprises both the experienced road load and the required power to undergo the prescribed acceleration. In accordance with the WLTP, the correction factor k_r is set to 1.03. Road load forces for chassis dynamometer applications can commonly be obtained by coast down techniques or torque meter methods. Both are not viable for engine dynamometer applications. However, the WLTP outlines an alternative road load calculation based solely on vehicle parameters [253]:

$$F_c = f_0 + f_1 \cdot v_i + f_2 \cdot v_i^2 \tag{3.29}$$

with:

$$f_0 = 0.14 \cdot m_v \tag{3.30}$$

$$f_1 = 0 \tag{3.31}$$

$$f_2 = 2.8 \cdot 10^{-6} \cdot m_v + 0.017 \cdot w_v \cdot h_v \tag{3.32}$$

where:

f_0 is the constant road load coefficient (N);

f_1 is the first-order road load coefficient (N);

f_2 is the second-order road load coefficient (N);

w_v is the vehicle width excluding mirrors (m);

h_v is the vehicle height (m).

The gears are subsequently selected based on the required power and the available engine power according to the full load power curve. Moreover, the WLTP defines guidelines regarding gear selection and shift points to enable driveability and consistency. The resulting engine speed and engine brake torque curves are shown in Figures 3.12 and 3.13, respectively. The engine speed remains between 860 rpm and 2300 rpm for most of the driving cycle, except for the extra high phase with a maximum of 3250 rpm. In contrast, the required engine brake torque does not exhibit such distinct levels.

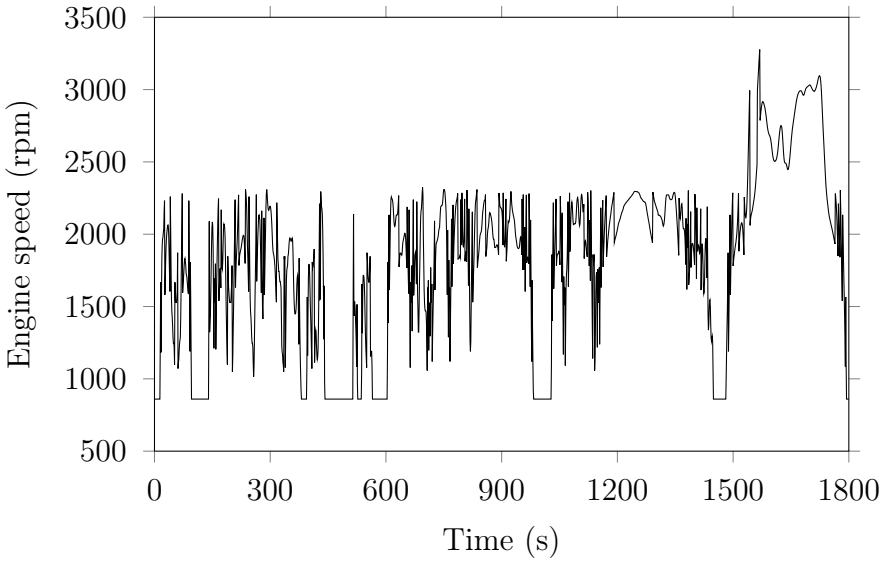

Figure 3.12: Engine speed over time during the complete WLTC class 3b driving cycle for the reference vehicle.

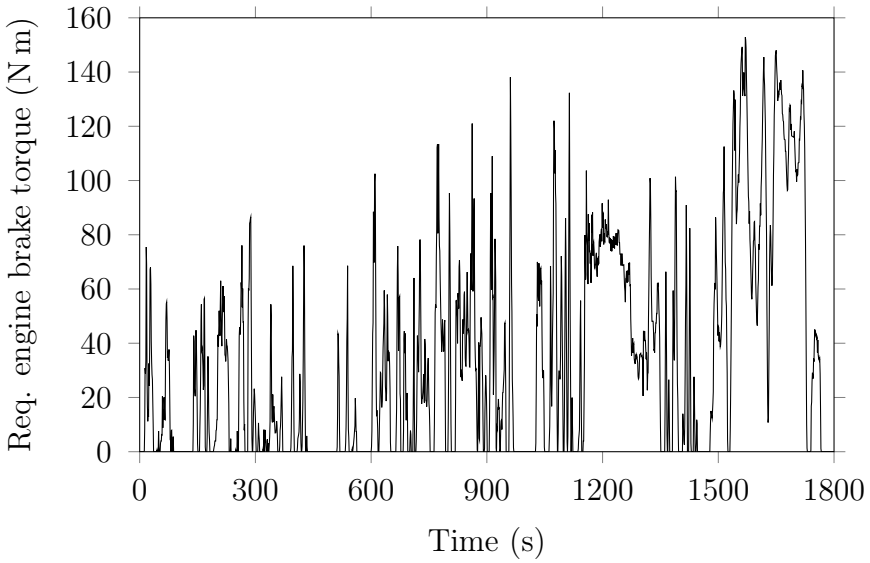

Figure 3.13: Required brake torque over time during the complete WLTC class 3b driving cycle for the reference vehicle.

To identify relevant steady-state conditions, engine speed and torque pairs were grouped in increments of 200 rpm and 20 Nm, respectively (see Figure 3.14a). The single largest steady-state point with 14 % can be found at 860 rpm without any applied load, i.e. idling at 0 Nm. Over 60 % of the time during the driving cycle is spent in the range of 1600 rpm to 2400 rpm with 0 Nm to 80 Nm. The engine only operates a small portion of time (1.9 %) at high-load, high-speed conditions of over 3000 rpm with over 100 Nm. Low-load, low-speed conditions of under 1600 rpm (excluding idling) with under 40 Nm account for 12.3 %.

As elevated emission levels are particularly troublesome for cities with high traffic volume, additional focus was placed on the city cycles. The respective scatter chart is shown in Figure 3.14b. Clear speed cutoffs can be observed at 1000 rpm and 2400 rpm. Moreover, the group of high-speed high-load conditions is absent. Instead, the contribution of idling increases to 21 %.

Due to project constraints on conditions for the test schedule into which the tests for this thesis are embedded, a brake torque limit of 40 Nm (ca. 5 bar BMEP) was imposed on the test matrix. This limit was intended to minimise the impact on the injector fouling state and prevent uncontrolled burn-off. Consequently, the engine tests will focus on medium-range engine speed conditions with low to medium loads. This will be facilitated by steady-state conditions from 1250 rpm to 2250 rpm in steps of 250 rpm, and loads of 0 Nm to 40 Nm in steps of 20 Nm.

3.4.2 Engine Operating Parameters

The engine operating parameters were controlled by the ECU. It contained optimised settings as per the manufacturer engine mapping. In the following, extracts of the mapped settings are presented for the selected test matrix. Valve timings are adjusted via the available twin independent variable camshaft timing, with the IVO and EVC timings as in Tables 3.4 and 3.5, respectively. The resulting valve overlap is additionally provided

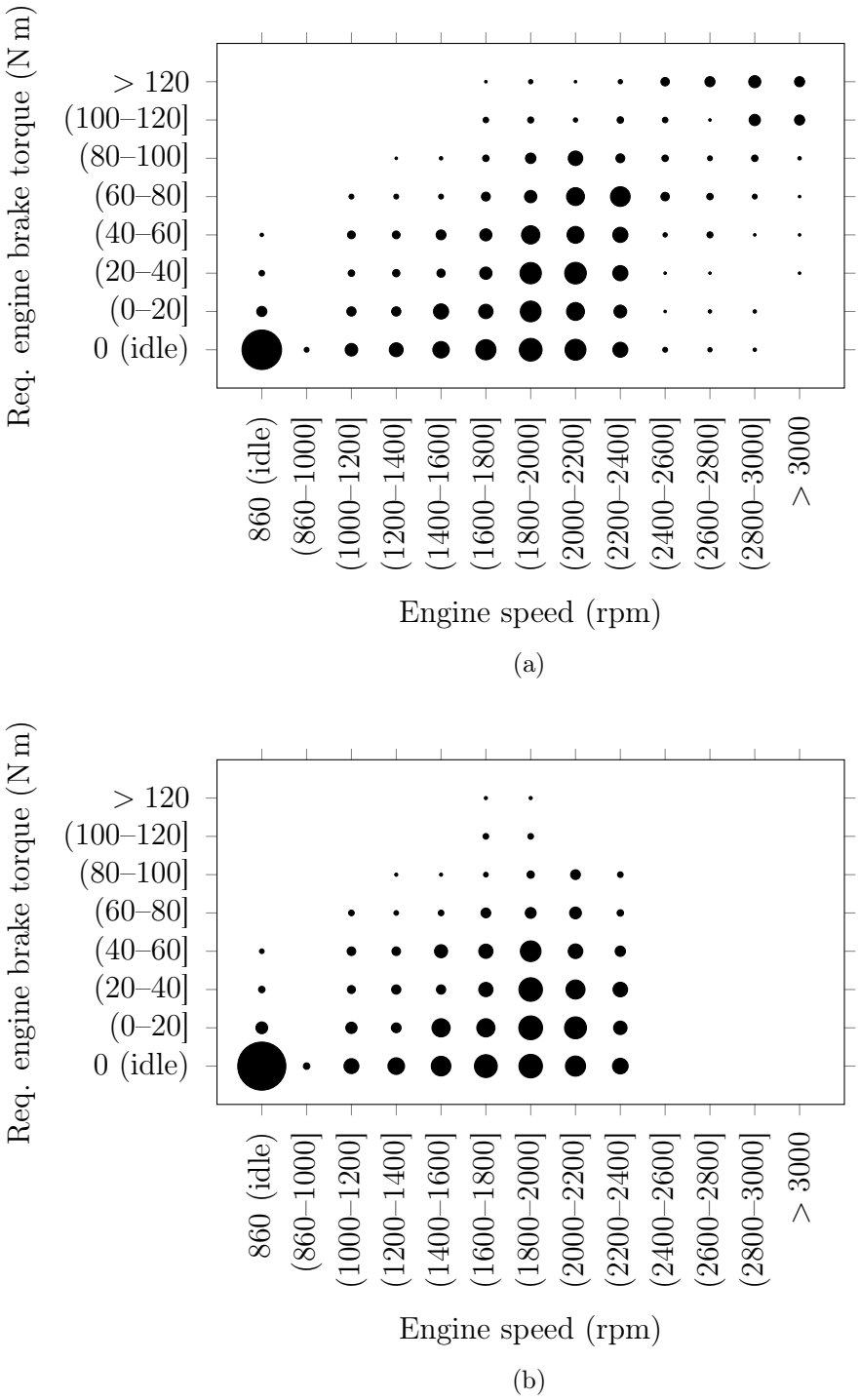

Figure 3.14: Scatter chart of operating conditions of the reference vehicle over the entire WLTC class 3b driving cycle (a) and over the respective city cycles (b).

in Table 3.6. The impact of changes in valve timings on soot formation was previously observed to be lower than the effects of altered fuel injection timings or pressures. However, differences in valve overlap, phasing of the valve overlap, and changing manifold pressures, could affect the fraction of residual gases, i.e. internal EGR.

The used spark timings are presented in Table 3.7. This parameter was again chosen as per the manufacturer mapping and was not actively checked or optimised to achieve MBT. Even though particulate emissions can generally be minimised by using MBT timing for the spark, such early spark timings are also associated with fuel efficiency penalties [198]. Thus in practice, delayed ignition timings are often used to achieve better engine efficiency. However, the MBT timing remains a useful reference point in the discussion of particulate emissions. The timing can be identified not only by conducting a spark sweep but also by the combustion phasing. For MBT spark timing, the position of CA50 (i.e. 50 % MFB) is considered to be at 10 °CA aTDC [248, p. 375]. Consequently, this parameter will be used additionally to allow for a better interpretation of the PN measurements.

The fuel injection timing varied from 252 °CA bTDC to 273 °CA bTDC (see Table 3.8) and the injected fuel quantity per cycle from 4 mg to 17 mg (see Table 3.9). For the selected test matrix, the pressure ranged from 54 bar at fast-idle at 1250 rpm to a maximum of 200 bar for all speeds at 40 Nm.

3.4.3 Engine Conditioning and Repeatability

To ensure repeatable conditions, a defined procedure for starting and conditioning the engine. Upon starting the engine, a conditioning setpoint at 1750 rpm with 20 Nm brake torque was used for warm-up. Two criteria were used to determine the stability of a set operating condition: coefficient of variation (CoV) of the net IMEP below 3 % and change in oil temperature below 0.5 °C/min. However, the CoV criterion was not feasible for fast-idle conditions without any brake torque applied. These conditions exhibit higher

Table 3.4: IVO as per ECU mapping in °CA aTDC.

Nm \ rpm	1250	1500	1750	2000	2250
0	20	20	20	20	20
20	11	9	8	8	8
40	−15	−17	−17	−18	−19

Table 3.5: EVC as per ECU mapping in °CA aTDC.

Nm \ rpm	1250	1500	1750	2000	2250
0	30	30	30	30	30
20	36	38	38	38	38
40	50	50	50	50	50

Table 3.6: Valve overlap as per ECU mapping in °CA.

Nm \ rpm	1250	1500	1750	2000	2250
0	10	10	10	10	10
20	25	29	30	31	31
40	65	67	67	68	69

Table 3.7: Spark timing as per ECU mapping in °CA bTDC.

Nm \ rpm	1250	1500	1750	2000	2250
0	38	38	39	40	40
20	27	28	28	28	28
40	21	22	23	25	25

Table 3.8: SOI as per ECU mapping in °CA bTDC.

Nm \ rpm	1250	1500	1750	2000	2250
0	254	252	258	264	273
20	256	256	260	264	270
40	257	261	263	265	267

Table 3.9: Fuel injection quantity per cycle as per ECU mapping in mg.

Nm \ rpm	1250	1500	1750	2000	2250
0	6	5	5	5	4
20	10	9	9	9	9
40	17	15	14	14	14

Table 3.10: Fuel injection pressure as per ECU mapping in bar.

Nm \ rpm	1250	1500	1750	2000	2250
0	54	123	124	118	118
20	78	200	200	200	200
40	200	200	200	200	200

Table 3.11: Procedure for engine warm-up, conditioning, and test points for repeatability.

No.	Description	Condition	Duration
1	Warm-up	20 Nm @ 1750 rpm	Until oil temp. stable
3	Ref. Point 0	20 Nm @ 1750 rpm	Stabilising, then recording 90 s time-resolved and 200 cycles (CA-resolved)
4	Ref. Point 1	20 Nm @ 1500 rpm	
5	Ref. Point 2	8 Nm @ 1500 rpm	
6	Ref. Point 3	8 Nm @ 2000 rpm	

CoV as variations in FMEP are proportionally more significant for low loads, and the combustion is less stable. The warm-up was completed once the temperature criterion was fulfilled, usually, once the oil reached 85 °C.

After the engine had been conditioned in this way, a series of three reference points (RPs) was used to assess and monitor the state of the engine across test days (see Table 3.11). The warm-up operating condition was used as a "zeroth" RP, recorded just upon completion of the warm-up and prior to the other three points. After these initial recordings had been completed, all test points of the scheduled test block were assessed. Upon completion, the RPs were performed again. The monitoring of these RPs includes several metrics: in-cylinder peak pressure p_{max}, PMEP, FMEP, fuel injection duration t_{inj}, and the isentropic coefficients γ for the compression and power phases of the engine cycle. This allows for any changes in the system to be identified, thus ensuring that any observed effects are indeed due to changes in operating conditions. The engine testing for this work was carried out over the course of several days. The obtained measurements of the repeatability metrics are discussed in the following. As the 95 % confidence intervals are relatively narrow for all metrics and RPs (cf. Figures 3.15 to 3.20), the data is plotted with additional bars to visualise the standard deviation, therewith enabling a better appreciation of the significance of the changes.

First, the FMEP is presented in Figure 3.15. The friction is generally higher at the slower speed RPs (i.e. at 1500 rpm), with ca. 0.91 bar and 0.87 bar for RP1 and RP2, respectively. The faster RP0 and RP3 exhibit 0.84 bar and 0.74 bar, respectively. While the variation for RP0, RP1, and RP2 remains mostly within the range of the 95 % confidence intervals, more considerable changes can be observed for the first half of the plot for RP3 (see Figure 3.15d). However, despite the more pronounced fluctuations, the value returns to the initial level, and no underlying trend remains. No continuous trend or sudden jump to a steady new level can be observed for any of the RPs. Consequently, it can be assumed that no change in the frictional properties—i.e. the characteristics of bearings and lubricated surfaces—occurred during the engine test schedule.

Secondly, the PMEP measurements are shown in Figure 3.16. The data exhibits a smaller variation for all RPs than for the FMEP. A minimal negative trend can be observed for RP0 and RP1; however, the change is small with about 0.01 bar and only for the latter RP beyond confidence interval. In contrast, the difference between the lower and higher load RPs at the same speed is above 0.1 bar, e.g. RP1 and RP2 with 0.52 bar and 0.65 bar, respectively. Nevertheless, a considerable overlap of the standard deviations can be noted. Some variation without a specific trend can further be observed for the lower load RP2 and RP3. Of particular concern would be an apparent increase in PMEP that could, for example, indicate the build-up of deposits on the intake valves. As no such change can be observed, it can be assumed that the valves and the overall air intake and exhaust system remained stable.

The isentropic coefficients γ for the compression and power phase are displayed in Figure 3.17 and Figure 3.18, respectively. The coefficient is somewhat higher for the power phase with 1.31 than for the compression phase with 1.30. The point-to-point fluctuation is higher for the lower load conditions of RP2 and RP3. However, both coefficients exhibit no

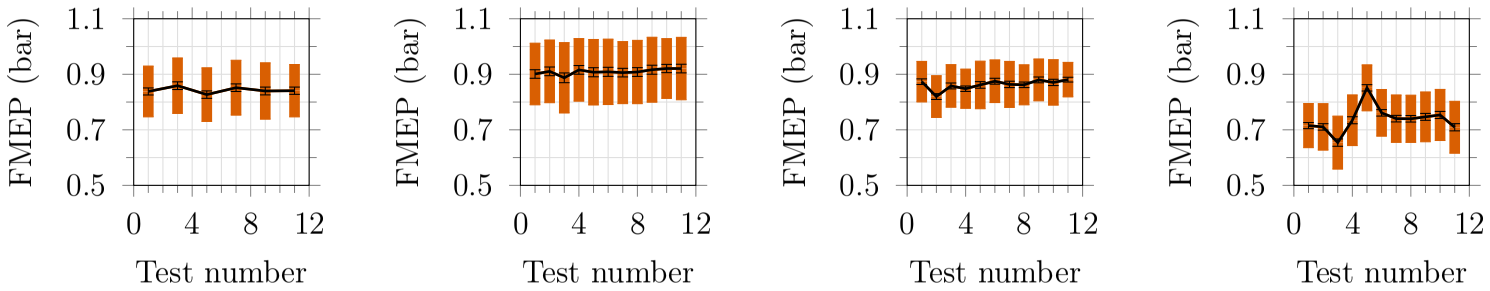

(a) RP0 (b) RP1 (c) RP2 (d) RP3

Figure 3.15: FMEP measurements for the RPs assessed along the test schedule. Error bars indicate 95 % confidence intervals and the orange bars indicate the standard deviation.

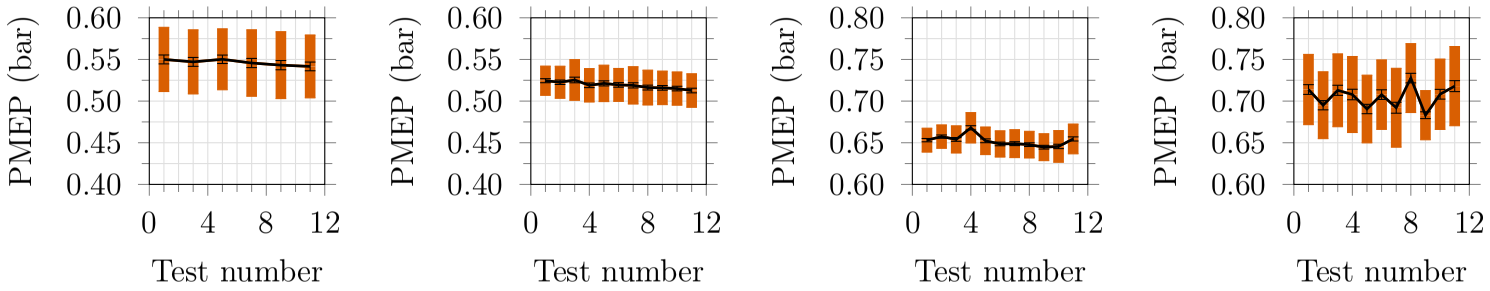

(a) RP0 (b) RP1 (c) RP2 (d) RP3

Figure 3.16: PMEP measurements for the RPs assessed along the test schedule. Error bars indicate 95 % confidence intervals and the orange bars indicate the standard deviation.

apparent trend for any of the four RPs indicating that the combustion chamber seals remain unchanged.

The maximum in-cylinder pressure p_{max} is shown in Figure 3.19. As to be expected, a distinct difference can be observed between the higher load conditions of RP0 and RP1 (p_{max} ca. 23.5 bar), and the lower load RP2 and RP3 (p_{max} of 15.5 bar and 13.8 bar, respectively). The peak pressure is lower for RP3 than RP2 by 1 bar to 2 bar due to the elevated speed, i.e. 2000 rpm instead of 1500 rpm. A similar change cannot be observed between RP0 and RP1. The standard deviation for the higher load conditions is somewhat higher with up to ±2.9 bar compared to ca. ±2 bar of the lower load conditions. Despite this variation within a single measurement, no significant trend can be observed across tests. This further confirms that the seals are not compromised, and their state is not changing.

Lastly, the fuel injection duration t_{inj} is presented in Figure 3.20. The duration is longer for RP1 and RP2 at 1500 rpm, compared to the respective conditions at the same load but faster speeds: 0.58 ms and 0.37 ms for RP1 and RP2 compared to 0.54 ms and 0.34 ms RP0 and RP3, respectively. A particular concern would be if a distinctly increasing trend of the injection duration could be observed as this would indicate fouling of the fuel injectors, i.e. build-up of deposits. Despite some noticeable variation between tests, no overall increasing trend can be identified.

To summarise, all of the analysed engine metrics remained stable throughout the test schedule. The variation of the measurements could be contextualised by comparison between the RPs and across tests. No underlying drifts could be observed, and only some fluctuations of individual RPs could be noted. Thus, no appreciable changes to the condition of bearings, seals, valves, and other engine components are assumed to have occurred over the course of the testing. Any observations from particulate measurements in subsequent analyses can consequently be attributed to the changes in operating conditions.

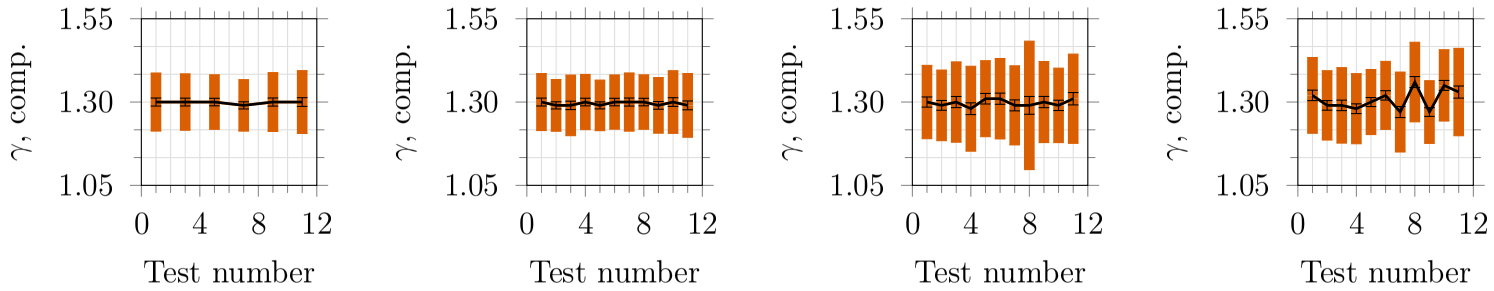

(a) RP0 (b) RP1 (c) RP2 (d) RP3

Figure 3.17: Isentropic coefficient γ for the compression phase of the RPs assessed along the test schedule. Error bars indicate 95 % confidence intervals and the orange bars indicate the standard deviation.

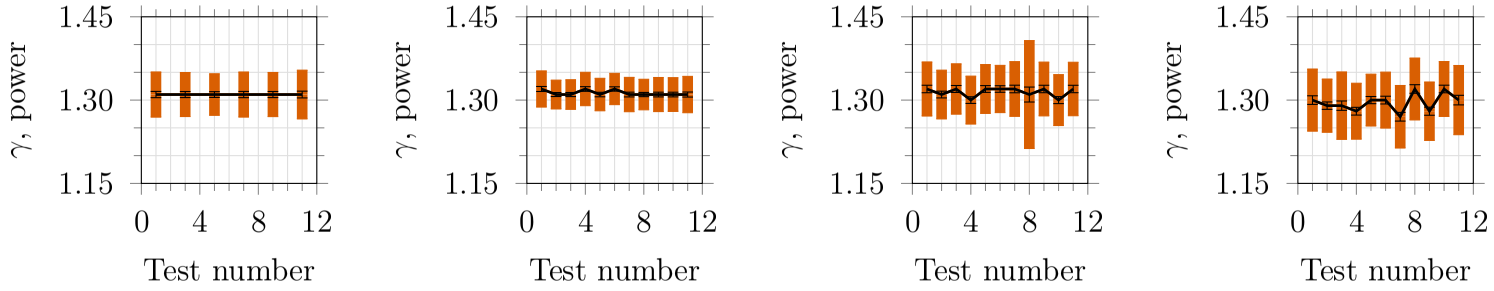

(a) RP0 (b) RP1 (c) RP2 (d) RP3

Figure 3.18: Isentropic coefficient γ for the power phase of the RPs assessed along the test schedule. Error bars indicate 95 % confidence intervals and the orange bars indicate the standard deviation.

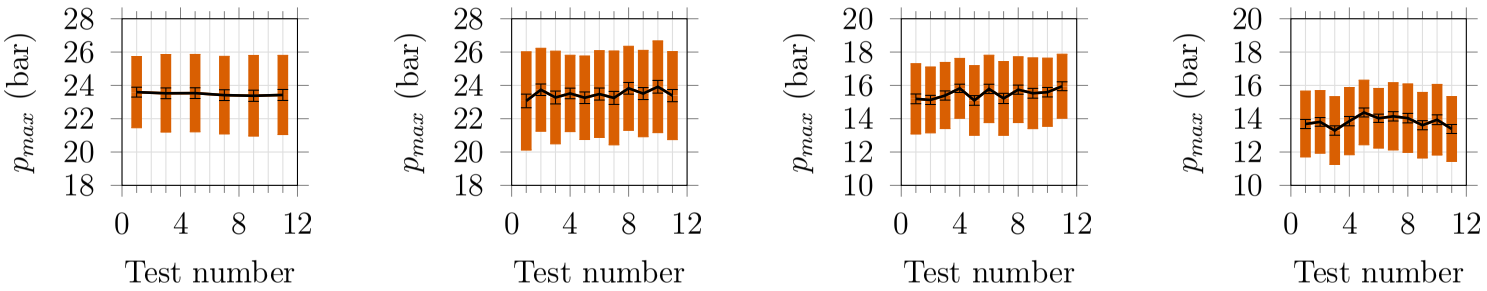

Figure 3.19: In-cylinder peak pressure p_{max} measurements for the RPs assessed along the test schedule. Error bars indicate 95 % confidence intervals and the orange bars indicate the standard deviation.

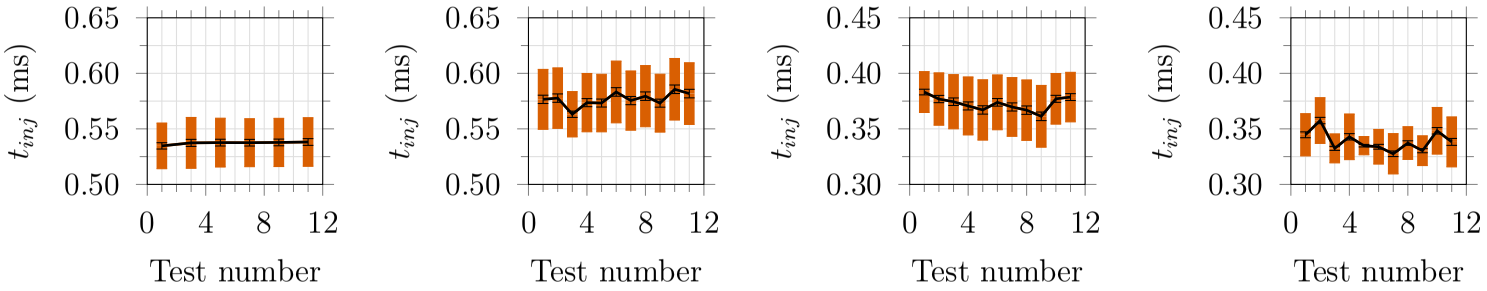

Figure 3.20: Fuel injection duration measurements for the RPs assessed along the test schedule. Error bars indicate 95 % confidence intervals and the orange bars indicate the standard deviation.

3.5 Oil Samples and Preparation Methods

Beyond the testing scope outlined above with the 1.0 l GDI engine, further interest lies in the analysis of the emitted particles using additional ex-situ techniques and the comparison of GDI soot with other soot types. However, extended engine runs are necessary to generate the bulk sample required for some of the analysis techniques. Due to limited resources—in terms of both time and budget—it was not feasible to carry out such extended runs and additional testing on other engines with different fuel types. Instead, an alternative approach was taken: analysis of soot-laden lubricating oil samples, predominantly acquired from in-vehicle operated engines. The starting point for this idea was an available vehicle with a similar three-cylinder 1.0 l GDI Ford EcoBoost engine from the same manufacturer. This car was driven over an extended period of time under primarily urban driving conditions with activated start-stop mode. Oil drain samples were collected after three different oil mileages (i.e. the mileage since the last oil change): 5715 km, 6733 km, and 8488 km. The 8488 km sample was used as the primary sample for the investigation in Chapters 4 and 5, labelled as '1.0L GDI' in the following. The other two samples were used to investigate the soot deposition rate into the lubricating oil. A second GDI soot-in-oil sample was collected from a four-cylinder 1.4 l GDI Volkswagen engine ('1.4L GDI' in the following) that was primarily operated in extra-urban driving conditions for 20 284 km in-vehicle with automatic cylinder deactivation enabled.

In addition to the GDI samples, two samples from diesel engines and one flame generated soot were analysed. The first diesel sample was obtained from the oil drains of a 2.0 l four-cylinder Jaguar engine ('2.0L Diesel' in the following) that was run for 12 875 km in-vehicle under light-duty operating conditions. The other diesel oil sample was obtained from a 550 cc single-cylinder variant of a multi-cylinder diesel engine ('SC Diesel' in the following). In a previous project, the engine was filled with clean

oil and subsequently operated for a total of 30 h on a laboratory test stand under operating conditions representing light-duty diesel applications. Upon completion of the test runs, samples were drawn from the oil sump. The flame generated soot was the commercially available carbon black 'Cabot Monarch 120' ('carbon black' in the following).

For TEM analysis, the soot has to be separated from the used engine lubricating oil. For this extraction of particulates, a cleaning protocol was applied as outlined by La Rocca et al. [34]. Oil sample quantities of 2 ml were placed in several hermetically sealed centrifuge tubes. These were then placed in an ultrasonic bath at 20 °C for 10 min to remove contaminants that are bonded to the soot particles. Subsequently, the tubes were placed in an Eppendorf Centrifuge 5418R at 14 000 rpm (relative centrifugal field value of 16 873 g) for 90 min at 25 °C. The centrifugal force exerted on the sample separated the soot particles from the lubricating oil due to the difference in density. Thus, the supernatant liquid phase could be carefully extracted and replaced by an equal amount of pure n-heptane. This cycle of ultrasonic bathing, centrifugation and heptane replacement was subsequently repeated six times. Therewith, the lubricating oil fraction was increasingly replaced by n-heptane, while the soot remained almost entirely in the tube. An effective dilution ratio of 1 : 75 000 compared to the initial oil sample was obtained. While the centrifugation cleaning procedure can alter the sample morphology, the primary particle nanostructure is not affected, as observed by La Rocca et al. [34].

Small amounts of the such prepared soot-in-oil samples were then transferred onto TEM grids. The grids consisted of a copper mesh grid coated with lacey amorphous carbon and graphene oxide support film. Upon deposition, the heptane evaporated in ambient conditions. Subsequently, the grids were washed with diethyl ether to further remove oil contamination and therefore improve image quality [34, 67].

For Raman spectroscopy, most of the supernatant liquid phase was removed after the final round of centrifugal cleaning. The solid deposits

at the bottom of the vial were then dissolved again in the small residual liquid fraction by manual agitation. The solutions were subsequently drop-casted onto Si wafers. For NTA, the oil samples were simply diluted in n-heptane. TGA could be performed on the lubricating oils without any additional preparation.

3.6 Ex-Situ Analysis

3.6.1 Transmission Electron Microscopy

TEM imaging was carried out on a JEOL 2100F TEM with a Gatan Orius CCD camera, based in the Nanoscale and Microscale Research Centre (nmRC) at the University of Nottingham. An incident electron beam voltage of 200 kV was used with various magnifications up to 600 000 ×. For the HRTEM images analysed by fringe analysis in this chapter, a magnification of 500 000 × was employed and yielded a resolution of 0.025 nm/px. The TEM was further equipped with an Oxford Instruments X-MaxN 80 T that was used for EDX spectroscopy and a Gatan GIF Tridiem was used for electron energy loss spectroscopy (EELS).

For the acquisition of repeated images of the same primary particle, the total beam exposure time was 12.5 s for a series of six images with exposure durations of 0.5 s. The average electron rate was $1.068 \cdot 10^5$ electrons/(nm^{2}s), which resulted in a total electron dose of $1.335 \cdot 10^6$ electrons/nm^2 for each image series. No decomposition of the sample under the electron beam was observed.

3.6.2 Fringe Analysis

A semi-automatic approach was chosen here for the analysis of particle nanostructures. The methodology used was adapted from Yehliu et al. [70] and written in MATLAB. The individual stages are visualised in Figure 3.21

and described in the following. The region of interest (ROI) was initially selected by the user for each image and subsequently kept constant for all iterations with various processing parameters. It should be pointed out that only the graphitic layers were chosen for the analysis. Disordered regions, either due to the amorphous nature of the particle core itself or higher particle thickness towards the centre disguising the nanostructure, were excluded. The manual selection further allowed for overlapping particles, noisy regions, or carbon of the TEM grid to be excluded as well.

In the raw, bright-field TEM images, the fringes appear dark, as the dominant contrast mechanism is due to electrons in the respective positions being scattered or absorbed due to interaction with the carbon atoms. Thus, negative transformation is initially applied to the image. The subsequent script optimises the image so that the fringes remain as positive information (i.e. ones) on a dark background (i.e. zeros). Instead of general histogram equalisation, contrast limited adaptive histogram equalisation (CLAHE) was used here. The adaptive histogram equalisation (AHE) divides the ROI into 64 regions (8×8) and determines the ideal contrast within these. This division allows for better consideration of local contrast requirements; however, noise levels can be significantly elevated [254]. By imposing a contrast limitation, i.e. using CLAHE, sharp peaks in the histogram of noisy homogeneous areas are redistributed and noise is reduced. To further reduce noise from the histogram equalisation, a Gaussian low-pass filter was employed. White top-hat transformation using disk-shaped elements was included to reduce artefacts due to uneven illumination. Subsequently, the image was processed by threshold binarisation. Lastly, the visible fringes were skeletonised by reducing their thickness to a single pixel.

The specific processing parameters are only scarcely reported in the literature. In the initial publication of the commonly used method by Yehliu et al. [70], a Gaussian low-pass filter standard deviation of 1.0 is used with a filter size of 11 px. Moreover, a disk-shaped white top-hat transformation element with 5 px in size was used. The threshold was calculated using Otsu's method,

(a) (b) (c) (d) (e)

Figure 3.21: Inverted images of various stages of the fringe analysis algorithm. Raw ROI (a). After CLAHE, Gaussian blur and white top-hat transformation (b). After threshold binarisation (c). After skeletonisation (d). After qualitative cleaning of ROI-border-crossing and branched fringes, fringes below size threshold and above threshold (e).

which yielded a value of 0.1608 for the analysed image. Similar values were used by Gaddam et al. [35]; however, the threshold value was varied from 0.1333 as calculated using Otsu's method, to 0.0863 and 0.1. Botero et al. [255] employed a Gaussian filter standard deviation of 2.0, filter size 7 px, white top-hat transformation disk size 2 px and automatically calculated Otsu threshold values. A subsequent study by the same author used the same values except for a Gaussian filter standard deviation of 3.0 [95].

Upon extraction of the raw fringes, a series of automated steps for qualitative cleaning was performed. First, fringes near the ROI border were removed. These could have been partially cut off during the ROI cropping, thus not representing real fringes. Secondly, a minimum fringe length threshold was imposed as fringes below this set length are likely to be artefacts. The value for this threshold varies across the literature. The range spans from values as small as the size of a single aromatic ring as used by Galvez et al. [94], to the crystallite size of 1.5 nm as used by Shim et al. [93]. For this study, a value of 0.4 nm was employed in the methodology by Yehliu

et al. [70] and previously suggested by Vander Wal et al. [256]. Moreover, branched fringes can occur due to artefacts from previous image processing or graphitic defects of the sample. Such fringes were resolved by disconnection at the branch point and subsequent reconnection of the longer branches with similar orientation. Lastly, a maximum fringe tortuosity threshold was imposed. Fringes with a tortuosity greater than three were disregarded in this study, as these were assumed to stem from image processing errors rather than represent fringes in a graphitic structure.

To measure fringe separations, pairs of fringes were manually selected by the user to ensure that only separations of truly adjacent fringes were considered. The average distance between the fringes was measured perpendicular to the geometric axis of the first selected fringe, i.e. its overall orientation. An upper threshold of 0.5 nm was used, as previously employed by Yehliu et al. [107]. Furthermore, separations of less than 0.34 nm were disregarded due to the minimum interlayer spacing limit in graphite.

3.6.3 Raman Spectroscopy

Information on the molecular-level structure of soot and the presence of contaminants was further obtained by Raman spectroscopy using a Horiba LabRAM HR spectrometer at the nmRC at the University of Nottingham. Single-point spectra were acquired using a 532 nm laser (at 0.25 mW), a 100x objective and a 300 µm confocal hole. The laser power was limited to 0.25 mW as spectra acquired at higher powers resulted in significant down-shifting of the vibrational modes, consistent with sample heating expected when analysing black materials using visible laser excitation with extended acquisition times [257], and in extreme cases resulted in the photothermal degradation of the sample microstructure. To simultaneously scan a range of Raman shifts, a 600 lines/mm rotatable diffraction grating along a path length of 800 mm was employed. Spectra were acquired using a Synapse CCD detector (1024 pixels) thermoelectrically cooled to −60 °C.

The spectral resolution in this configuration is better than 1.7/cm. Before spectra collection, the instrument was calibrated using the zero-order line and a standard Si(100) reference band at 520.7/cm. In all cases, spectra acquired from different areas of the sample showed only minimal variation, providing strong evidence for the homogeneity of the samples at the length scales appraised (microns).

To evaluate the effect of dilution and centrifugation on the extent of fluorescence observed in the Raman spectra of the soot extracted from the 1.0L GDI oil, samples were retained at various stages (i.e. different dilution ratios) of the centrifugation extraction procedure. Samples were prepared by drop-casting the respective n-heptane soot dispersions onto Si wafers and subsequent spectra collected within the range of 650/cm to 2220/cm with an acquisition time of 15 s and 64 accumulations to automatically remove the spikes due to cosmic rays and improve the signal to noise ratio.

To quantitatively investigate the molecular-level structure of the soot, extracted from both the 1.0L GDI and 2.0L Diesel oils, and carbon black, samples were prepared as described above and subsequent spectra collected within the range of 650/cm to 2220/cm with an acquisition time of 60 s to 120 s and 16 to 64 accumulations. Prior to spectra collection, the soot samples were photobleached for 30 min in an attempt to deplete the small number of residual artefacts given rise to fluorescence. The acquired spectra were baseline corrected using a third-order polynomial fit. Band deconvolution using the five-band model as proposed by Sadezky et al. [109], comprising four Lorentzian and one Gaussian peak profiles, was attempted. However, the D2 mode peak consistently relaxed to zero intensity and was thus not included, consistent with previous reports [42]. Numerous fitting models were explored, yet the only fit that resulted in convergence across all three samples, normalised to fitting parameters and analysis conditions, was obtained using mixed symmetric Gaussian-Lorentzian functions for the G and D1 modes and mixed asymmetric Gaussian-Lorentzian functions to fit the D3 and D4 modes.

3.6.4 Nanoparticle Tracking Analysis

The NTA was carried out on a Malvern Nanosight LM14 based in the nmRC at the University of Nottingham, with a laser of 405 nm wavelength. Video recordings were obtained using a CCD camera at 30 fps and subsequently processed with the NTA V3.2 software. The temperature of the sample throughout was held at 20 °C, and the reference value of viscosity for this temperature was 0.4 mPa s. 20 µl of the oil sample were diluted in 25 ml n-heptane, yielding a dilution ratio of 1:1250, and then dispersed by vortex mixing for approximately one minute. At the dilution ratio used, the effect of soot viscosity is low and can be neglected. Approximately 500 µl of the suspension were loaded into the sample chamber. Analysis with a higher dilution of 1:12 500 was attempted; however, a greater contribution from noise was observed due to the reduced number of particles. In addition, recordings of pure n-heptane were taken to rule out any influence by the dilution process. No particles were observed. Therefore, all observed particles in the oil dilution are assumed to be genuine particles of the oil sample itself. The identification and tracking of particles were optimised using a detection threshold value of five and automatic settings for blur size and maximum jump distance. The analysis was carried out in batch series of five recordings of 60 s each to account for statistical errors.

3.6.5 Thermogravimetric Analysis

An assessment of the soot mass was carried out on a TA Instruments Q500 thermogravimetric analyser, with a resolution of 0.1 µg. The methodology was adapted from the ASTM D5967-08 test standard and was previously used by La Rocca et al. [258]. 20 mg of the undiluted oil samples were placed in platinum TGA pans and loaded into the instrument chamber. Nitrogen was initially used as purge gas at a flow rate of 100 ml/min. The sample was isothermally held at room temperature for 20 min before being heated to 50 °C at a rate of 5 °C/min. After a minute of isothermal hold

at 50 °C, the sample was heated to 550 °C at a rate of 50 °C/min. After one minute of isothermal hold at 550 °C, the sample was heated at a slower rate of 20 °C/min to 650 °C. Subsequently, the purge gas was switched to air and the sample further heated at a rate of 20 °C/min to 750 °C, where it was isothermally held for 5 min.

3.7 Summary

This chapter was focused on aspects regarding the experimental background of the engine testing conducted for this thesis. First, a description of the equipment and instrumentation was provided, including information on the apparatus and sampling procedure of soot from the exhaust gas stream onto TEM grids. Next, the methodology for processing the acquired in-cylinder pressure data was outlined, comprising calculations of mean effective pressures, isentropic coefficients and heat release parameters. Moreover, an approach to obtaining the fuel injection duration and timing was detailed. To determine relevant operating conditions, a simulation of a WLTP driving cycle was carried out with particular focus on the city cycles of the WLTC. The resulting test matrix comprises low to medium engine speeds with relatively low loads. Furthermore, the respective engine parameters for this test matrix were outlined (i.e. valve and spark timings as well as fuel injection timing, pressure, and quantity). A procedure for engine conditioning and stability criteria for setting operating conditions were specified. This approach included reference points to monitor engine health. The corresponding analysis of these points was included here as well, confirming acceptable repeatability of the engine tests. Beyond the laboratory engine equipment, soot-in-oil samples were described in terms of their origin—i.e. diesel and GDI engines—and operating conditions. Moreover, the method for the extraction of particulates from these oils was outlined. Lastly, experimental details for several ex-situ techniques were provided.

4 Optimising Fringe Analysis

The nanostructure of primary particles is a central characteristic of soot samples due to its link to the oxidative reactivity [86, 259]. Knowledge of the reactivity of soot, in turn, is essential for applications such as the formulation of lubricating oils and the design of particulate filters. Established fringe analysis algorithms can readily quantify graphitic structures of primary particles. However, a gap in the literature regarding the detailed aspects of these algorithms was identified in Chapter 2. The effect of varying processing parameters and variations in TEM imaging quality have only scarcely been covered.

In this chapter, the impact of three parameters is investigated: the standard deviation of the Gaussian low-pass filter, the disk size of the white top-hat transformation, and the binarisation threshold. Moreover, the influence of the TEM focus point, as well as the contribution of quality and noise level of the obtained images, are assessed. Lastly, the effect of various ROI sizes is examined. Three of the samples described in Section 3.5 were used for this investigation. Details of the chosen parameter ranges and further information on the procedural approach are outlined in the first section of this chapter.

Parts of this chapter have previously been published in the journal Combustion and Flame:

S.A. Pfau, A. La Rocca, and M.W. Fay. Quantifying soot nanostructures: Importance of image processing parameters for lattice fringe analysis. Combustion and Flame, 211:430-–444, 2020, DOI 10.1016/j.combustflame.2019.10.020.

4.1 Assessed Parameter Range

A default value of 2.0 was chosen for the Gaussian low-pass filter standard deviation, as it lies within the previously reported range. Moreover, a range of several standard deviations was assessed to cover previously reported values (see Table 4.1). The respective filter sizes were chosen accordingly as the next odd integer of six times the standard deviation, i.e. filter size 13 for the standard deviation 2.0. For the structuring element of the white top-hat transformation, a disk shape was chosen. The disk is constructed around a centre pixel and as such the minimum disk size is 3 px. The default size was chosen to be 9 px and a total range from the minimum disk size to a maximum value of 15 px assessed (see Table 4.1). The threshold value was calculated for the respective ROI using Otsu's method [111]. A range of values was additionally tested to assess the impact of the threshold value on the fringe metrics (see Table 4.1).

Primary particles of the soot from the 1.0L GDI and 2.0L Diesel engines as well as the carbon black were analysed. The selected ROIs measured 361 nm^2, 144 nm^2, and 348 nm^2, respectively. The particles are depicted in Figure 4.1 with the respective regions marked as annotations, and enlarged

Table 4.1: Range of processing parameters for fringe analysis. Baseline value in bold.

Processing parameter	Value range						
Gaussian low-pass filter standard deviation	0.5	1.0	1.5	2.0	2.5	3.0	3.5
Gaussian low-pass filter window size (px)	3	7	9	13	15	19	21
White top-hat transformation disk size (px)	3	5	7	9	11	13	15
Binarisation threshold	0.005	0.025	0.05	0.075	0.1	0.125	0.15

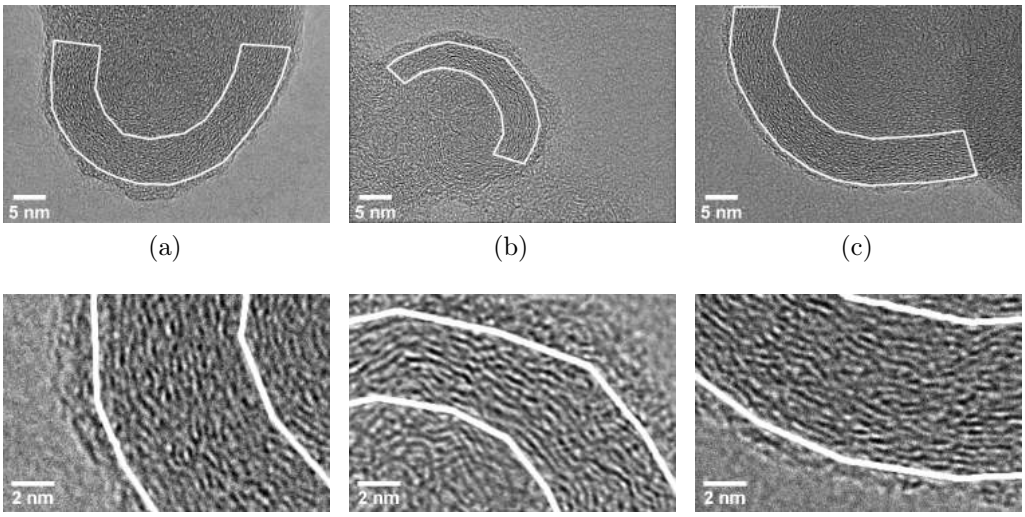

(a) (b) (c)

(d) (e) (f)

Figure 4.1: HRTEM images of 1.0L GDI soot (a), 2.0L Diesel soot (b), and carbon black (c) primary particles with the respective annotated ROI. Further, enlarged sections of these selected ROIs for 1.0L GDI soot (d), 2.0L Diesel soot (e), and carbon black (f).

sections for better display of the nanostructure. To assess the influence of image quality and to simulate differences in camera equipment, repeated images of the same particles were obtained. A total of six images for four different particles of the carbon black sample was acquired. The images were aligned using the script StackReg for ImageJ [260] to correct for any stage or particle drift. Subsequently, the respective sections of the stacked images were averaged based on intensity.

To investigate the influence of the ROI size, several particles were analysed for each sample: 15 particles with a total ROI size of 3861 nm^2 for the 1.0L GDI sample, 22 particles with total ROI size of 4026 nm^2 for the 2.0L Diesel sample, and 11 particles with total ROI size of 3736 nm^2 for the carbon black sample. The ROI sizes for the individual particles ranged from 85 nm^2 to 512 nm^2. An assessment of the corresponding fringe metrics is carried out in Section 5.3.2.

4.2 Gaussian Low-Pass Filter Standard Deviation

The effect of changes to the standard deviation of the Gaussian low-pass filter was assessed by varying the parameter as described in Table 4.1. For the white top-hat transformation disk-shaped element, the default value was used throughout, and the binarisation threshold was calculated for each parameter case using Otsu's method. The fringe length remains mostly stable for standard deviations of 1.5 and above (see Figure 4.2a). Slightly lower fringe lengths for standard deviations for 1.0 and even more so for 0.5. This can be particularly observed for the 1.0L GDI soot and carbon black particles with sudden decreases of 38 % and 41 %, respectively. The 2.0L Diesel particle exhibits a rather linear decrease in fringe length for standard deviations greater 2.0 by 3.8 % to 5.5 % per step.

Similar to the fringe length, the fringe tortuosity does only change slightly for filter standard deviations between 1.0 and 3.5 (see Figure 4.2b). However, instead of a sudden drop in tortuosity, a steep increase can be observed for the lowest standard deviation. This is the case for both the 1.0L GDI soot and the carbon black particle with increases of 72 % and 61 %, respectively. In contrast, the 2.0L Diesel soot particle exhibits a tortuosity increase of only 4.4 % from the standard deviation 1.0 to 0.5. While the fringes of all three particles decrease almost continuously from the parameter cases of 1.0 to 3.5, the 1.0L GDI soot particle shows a more noticeable overall increase of 17 % compared to 9.6 % and 5.6 % for carbon black and 2.0L Diesel soot, respectively.

The calculated binarisation threshold continuously decreases for all particles with increasing filter standard deviation (see Figure 4.2c). For the value range of 1.0 to 3.5 this change occurs almost linearly. This is most noticeable for the carbon black particle. While the binarisation value for the 1.0L GDI and 2.0L Diesel soot particle decreases less uniformly, a linear trend is still clearly

visible. In contrast to the 2.0L Diesel soot particle, the other two particles exhibit a much higher threshold value for the 0.5 standard deviation case.

To evaluate changes in the number of fringes, the total fringe count for the parameter cases were normalised with respect to the 2.0 default filter standard deviation point. A decrease in total fringe number with increasing standard deviation can be observed for all particles (see Figure 4.2d). While both the 1.0L GDI soot and the carbon black fringe counts suddenly decrease for the minimal standard deviation of 0.5, the 2.0L Diesel soot particle increases even further to its maximum fringe count. The largest number of fringes for the former two former particles is extracted at 1.0 filter standard deviation.

To better understand these observations, overview sections of the extracted fringes for several parameter cases are presented (see Figure 4.3). Noticeably, both the 1.0L GDI soot and the carbon black particles exhibit drastically fewer fringes for the 0.5 standard deviation case. The remaining fringes appear distorted, short, and twisted, rather than representing any actual graphitic carbon structure. This clearly explains the decrease in fringe length and spike in tortuosity. In contrast, the image of the 2.0L Diesel soot primary particle does not exhibit this behaviour. All initial TEM images were taken at the same magnification and using the same settings, i.e. yielding the same spatial resolution of 0.025 nm/px. A potential cause could be the relatively small filter size of 3 px; however, this would not explain why the 2.0L Diesel soot particle is not affected. Thus, the difference could instead stem from the different sizes of the selected ROI; the 2.0L Diesel soot particle ROI is approximately 60 % smaller than the ROI of the other two particles.

Aside from the lowest standard deviation, a similar appearance of the nanostructure can be observed for the three particles. Compared to the 2.0 baseline standard deviation, the density of fringes is noticeably higher for the lower 1.0 standard deviation, as it could be expected with a higher total number of fringes. However, many of these fringes are less well aligned to the surrounding fringes. These fringes are more likely to stem from

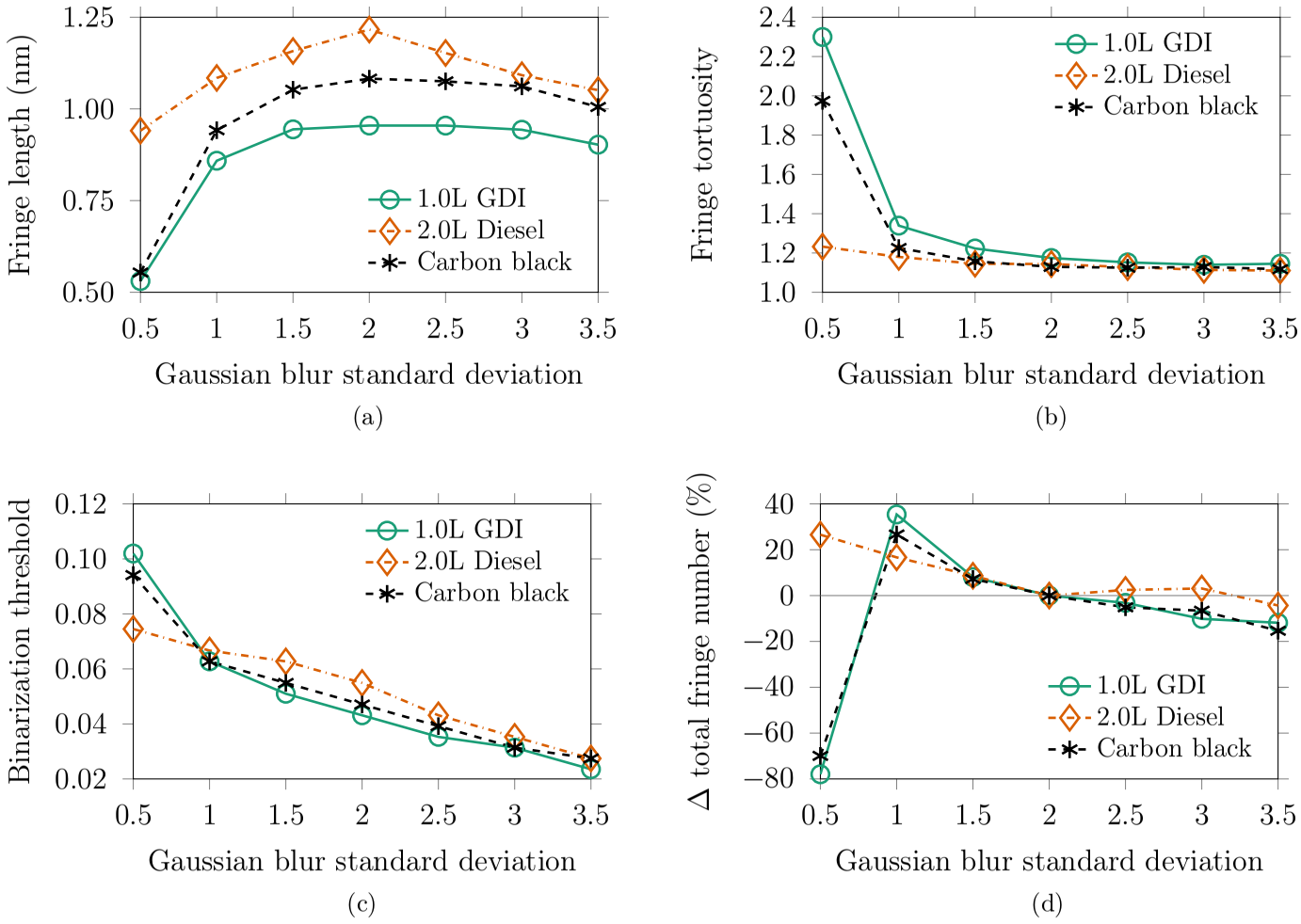

Figure 4.2: Variation of fringe length (a), tortuosity (b), binarisation threshold (c), and normalised total fringe number (d) with different values for the Gaussian low-pass filter standard deviation.

Figure 4.3: Changes in fringe appearance with varying standard deviation of the Gaussian low-pass filter.

remaining noise due to insufficient filtering rather than representing the actual graphitic carbon nanostructure. In contrast, the density of fringes reduces with higher standard deviations. While the difference between 2.0 and 3.0 standard deviation is only minor, the highest standard deviation of 3.5 visibly appears to reduce the number and length of genuine fringes of the graphitic structure. The former two parameter values have also yielded similar fringe length and tortuosity, as described above. Thus, values between 2.0 and 3.0 can be deemed suitable. This is in line with values used by Botero et al. [95, 255] but higher than the standard deviation used in the initial publication of Yehliu et al. [70].

4.3 White Top-Hat Transformation Disk Size

The effect of the element size in the morphological processing on the fringes was assessed by performing a white top-hat transformation on the images with varying disk sizes as described in Table 4.1. Gaussian low-pass filtering was carried out prior to the transformation using the default standard deviation of 2.0. The threshold value was calculated using Otsu's method upon completion of the transformation.

Across all three particles, a linear increase in fringe length can be observed with larger disk sizes (see Figure 4.4a). In addition to correcting for uneven illumination, the white top-hat transformation also removes any elements that are larger than the structuring element. As such, less information is being deleted with larger disk sizes. Thus, less noise is removed, and fringes appear longer. Noticeably, the increase in fringe length is more linear and steeper for disk sizes above the default value of 9 px than for values below this point. For disk sizes smaller than the default value, both the 2.0L Diesel soot and the carbon black particle exhibit a local maximum in fringe length at 5 px and 7 px, respectively. In contrast, the 1.0L GDI soot particle exhibits a continuously increasing fringe length with increasing disk size, but at a slower rate below the default disk size than above.

Similarly, the tortuosity increases more steadily for disk sizes above the default value (see Figure 4.4b). While all particles exhibit an overall increasing trend for the tortuosity with larger disk sizes, the changes are not uniform. For both the 1.0L GDI and the 2.0L Diesel soot particles a local maximum can be observed at 5 px and a larger increase in tortuosity when comparing the disk size 11 px to 13 px. For the carbon black particle, a distinctive peak in tortuosity can be observed at 7 px disk size. After a drop for the 9 px default disk size, the tortuosity increases again very linearly towards the maximum disk size.

As for the change in fringe lengths, a linear increase of the binarisation threshold with the transformation disk size can be observed (see Figure 4.4c). This can be traced back to the varying extent of information removed and residual noise. As more noise remains in the image, a higher threshold value must be used to attain the same maximum separability of the resulting binary classes. The increase appears to occur in two phases with different rates. Below the default value of 9 px the threshold increases at a rate of 0.007 /px, while above this value, the rate is more than twice as high with 0.017 /px.

In contrast to the aforementioned characteristics, the total number of fringes exhibits an overall decreasing trend with increasing disk size (see Figure 4.4d). However, the highest number of fringes can be extracted for the 2.0L Diesel soot and carbon black particle with a disk size of 7 px. For both particles, the total fringe number decreases not just towards larger disk sizes but also for the smallest 3 px disk. The 1.0L GDI soot particle exhibits the highest number of fringes at 5 px. While 1.0L GDI soot and carbon black particle fringe count decrease at a similar rate towards larger disk sizes, the number of fringes from the 2.0L Diesel soot particle decreases more rapidly.

To better understand the changes in fringe characteristics, overview sections of the extracted fringes for several parameter cases are provided in Figure 4.5. With smaller disk sizes, the fringes shrink noticeably as meaningful information is removed together with the noise. At the same time, the total number of fringes generally increases except for the carbon black

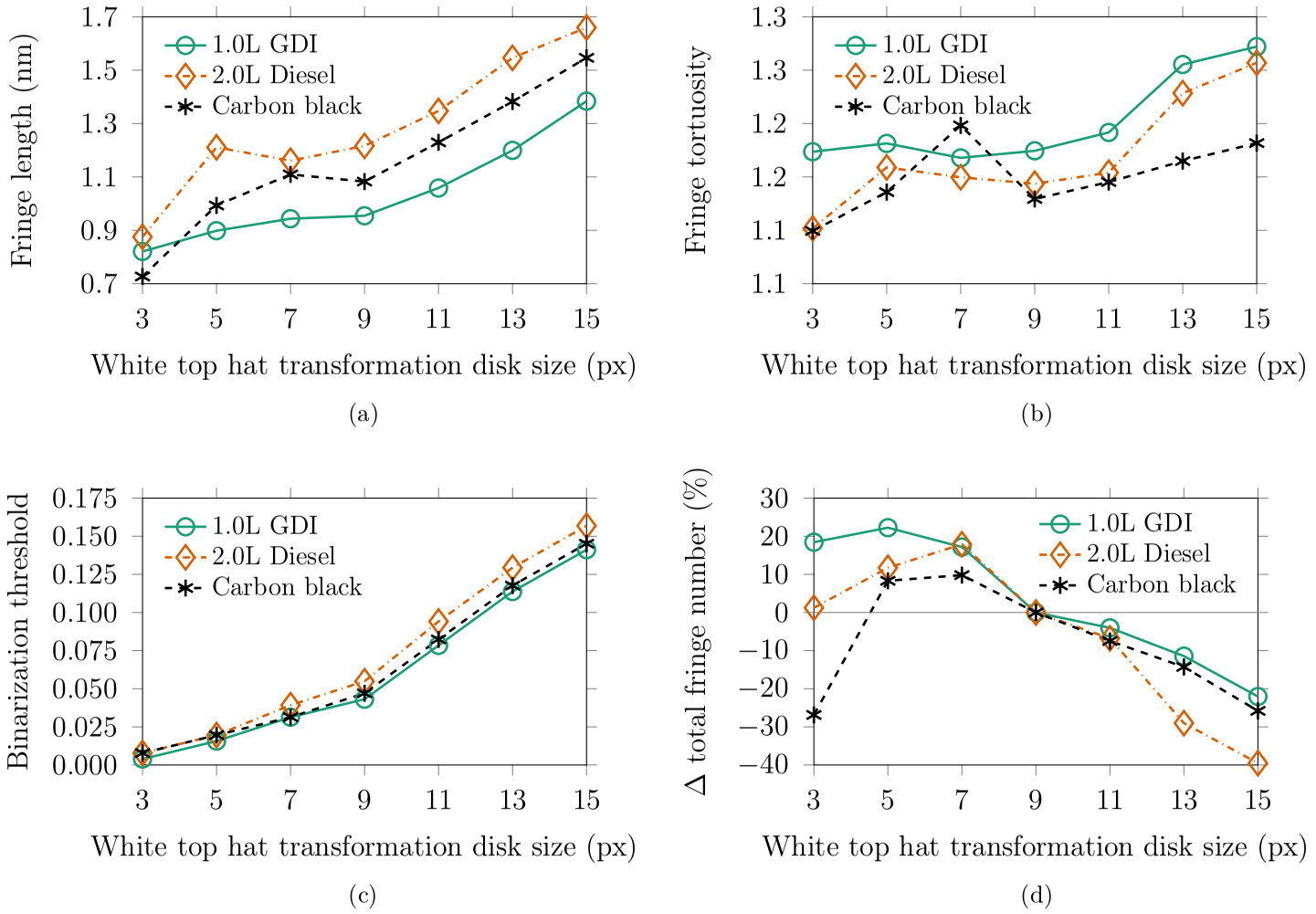

Figure 4.4: Variation of fringe length (a), tortuosity (b), binarisation threshold (c), and normalised total fringe number (d) with different values for the white top-hat transformation disk size.

Figure 4.5: Changes in fringe appearance with varying disk size of the white top-hat transformation.

particle at the minimum disk size parameter case. This can be attributed to longer fringes being split into multiple sections. The obtained set of fringes exhibits larger spaces and voids and is thus less representative of the actual nanostructure. For larger disk sizes, fringes appear to grow and merge as less information is removed. This poses the opposite problem, of fringes growing being lengthened due to artefacts becoming part of the fringes. Therewith, the nanostructure is again not accurately represented in such cases. Disk sizes between 5 px and 9 px appear to yield the most realistic representation of the graphitic structure. The average variation in fringe length and tortuosity between these disk sizes is 4.9 % and 2.4 %, respectively. Due to the higher total number of fringes, the disk sizes of 5 px and 7 px are here recommended for future studies.

4.4 Binarisation Threshold

As observed in Sections 4.2 and 4.3, the image processing parameters Gaussian low-pass filter standard deviation and white top-hat transformation disk size can greatly influence the threshold as calculated by Otsu's method. Moreover, the information and quality of the fringe analysis depend on the residual noise as well as image properties, i.e. brightness and contrast. To assess the impact of the threshold value itself, a series of binarisation threshold values was employed as described in Table 4.1. For the Gaussian low-pass filter and the white top hat transformation disk size the default values were used, i.e. 2.0 and 9 px, respectively. The Otsu threshold values using these parameters are 0.043, 0.055, and 0.047 for the 1.0L GDI soot, 2.0L Diesel soot, and carbon black particle, respectively.

For all three particles, the fringe length is the highest at the binarisation threshold of 0.025 and appears to decay exponentially for larger threshold values (see Figure 4.6a). However, for the smaller threshold of 0.005, the fringe length decreases across all particles. Similar observations can be made for the fringe tortuosity (see Figure 4.6b). The highest tortuosity

of the fringes can be observed at 0.025 and decrease from there for both higher and lower threshold values. However, the decrease towards higher threshold values is less exponential but rather exhibits two phases. While the tortuosity decreases rapidly until the threshold value 0.075, the reduction beyond this parameter case is smaller.

To evaluate the effect on the number of fringes, the respective fringe counts were normalised with respect to the number of fringes, as for the parameter case using the Otsu threshold. The fringe counts appear to be normally distributed with the maximum around the Otsu threshold and positively skewed towards larger threshold values (see Figure 4.6c). While a lower threshold of 0.025 yields a higher number of fringes for the 1.0L GDI soot particle, the Otsu threshold generally extracts the most fringes. Across all particles, the number of fringes rapidly drops to zero for the lowest threshold value. Towards larger threshold values the decrease is smaller.

The changes also become noticeable when looking at overview sections of the extracted fringes (see Figure 4.7). For both the highest and lowest threshold value, almost no fringes were extracted. The threshold closest to the individual Otsu threshold values is 0.05. For the 1.0L GDI soot and carbon black particle, apparent changes can be observed if the fringes at 0.05 threshold are compared to the fringes of the adjacent threshold values. For the 0.025 threshold value, the fringe network appears denser, i.e. the fringes are longer and do not just follow the parallel graphitic layers but also extend across the interlayer spaces. In contrast, for the 0.075 threshold value, the fringes are noticeably shorter and lower in number. The 2.0L Diesel soot particle shows similar tendencies but at a slower rate, indicating a wider spread distribution.

The specific values for the observed fringe length and tortuosity values would change for different settings of Gaussian low-pass filter size and white top-hat transformation disk size. However, the analysis here is made relative to the respective Otsu threshold, with subsequent deviation from it. Any changes due to parameter influence would shift the values but not the observable

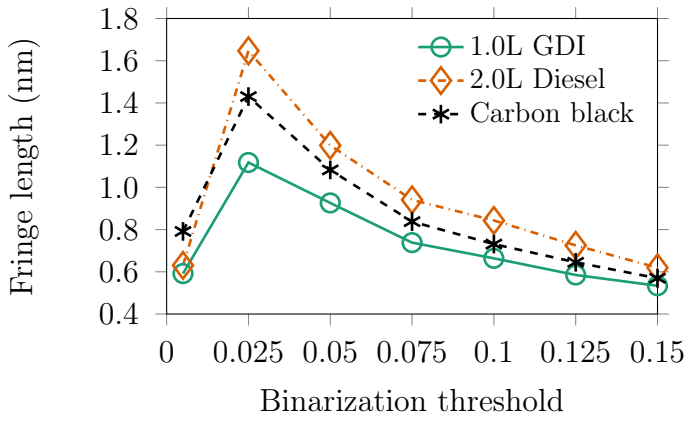

(a)

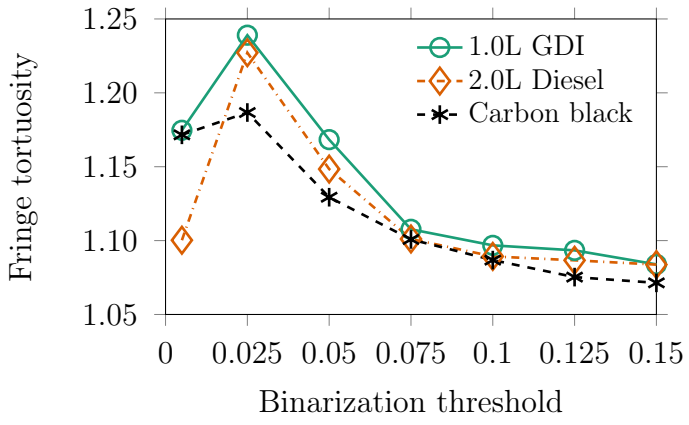

(b)

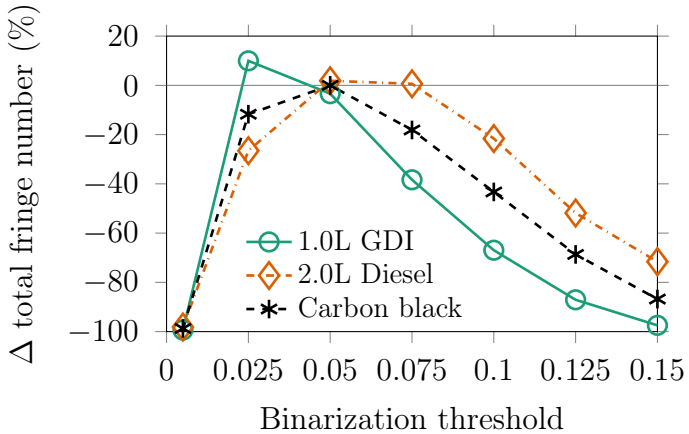

(c)

Figure 4.6: Variation of fringe length (a), tortuosity (b), and total fringe number (c) with different values for the binarisation threshold.

Figure 4.7: Changes in fringe appearance with varying binarisation threshold.

trend. For future studies, the use of the threshold value as calculated by Otsu's method is here recommended. This approach is clearly defined, yields among the highest number of fringes, and no beneficial reason for any deviation could be identified.

The findings presented here contradict earlier results by Gaddam et al. [35]. In their study, no significant variation of the fringe metrics with varying threshold values was observed. The maximum difference in fringe length was 0.05 nm. The change in fringe length here from the parameter case closest to the respective Otsu threshold values (0.05) to the neighbouring cases ranges from 0.19 nm to 0.45 nm. While the change in metrics decreases to 0.05 nm to 0.1 nm per parameter step towards larger threshold values, differences between parameter cases are still notable.

4.5 TEM Focus Point

To assess the influence of the focus of the TEM on the observed fringes, four particles of the carbon black sample were used (labelled as P1, P2, P3, and P4). Five images with different focus points were acquired for each particle. The baseline focus point at which the particle is deemed 'in focus' was set by the TEM operator visually and aided by the fast Fourier transformation (FFT) of the particle region. When the particle region is in focus, the respective FFT shows only one bright circle. With increasing defocus, additional dark and bright rings become apparent (see Figure 4.8). From the central neutral focus point, the focus was changed by a total of 90 nm in two equal steps each way.

The longest fringes can be obtained for each particle when the microscope is in the central focus point (see Figure 4.9a). Even when compared at the same focus point, the fringe length varies by up to 0.25 nm between the particles of the same sample. This intra-sample variation, i.e. particle-to-particle differences, have also previously been observed by Zhang et al. [261]. By

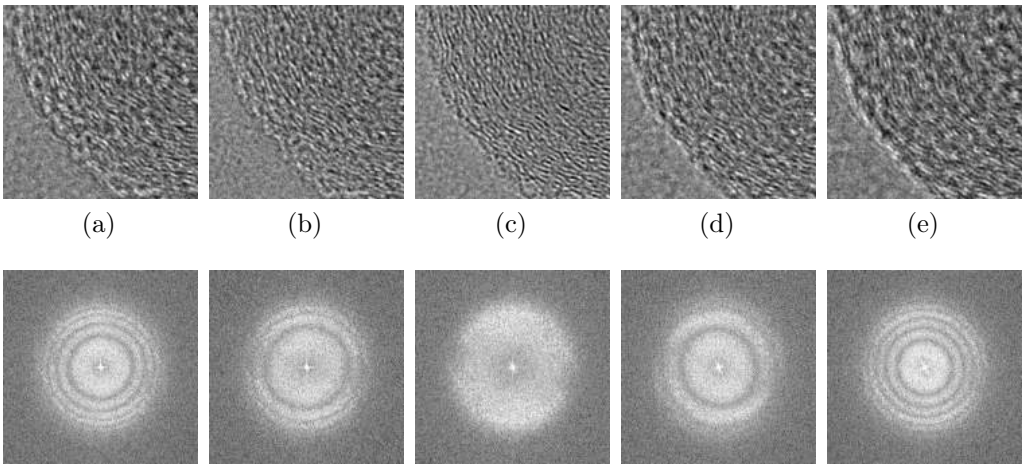

Figure 4.8: TEM images of particle P2 of the carbon black sample in different focus points and corresponding fast Fourier transformations: under-focused by 90 nm (a,f), under-focused by 45 nm (b,g), neutral-focused (c,h), over-focused by 45 nm (d,i), over-focused by 90 nm (e,j).

under- and over-focusing the fringe length can change by as little as 0.14 nm and up to 0.33 nm for particles P2 and P4, respectively. As the variations due to changes in the focus point are larger than the intra-sample variation, there is a case for carefully choosing the focus. While the effective variation of focus selection within sessions or even between TEM operators might be smaller than the stated values, these findings highlight the importance of this parameter for fringe lengths.

In contrast, no apparent trends can be observed in terms of tortuosity (see Figure 4.9b). For both particles P1 and P4, the values remain relatively constant. Particle P2 shows increases for both under- and over-focusing as compared to the neutral focus point. However, the changes remain on a similar level as the difference across the individual particles themselves. P3 also exhibits some changes of tortuosity with varying focus points; however,

these changes again do not follow any apparent trend. Similar observations can be made for the change in the number of fringes.

To assess any variations, the total number of fringes is normalised with respect to the neutral focus point. Fringe counts for particle P1 remain relatively stable around the baseline, except for the furthest under-focused point at which the number increases suddenly by 19.3 % (see Figure 4.9d). Smaller differences can be observed for P2 and P3 with up to 1.6 % and −12.2 %, respectively. Total fringe numbers for both slightly decrease towards the over-focused side but do not show a clear tendency when under-focusing. Particle P4 shows the greatest changes in total fringe number with 26 % and −22 % for under- and over-focusing, respectively. However, no clear trend in the change of total fringe number can be observed with changes in the focus across the particles.

The binarisation threshold, as determined by Otsu's method, shows a clear peak across all particles for the centre focus point (see Figure 4.9c). For the two under-focused points, the threshold drops to a lower value for all particles regardless of the degree of under-focusing. On the over-focused side, the threshold values for P2 and P4 exhibit a similar pattern. While the respective values for P1 and P3 also decrease, this reduction is more pronounced with a higher degree of defocus. This pattern appears to be similar to the observed changes in fringe length. Contrary to the inverse correlation mentioned above, the fringe length decreases despite the reduction in the binarisation threshold. Therefore, the changes in the fringes are not an artefact of altered contrast but rather directly affected by the distorted image of the nanostructure. Previously, Wan et al. [112] suggested, based on simulated images, that the TEM focus could have a considerable influence on the fringe metrics. The experimental approach in this study provides the necessary evidence to confirm this hypothesis. Consequently, the uniform and consistent setting of the focus point across samples and particles is paramount for meaningful results. As of today, this decision heavily relies on the TEM operator. Previously, Kondo et al. [113] observed that the

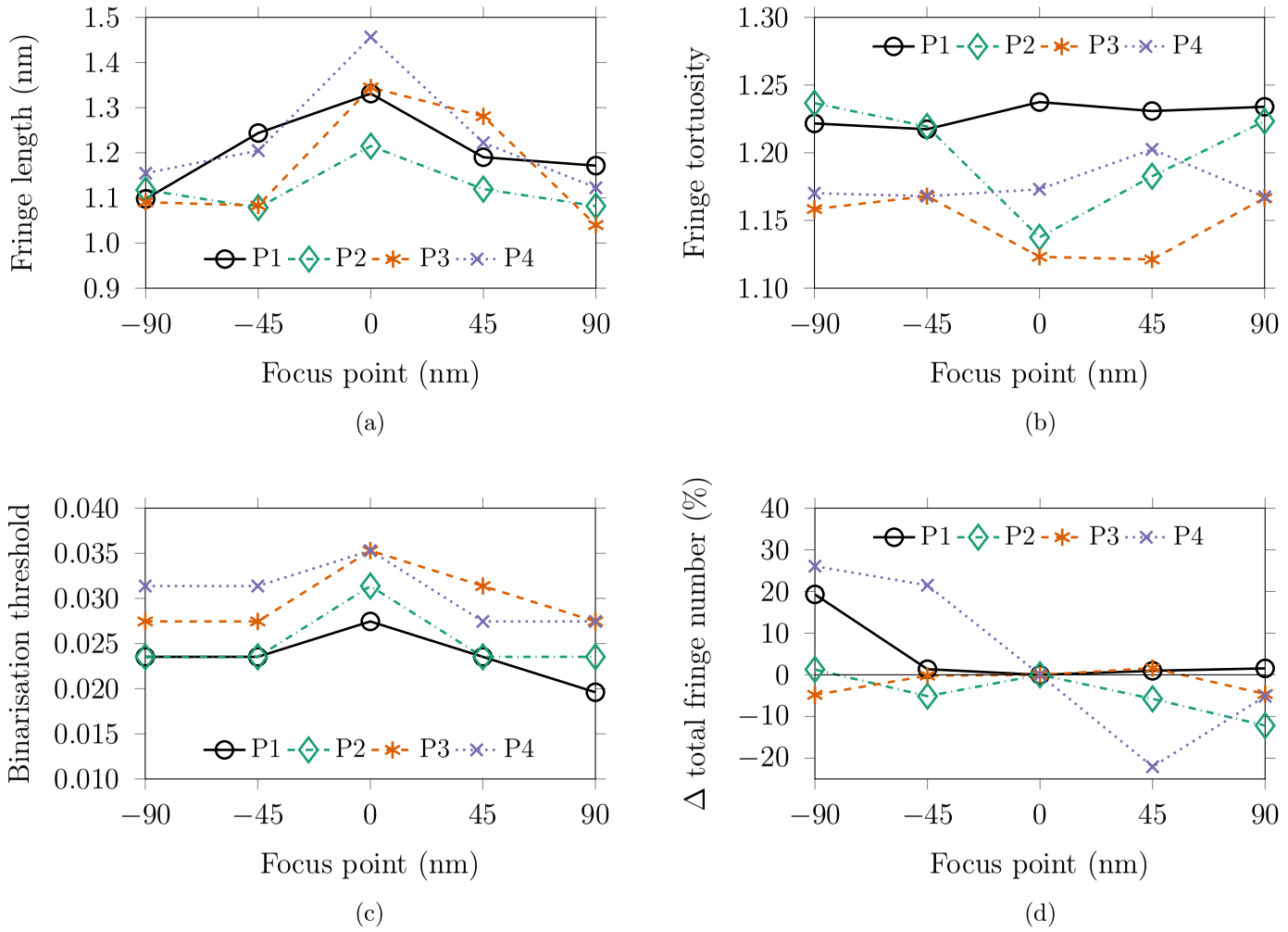

Figure 4.9: Variation of fringe length (a), tortuosity (b), binarisation threshold (c), and normalised total fringe number (d) with different TEM focus points for the four particles P1, P2, P3, and P4.

operator's experience could significantly affect the selection of characteristic regions of a given agglomerate. It is here suggested that this could also apply to the focus point. The point of focus is commonly selected by the visual appearance and aided by live FFT of the respective particle region. However, implementing a tool for automatic calculation of the Otsu binarisation threshold could quantitatively aid this process in the future.

4.6 Image Quality and Noise

As outlined above, several aspects of image quality such as uneven image illumination or TEM focus can influence the fringe analysis results. Likewise, metrics such as spatial resolution and signal-to-noise ratio can play a role. Both are affected by the standard of the available camera as well as parameters such as exposure times. For this study, a Gatan Orius CCD camera was used, yielding a spatial resolution of 0.025 nm per pixel at 500 000 × magnification. Images were acquired with an exposure time of one second. Longer exposure times give better signal-to-noise ratios but can prove particularly challenging due to stage and sample drift. Hence, a series of six images was acquired for each of the four particles to assess the effect of image quality. The images were aligned using the script StackReg for ImageJ [260] to account for any drift between images. The images were progressively stacked and intensity averaged.

Some noticeable fluctuation can be observed for the fringe lengths to different extents across the particles (see Figure 4.10a). While the variation between stacks of different images is only up to 3 % for P1, P3 exhibits differences of up to 9 %. However, the standard deviation of the values across the averaged image stacks is similar for all particles with 3 % to 4 %. Despite the variations in the measurements, no apparent trend in the data can be identified.

Similar observations can be made for the fringe tortuosity (see Figure 4.10b). However, the variation between image stacks is relatively lower with up

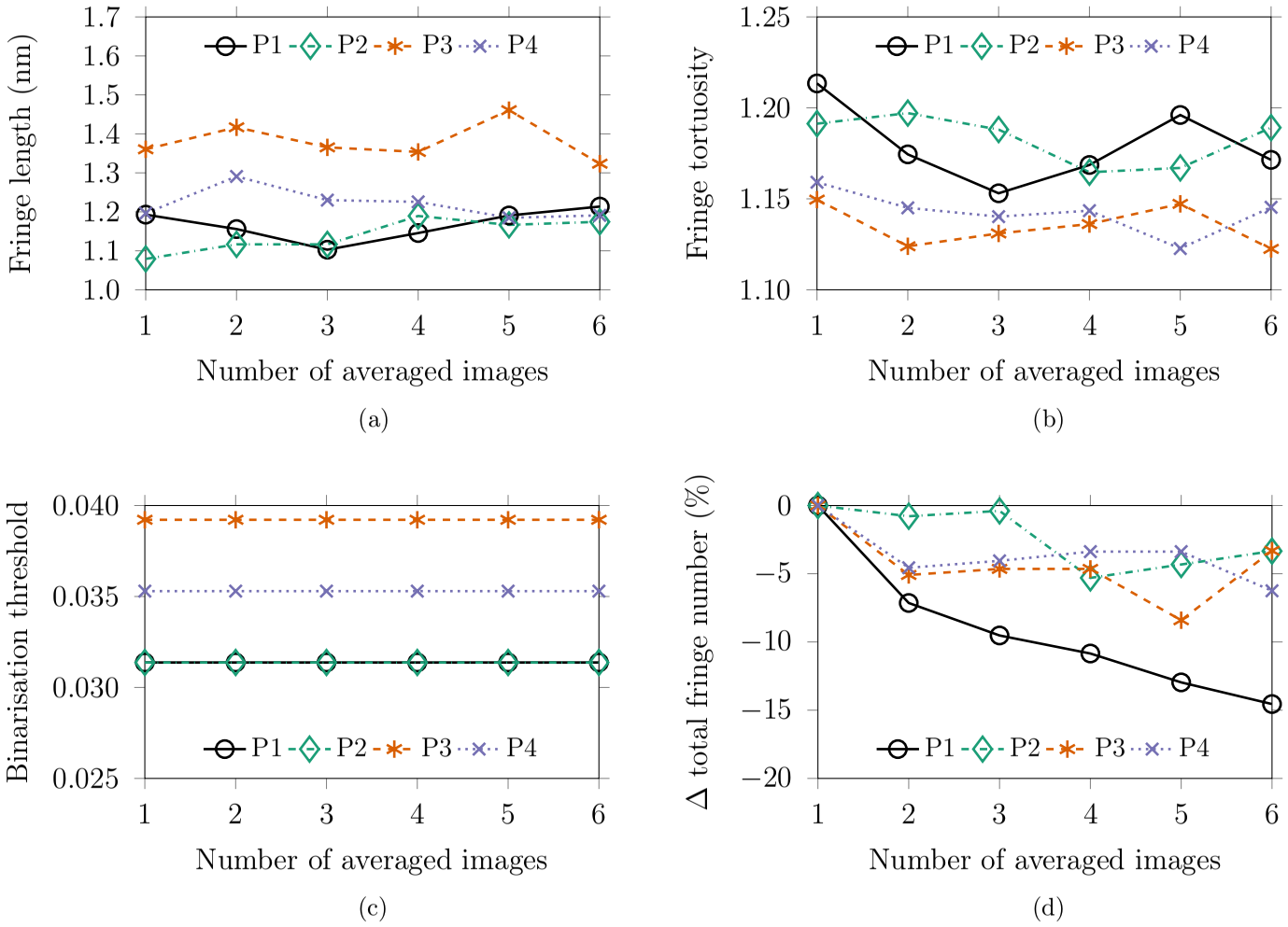

Figure 4.10: Variation of fringe length (a), tortuosity (b), binarisation threshold (c), and normalised total fringe number (d) with the number of images averaged for the four particles P1, P2, P3, and P4.

to 3 % for P1 and 2 % for the remaining particles. Likewise, the standard deviation across the averaged images is 2 % for P1 and 1 % for the other particles. As for the fringe length, there is no evident trend of the tortuosity across the averaged images.

The Otsu threshold does not change for any of the particles with the number of averaged images (see Figure 4.10c). In contrast, the total fringe number decreases with an increasing number of averaged images (see Figure 4.10d). For particle P1 the number of fringes decreases almost linearly by around 2 % after an initial drop of 7 % for the second image added to the averaged stack. The fringe count for P2 remains relatively constant until 3 images, after which the number of fringes creases by 5 %. Despite slightly increasing afterwards by 1 %, the number remains at a lower level. P3 and P4 also decrease with the second image added to the averaged stack as P1, but only by 4 % to 5 %. Contrary to P1, the total fringe number does not decrease further linearly but remains on a similar level despite some fluctuations. It should be noted that the observed changes of total fringe numbers for averaged images are on a lower scale as compared to the previous processing parameters as well as the TEM focus points. As the two fringe measurements do not show any noticeable trend, it is suggested that the used camera is either sufficient for this purpose or the contribution of this aspect is relatively minor.

4.7 Region of Interest Size

The purpose of any fringe analysis is the characterisation and, ultimately, the comparison of different samples. Qualitative reliability has been established above by determining the appropriate values for the used processing filters as well as investigating the influence of the TEM focus point and image quality. The requirements for quantitative reliability have to be established to allow for a meaningful comparison of samples. This can be achieved by means of a sufficient number of analysed fringes for statistical significance. Zhang et al. [261] had suggested a threshold of seven primary particles with a total

of 3500 fringes for reliable fringe metrics. Here, a slightly higher number of fringes was extracted for each sample. A total fringe number of 4066, 4045, and 4034 was obtained for the 1.0L GDI, 2.0L Diesel, and carbon black sample, respectively. These were extracted from 15 particles with a total ROI size of 3861 nm^2 for the 1.0L GDI sample, 22 particles with total ROI size of 4026 nm^2 for the 2.0L Diesel sample, and 11 particles with total ROI size of 3736 nm^2 for the carbon black sample. The ROI size for each individual particle ranged from 85 nm^2 to 512 nm^2. The objective was to assess any potential influence of the selected ROI size on the obtained fringe metrics. For this purpose, the total fringe number, fringe length, and fringe tortuosity were plotted against ROI size (see Figure 4.11). Moreover, linear regression models (LRM) were fitted for each collective data set. The full quantitative analysis of the obtained metrics is discussed in Section 5.3.2.

The total fringe number shows a strong correlation with the ROI size as the model fits the data well with a coefficient of determination $R^2 = 0.99$. The associated $p = 1 \cdot 10^{-46}$ indicates strong statistical significance. In contrast, the linear models for fringe length and tortuosity cannot explain the observed variation with $R^2 = 3 \cdot 10^{-4}$ and $R^2 = 7 \cdot 10^{-4}$, respectively. Based on the respective p-values of $p = 0.91$ and $p = 0.86$, no significant linear correlation between the fringe metrics and the ROI size can be observed.

If the processing parameters for the analysis of a given nanostructure image were to be changed, the number of fringes and the fringe metrics themselves would be altered as observed in Sections 4.2 to 4.4. Such changes would be expected to manifest in the form of a non-linear trend in the total fringe number as well as linear trends in the fringe metrics over different ROI sizes. Neither could be observed here. Thus, the size of the ROI only affects the total number of fringes due to a different size of particle nanostructure covered.

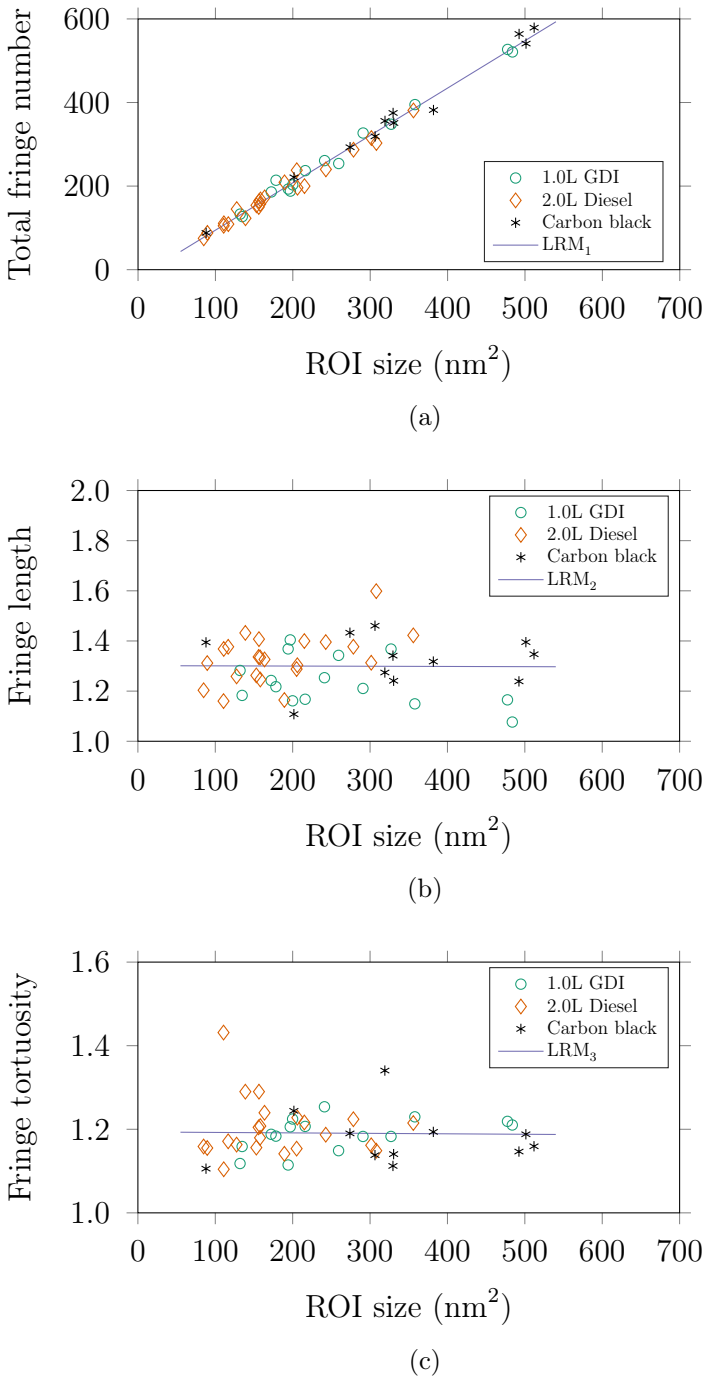

Figure 4.11: Total fringe number (a), fringe length (b), and fringe tortuosity (c) of the respective ROI with fitted linear regression model. (LRM1: $R^2 = 0.99$, $p = 1 \cdot 10^{-46}$. LRM2: $R^2 = 3 \cdot 10^{-4}$, $p = 0.91$. LRM3: $R^2 = 7 \cdot 10^{-4}$, $p = 0.86$)

4.8 Summary

Soot particles from different emission sources were used to assess the influence of three image processing parameters of an established fringe analysis methodology:

- The effect of the Gaussian low-pass filter standard deviation is minor for a range of values. However, noticeable changes in the structure of extracted fringes occur for values of 1.0 and below as well as larger than 3.0. Based on the findings, standard deviations between 2.0 and 3.0 are recommended.
- A linear correlation between the white top-hat transformation disk size and fringe length, tortuosity, and Otsu threshold was observed. Moreover, an inverse correlation between the disk size and the total number of fringes was found. For a realistic representation of the nanostructure and optimised fringe numbers, the disk sizes 5 px and 7 px are here recommended.
- The use of individually calculated Otsu threshold values generally yields the highest number of fringes. For larger threshold values, the total fringe number as well as both the fringe length and the tortuosity decay exponentially. Similarly, for considerably smaller values—i.e. close to 0—almost no fringes could be extracted. For best results and good repeatability, the use of the Otsu threshold without alterations is advised.

These parameters were determined for a spatial resolution of 0.025 nm/px at a magnification of 500 000 ×. As both the Gaussian low-pass filter standard deviation and the white top-hat transformation disk size are dependent on spatial resolution, similar investigations as in this study would need to be carried out if other magnifications were to be employed.

Moreover, two aspects of the TEM operation and their implications for the extracted fringes were considered:

- Deviating from the selected TEM focus point by under- and over-focusing resulted in distinctive drops in both fringe length and Otsu threshold. Despite some variations, no noticeable trends could be observed for the fringe tortuosity and total fringe number. However, to obtain reliable results, consistent focusing with the help of FFT is necessary across particles and samples.
- The effect of extended exposures and signal-to-noise ratio was found to be minor beyond the image acquisition equipment used. While the number of fringes decreased with multiple intensity-averaged images, the fringe length and tortuosity metrics did not show a trend in either direction.

Lastly, the size of the ROI correlated linearly with the total number of extracted fringes ($R^2 = 0.99$, $p = 1 \cdot 10^{-46}$). However, the fringe metrics were not influenced by the size, as assessed by linear regression models for both fringe length ($R^2 = 3 \cdot 10^{-4}$, $p = 0.91$) and tortuosity ($R^2 = 7 \cdot 10^{-4}$, $p = 0.86$).

5 Comparison of Soot Types

Exhaust particulate emissions from GDI engines are known to be about one order of magnitude lower compared to diesel engine-out emissions. Similarly, the deposition rate of soot into the lubricating oil would be expected to be lower; however, this aspect has not been covered previously in the literature. Therefore, three oil samples that were collected from a GDI engine with different oil mileages are used in the first part of this chapter to investigate the deposition rate. Subsequently, a set of five samples from different sources are characterised to identify possible differences between soot types. Four soot-in-oil samples are from internal combustion engines—two GDI and two diesel engines—and the fifth sample is a carbon black. Detailed information on the samples and the preparation methods was provided in Section 3.5. The characterisation of the particulates covers their morphology, aggregate size, and primary particle diameters. Moreover, fringe analysis is carried out. A larger number of fringes is used for a subset of three samples—one sample from each soot type—to assess the required threshold for robust analysis results, building upon the work of Chapter 4. Lastly, the same three samples are analysed by Raman spectroscopy to assess the validity of fringe analysis findings.

Parts of this chapter have previously been published in the journal Carbon, as an SAE Technical Paper that was presented at the SAE 2019 WCX World Congress Experience in Detroit, and in the journal Combustion and Flame:

S.A. Pfau, A. La Rocca, E. Haffner-Staton, et al. Comparative nanostructure analysis of gasoline turbocharged direct injection and diesel soot-in-oil with carbon black. Carbon, 139:342-–352, 2018, DOI 10.1016/j.carbon.2018.06.050.

S.A. Pfau, A. La Rocca, E. Haffner-Staton, et al. Soot in the lubricating oil: An overlooked concern for the gasoline direct injection engine? SAE Technical Paper 2019-01-0301, 2019, DOI 10.4271/2019-01-0301.

S.A. Pfau, A. La Rocca, and M.W. Fay. Quantifying soot nanostructures: Importance of image processing parameters for lattice fringe analysis. Combustion and Flame, 211:430—444, 2020, DOI 10.1016/j.combustflame.2019.10.020.

5.1 Deposition Rate

The content of soot in the lubricating oil was identified by TGA. For the three samples from the same GDI engine (as described in Section 3.5), the contents are 0.40 wt%, 0.42 wt%, and 0.51 wt% for the 5715 km, 6733 km, and 8488 km samples, respectively (see Figure 5.1). A numerical increase of soot content can be observed with increasing oil mileage. For diesel engines, the deposition rate for soot in the lubricating oil was found to correlate linearly with the oil mileage [121]. A broad study by Di Liberto et al. [122] of several diesel soot-in-oil samples from vehicles operated in various driving conditions suggested a deposition rate of approximately 1 wt% per 15 000 km with a standard deviation 0.4 wt%. Thus, it was attempted to fit a linear deposition rate model for the obtained measurements as well. The soot content was scaled from the respective oil mileage to 15 000 km and subsequently averaged over the three samples. The mean deposition rate using this approach is 0.96 wt%, with a standard deviation of 0.08 wt%. While this deposition rate appears to be slightly lower than the diesel model (see Figure 5.1), the standard deviation is five times lower. This could be due to the limited number of data points included here. The range of vehicles included in the study by Di Liberto et al. [122] was broader, thus allowing for a more general estimate of the soot deposition rate for diesel engines. The obtained measurements of this study fit within this established diesel model. This agreement suggests that soot accumulation in the lubricating oil is of similar importance for GDI engines as it is for diesel engines. However,

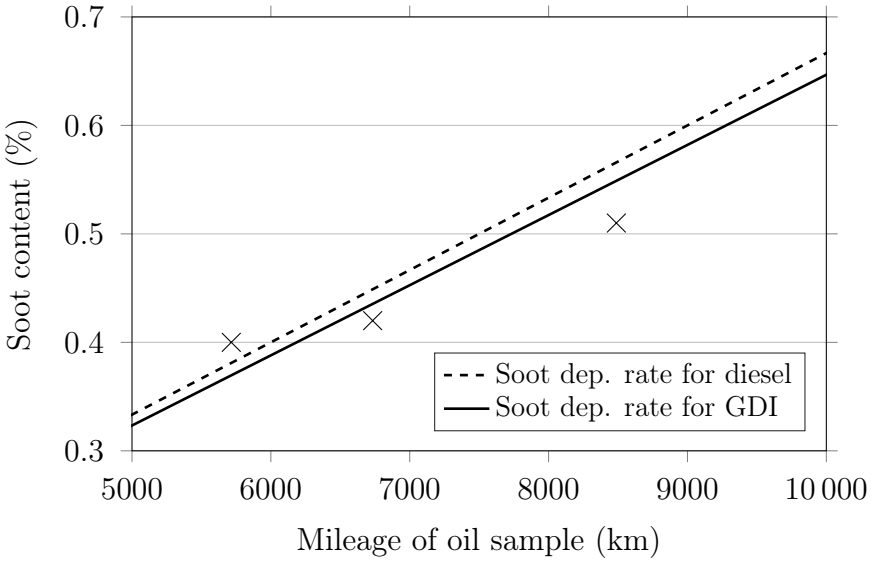

Figure 5.1: Soot content measurements by TGA of the three 1.0L GDI oil samples, previously reported soot deposition rate in oil for diesel engines [122], and discovered soot deposition rate in oil for GDI engines.

to confirm the observation and establish the quantitative dimension of the deposition rate, further studies of a larger scale would be required.

5.2 Characterisation of Soot Particulates

5.2.1 Morphology

Nanoscale images of the carbon black sample show a distinctive core-shell structure of the primary particles (see Figures 5.2a and 5.2b). The centres consist of amorphous nuclei that are surrounded by graphitic carbon layers. Agglomerates of multiple particles were imaged clearly with high resolution (see Figure 5.2c). In line with previous findings of Clague et al. [16], both the 2.0L Diesel (see Figure 5.2d) and the SC Diesel (see Figure 5.2g) exhibit a similar nanostructure. However, some diesel soot particle cores comprise

multiple nuclei (see Figures 5.2e and 5.2h). As these nuclei are more abundant during the early stage of soot formation [65], the present particles are likely to originate from this phase. Wan Mahmood et al. [262] conducted simulations on the in-cylinder formation and distribution of soot. The findings suggested that it is most likely the soot early in the combustion stroke that predominantly migrates into the lubricating oil via the oil film on the cylinder walls. Despite similar nanostructure, much smaller particles in fractal-like agglomerates can be observed (see Figures 5.2f and 5.2i); however, the sizes of these have been shown to be affected by the centrifugation cleaning process by La Rocca et al. [34].

Soot samples from the two GDI engines appear to have a more diverse morphology and nanostructures. Some particles exhibit a similar core-shell structure to the diesel soot particles, including the presence of multiple cores (see Figures 5.2j and 5.2m). Likewise, soot agglomerates consisting of several primary particles can be observed with fractal shapes (see Figure 5.3). In contrast to other types of soot, entirely amorphous particles are observed, lacking any apparent long-range order (see Figure 5.2k). Furthermore, the samples contain particles which were previously described as "sludge-like" by Uy et al. [48] and noted to be particularly prone to contamination (see Figure 5.2n). However, contrary to their report, no decomposition under the electron beam of the TEM was observed here, even after prolonged exposure at 200 kV. Some amorphous particles further include small particles with diameters of only a few nanometres embedded within them (see Figures 5.2l and 5.2o). On the nanoscale, these particles exhibit localised crystalline structures (see Figure 5.4).

Similar regions were observed by La Rocca et al. [67] on the surface of regular graphitic primary particles of GDI soot-in-oil. While the surface crystalline regions decomposed under the electron beam, indicating volatiles as their source, the small particles here remained without any sign of decomposition. For diesel soot-in-oil, Sharma et al. [123] also found crystalline regions within particles with EDX measurements pointing towards lubricant oil and engine

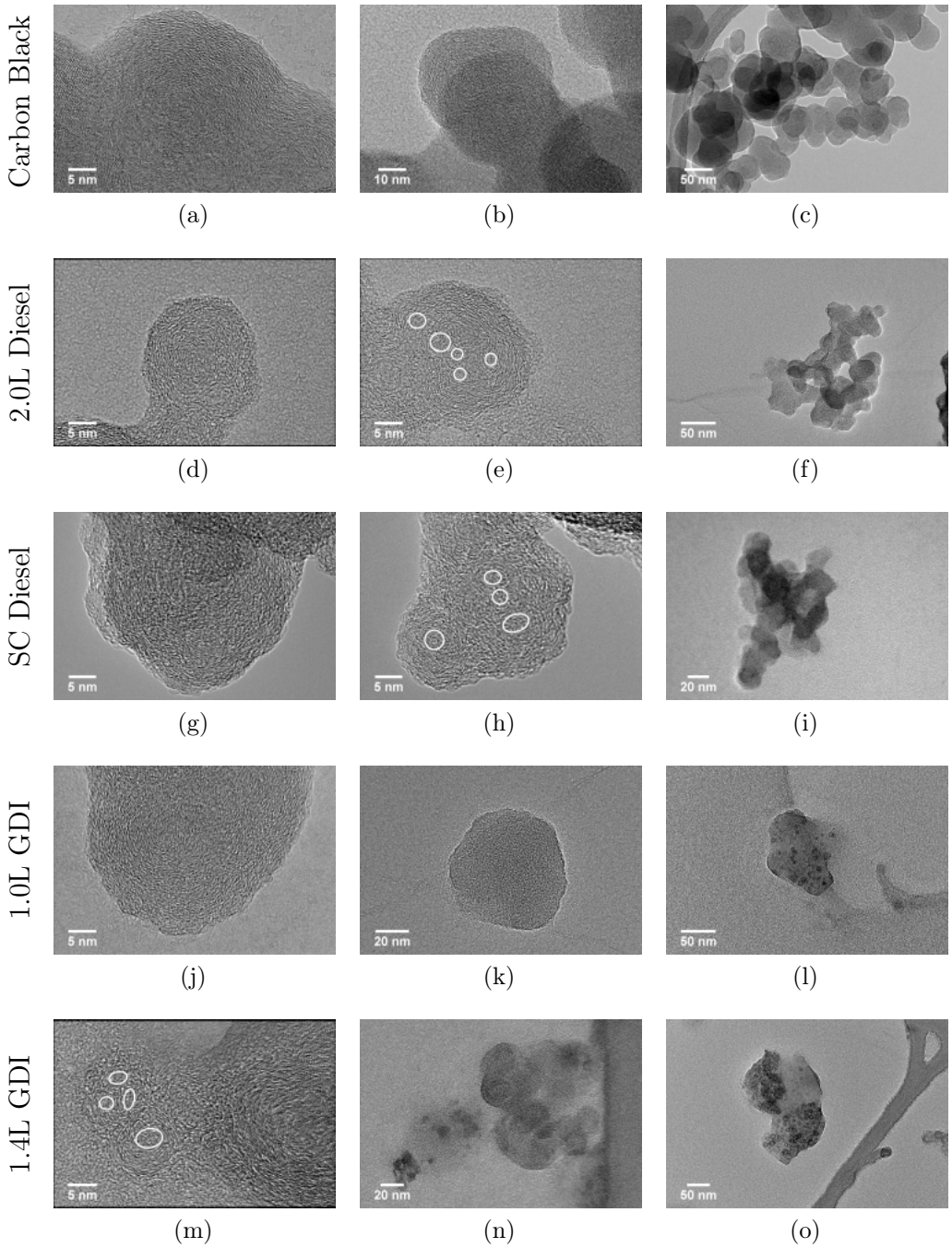

Figure 5.2: HRTEM images of carbon black (a-c), 2.0L Diesel (d-f), SC Diesel (g-i), 1.0L GDI (j-l), and 1.4L GDI (m-o) soots.

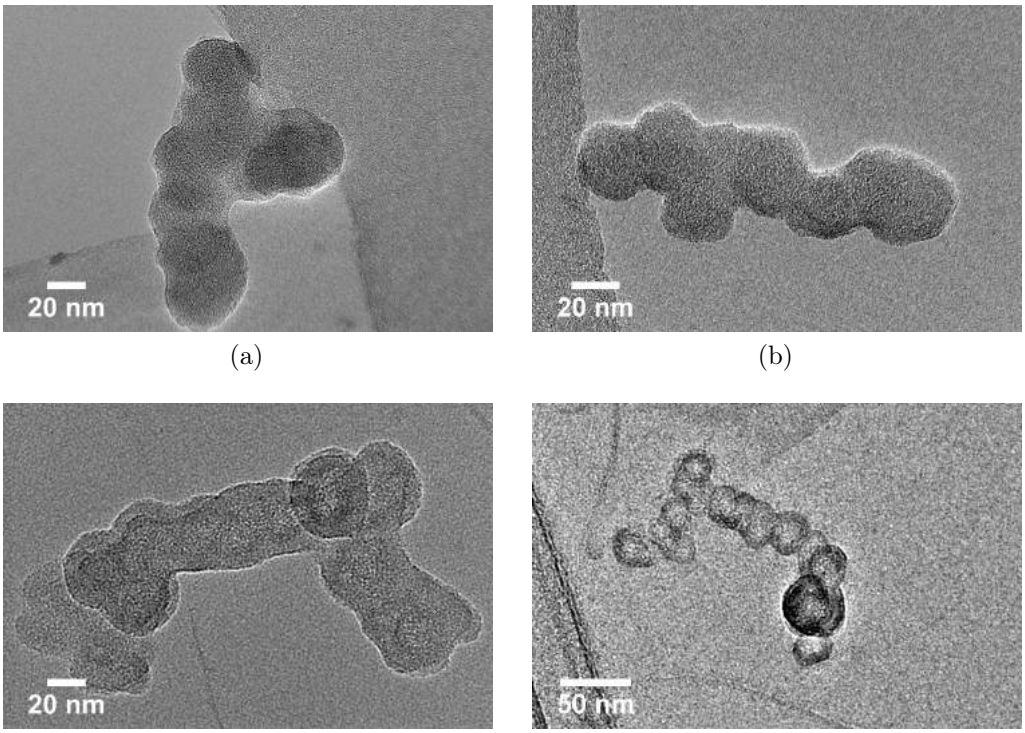

(a) (b)

(c) (d)

Figure 5.3: TEM images of fractal soot agglomerates from the 1.0L GDI sample, consisting of several primary particles.

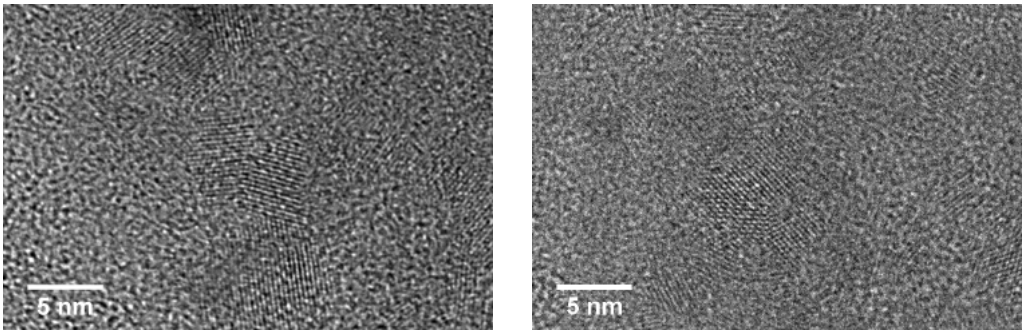

(a) (b)

Figure 5.4: Enlarged HRTEM images of crystallite regions within 1.0L GDI (a) and 1.4L GDI soots (b).

wear. EDX measurements of the crystalline regions in amorphous particles (see Figure 5.4) show traces of various elements (see Table 5.1). Ca, S, and P are commonly associated with additives in the lubricating oil, while Fe, Cr, and O likely stem from the engine wear [48, 123, 263]. However, Fe and Cr might also be detected due to scattering from the microscope pole piece. F, Na, and Si can originate from multiple sources such as further oil additives or contamination. C and O are associated with the TEM grid and the supporting film respectively; however, the latter can also stem from organic fractions. Despite most of the C stemming from the soot particles, some is attributable to the supporting graphene oxide film.

Crystalline regions embedded within the soot structure were previously found to promote wear and abrasion in engines [264]. Sharma et al. [265] observed such behaviour in diesel engines, particularly with increasing engine age. However, here crystalline regions, as well as entirely amorphous particles, are only observed in the GDI samples, suggesting a difference between the soot types. Antusch et al. [43] suggested different nanostructures to cause altered reactivity of the soot. This was subsequently supported by studies conducted by Vander Wal and Tomasek [259] as well as Alfè et al. [86]. Altered reactivity due to nanostructure changes could further suggest a higher degree of interaction with the lubricating oil. As a result, the effectiveness of oil additives could be diminished and wear thus be enhanced [44].

5.2.2 Aggregate Size

Measurements of soot agglomerates directly in an oil-heptane solution of the 1.0L GDI were obtained by NTA (see Figure 5.6). The size distribution exhibits an asymmetric shape with particle numbers shifted towards larger sizes from the mode at 100 nm, and the mean agglomerate size is 132 nm. On the lower side of the mode, the particle numbers fall sharply, consistent with the expected limit of detection. Additional populations are present at 155 nm and 241 nm, with 300 nm representing an upper size limit for this

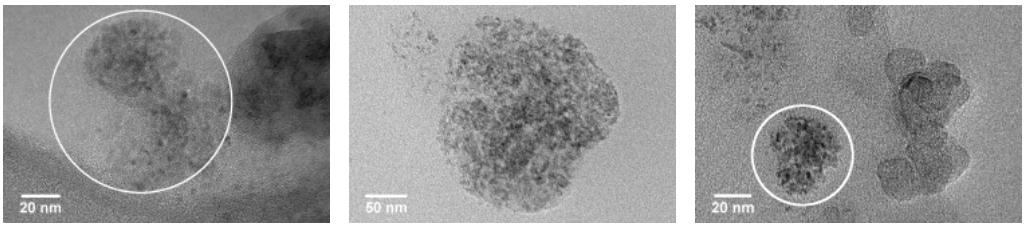

(a) (b) (c)

Figure 5.5: HRTEM images of amorphous regions with embedded particles and crystallite regions within 1.0L GDI (a) and 1.4L GDI soots (b,c) analysed by EDX.

Table 5.1: EDX measurements of 1.0L GDI and 1.4L GDI particles.

Element	1.0L GDI	1.4L GDI	
(At%)	Figure 5.5a	Figure 5.5b	Figure 5.5c
C	83.3	84.2	87.1
O	6.9	6.8	6.2
F	4.0	4.1	2.8
Na	0.0	0.1	0.0
Si	1.6	0.9	1.0
P	0.4	0.3	0.5
S	0.2	0.5	0.2
Ca	3.0	2.8	1.8
Cr	0.2	0.1	0.0
Fe	0.2	0.1	0.2
Co	0.2	0.1	0.0

principal distribution. The inset in Figure 5.1 shows an enlarged view of the size range of 300 nm to 500 nm. Almost no agglomerates are present in the range of 350 nm to 400 nm; however, a second mode at 426 nm becomes apparent. Nevertheless, the concentration is significantly lower than the first mode by three orders of magnitude, i.e. $3.7 \cdot 10^4$ compared to $2.2 \cdot 10^7$. No such feature could be observed for smaller particle sizes, i.e. below 100 nm.

As NTA is a novel technique and has only been used in a few studies, the obtained measurements are compared with literature based on dynamic light scattering (DLS) in addition to studies using NTA. An initial study by La Rocca et al. [258] had compared DLS and NTA measurements for soot-in-oil samples of two diesel engines. The NTA values were found to be lower than the values here, with mean particle sizes of 115 nm to 126 nm and main modes at 98 nm to 110 nm. The results from the DLS analysis differed only by few nanometres from the NTA findings. In a subsequent study, a similar second peak at larger agglomerate sizes was observed for diesel soot-in-oil [116]. In a comparative study, Key et al. [80] reported agglomerate sizes of 91.8 nm and 116.8 nm for two types of carbon black, as well as 96.5 nm for diesel soot-in-oil. Moreover, both studies showed that the dimensions obtained by NTA correlated well with the skeleton length of the agglomerates, as observable in TEM images. Kim et al. [266] used 16 oil formulations in two diesel engines for 25 h test-runs, and subsequently analysed the soot-laden oil samples by DLS. The average agglomerate size ranged from 98.4 nm to 163.8 nm among the oils. However, it should be noted that the analysis in the study showed a high variation, i.e. duplicate runs for different batches of the same sample yielded average values of 122.2 nm and 163.8 nm. Liu et al. [267] also operated diesel engines with lubricating oils of different formulations. Measurements with DLS found mean particle sizes ranging from 111 nm to 266 nm, depending on oil formulation and temperature at which the measurements were carried out. Overall, it can be noted that the range of NTA and DLS measurements for diesel soot is extensive. Here, the observed mean and mode values lie within this range.

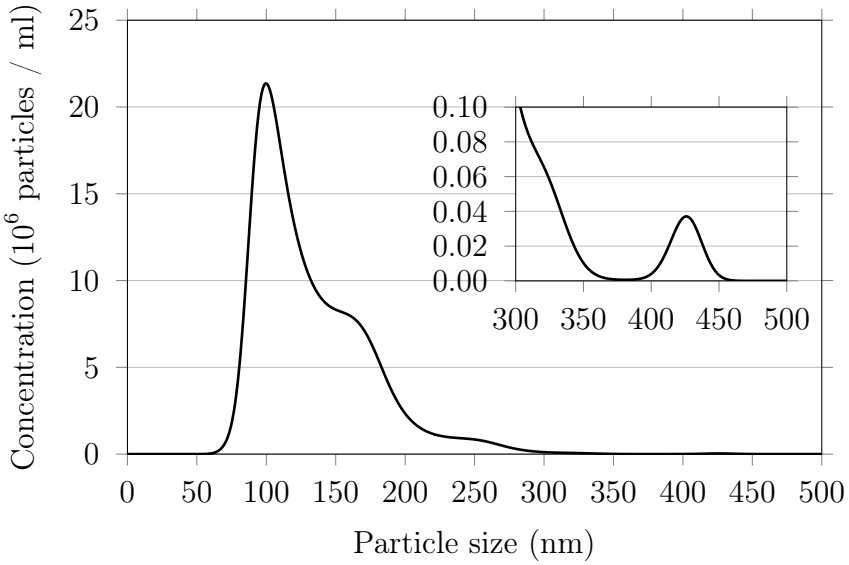

Figure 5.6: Size distribution and volume concentration of soot particles in used lubricating oil of the 1.0L GDI sample, measured by NTA.

However, as the technique appears to be sensitive to engine parameters and measurement conditions, more information could be obtained by a direct comparative assessment of samples.

5.2.3 Primary Particle Diameter

To assess the similarity to other types of soot quantitatively, the sizes of 171 primary particles of the 1.0L GDI sample were measured (see Figure 5.7). Two perpendicular measurements were taken for each particle and the average ratio between the two values was 1.09 (standard deviation of 0.08). The ratio indicates that the particles are on average slightly oval, but still close to a spherical, round shape. Thus, the arithmetic mean between the two measurements is used as diameter for each particle. The diameters range from 12 nm to 55 nm, with a mode at 31 nm and a mean of 30 nm. The range is lower than previous findings for GDI soot-in-oil, i.e. 20 nm to 90 nm [67]. However, the measurements are similar to findings for GDI

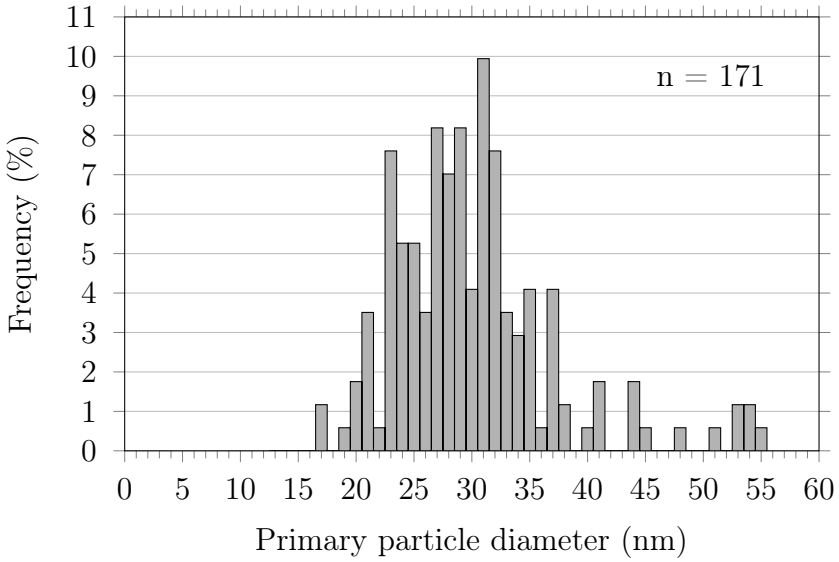

Figure 5.7: Frequency distribution of the primary particle diameter as measured in TEM images of agglomerates from the 1.0L GDI sample.

exhaust soot samples that exhibited primary particle diameters from as low as 5 nm [49] up to 65 nm [47]. Similarly, the mean value better fits with the findings for exhaust soot than for soot-in-oil. In contrast, the mode found here is in line with previous findings for GDI soot-in-oil, while lower modes from 10 nm [46, 49] to 22 nm [47] were observed for GDI exhaust soot.

Qualitative assessment of the primary particles showed a prevalence of the typical core-shell nanostructure (see Figures 5.8a and 5.8b). In Figure 5.8c both the amorphous core and the graphitic shell are marked as well as an unusual surrounding amorphous layer. This observation is in line with a previous study by La Rocca et al. [67]. Details of the particle nanostructure are presented in Figures 5.8d and 5.8e. Both images were contrast-enhanced and binarised to improve the visibility of the structure. The surrounding layer exhibits a significantly lower degree of order compared to the graphitic shell. The subsequent higher amount of edge sites is likely to increase overall reactivity, as reported by Vander Wal and Tomasek [259].

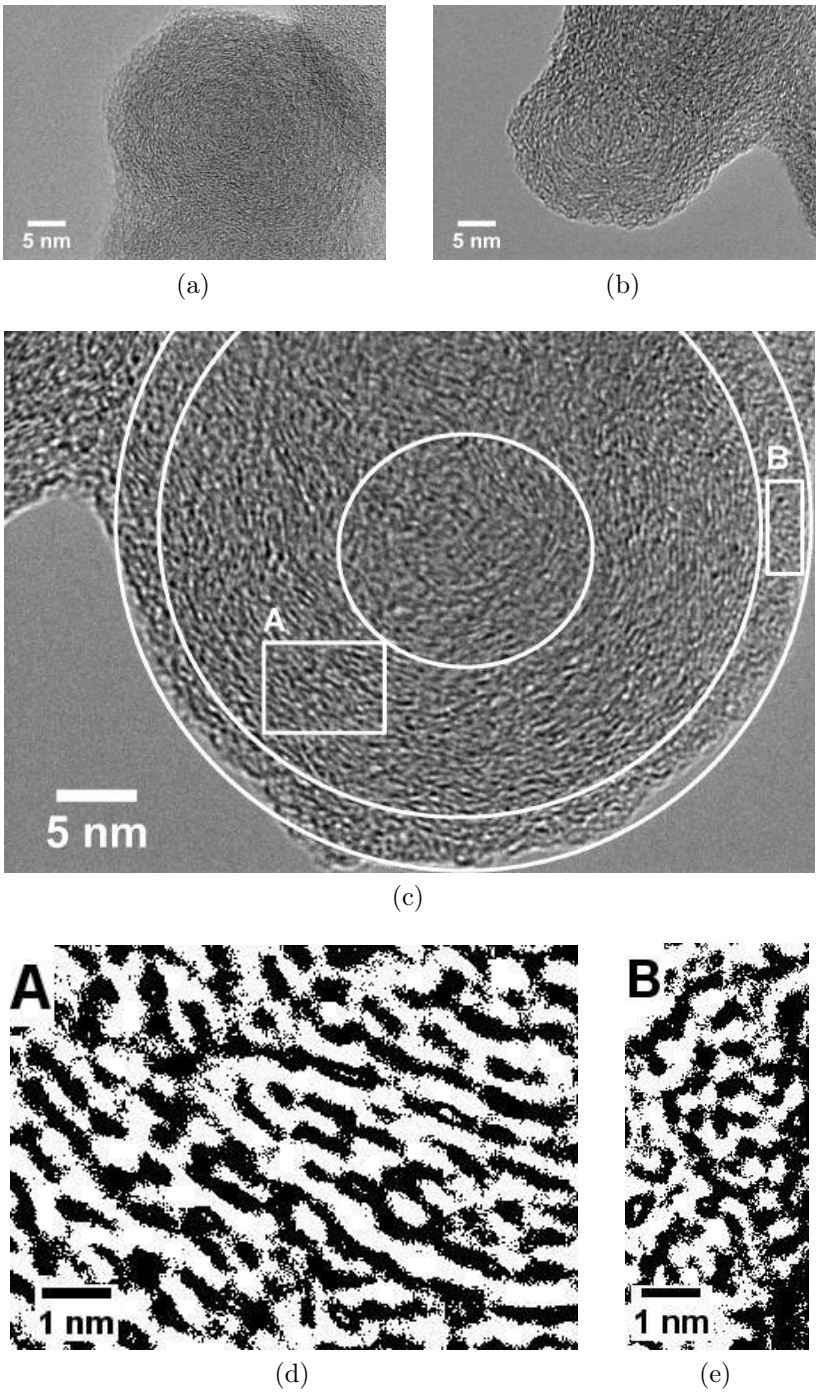

Figure 5.8: TEM images of soot primary particles from the 1.0L GDI sample (a,b). Marked primary particle with central core, graphitic shell and surrounding amorphous layer (c). Enlargements A and B show details of nanostructure (d,e).

5.3 Nanostructure Analysis

Initial measurements of primary particle nanostructures were carried out for all five samples in Section 5.3.1: A minimum of 1000 fringes was obtained per sample, of which separations for at least 180 fringe pairs were measured. Parameters for the processing steps were selected based on the pixel scale of the image to account for different magnifications. However, the values were adjusted manually to account for variations in brightness due to sample thickness. Based on the optimal processing parameters established in Chapter 4, a larger number of particles was analysed in Section 5.3.2 to assess the impact of the total fringe number on the fringe length and tortuosity. For this second part, a reduced set of three samples was used. In addition to the carbon black, the 1.0L GDI and 2.0L Diesel samples were used (referred to as 'GDI' and 'Diesel', as in Chapter 4).

5.3.1 Sample Comparison

Computational analysis of the graphitic nanostructure made differences between the samples apparent (see Figure 5.9). The carbon black sample exhibits the longest fringes of 1.13 nm. The average fringe length for the 2.0L Diesel and SC Diesel is shorter with 1.08 nm and 1.07 nm respectively. The gap between carbon black and the GDI samples is larger, with 0.97 nm and 0.99 nm for the fringes of 1.0L GDI and 1.4L GDI, respectively. These values differ from previously reported findings. Gaddam and Vander Wal [47] found lamellae of GDI soot ranging from 0.72 nm to 0.82 nm, depending on the operating conditions of the engine. A study by Wu et al. [76] on GDI soot showed that the fringe length also varied with the air-fuel-ratio of the engine, from 0.83 nm to 0.91 nm. For soot obtained from diesel engines, Jaramillo et al. [73] and Sakai et al. [71] reported similar fringe lengths of 0.98 nm and 1 nm respectively. However, in studies by Li et al. [74] and Xu et al. [72] the fringe length of diesel soot was observed to be affected by fuel injection splitting (1.16 nm to 1.2 nm) and injection timing (1.12 nm to

1.4 nm), respectively. Overall, the reported fringe length ranges for GDI soot (0.72 nm to 0.91 nm) and diesel soot (0.98 nm to 1.4 nm) show a clear minimum separation of 0.07 nm. The difference between both soot types is ca. 0.1 nm, therewith confirming this observation.

In all of the aforementioned studies, the soot samples were collected either directly or after dilution from the exhaust gas of internal combustion engines run at specific operating conditions. As the soot samples here were obtained from the lubricating oil, the soot represents a range of operating conditions. Moreover, primarily early soot migrates into the lubricating oil as mentioned above [262]. Thus, the soot-in-oil would be less oxidised than the soot from the exhaust gas due to a shorter residence time in the combustion chamber. Jaramillo et al. [73] found a linear decrease of the fringe length with increasing degree of oxidation of diesel soot. Similarly, Rohani and Bae [268] observed lower fringe length and higher tortuosity for soot obtained directly from the in-cylinder spray than for particles from the exhaust gas. This would explain the numerical difference between the obtained fringe lengths for the samples in this study and the previously reported values.

Regarding carbon black, Jaramillo et al. [73] observed the fringe length to be shorter than for diesel soot (0.8 nm to 0.9 nm). In contrast, Seong and Boehman [110] found that the crystallite width is higher for carbon black than for engine soots. The latter is supported by measurements in this work. However, different types of carbon black were analysed across these studies. The nanostructure can change significantly with the type of carbon black and sample preparation, as shown by Yehliu et al. [107] for various heat treatments. The carbon black sample that was analysed here appears to be a particularly ordered/graphitic type.

The fringes of all engine soot samples exhibit almost the same degree of tortuosity with 1.13 for all but the SC Diesel sample with 1.12 (see Figure 5.9b). In contrast, the carbon black sample exhibits the least tortuous graphitic layers with a value of 1.09. Hence, it is assumed that the difference stems from the sample origin, i.e. flame generated carbon black compared to

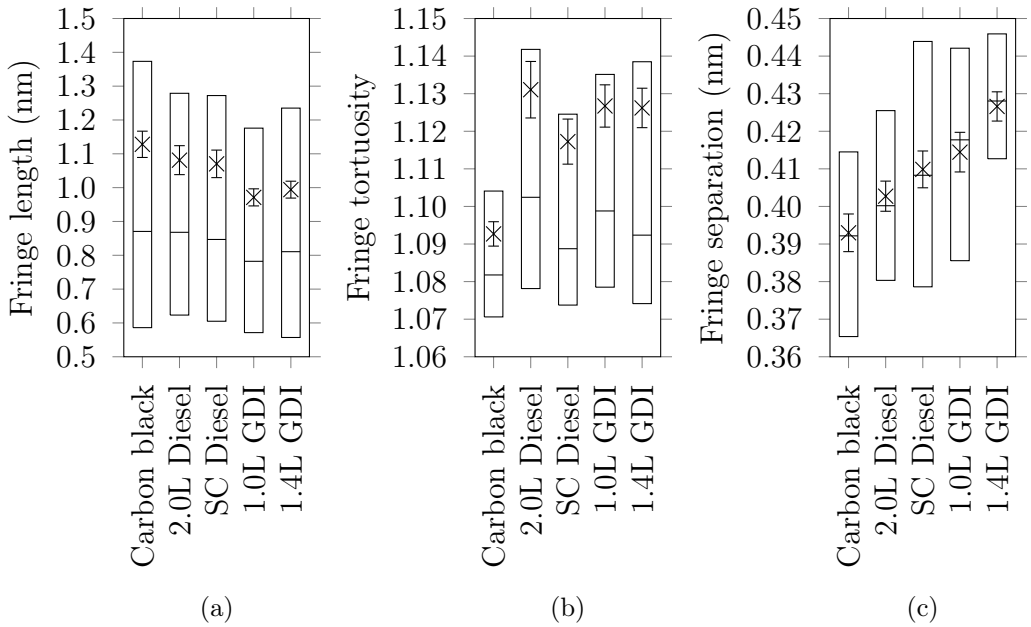

Figure 5.9: Comparison of the fringe length (a), the fringe tortuosity (b), and the fringe separation (c) of carbon black, 2.0L Diesel, SC Diesel, 1.0L GDI, and 1.4L GDI obtained by fringe analysis of HRTEM images. The boxes indicate the median with interquartile range; the markers indicate the mean values with 95 % confidence intervals as error bars.

soot from internal combustion engines. Again, previously reported numbers differ slightly from the obtained measurements. Gaddam and Vander Wal [47] found the tortuosity of GDI soot to be between 1.18 and 1.21 depending on the operating conditions of the engine. Wu et al. [76] observed a tortuosity range of 1.44 to 1.49 by varying the air-to-fuel ratio of a GDI engine. For diesel engine soot, Sakai et al. [71] identified a fringe tortuosity of 1.23 and Jaramillo et al. [73] of 1.17. In a study by Li et al. [74] changes to the diesel fuel injection, i.e. single or multiple injections, lead to a tortuosity range of 1.13 to 1.2. Furthermore, Xu et al. [72] reported a similar range of 1.12 to 1.25 for different injection timings and cylinder pressures of a diesel engine. Overall, the reported tortuosities for diesel soot (1.12 to 1.25) lie

within the range of tortuosities for GDI soot (1.18 to 1.49). Tortuosities observed in this study are at the lower end of these ranges. However, this could again be attributed to early migration of the soot into the lubricating oil and thus a comparatively lower degree of oxidation.

Unlike the two aforementioned parameters, the samples show no kind of grouping in terms of fringe separation. The graphitic layers in carbon black are the closest with average separation of 0.393 nm (see Figure 5.9c). The remaining samples exhibit increasingly larger separations: 0.403 nm, 0.410 nm, 0.414 nm, and 0.427 nm for 2.0L Diesel, SC Diesel, 1.0L GDI and 1.4L GDI soots, respectively. All engine soots exhibit larger spacings between graphitic layers, with GDI soot lamellae more apart than those of diesel soot. However, the difference among the samples of the same fuel type is larger than the gap between the two closest GDI and diesel samples. In a previous study by Wu et al. [76] the fringe separation of GDI soot samples obtained from the exhaust gas ranged from 0.38 nm to 0.41 nm depending on the air-to-fuel ratio. Sakai et al. [71] found a greater fringe separation of 0.42 nm for the graphitic layers of diesel soot sampled from the in-cylinder spray flame. This could potentially stem from the point of sampling. Soot obtained from the exhaust gas is more oxidised than the soot sampled in the combustion chamber, as mentioned above. For carbon black, Yehliu et al. [107] found decreasing fringe separation for more graphitic samples. A more ordered nanostructure reduces the number of defects and thus allows the layers to be stacked more closely. Hence, it is here suggested that the fringe separation decreases with progressing oxidation of soot, as the lamellae in the graphitic structure realign. This assumption is supported by the obtained results.

Overall, the three soot types exhibit distinct nanostructure differences. The GDI soot is the least ordered of the three, followed by the diesel soot samples and carbon black with the most ordered nanostructure. This can affect both the reactivity and the oxidation behaviour of the soot [76]. The less ordered the carbon structure, the more graphene layer edge sites are present.

Consequently, the soot would be more prone to oxidation and could interact with the lubricating oil to a greater extend [269]. The wear behaviour would be altered and the effectiveness of detergents in the lubricating oil would be impaired [264].

5.3.2 Total Fringe Number

Although the ROI size does not influence the fringe metrics, as shown in Section 4.7, the total number of extracted fringes can play a role. This aspect was to date only addressed as part of a study by Zhang et al. [261]: Fringe analysis was performed on several primary particles and the cumulative moving average (CMA) of the fringe metrics was subsequently assessed. It was observed that the 95 % confidence intervals decreased with higher numbers of processed images of primary particles, i.e. increased quantitative reliability. Both averaged fringe length and tortuosity converged for more than seven primary particles or 3500 fringes. However, the number of fringes that were extracted from each particle was not further specified. As this number can vary noticeably, the following analysis here is based on the total fringe number. The processing was conducted with the suggested parameters of Chapter 4, i.e. a Gaussian low-pass filter standard deviation of 2.0, white top-hat transformation disk size of 7 px, and the Otsu's threshold value for the binarisation were used. The CMA fringe length and tortuosity is plotted over the cumulative total fringe number in Figure 5.10. To assess the statistical significance, 95 % confidence intervals were calculated every 500 fringes.

The highest fluctuation can be observed below 500 fringes, with confidence intervals of the three samples overlapping considerably. Some further changes in mean values occur between 500 and 2000 fringes. In terms of fringe length, GDI soot sample remains stable beyond 2000 fringes, whereas both the diesel soot and carbon black sample drift before crossing at 3000 fringes and then stabilising. A clear difference between the GDI soot and the two other samples can be observed, with a gap of 0.14 nm and 0.1 nm to the mean

values of diesel soot and carbon black sample, respectively, at 4000 fringes. The fringe length confidence intervals of all samples at this data point are just under ±0.03 nm. Despite the difference and drifts in mean values between diesel soot and carbon black, the confidence intervals overlap consistently and are almost identical at 3000 fringes. Thus, no statistically significant difference between the fringe lengths of these two samples can be identified with this analysis. Regarding fringe tortuosity, the appearance of the CMA plots is different, with drifts continuing longer. A slight positive drift can be observed for the GDI soot sample, and an even stronger drift for the carbon black sample. Both values stabilise around 3000 fringes. In contrast, the CMA tortuosity for the diesel soot sample does not converge but rather shows a subtle negative trend with an increasing number of fringes. Similar tortuosity values with overlapping error bars are observed for the GDI and diesel soot samples up to 3000 fringes. Above this point, the tortuosity is lower for the diesel soot sample. The carbon black particles exhibit a lower tortuosity CMA throughout the total fringe number range. The mean values of the GDI and diesel soot samples are higher by 0.021 and 0.01, respectively. The confidence intervals range between 0.0046 (carbon black) and 0.0052 (GDI soot) and despite being close, they do not overlap across the samples.

These findings confirm the observation of Section 5.3.1 that GDI soot appears to be of lower structural order compared to carbon black. The results for diesel soot diverge. The fringe length is similar to carbon black, but the tortuosity is different. Meanwhile, the gaps between the samples analysed here are comparable to samples with different nanostructures analysed in other works. The additionally reported confidence intervals allow for better appraisal of the results in terms of significance. In terms of the total fringe number required for reliable data, 3000 fringes appear to be a lower limit for convergence of the CMA. It is recommended here that 4000 fringes should be used as the threshold value for analysis to ensure a stabilised window of roughly 1000 fringes prior to the data point used.

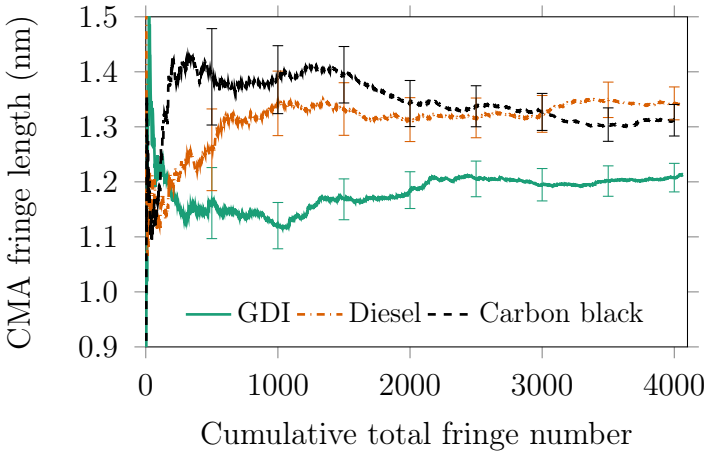

(a)

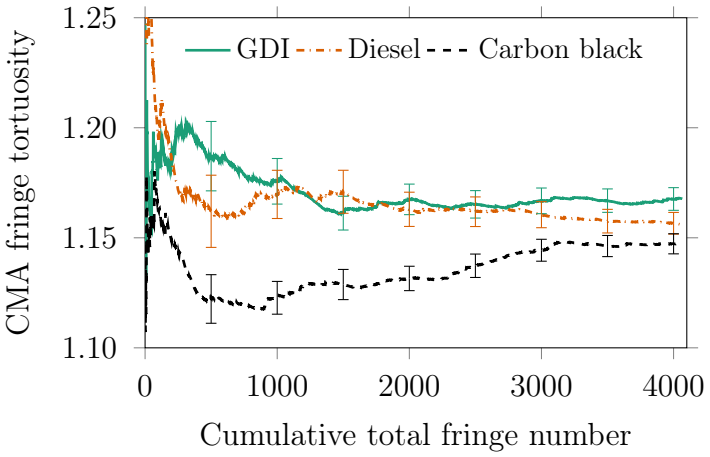

(b)

Figure 5.10: Cumulative moving average (CMA) of fringe length (a) and tortuosity (b) for the cumulative total fringe number. The error bars are indicative of 95 % confidence intervals.

5.4 Verification by Raman Spectroscopy

To probe the effectiveness of the combined dilution and centrifugation procedures to remove the contaminants from the 1.0L GDI oil—which are giving rise to fluorescence under visible excitation—532 nm Raman spectra from soot sampled at different extents of purification were analysed (see Figure 5.11). The pilot study with only four centrifugation cycles ($1 : 2 \cdot 10^3$ oil:heptane dilution ratio) yielded a significant background from fluorescence and thus a spectrum too noisy to be informative. Further centrifugation and increasing the oil:heptane ratio significantly decreased the background fluorescence, most noticeable when increasing the dilution from $1 : 2 \cdot 10^3$ to $1 : 7.5 \cdot 10^4$, which reduces the background fluorescence at 700/cm (553 nm) three-fold from 17 800 counts to 5900 counts. Beyond $1 : 7.5 \cdot 10^4$ dilution, the reduction is less pronounced with only a 38 % reduction in fluorescence from 5900 counts to 3650 counts when increasing the dilution to $1 : 5 \cdot 10^8$. Further purification was not deemed necessary as residual fluorescence could be effectively removed by photobleaching the appraised area of the sample immediately prior to spectra acquisition. Interestingly, the residual fluorescence observed in the Raman spectrum of gasoline soot was approximately ten times higher than that noted for diesel soot under the same dilution ratio and spectral acquisition parameters. This would imply that gasoline soot contains a higher proportion of organic compounds, such as aromatics and PAH, which is supported by the higher PN associated with GDI engines, a result of increased nucleation during combustion. The observation of high quantities of organic matter, giving rise to fluorescence, in the GDI sample is supported by the reports of Uy et al. [48] and Gaddam et al. [47], the former of which used an analogous procedure to that reported here in an attempt to remove the contaminants. It is interesting to note, however, that despite the authors utilising more centrifugation steps, high fluorescence continued to be observed, suggesting that the dilution factor ($1 : 4$ oil:hexane in Uy et al. [48]; up to $1 : 5 \cdot 10^8$ oil:heptane here) was more critical for effective purification.

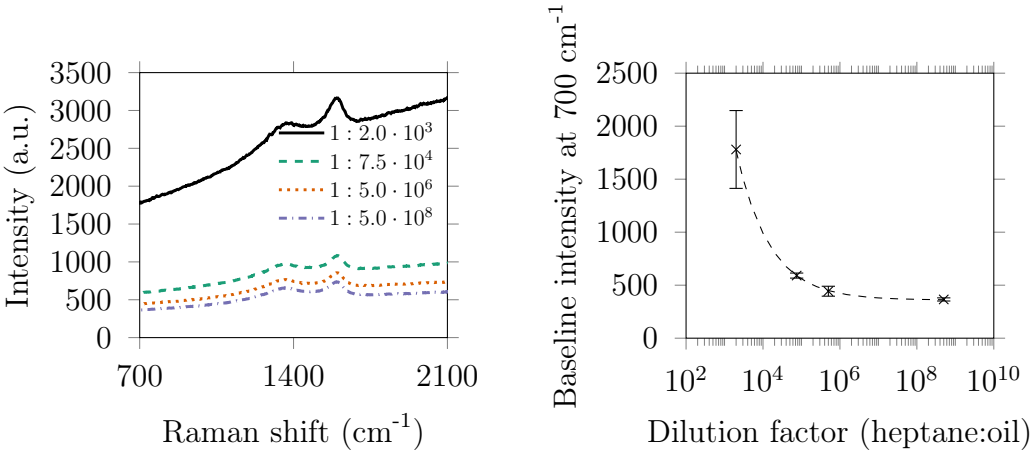

Figure 5.11: Effect of heptane dilution on the background intensity of fluorescence in Raman spectra (a) and baseline intensity at 700/cm for 1.0L GDI with dashed trendline (b).

Raman spectroscopic analysis of carbon black (see Figure 5.12a)—which required no specific preparation and only minimal baseline subtraction—yielded a spectrum with high signal to noise and effectively no fluorescence as expected for a non-contaminated sample, which was fit using a four-band model (G, D1, D3 and D4 bands). The goodness of fit was $\chi^2 = 2.98$, suggesting effect convergence to a local minimum and therefore an acceptable fit [109]. The baseline-corrected spectra relating to the purified diesel and GDI soot samples (see Figures 5.12b and 5.12c, respectively) were also fitted with the same four-band model, both achieving $\chi^2 = 2.97$. This goodness of fit matches that obtained for carbon black, highlighting the success of the cleaning procedure for the soot samples. The four-band model utilised in this study represented the best possible fit achievable for these samples; the self-consistency of fitting parameters ensures that the trends observed for the samples explicitly investigated here are meaningful. Furthermore, owing to the improved accuracy and relevance of peak areas (as opposed to peak heights) and the asymmetric nature of the D3 and D4 bands, it was decided

that the integrated area under the curve was the most suitable diagnostic for band intensity and thus relative spectral contribution. The ratio of band areas A_{D1} (arising from the graphene layer edge sites suggesting defective graphitic structures) and A_{D3} (arising from amorphous carbon), relative to A_G (arising from graphitic carbon), were the two metrics used to compare the samples. The 0.49 increase seen in A_{D1}:A_G (the ratio of disorder to order within the graphic lattices) between carbon black and diesel soot is related to a decrease in the lamella size (fringe length) and an increase in the disorder (tortuosity) within the sample. While the 0.49 increase represents a 26 % increase for diesel over carbon black, the 1.0L GDI soot shows a 1.97 increase, equivalent to 105 %. This value suggests that the 1.0L GDI soot contains much smaller lamella, a substantial decrease in the basal plane to edge site carbon atoms fraction, and a significant increase in reactivity over both the diesel soot and the carbon black. In addition, A_{D3}:A_G (the ratio of amorphous to graphitic carbon) was 100 % higher for diesel soot relative to carbon black. The relative increase between 1.0L GDI soot and carbon black is less significant compared to diesel soot showing only a 120 % increase. This implies that the high amorphous carbon content is characteristic of engine-produced soot, while more defective carbon is present in the gasoline produced soot.

These observations are in line with the findings of the initial fringe analysis in Section 5.3.1. The obtained fringe parameters were directly compared with the corresponding A_{D1}:A_G ratios of the respective samples (see Figure 5.13). A strong linear correlation was found in terms of the fringe length and an inverse correlation for fringe separation, with R^2 values of 0.997 and 0.936, respectively. Thus, the fringe analysis was validated as samples with a larger fraction of defective graphitic structures would also exhibit shorter and less densely aligned carbon layers. In contrast, the tortuosity values do not correlate linearly with the A_{D1}:A_G ratios ($R^2 = 0.385$). Instead, it appears that there is a difference in tortuosity between soot from internal combustion engines and carbon black.

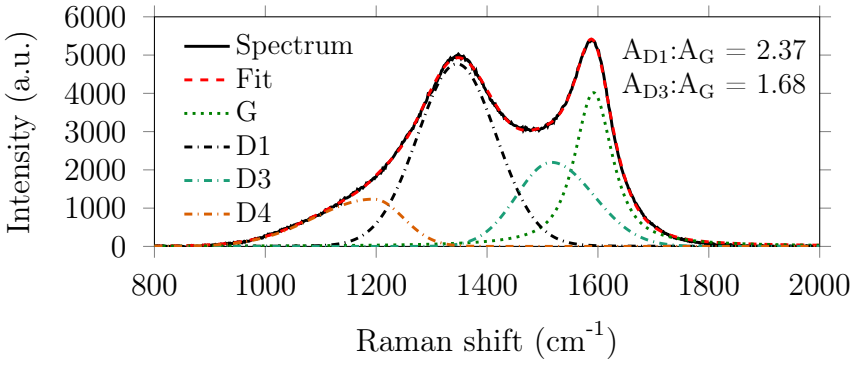

(a)

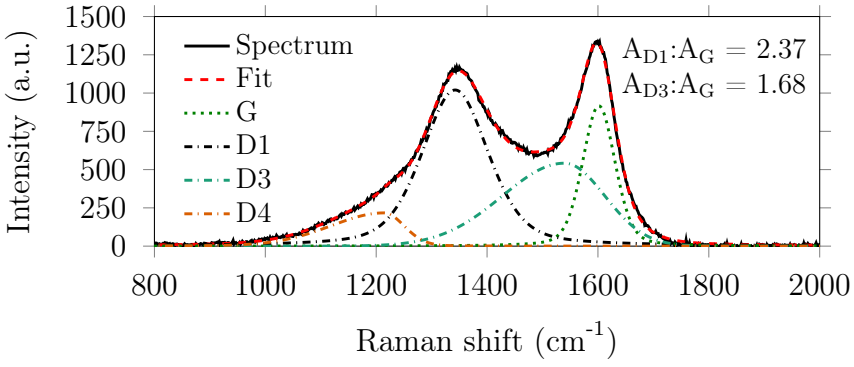

(b)

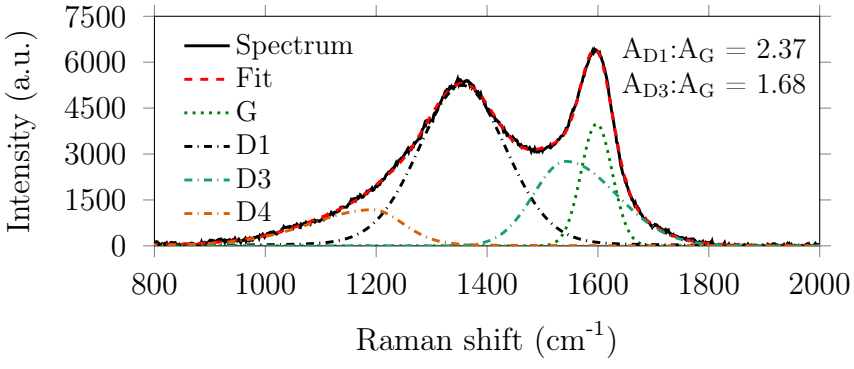

(c)

Figure 5.12: Baseline corrected Raman spectra with fitted G, D1, D3, and D4 bands Raman spectra of carbon black (a), 2.0L Diesel (b) and 1.0L GDI (c). The goodness of fit χ^2 is 2.98, 2.97, and 2.97 respectively.

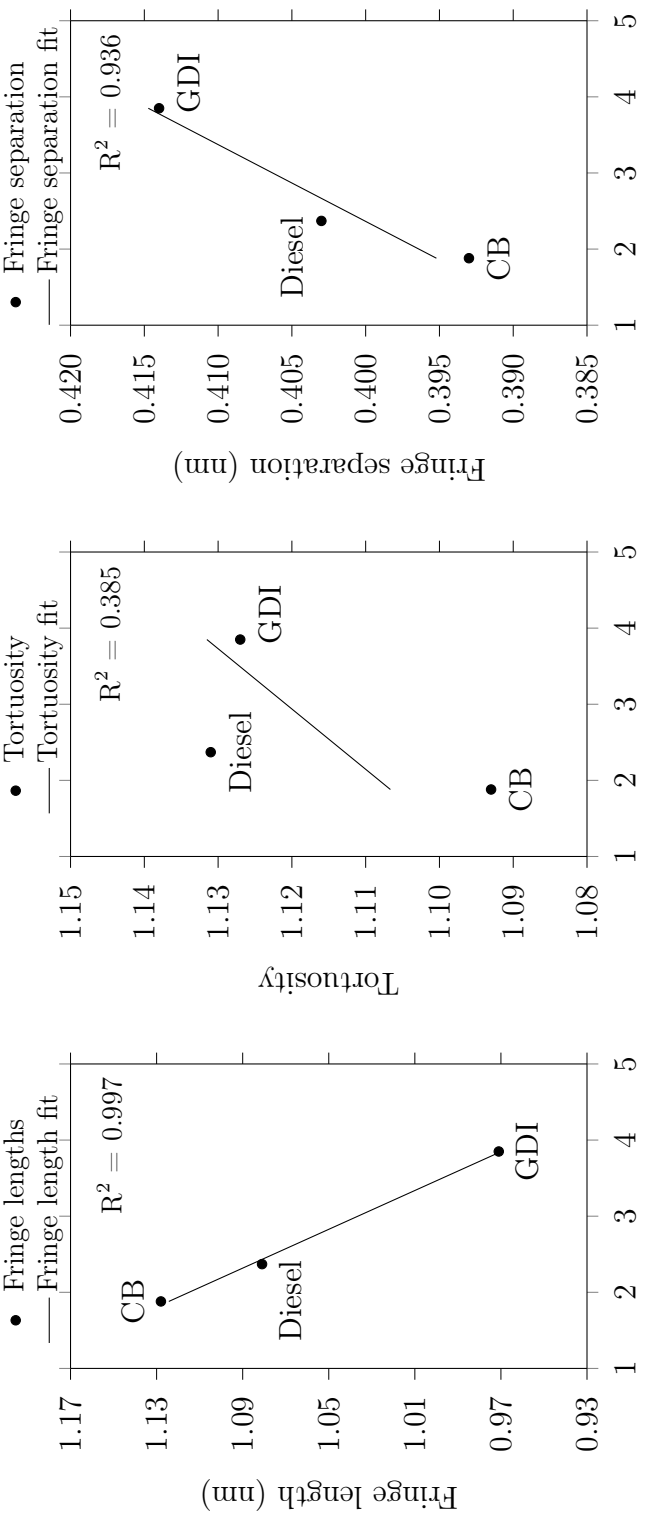

Figure 5.13: Correlation of A_{D1}:A_G ratio from Raman spectroscopy with fringe length and separation (a) and with fringe tortuosity (b) from fringe analysis for carbon black (CB), 2.0L Diesel (Diesel), and 1.0L GDI (GDI).

5.5 Summary

Soot-in-oil samples from two GDI and two diesel engines have been comprehensively characterised along with one carbon black sample. The findings suggest that soot-in-oil levels in GDI engines can be comparable to those of diesel engines. The same applies to the agglomerate and primary size distributions. However, the particle nanostructure can differ significantly from traditional core-shell particles, with some entirely amorphous particles being observed. This could imply a different interaction with the lubricating oil and subsequently altered wear behaviour of GDI soot. In particular, the work has led to the following conclusions:

- The soot content in the 1.0L GDI oil samples was assessed by TGA. A linear trend model was fitted, showing a deposition rate of 0.96 wt% per 15 000 km with a standard deviation of 0.08 wt%. The model is in agreement with linear deposition rate models for diesel engines. Thus, it is suggested that soot in the lubricating oil is of similar importance for GDI engines.
- HRTEM images show a common core-shell nanostructure among all samples. While the diesel samples only diverge slightly from the highly ordered carbon black, the GDI samples show a greater diversity in structure types. Entirely amorphous particles were observed, with some exhibiting crystalline regions. Subsequent EDX analysis suggested additives of lubricant oil and wear materials as the source of these embedded phases. In contrast to previous studies, no decomposition under the electron beam was observed.
- Primary particles were subsequently measured as captured in the TEM images. A unimodal size distribution was observed, with a mode at 31 nm and mean of 30 nm.
- Analysis of agglomerate sizes was carried out by NTA and revealed an asymmetric distribution. The principal population was observed

with a modal value of 100 nm, with additional, smaller populations at 155 nm and 241 nm. While almost no particles were observed in the range of 350 nm to 400 nm, an additional population was found at 426 nm. However, particle numbers of this population were lower by three magnitudes compared to those in the range of 100 nm to 350 nm.

- Fringe analysis allowed for quantification of differences between particles with similar graphitic nanostructure. The fringe length varied depending on the type of soot, with GDI soot exhibiting the shortest fringes of 0.97 nm to 0.99 nm and longer fringes for diesel soot with 1.07 nm to 1.08 nm (9.7 %) as well as carbon black with 1.13 nm (15.1 %). Fringe tortuosity was similar among the engine soot samples with 1.12 to 1.13, but was lower for carbon black by 3.3 % (1.09). Fringe separation showed a continuous trend between samples: Carbon black exhibited the closest layers (0.39 nm), diesel soot in the mid range (0.40 nm to 0.41 nm), and GDI soot the largest separation (0.41 nm to 0.42 nm).
- The quantitative reliability of fringe analysis was assessed using a larger number of fringes, of up to 4000. The highest fluctuations in the cumulative moving average of both the fringe length and the tortuosity can be observed below a total number of 500 fringes, with further jumps up to 2000 fringes. The fringe metrics mostly converge when reaching 3000 fringes. It is recommended that 4000 fringes should be used as a threshold to ensure a stabilised window of roughly 1000 fringes prior to the data point used.
- Using this criterion, the three soot types were again compared quantitatively. The findings confirmed that GDI soot sample was most distinctively different from the other two samples. While the diesel soot sample shares some similarity with the carbon black in terms of fringe length, differences in fringe tortuosity can be appreciated.
- Assessment of the sample preparation on the quality of Raman spectra showed a three-fold reduction of fluorescence when increasing the dilution ratio from $1 : 2 \cdot 10^3$ to $1 : 7.5 \cdot 10^4$. However, further increases

in dilution ratio above this point did not yield significant reductions in fluorescence.

- Fitting of the obtained Raman spectra with a four-band approach, excluding the contribution from the D2 band, gave acceptable goodness of fit ($\chi^2 < 3$). The A_{D1}:A_G values were 1.88 for carbon black, 2.37 for 2.0L Diesel soot and 3.85 for 1.0L GDI soot, suggesting 1.0L GDI soot was the most structurally disordered sample. The A_{D3}:A_G values showed a similar trend with 0.84 for carbon black, 1.68 for 2.0L Diesel soot and 1.85 for 1.0L GDI soot, indicating the highest fraction of amorphous carbon in 1.0L GDI soot.
- A strong linear correlation was found between A_{D1}:A_G and the fringe length as well as the fringe separation with R^2 values of 0.997 and 0.936 respectively, validating the fringe analysis. However, fringe tortuosity showed no linear correlation, but rather a difference between carbon black and soot from internal combustion engines could be identified.

6 Processing Methods for DMS Measurements

The comparison of soot-in-oil samples from diesel and GDI engines in Chapter 5 provided valuable information for a variety of applications. Moreover, a range of techniques was used, and their applicability could be assessed. However, regulatory measurements of particulate emissions are taken directly from the exhaust gas. The PMP prescribes the use of PNCs, while electrical mobility measurements are often used in research contexts. The latter is used here in the form of a DMS. The resulting PSDs provide more information compared to the PN metric from PNCs; however, additional processing is required for the comparison of these measurements with the regulatory metrics.

In this chapter, different approaches to the required data processing are investigated, particularly in the light of upcoming regulation changes towards sub-23 nm measurements. A reduced set of operating conditions is used as example cases. Two approaches are outlined: fitting of lognormal functions and applying digital filtering functions. For the latter, some functions for sub-23 nm exist, but none of these had been designed for the proposed counting efficiencies of future regulations. Hence, a new equation is proposed. The discrete size spectra are analysed for the example cases before both processing methods are applied to the data and compared.

Parts of this chapter have previously been published as an SAE Technical Paper that was presented at the SAE 2021 WCX Digital Summit:

S.A. Pfau, E. Haffner-Staton, and A. La Rocca. Measurement of sub-23 nm particulate emissions from GDI engines: A comparison of processing methods. SAE Technical Paper 2021-01-0626, 2021, DOI 10.4271/2021-01-0626.

6.1 Reduced Set of Engine Operating Conditions

For the initial assessment of the various data processing methods, a smaller set of operating conditions from the test matrix derived in Section 3.4.1 was used. Four test conditions (TCs) were investigated: two load levels of fast-idle and 40 Nm, each load tested at two speeds of 1750 rpm and 2250 rpm. The engine was conditioned as outlined in Section 3.4.3. Measurements with the DMS500 were acquired over a shorter window of 60 s. Additional measurements of key engine metrics are reported in Table 6.1. The temperature of the coolant liquid and lubricating oil were regulated by the ECU. While the coolant temperature remained similar for the test cases, the temperature of the oil increased marginally for increased engine speed and load. The CoV is considerably higher for the fast-idle conditions partly due to the greater influence of cycle-to-cycle variations of the pumping and friction losses compared to the net IMEP. Further insight into the combustion quality can be gathered using the LNV [270]. This property indicates the lowest single gross IMEP value over all cycles normalised by the overall mean gross IMEP. While this metric is high for both 40 Nm conditions with over 90 %, the fast-idle conditions exhibit misfires (i.e. LNV < 0). However, these events only occur in 1 % and 0.17 % of cycles for the 1750 rpm and 2250 rpm fast-idle conditions, respectively. The reason for this poor combustion performance could lie in a suboptimal ECU calibration for these conditions. A full assessment of the repeatability was conducted in Section 3.4.3.

Table 6.1: Summary of measured engine metrics for the TCs.

Parameter	Unit	TC1	TC2	TC3	TC4
Speed	rpm	1750	1750	2250	2250
Load	Nm	1.0	39.6	0.7	40.2
Net IMEP	bar	0.88	5.87	0.88	6.01
CoV	%	42.9	2.8	23.8	1.1
LNV	%	−5.54	91.9	−4.32	97.0
CA50	°CA aTDC	14.3	5.9	15.3	6.3
T-Coolant	°C	89.0	89.2	89.7	89.4
T-Oil	°C	84.9	87.1	85.5	88.6
T-Intake	°C	33.8	31.7	32.4	31.3
T-Exhaust	°C	353	449	384	493

6.2 Approaches to Data Processing

The Cambustion DMS500 software provides two analysis options for the electrometer currents: linear approximation and lognormal parametrisation. The relevant calculations are detailed by Symonds et al. [152]. In the following, a brief overview is outlined.

The linear approximation uses the following equation with discrete size bins:

$$i = A \cdot s + e \tag{6.1}$$

where:

- i is the electrometer ring current vector;
- A is the instrument transfer function matrix;
- s is the particle size spectrum vector;
- e is the error term.

The best spectrum is the solution with minimal error. Calculations are performed by least-squares minimisation with linear regularisation and a non-negative constraint for the error term. The software uses 38 size bins ranging from 4.87 nm to 1000 nm. The instrument transfer function—or inversion matrix—is generally provided by the manufacturer for each instrument. It is determined based on empirical calibration data as well as underlying models of charging and classification.

The lognormal parametrisation uses continuous lognormal functions for k_{lm} modes instead of discrete size bins:

$$i = \sum_{j=1}^{k_{lm}} \left(n_{p,j} \cdot A_j \cdot l(\mu_{d,j}, \sigma_{g,j}) \right) + e \tag{6.2}$$

where:

k_{lm} is the number of modes in the distribution;

l is the lognormal function;

μ_d is the count median diameter;

σ_g is the geometric standard deviation.

The function can be solved with a Bayesian statistical algorithm, as further outlined in [152]. The same instrument transfer function as for the linear approximation can be used here. However, this approach would also allow for different transfer functions to be used for the respective modes. For internal combustion engines, two modes are widely used and are included in the software: nucleation mode and accumulation mode. The algorithm uses a probability map to classify a peak, based on the lognormal function parameters count median diameter (CMD) and geometric standard deviation (GSD), i.e. peak position and width. Combined with the particle number concentration, these metrics provide a brief description of the distribution and enable easy comparisons between different operating conditions.

It should be noted that the spectral measurements are commonly presented as size spectral density $\mathrm{d}\, n_p \,/\, \mathrm{d} \log d_p$. This normalises the concentrations by bin size and simplifies the comparison between measurements of different instruments with possibly different spectral resolution. The total particle number (TPN) for a such expressed discrete distribution can be obtained from the respective function of a continuous spectrum:

$$\begin{aligned} N_p &= \int_{d_{p1}}^{d_{p2}} \frac{\mathrm{d}\, n_p}{\mathrm{d} \log(d_p)} \, \mathrm{d} \log(d_p) \\ \Rightarrow N_p &= \sum_{d_{p1}}^{d_{p2}} \frac{\mathrm{d}\, n_p}{\mathrm{d} \log(d_p)} \, \Delta \log(d_p) \end{aligned} \tag{6.3}$$

where:

N_p is the total particle number ($\#/\mathrm{cm}^3$);

n_p is the particle size concentration ($\#/\mathrm{cm}^3$).

For logarithmically spaced size classes:

$$d_p \rightarrow d_p \cdot 10, \; \Delta \log_{10}(d_p) = 1 \tag{6.4}$$

The DMS500 has 16 evenly logarithmically spaced size classes per decade, thus:

$$\Delta \log(d_p) = \frac{1}{16} \tag{6.5}$$

With Equation 6.5 in Equation 6.3 follows for the TPN:

$$N_p = \frac{1}{16} \sum_{d_{p1}}^{d_{p2}} \frac{\mathrm{d}\, n_p}{\mathrm{d} \log(d_p)} \tag{6.6}$$

A frequently used metric for size distributions that can also be employed after filtering is the geometric mean diameter (GMD). The use of a geometric

mean is preferable to using an arithmetic mean due to the logarithmic spacing of the size classes and the lower sensitivity to outliers. The GMD can be calculated as:

$$\overline{d}_{p,g} = \left(\prod_{j=1}^{k_{sc}} (d_{p,j})^{n_{p,j}} \right)^{1/\left(\sum_{j=1}^{k_{sc}} n_{p,j}\right)} \tag{6.7}$$

where:

$\overline{d}_{p,g}$ is the particle geometric mean diameter;

k_{sc} is the number of size classes;

Despite the lack of a VPR, DMS500 measurements were found to be similar to PMP compliant measurements if only the accumulation mode is considered [7]. This step is considered as a "software" VPR as the nucleation mode with its volatile fraction is removed [271]. However, an accurate representation of the data with a lognormal fit is not necessarily guaranteed. Limiting factors can be the shape of the underlying PSD as well as the boundary conditions of the probability map.

An alternative approach to processing the data by lognormal fitting can be found in applying size filtration functions digitally to the linear approximation spectrum as part of the data post-processing. Instead of attempting to resolve the PSD with a series of distinct modes, digital filtration functions impose specified counting efficiencies. This processing step mimics the prescribed counting efficiencies of CPCs as outlined in the PMP. Rather than discarding volatile species using a nucleation mode, the filtration functions gradually reduce the extent to which particulate counts are included for smaller size classes. This method was first proposed by Felix Leach [272]. The function was based on the structure of a Wiebe function, a zero-dimensional or energy balance model for the mass fraction burned of an engine:

$$x_b(\theta) = 1 - \exp\left[-a \left(\frac{\theta - \theta_0}{\Delta\theta} \right)^{m+1} \right] \tag{6.8}$$

The modified function with the implemented PMP counting efficiencies (i.e. $d_{50} = 23\,\text{nm}$ and $d_{90} = 41\,\text{nm}$) was described as:

$$f_e(d_p) = \begin{cases} 1 - \exp\left[-3.54\left(\frac{d_p - 14}{40}\right)^{1.09}\right] & \text{for } d_p \geq 14 \\ 0 & \text{for } d_p < 14 \end{cases} \tag{6.9}$$

where:

f_e is the counting efficiency function;

d_p is the particle diameter (nm).

This filter is in the following referred to as 'Filter A'. As part of the initial proposal of the function, digital filtering was observed to deliver more representative results than using the accumulation mode only [272]. The method was then successfully also used in subsequent studies by Leach et al. [210, 273, 274]. As outlined in Section 2.5.3, future emissions regulations—which are currently being developed—are set to include solid particulates below 23 nm, prompting a series of research projects in this area. As part of one of these, the PEMs4Nano program, a report was published in 2017 proposing lower counting efficiencies of $d_{50} = 10\,\text{nm}$ and $d_{90} = 15\,\text{nm}$ in combination with additional changes [189]. Due to the absence of a VPR in the established DMS500 setup, the validity of nucleation mode particle measurements is limited due to the possibility of volatile artefacts. However, given the availability of data collected with this equipment, Leach et al. [275] proposed two alternative counting efficiency functions in 2019. The first function was based on $d_{50} = 10\,\text{nm}$ and $d_{90} = 23\,\text{nm}$ which were used in JRC and PMP research activities leading up to 2018 [184]:

$$f_e(d_p) = \begin{cases} 1 - \exp\left[-3.8\left(\frac{d_p - 4}{30.7}\right)^{1.04}\right] & \text{for } d_p \geq 4 \\ 0 & \text{for } d_p < 4 \end{cases} \tag{6.10}$$

The second function facilitates the proposed counting efficiencies of the mentioned PEMs4Nano report [189], i.e. $d_{50} = 10\,\text{nm}$ and $d_{90} = 15\,\text{nm}$:

$$f_e(d_p) = \begin{cases} 1 - \exp\left[-4\left(\frac{d_p - 4}{14.7}\right)^{1.96}\right] & \text{for } d_p \geq 4 \\ 0 & \text{for } d_p < 4 \end{cases} \tag{6.11}$$

The two new functions were applied to data sets that had been processed previously with the PMP inspired function. The counted PN increased by ca. 10 % to 20 % for lower loads with naturally aspirated engine operation, while PN increases of ca. 30 % to 70 % were found for boosted operation with part load and higher loads [275]. It was noted that the second function (i.e. Equation 6.11) generally counted 9 % higher PN compared to the first function (i.e. Equation 6.10).

Throughout early- to mid-2020, proposals for a new measurement protocol have been discussed in meetings of the UNECE [193, 194] and relevant reports [195]. This protocol includes lowered counting efficiencies of $d_{65} = 10\,\text{nm}$ and $d_{90} > 15\,\text{nm}$ (as described in Section 2.5.3). Moreover, the proposed margin for the detection efficiency at 10 nm is ±15 %. This is an increase to the previous ±12 % at 23 nm (i.e. d_{50}) of the PMP. As this proposal differs noticeably at the lower threshold, a new function is here proposed:

$$f_e(d_p) = \begin{cases} 1 - \exp\left[-5\left(\frac{d_p - 5}{20}\right)^{1.12}\right] & \text{for } d_p \geq 5 \\ 0 & \text{for } d_p < 5 \end{cases} \tag{6.12}$$

This equation is designed based on the shape of Filter A, having previously yielded data comparable to the PMP, as well as the counting efficiency curves presented in the UN/ECE meeting [193]. The newly proposed filter is visualized in Figure 6.1 as 'Filter C' alongside the aforementioned Filter A and the filter from Equation 6.11 as 'Filter B'. The inverse exponential shape of Filter C facilitates the increased counting efficiency of 65 % at

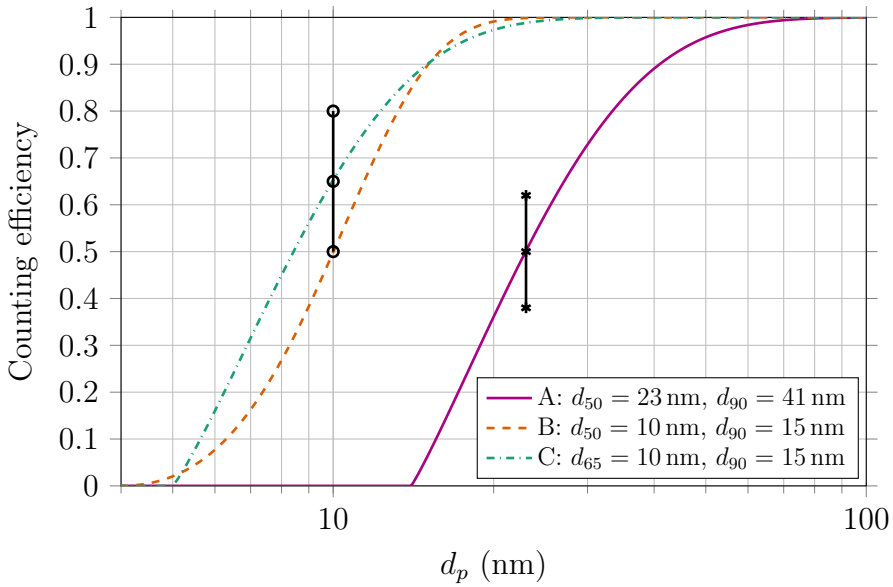

Figure 6.1: Comparison of the counting efficiencies of the digital filtering functions Filter A, Filter B, and Filter C. Annotated are the tolerance ranges of d_{50} for PMP SPN23 (—*—) and d_{65} for the proposed PMP SPN10 (—o—).

10 nm, compared to 50 % of Filter B with an S-shape. Integration of the filter efficiency curve areas reveals that the change from Filter B to Filter C results in a counting efficiency increase of 6.7 % for particles below 23 nm. From Figure 6.1 it can further be noted that even Filter A includes particles below 23 nm to a small extent. However, the cumulative counting of particles in this size range with Filter A represents only 18 % of the cumulative counting efficiency with Filter C.

6.3 Discrete Size Spectra

Henceforth, the discrete size spectrum as obtained by linear approximation is referred to as the (raw) PSD. The PSDs for all operating conditions are shown as time series plots in the left columns of Figures 6.2 and 6.3.

For the higher load-level of TC2 and TC4, two separate peaks can be observed in the respective PSD. The first mode ranges predominantly from 5 nm to 20 nm with a peak at 8.5 nm and 5.5 nm for TC2 and TC4, respectively. The second mode includes mostly particles between 80 nm and 200 nm for TC2 and 70 nm to 600 nm for TC4, with the peak for both at ca. 180 nm. The particle concentration of the first mode is similar for both TCs with $3.59 \cdot 10^5$ #/cm^3 and $3.90 \cdot 10^5$ #/cm^3 for TC2 and TC4, respectively. However, the second mode is considerably more pronounced for TC4 with $1.23 \cdot 10^5$ #/cm^3 compared to $2.59 \cdot 10^4$ #/cm^3. The lower mode appears to be relatively stable over the 60 s measurement window with respect to size position and particle concentration for both TCs. The higher mode exhibits more variability in its width of particle sizes as well as concentrations.

In contrast, the PSDs for the fast-idle conditions TC1 and TC3 exhibit a unimodal shape. The particle concentration of the PSD peak is noticeably higher than for the higher load TCs by one order of magnitude, with peaks of $2.51 \cdot 10^6$ #/cm^3 and $1.53 \cdot 10^6$ #/cm^3 for TC1 and TC3, respectively. Moreover, the position of these peaks is at marginally higher particle sizes with 10 nm and 11.5 nm for the two respective TCs. For TC3, a distinct drop in concentration around 50 nm can be observed which is consistent over the measurement window. A more gradual shift towards larger particle sizes can be observed in the time-series plot for TC1. However, the size distribution also exhibits some degree of variability in terms of particle concentration.

6.4 Lognormal Fittings

Two lognormal functions were fitted for all four TCs, one each for the nucleation and the accumulation mode (i.e. NM and AM). The obtained fits are plotted along with the raw PSDs and presented in the right columns of Figures 6.2 and 6.3. In addition, the GMDs for the lognormal fits and the linear approximation are presented in Table 6.2. For the fast-idle conditions TC1 and TC3, the fitting of two separate modes is not beneficial due to

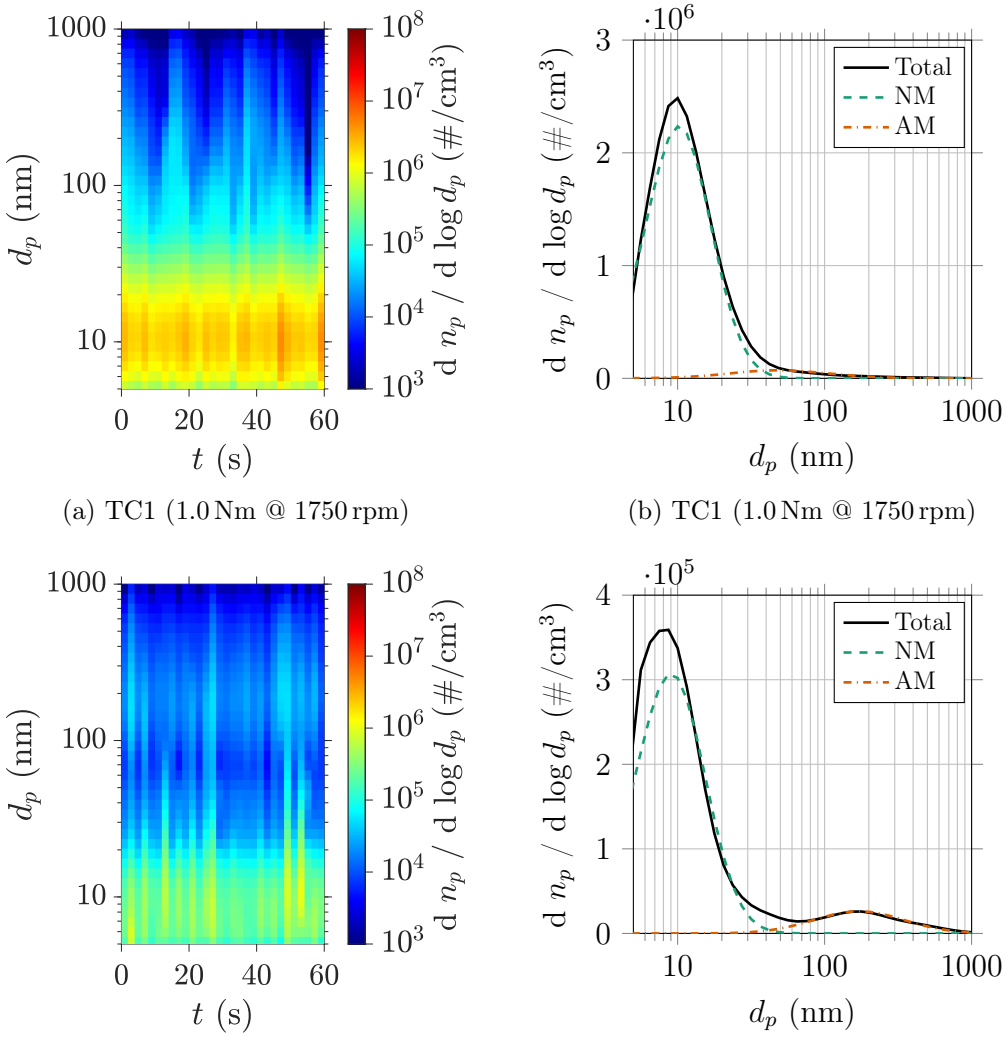

(a) TC1 (1.0 Nm @ 1750 rpm)

(b) TC1 (1.0 Nm @ 1750 rpm)

(c) TC2 (39.6 Nm @ 1750 rpm)

(d) TC2 (39.6 Nm @ 1750 rpm)

Figure 6.2: Contour plots of discrete linear approximation over measurement period (a,c) and overlay plots of averaged discrete linear approximation (Total) with lognormal fitted nucleation mode (NM) and accumulation mode (AM) (b,d) for TC1 and TC2.

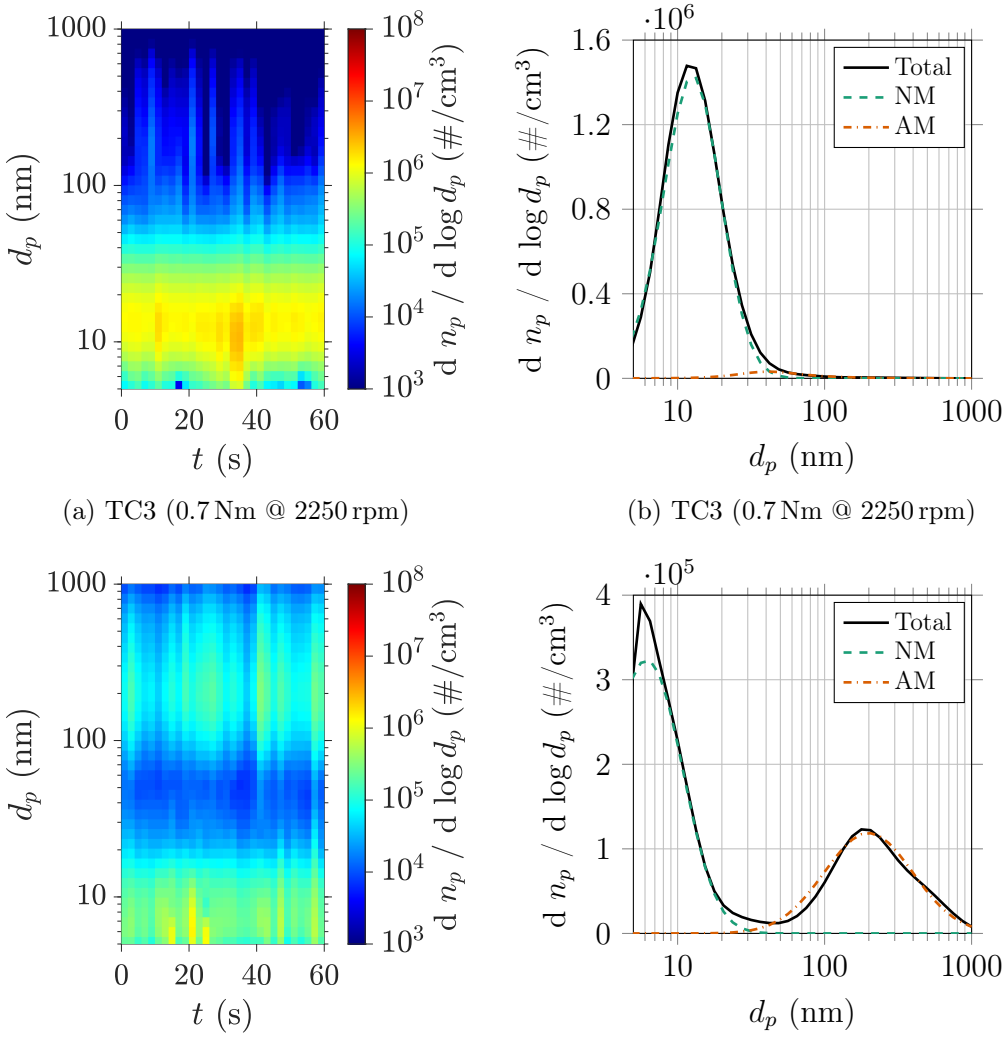

(a) TC3 (0.7 Nm @ 2250 rpm)

(b) TC3 (0.7 Nm @ 2250 rpm)

(c) TC4 (40.2 Nm @ 2250 rpm)

(d) TC4 (40.2 Nm @ 2250 rpm)

Figure 6.3: Contour plots of discrete linear approximation over measurement period (a,c) and overlay plots of averaged discrete linear approximation (Total) with lognormal fitted nucleation mode (NM) and accumulation mode (AM) (b,d) for TC3 and TC4.

Table 6.2: GMDs for the nucleation mode (NM) and the accumulation mode (AM) lognormal fits as well as the discrete linear approximation for the four TCs.

	GMD (nm)			
Processing method	TC1	TC2	TC3	TC4
Lognormal Fit (NM)	10.5	9.7	12.4	7.9
Discrete Lin. Approx.	11.6	12.8	13.0	26.2
Lognormal Fit (AM)	49.4	168.5	46.7	195.3

their unimodal PSDs. This is further supported by the close alignment of the GMD of their nucleation mode (NM) fit with the linear approximation GMD; these differ by only 1.1 nm for TC1 and 0.6 nm for TC3. However, no appreciable accumulation mode can be observed in the PSDs and thus the accumulation mode (AM) fits are not meaningful. For the higher load TC2 and TC4, the NM fits do not match the PSDs as good as for the fast-idle conditions; the peak concentrations are below the PSD mode concentrations and the positions are marginally shifted. Due to the second mode in the size spectra, the GMDs for the linear approximations become less meaningful. The AM fits become useful in this case. For TC2, the AM fit closely matches the linear approximation for particle sizes above 80 nm. The peak position of the AM fit for TC4 is similarly well aligned; however, the fit distribution is wider than the mode in the raw PSD.

6.5 Digital Filtering Functions

Subsequently, three filters were applied to the raw PSDs of the four TCs: Filter A, Filter B, and Filter C. The results are displayed in Figure 6.4. The filtered PSDs closely match the raw PSDs above the d_{90} of the respective filter, 41 nm for Filter A and 15 nm for both Filter B and Filter C. Below this point, the filtering effect becomes apparent. Filter A removes the

concentration of particles below 20 nm most noticeably, as intended for the filter modelling the regulations of the current PMP. For TC1 and TC3 the single-mode is shifted in its position from under 10 nm to just over 20 nm. The particle concentration of the mode peak is reduced by more than an order of magnitude. The concentration of the mode at 8 nm for TC2 is reduced to the same level as the larger particle size mode at above 100 nm. Moreover, its position is shifted to just above 20 nm as for TC1 and TC3. Due to the lower particle mode position at below 6 nm for the PSD of TC4, the change to this mode is more considerable. The mode is removed as such, and the particle concentrations below 50 nm only form a trailing end of the second mode just below 200 nm.

The lowered counting efficiency setpoints of Filter B and Filter C change the filtration effect on the PSD shape. The single mode in TC1 and TC3 is shifted to 12 nm for Filter B and to 10.5 nm for Filter C. The flattened mode in TC2 remains as a peak with Filter B and Filter C. Similarly, the mode for TC4 is only reduced in concentration and shifted, rather than being cut off at around 12 nm. The difference between the PSDs obtained from Filter B and Filter C becomes larger the lower the mode position. The change with the newly proposed filter is small for TC3, with a mode position at 12 nm. However, an increase in the mode peak concentration of almost 50 % can be observed for TC4, with a mode position below 6 nm. Further insight into the differences between the filtration models and processing methods can be obtained by comparing the respective TPN (see Table 6.3), the PN fraction of sub-23 nm particulates (see Table 6.4), and the GMD (see Table 6.5).

As to be expected, the TPN continuously increases when moving from AM lognormal fit to Filter A, Filter B, and Filter C. The most noticeable differences can be observed for the fast-idle load conditions TC1 and TC3 which only contain a smaller particle size mode. For these, the processing with Filter A yields an almost 2.5x increase in TPN for TC1 and more than fivefold increase for TC3, compared to the AM lognormal fits. The change from Filter A to Filter B again increases the TPN, by a factor of

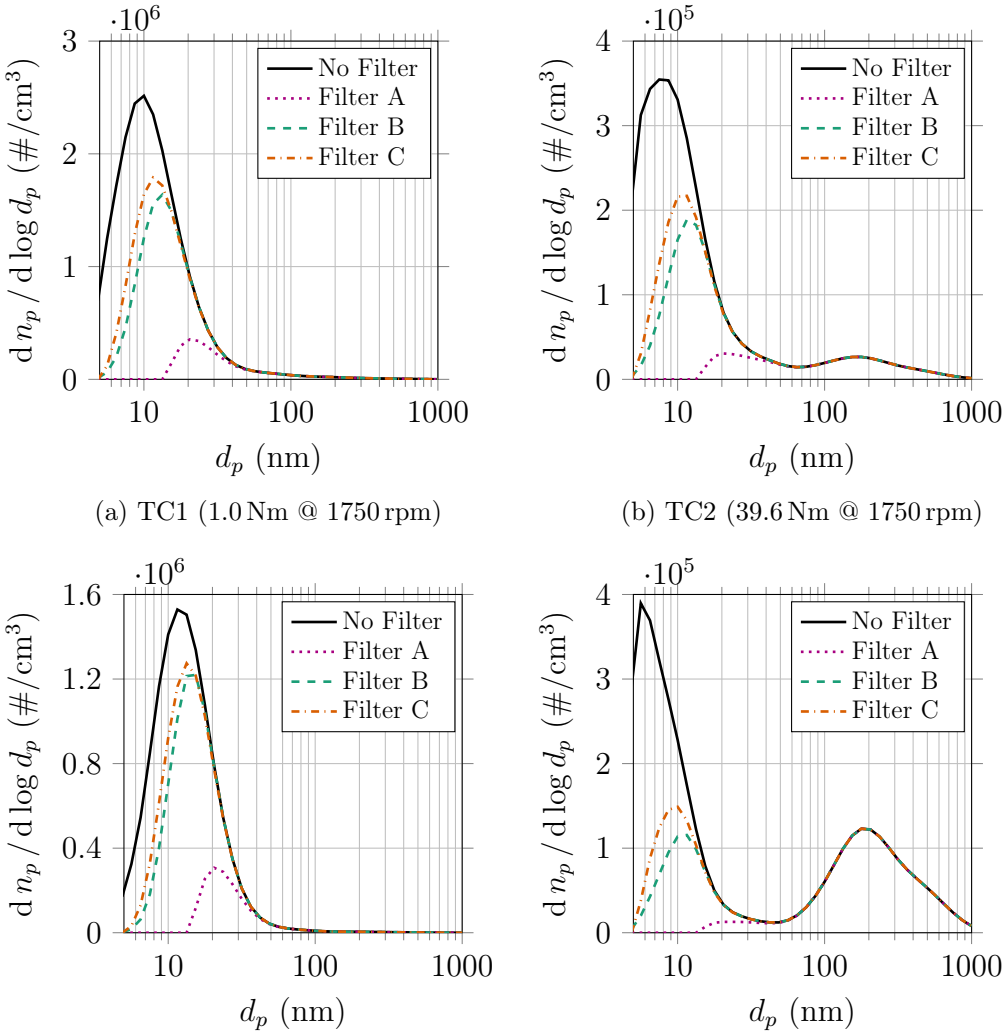

(a) TC1 (1.0 Nm @ 1750 rpm)

(b) TC2 (39.6 Nm @ 1750 rpm)

(c) TC3 (0.7 Nm @ 2250 rpm)

(d) TC4 (40.2 Nm @ 2250 rpm)

Figure 6.4: Overlay plots of the averaged discrete linear approximations with applied filters for each of the four TCs. Filter A: $d_{50} = 23\,\text{nm}$, $d_{90} = 41\,\text{nm}$. Filter B: $d_{50} = 10\,\text{nm}$, $d_{90} = 15\,\text{nm}$. Filter C: $d_{65} = 10\,\text{nm}$, $d_{90} = 15\,\text{nm}$.

just below 5. Applying the newly proposed Filter C leads to an increase of more than 10 % as compared to Filter B. Despite the significant increases in TPN, even with Filter C, the filtered PN is only 64 % and 73 % of the linear approximation PN for TC1 and TC3, respectively. These observed increases in TPN can be largely attributed to including a higher fraction of sub-23 nm particles. The lognormal AM contains 15 % and 11 % of such particulates for TC1 and TC3, respectively. With Filter A the sub-23 nm fraction is 32 % and 40 % for TC1 and TC3, respectively. The fraction increases with Filter B to 81 % and 82 % for the two respective filters. Filter C further increases the fraction of sub-23 nm particulates for these two TCs by up to 3 %. In contrast, the fraction of such particulates in the raw PSDs is 89 % and 88 % for TC1 and TC3, respectively. With higher fractions of smaller particles in the PSD, the GMD also decreases. The GMD for the lognormal AM fit is just below 50 nm for both TCs and almost halves with the subsequent steps to Filter A and Filter B. Applying Filter C further reduces the GMD by a smaller amount, from 15.7 nm to 14.5 nm for TC1 and from 15.8 nm to 15.0 nm for TC3.

The changes with different processing methods manifest differently for TC2 and TC4 due to the overall lower level of particulate concentrations and the presence of an accumulation type particle mode in the PSDs. For TC2, the TPN increases by 67 % with Filter A compared to the lognormal AM fit and triple with the subsequent application of Filter B. Filter C elevates the TPN by a further 17 % but still reduces the TPN to 58 % of the value of the discrete linear approximation. These differences are smaller than for TC1 and TC3, yet these are comparable to an extent. The reason for this similarity is the relatively small magnitude of the accumulation type mode in the PSD of TC2. Consequently, different observations are to be expected for TC4 with a more pronounced accumulation type mode. The TPN as obtained with the lognormal AM fit and with Filter A are within 0.3 %. Applying Filter B only increases the TPN 50 % as compared to multifold increases for the other TCs. However, Filter C still yields an increase of

9 % above Filter B. The fraction of sub-23 nm particles is considerably lower with almost no such particles for the AM fit and Filter A. The fraction for Filter B and Filter C is 33 % and 40 %, respectively. This is half that of the respective fractions observed for TC1 and TC3. The GMD is higher for both TC2 and TC4 across most processing methods. For the raw PSD of TC2, the GMD is similar to TC1 and TC3 with 12.8 nm; however, it is more than double for TC4 with 26.2 nm. Likewise, the GMD for TC2 with Filter B and Filter C is above those of TC1 and TC3, by a margin of ca. 5 nm and 7 nm, respectively. Only for Filter A and the AM lognormal fit, the difference becomes up to three-fold. In contrast, the GMD for TC4 is four-fold or above compared to the GMDs of the fast-idle load conditions TC1 and TC3. For Filter A and the lognormal AM fit, the difference is even up to seven-fold.

Analysis of this data indicates that the influence of the processing method is most pronounced if the PSD contains both a nucleation type mode of particulates below 20 nm and an accumulation type mode of particles above 70 nm. In such cases, the newly proposed Filter C can shift the GMD by up to 15 nm. However, for any PSD with a pronounced nucleation type mode, the proposed filter increases the TPN by 10 % to 17 %.

Table 6.3: TPN emissions for the four TCs with different processing methods.

	TPN (#/cm^3)			
Processing method	TC1	TC2	TC3	TC4
Lognormal fit (NM)	$1.28 \cdot 10^6$	$1.72 \cdot 10^5$	$7.29 \cdot 10^5$	$1.46 \cdot 10^5$
Lognormal fit (AM)	$6.20 \cdot 10^4$	$2.01 \cdot 10^4$	$1.95 \cdot 10^4$	$8.92 \cdot 10^4$
A: $d_{50} = 23\,\text{nm}$, $d_{90} = 41\,\text{nm}$	$1.54 \cdot 10^5$	$3.36 \cdot 10^4$	$1.06 \cdot 10^5$	$8.94 \cdot 10^4$
B: $d_{50} = 10\,\text{nm}$, $d_{90} = 15\,\text{nm}$	$7.42 \cdot 10^5$	$1.03 \cdot 10^5$	$5.07 \cdot 10^5$	$1.34 \cdot 10^5$
C: $d_{65} = 10\,\text{nm}$, $d_{90} = 15\,\text{nm}$	$8.50 \cdot 10^5$	$1.20 \cdot 10^5$	$5.59 \cdot 10^5$	$1.47 \cdot 10^5$
Discrete lin. approx.	$1.32 \cdot 10^6$	$2.06 \cdot 10^5$	$7.61 \cdot 10^5$	$2.35 \cdot 10^5$

Table 6.4: Fraction of sub-23 nm particulates of the TPN emissions for the four TCs with different processing methods.

	Sub-23 nm fraction			
Processing method	TC1	TC2	TC3	TC4
Lognormal fit (NM)	94 %	96 %	90 %	99 %
Lognormal fit (AM)	15 %	0.2 %	11 %	0.1 %
A: $d_{50} = 23\,\text{nm}$, $d_{90} = 41\,\text{nm}$	32 %	13 %	40 %	2 %
B: $d_{50} = 10\,\text{nm}$, $d_{90} = 15\,\text{nm}$	81 %	69 %	82 %	33 %
C: $d_{65} = 10\,\text{nm}$, $d_{90} = 15\,\text{nm}$	84 %	73 %	84 %	40 %
Discrete lin. approx.	89 %	84 %	88 %	62 %

Table 6.5: Comparison of the number weighted GMDs for different processing methods for the four TCs.

	GMD (nm)			
Processing method	TC1	TC2	TC3	TC4
Lognormal fit (NM)	10.5	9.7	12.4	7.9
Lognormal fit (AM)	49.4	168.5	46.7	195.3
A: $d_{50} = 23\,\text{nm}$, $d_{90} = 41\,\text{nm}$	33.2	82.6	26.8	187.2
B: $d_{50} = 10\,\text{nm}$, $d_{90} = 15\,\text{nm}$	15.7	22.5	15.8	73.3
C: $d_{65} = 10\,\text{nm}$, $d_{90} = 15\,\text{nm}$	14.5	19.7	15.0	59.7
Discrete lin. approx.	11.6	12.8	13.0	26.2

6.6 Summary

Four operating conditions of a 1.0 l GDI engine were analysed for PN emissions. Different processing methods were applied to the obtained PSDs: discrete linear approximation, lognormal function fitting, and counting efficiency modelling by digital filtering functions. The results highly depended on the shape of the PSD in terms of number and position of modes. Moreover, a new filtering function was proposed based on the previously established method of filtering functions. The function was designed to match the proposed counting efficiencies for an updated PMP, covering sub-23 nm solid particulates. The following conclusions can be drawn from this investigation:

- Lognormal fitting for the accumulation mode can be closely matched with a digital filtering function. The approach is useful for the scope of the previous PMP with the exclusion of sub-23 nm particles. However, with proposed changes, particles of the corresponding nucleation type mode are included. Thus, this approach is not viable any longer.
- The new Filter C increases the TPN by 10 % to 17 % compared to the previous sub-23 nm Filter B. The PN levels are elevated even further if compared to the PMP-type Filter A; by 64 % to 452 %.
- The fraction of sub-23 nm particles is increased by 2 % to 7 % with the new Filter C compared to the previous Filter B. Compared to the PMP-type Filter A, the increase is 38 % to 60 %.
- The GMD is shifted towards smaller particle sizes by 0.8 nm to 13.6 nm with the new Filter C compared to the previous sub-23 nm Filter B and by 11.8 nm to 127.5 nm compared to the PMP-type Filter A.

7 DMS Measurements with a Catalytic Stripper

The filtering function for SPN10 that was proposed in Chapter 6 covers a part of the proposed changes to particulate measurement regulations, i.e. the lowered counting efficiency size thresholds. Another requirement of the updated PMP with the upcoming regulations is the removal of volatiles with a catalytic stripper. Consequently, measurements are acquired in this chapter using the DMS equipped with such a device. The impact of the catalytic stripper on the particulate number levels is investigated, and the different sub-23 nm filtering functions are assessed.

A matrix of operating conditions, that was derived from the WLTC in Chapter 3, is used to investigate the influence of operating conditions on the particulate emissions. Moreover, possible implications of the change from SPN23 to SPN10 are discussed, as simulated by configurations with and without catalytic stripper and the respective filtering functions. Finally, an analysis of possible correlations of the particulate emissions with the engine metrics is conducted.

Parts of this chapter have been included in a manuscript that was submitted for publication:

S.A. Pfau, E. Haffner-Staton, A. La Rocca, and M.W. Fay. Investigating the effect of volatiles on sub-23 nm particle number measurements for a downsized GDI engine with a catalytic stripper and digital filtering. Manuscript submitted for publication, 2021.

7.1 Digital Filtering Functions for Sub-23 nm Measurements

Different mathematical functions have been proposed for the sub-23 nm processing of DMS particulate emission measurements. However, none of the studies on this matter to date have used a sample gas conditioning setup that prevents volatile artefacts, i.e. catalytic strippers have not been used. To determine the extent to which digital filtering functions can affect the particulate number, two operating conditions are investigated in detail in the following. These conditions are fast-idle at 1250 rpm and 40 Nm load at 2250 rpm, representing the low and high endpoints of the test matrix selected in Section 3.4.1. As discussed in the following sections, these conditions exhibit considerable differences in their TPN and GMD (cf. Section 7.3), indicating underlying differences in their PSDs.

The PSDs acquired with a catalytic stripper and applied particle loss correction are presented in the left column of Figure 7.1. The entire PSD of the fast-idle condition only exhibits a single particulate mode at around 10 nm with a sharp drop towards smaller particle sizes and a more extended reduction in particle number concentration towards larger diameters. In contrast, the PSD of the second condition, 2250 rpm with 40 Nm brake torque, exhibits a bi-modal shape: a narrow mode at 10 nm and a broader mode at around 133 nm. The peak of the lower mode is roughly five times above the height of the second mode, with $2.65 \cdot 10^5$ #/cm^3 and $5.27 \cdot 10^4$ #/cm^3, respectively. The overall particulate number concentration level of the second condition is roughly three orders of magnitude below that of the first condition, with a mode peak of $5.03 \cdot 10^8$ #/cm^3. Moreover, the 95 % confidence intervals for the respective particle size classes are noticeably larger for the second condition, especially for sub-23 nm sizes. The higher variability could be explained by the lower particle concentration level itself. Despite the reduced sampling frequency of 0.5 Hz and prolonged sampling

duration of 180 s, a larger noise for measurements was experienced, leading to the larger confidence intervals.

Two of filters for sub-23 nm PN measurements have been applied. The functions of these filters are described in Section 6.2 as Equation 6.11 and Equation 6.12, proposed by Leach et al. [275] and in Section 6.2 of this thesis, respectively. In line with the use in Chapter 6, the functions are in the following labelled as 'Filter B' and 'Filter C', respectively. As both functions incorporate d_{90} counting efficiencies at 15 nm, their counting efficiencies are approaching 100 % at 20 nm. For better detail, enlarged views of both PSDs below 20 nm are shown in the right column of Figure 7.1. For the fast-idle 1250 rpm condition, the 95 % confidence intervals overlap marginally down to 13 nm. Below this point, apparent differences between the two filters can be observed beyond the certainty level of the confidence intervals. Consequently, the SPN10 changes from $1.73 \cdot 10^8$ #/cm^3 with Filter B to $1.93 \cdot 10^8$ #/cm^3 as Filter C is applied, i.e. an increase of 11.2 %. This change stems from a 15.6 % increase in sub-23 nm emissions. The SPN10 difference is less pronounced for the 2250 rpm condition with 40 Nm, increasing only 1.5 %. The change in the sub-23 nm emissions is 22.1 % with partially overlapping 95 % confidence intervals. Due to the second mode at 133 nm and a consequently higher fraction of larger particles, the overall particulate number is less affected.

These observations highlight that the identified sub-23 nm emissions can vary considerably between different filtering functions. However, the implications on the SPN10 metrics highly depend on the overall shape of the PSD. While the change would be less pronounced for bi-modal distributions, a distribution with a single mode at below 23 nm could see higher differences to its SPN10. In other words, the higher the fraction of sub-23 nm particulates of the overall emissions—i.e. the lower the GMD—the greater the effect of changing from Filter B to Filter C. This confirms the findings of measurements without a catalytic stripper in Chapter 6.

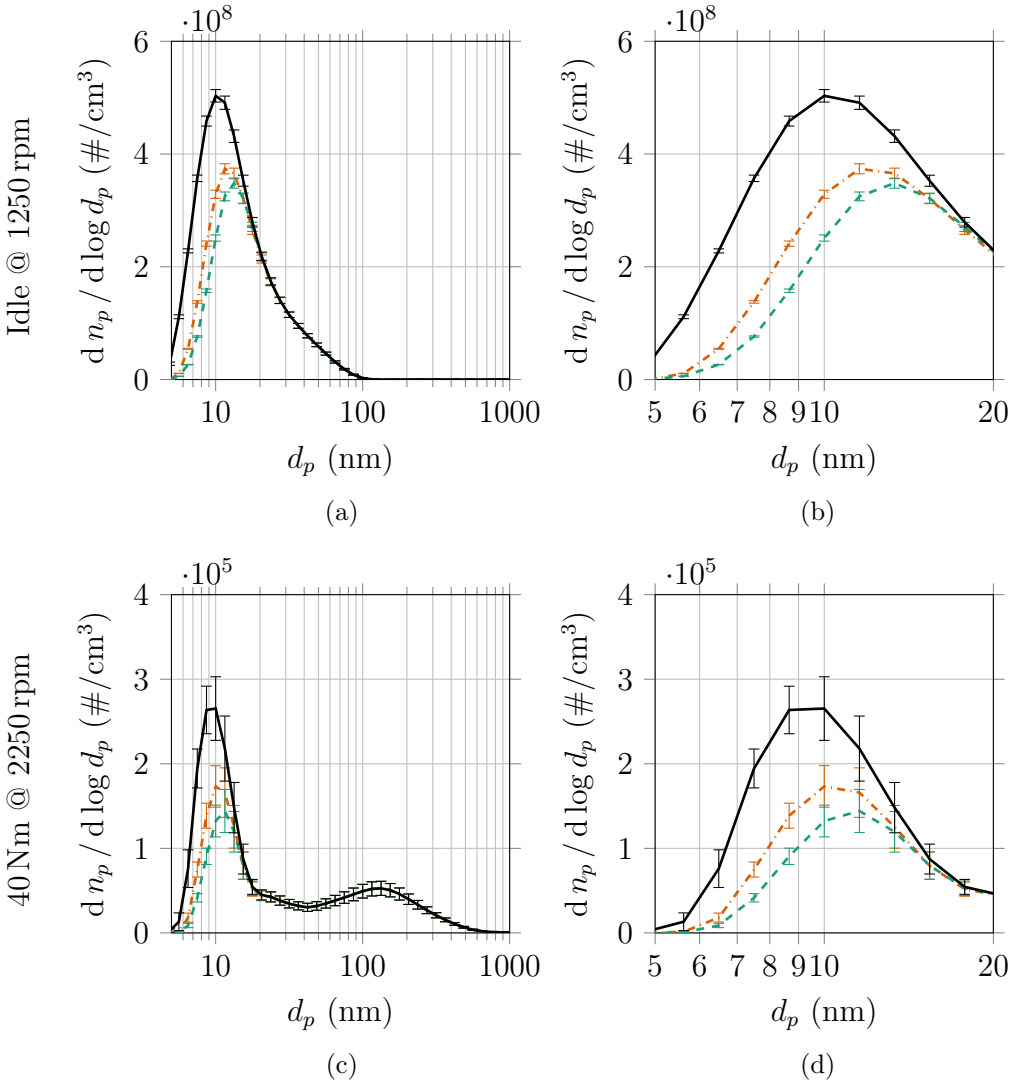

Figure 7.1: PSDs for DMS measurements with the catalytic stripper and applied particle loss correction. No filter (——). Filter B (- - -): $d_{50} = 10\,\mathrm{nm}$, $d_{90} = 15\,\mathrm{nm}$. Filter C (-·-·-): $d_{65} = 10\,\mathrm{nm}$, $d_{90} = 15\,\mathrm{nm}$. Error bars indicate 95 % confidence intervals.

7.2 Impact of the Catalytic Stripper

Another area of interest is the effect of the catalytic stripper on the observed PSD, as this is included in the proposals for an updated PMP SPN10 measurements [195]. The initial PMP encompasses an evaporation tube and counting efficiencies of d_{50} at 23 nm and d_{90} at 41 nm, modelled for DMS measurements with the digital filtering function Equation 6.9 ('Filter A' or 'F-A' for short) from Section 6.2. The proposed update for SPN10 is here modelled by applying Equation 6.12 (Filter C or 'F-C' for short) for the counting efficiencies d_{65} at 10 nm and d_{90} at 15 nm, combined with using the catalytic stripper. Firstly, the impact of using a catalytic stripper is assessed. The same two conditions as in Section 7.1 are also used here, with the unfiltered but loss-corrected PSDs with and without catalytic stripper shown in the left column of Figure 7.2. For the fast-idle 1250 rpm condition, an overall reduction in particle concentrations can be observed. The mode remains roughly at the same size position; however, its peak is reduced from $7.37 \cdot 10^8$ #/cm^3 to $5.03 \cdot 10^8$ #/cm^3. In contrast, the PSD for the 40 Nm condition at 2250 rpm without catalytic stripper exhibits a nucleation-type mode that is not only reduced in its concentration level from $4.46 \cdot 10^5$ #/cm^3 to $2.65 \cdot 10^5$ #/cm^3 but also shifted in its peak position from 6.5 nm to 10 nm by implementing sampling with a catalytic stripper. While particle number concentrations for the 1250 rpm condition are reduced in the 30 nm to 100 nm range as well, there does not appear to be a similar reduction for the 2250 rpm condition. The 95 % confidence intervals as included in the plots generally appear to be reduced with the inclusion of the catalytic stripper in the measurement setup. This is most noticeable for the 2250 rpm condition.

The right column of Figure 7.2 shows the PSDs with the respective digital filtering functions applied. For the PSDs acquired with the catalytic stripper, implementing the SPN10-inspired digital filtering function (Equation 6.12) leads to a reduction in the concentration level of the mode around 10 nm with

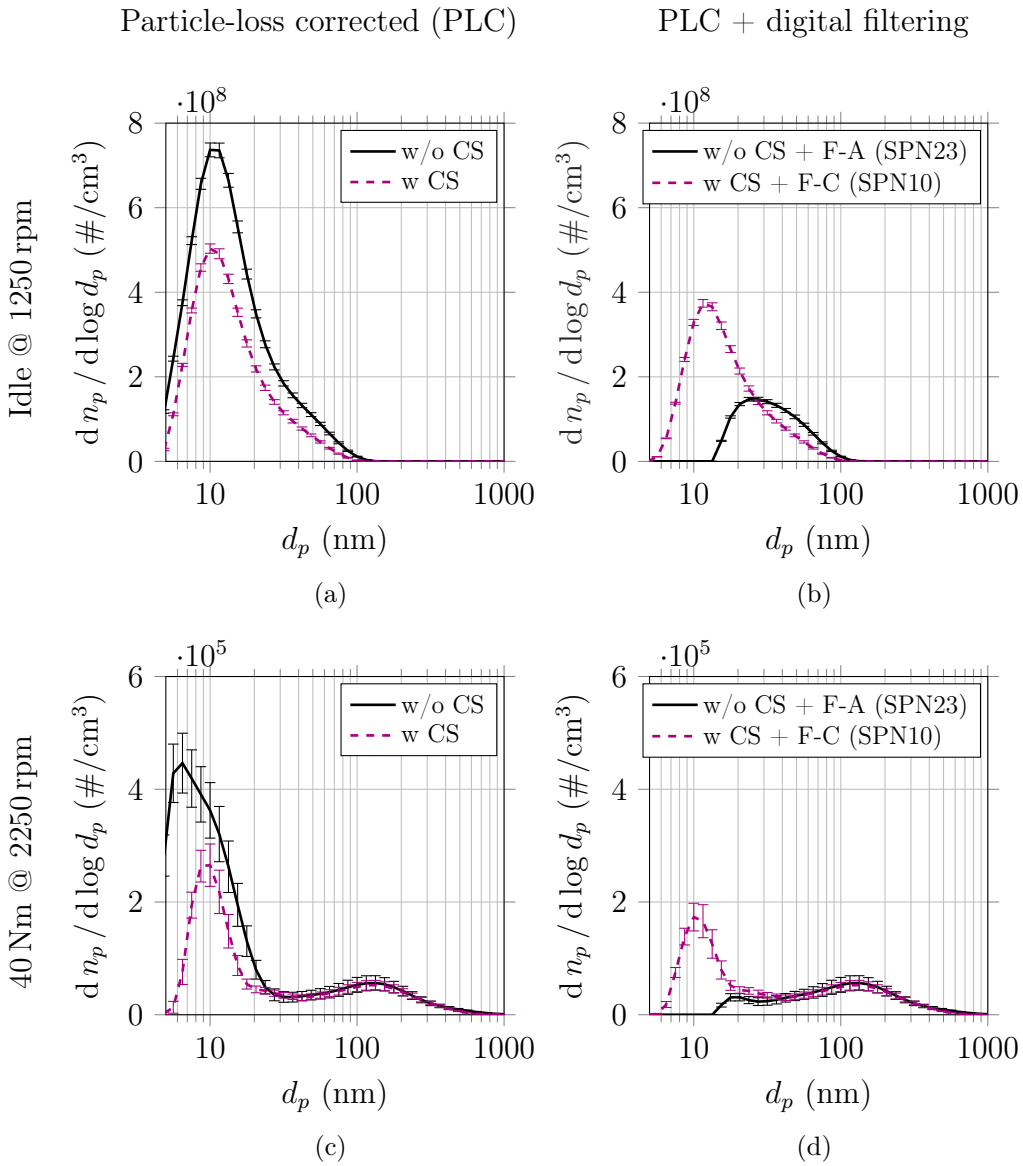

Figure 7.2: PSDs for DMS measurements with and without catalytic stripper (CS). In the left column, PSDs are particle-loss corrected only, while digital filtering functions were additionally applied to the same PSDs in the right column. F-A and F-C refer to Equation 6.9 for SPN23 and Equation 6.12 for SPN10, respectively. Error bars indicate 95 % confidence intervals.

a slight shift towards larger particle sizes as described in Section 7.1. The implications of filtering the PSD acquired without catalytic stripper for SPN23 is more profound, as it effectively removes most of the observed particles below 23 nm. As is apparent from Equation 6.9, no particles below 14 nm are counted. For the fast-idle condition at 1250 rpm (w/o CS), this processing step reduces the height of the mode by 80 %—from $7.37 \cdot 10^8$ #/cm^3 to $1.47 \cdot 10^8$ #/cm^3—and shifts the peak position from 10 nm to around 25 nm. Moreover, the shape of the mode is broader compared to the sharper peak in the unfiltered PSD. For the 2250 rpm condition (w/o CS), the SPN23 filtering removes the lower mode entirely. The peak at 133 nm becomes the predominant mode with an extended shoulder towards smaller particle sizes. Only a minimal peak remains at just at around 20 nm with a particle concentration of 55 % of the larger particle size mode: $3.10 \cdot 10^4$ #/cm^3 compared to $5.64 \cdot 10^4$ #/cm^3.

This detailed analysis of the PSD for two test conditions highlights the considerable implications that a change from SPN23 to SPN10 could have. The catalytic stripper appeared to be effective in reducing the variability. Sub-23 nm particles were more prominently represented in the particulate number with the lowered counting efficiency positions. A more extensive test matrix is discussed in the following to better understand the influence of operating conditions.

7.3 Particulate Emissions across the Test Matrix

A set of operating conditions was derived from a simulation of the WLTC with the available engine and a chosen reference vehicle (cf. Section 3.4.1). This test matrix comprises five speeds from 1250 rpm to 2250 rpm in equal steps, with three load steps of fast-idle, 20 Nm, and 40 Nm brake torque. The particulate emissions measurements for some conditions showed overall high

levels of noise, despite reduced sampling frequency of 0.5 Hz and prolonged sampling duration of 180 s. Specifically, this variability limitation was observed for the conditions at 2000 rpm and 2250 rpm with 20 Nm (w+w/o CS) and with 40 Nm (w CS), as well as 1750 rpm with 20 Nm (w CS). The following discussion of results uses the TPN as a metric for unfiltered data and denotes the particle count for the data sets with digital filtering functions as SPN10 and SPN23 due to ease of use and clarity. However, it should be pointed out that these differ from the metrics described in the PMP with similar terminology, denoted as #/km emitted from vehicles over a test cycle, rather than #/cm^3 measured here.

The contour plots of the various particulate number metrics exhibit an overall trend of high particulate number levels towards the fast-idle 1250 rpm condition (see Figure 7.3). The highest cumulative number can be observed for TPN (w/o CS) with $4.21 \cdot 10^8$ #/cm^3 and the lowest for SPN23 with $8.25 \cdot 10^7$ #/cm^3. The SPN10 at this point is $1.93 \cdot 10^8$ #/cm^3. The PN generally decreases for higher speeds and loads; however, some exceptions can be observed for the measurements without catalytic stripper. At the fast-idle condition at 2000 rpm, the PN is elevated when measurements are taken without the catalytic stripper. This can be seen in the (only) particle-loss corrected contour plot as a shoulder of the respective contour lines (see Figure 7.3a) and even more noticeable in the SPN23 plot as a distinct peak (see Figure 7.3b). The measurements at the fast-idle conditions could be influenced by an underlying issue with the combustion performance that likely stems from suboptimal calibration mapping for these conditions, as discussed in the following section.

Both TPN (w/o CS) and SPN23 increase for the highest two speeds with the highest load of 40 Nm. While not as noticeable for the two metrics derived from the measurements with the catalytic stripper, the lowest PN across the test matrix can be found at the 20 Nm load conditions at 2000 rpm and 2000 rpm for all four plots. The number of particulates generally increases when comparing SPN10 with SPN23, from as low as 27 % at 1250 rpm with

Figure 7.3: TPN by engine speed and load for DMS measurements with and without catalytic stripper (CS). Digital filtering with Equation 6.9 for SPN23 and Equation 6.12 for SPN10.

40 Nm up to an almost four-fold 390 % at 1750 rpm with 20 Nm. A decrease could only be observed for the fast-idle condition at 2000 rpm, with −73 %. The change is generally more pronounced for the fast-idle conditions with 182 % on average, compared to 162 % and 60 % for the 20 Nm and 40 Nm load conditions, respectively.

Additional information on the emitted particulates can be obtained from the GMD. This metric provides a more feasible way to summarise the size profile for larger data sets than comparing individual PSDs. In the following, the term GMD is used similar to TPN, while GMD10 and GMD23 are the corresponding metrics to SPN10 and SPN23, respectively, with the same processing approach.

Similarities can be observed between the contour plots for GMD (w CS), GMD10, and GMD23 (see Figure 7.4). The highest values for these three plots are located at the upper end of the test matrix in terms of speed and load. From there, the GMD decreases predominantly with engine load, while the effect of the engine speed on this metric is less clear. Overall, the level of the GMD23 is noticeably above the other GMD-metrics, as is apparent by the colour bar of the contour plot ranging from 0 nm to 80 nm rather than 0 nm to 40 nm as for the other plots. The largest size of 89.9 nm for GMD23 occurs at 2250 rpm with 40 Nm load, with the smallest size of 25.3 nm at fast-idle 2250 rpm. Similarly, the largest size for GMD10 occurs at 2000 rpm with 40 Nm load with 32 nm and the smallest size at fast-idle 2000 rpm with 13.7 nm.

The change in GMD derived from unfiltered to filtered PSDs is relatively homogeneous for measurements acquired with the catalytic stripper. No drastic changes in the shape of the contour plot can be observed but rather an average increase of 20 % from GMD (w CS) to GMD10. An entirely different observation can be made for the metrics derived from data acquired without catalytic stripper. The contour plot for GMD (w/o CS) exhibits high points at 1250 rpm with 40 Nm and fast-idle 2000 rpm with GMDs of 20.3 nm and 21 nm, respectively. The lowest points are at fast-idle 1500 rpm

Figure 7.4: GMD by engine speed and load for DMS measurements with and without catalytic stripper (CS). Digital filtering with Equation 6.9 for SPN23 and Equation 6.12 for SPN10.

and 2000 rpm with 40 Nm with GMDs of 9.2 nm and 11.5 nm, respectively. This observation could be interpreted as some volatile artefacts affecting the PSD shape. The noticeable shift in the contour plots would, in such a case, be the exclusion of said artefacts by the digital filtering, working as intended. Additional support for this hypothesis is the similarity between the GMD23 plot with the GMD (w CS) and GMD10 plots, i.e. those with assumed removal of volatiles. For the present test matrix, the shift from GMD23 to GMD10 effectively lowers the size thresholds, including particles of smaller diameters, without altering the underlying trends of speed and load. The measurements for the fast-idle conditions could be affected by an underlying combustion performance issue due to suboptimal calibration mapping, as discussed in the following section.

Information on the size distribution could also be presented as sub-23 nm fractions of the PN (see Figure 7.5). This alternative to the GMD metric reveals that most emitted particles for the assessed operating conditions fall in the size range below 23 nm. The overall range of sub-23 nm fractions is similar between measurements without and with the catalytic stripper with 52 % to 93 % and 58 % to 92 %, respectively. The SPN10 retains the majority of these particles and exhibits a range of 49 % to 88 % for this fraction. It should be noted that while the SPN23 removes most particles below 23 nm, still up to 35 % of particles included in this metric are smaller than 23 nm. The trends and changes with engine speed and load are similar to the observations made for the GMD metrics above. However, the representation as sub-23 nm fraction highlights the proportion of particles below 23 nm in the exhaust gas more comprehensibly.

7.4 Correlation with Engine Metrics

As the particulate emissions have now been characterised for the test matrix, additional engine metrics are presented in the following to gain further insight into the soot formation processes beyond the values of engine speed and

Figure 7.5: Fraction of sub-23 nm particles by engine speed and load for DMS measurements with and without catalytic stripper (CS). Digital filtering with Equation 6.9 for SPN23 and Equation 6.12 for SPN10.

load. Firstly, total unburned hydrocarbon (THC) emissions were measured. As any volatile species are derived from either the hydrocarbon fuel or some species of the lubricating oil formulation, this metric can be beneficial. The measured concentrations are displayed in Figure 7.6a as a methane-equivalent parts-per-million fraction. The highest THC concentration was observed for fast-idle at 1250 rpm with 4174 ppm, while the lowest value was recorded for 40 Nm load at 2000 rpm with 997 ppm. The contour plot for the investigated test matrix exhibits similarities in the underlying distribution shape to the plots for the particulate number emissions, measured both with and without the catalytic stripper (see Figure 7.3). However, the same does not apply to the different GMD plots. This suggests that while a higher THC level in the exhaust gas corresponds to an elevated PN level, this increase does not stem from a significantly higher fraction of volatile species or small particulates. The former would be noticeable by a drastic change in PN when the catalytic stripper gets used, and the latter would manifest as a corresponding drop in the GMD. Instead, the abundance of THCs promotes a high number of solid particulates. Notably, the PN spike at fast-idle 2000 rpm without catalytic stripper is not corresponding to a spike in THC. This would suggest that the species causing this spike are volatiles that are removable by the catalytic stripper but are not hydrocarbons detectable by the THC analyser.

The exhaust gas temperature increases relatively uniformly with both engine speed and load (see Figure 7.6b). The lowest temperature of 253 °C was observed at fast-idle 1250 rpm and the highest temperature was 510 °C at 2000 rpm with 40 Nm. For a diagonal half of the PN contour plots, the particulate levels increase similarly towards the fast-idle 1250 rpm condition as the exhaust temperature decreases. This could imply that less oxidation of soot occurs at these lower temperatures and thus PN levels are elevated. However, this effect cannot clearly be separated from other parameters and cannot be observed inversely for higher exhaust temperatures. While oxidation rates could theoretically be different for various particle sizes, no similarity between the exhaust temperature plot and the GMD maps can be identified.

The spark timing mainly changes with engine load and only to a minor degree with engine speed, being delayed for increases in both metrics (see Figure 7.6c). The earliest spark timing, 40 °CA bTDC, was set for the fast-idle condition at 2000 rpm, while the latest spark of 22 °CA bTDC was set at 1500 rpm with 40 Nm. Generally, particulate emissions are considered to decrease as the spark timing is moved from maximum brake torque: for advanced timings due to longer combustion duration and thus extended particle oxidation, and for delayed timings due to elevated exhaust gas temperatures promoting post-flame oxidation [199]. Several studies also observed higher PN emissions for advanced spark timings and attributed these to higher peak in-cylinder that promote nucleation and lower exhaust gas temperature [207, 223]. Despite clear patterns in the spark timings and exhaust gas temperatures, no clear trend with the measured PN and GMD distributions could be identified here.

An additional combustion metric is the position of 50 % MFB. The respective contour plot exhibits a more diverse shape (see Figure 7.7a). For the change from fast-idle to 20 Nm load, the MFB position advances for all speeds from a range of 13 °CA aTDC to 16 °CA aTDC to 3 °CA aTDC to 7 °CA aTDC. Faster speeds at fast-idle generally exhibit a later 50 % MFB by a few °CA. At 20 Nm and 40 Nm load, the 1500 rpm speed showed the latest MFB position, advancing for both increasing and decreasing speeds. Combined with the spark timing, the combustion is overall faster for higher loads compared to fast-idle conditions. The column-like shape in the MFB plot at 1500 rpm could be related to the lowered GMD and GMD10, observed at 1500 rpm when particulate emissions are measured with the catalytic stripper. However, the overall similarities between these plots are somewhat limited.

The engine performance can further be described by the LNV metric, as also discussed in Chapter 6. The calculated LNVs are presented in Table 7.1. Combustion performance is generally good for all conditions with applied brake torque, as the LNV is consistently above 90 %. In contrast, poor combustion performance can be observed for the fast-idle conditions. LNVs

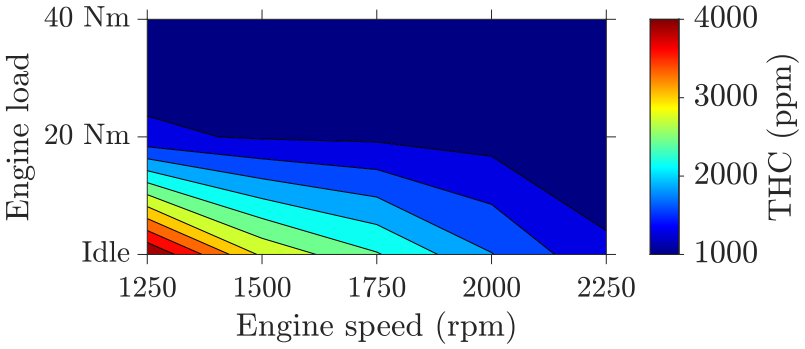

(a)

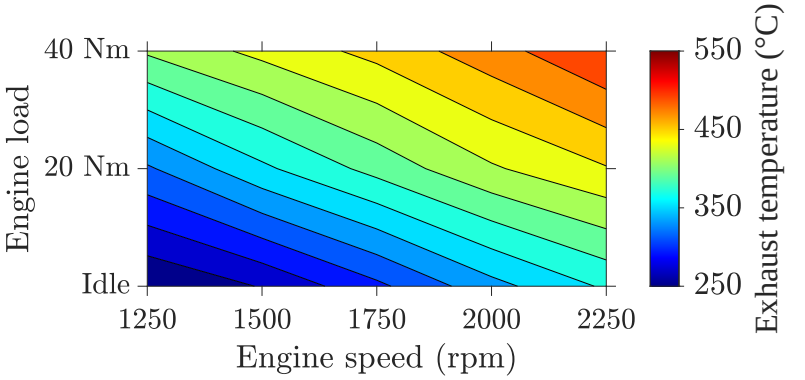

(b)

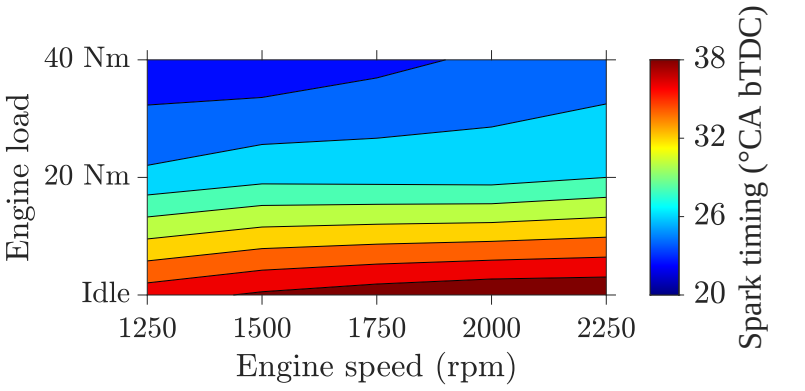

(c)

Figure 7.6: Engine metrics by engine speed and load: THC emissions (a), exhaust temperature (b), and spark timing (c).

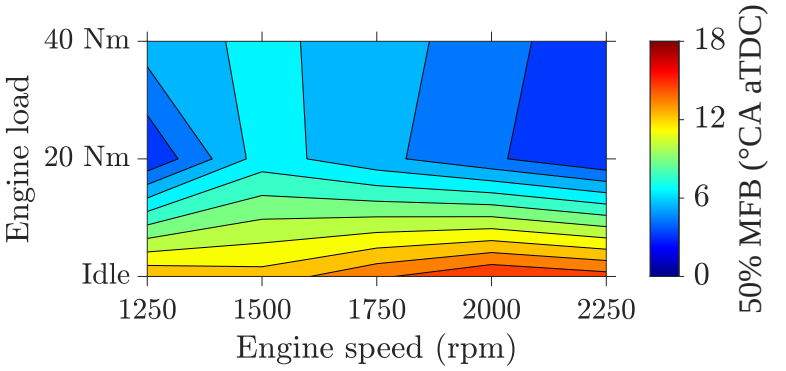

(a)

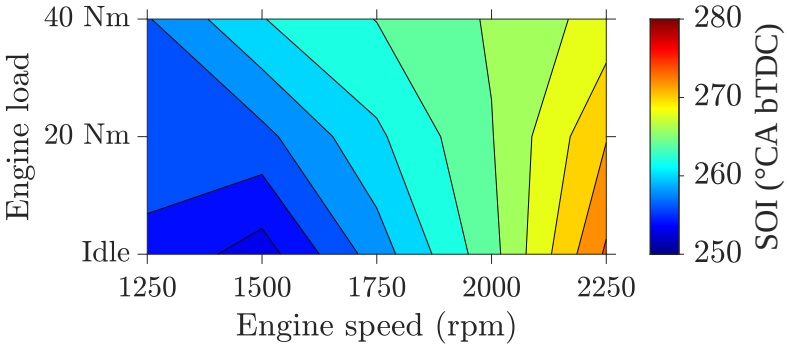

(b)

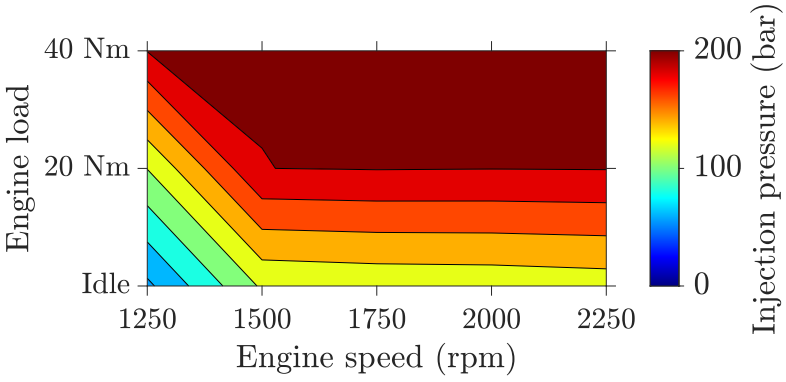

(c)

Figure 7.7: Engine metrics by engine speed and load: 50 % MFB position (a), SOI timing (b), and injection pressure (c).

Table 7.1: Lowest normalised values (LNVs) for the operating conditions of the test matrix.

	LNV				
Load	1250 rpm	1500 rpm	1750 rpm	2000 rpm	2250 rpm
40 Nm	96.1 %	92.1 %	94.5 %	95.1 %	95.5 %
20 Nm	95.4 %	91.9 %	90.2 %	94.8 %	93.6 %
Fast-idle	−5.38 %	16.1 %	1.71 %	−2.43 %	14.3 %

below 0 % indicate misfires, and values below 50 % are considered indistinguishable from misfires [270]. These undesired combustion events could be contributing to the elevated PN emissions observed at the fast-idle conditions and could explain the irregularities in the plots described above. A reason for this poor performance could be suboptimal calibration mapping for the fast-idle conditions. The combustion is delayed, as apparent from the MFB analysis above, and the spark timing is advanced, but perhaps not sufficiently far enough. Another consideration could be the valve overlap of 10 °CA (cf. Table 3.6). However, it is worth also mentioning the fraction of cycles that are affected by this. The fractions of cycles with a gross IMEP below 0 % and 50 % of the overall mean value are presented in Table 7.2. The highest fraction of affected cycles can be observed at 1250 rpm fast-idle with 2.3 % of cycles exhibiting a gross IMEP below 50 % of the mean. This corresponds to 14 cycles over the total of 600 recorded cycles. The lowest fraction of cycles can be observed at 1500 rpm with 0.17 %, corresponding to a single cycle.

Analysed metrics of the fuel injection system include the SOI timing and the injection pressure. The SOI generally was advanced with increasing engine speed (see Figure 7.7b). For 2000 rpm, the SOI mostly remained stable with increasing engine load, while the SOI was advanced with increasing load for speeds below this point and delayed for the 2000 rpm speed above. The earliest SOI of 274 °CA bTDC was at fast-idle 2000 rpm and the latest SOI of 252 °CA bTDC at fast-idle 1500 rpm. The injection pressure was set

Table 7.2: Fraction of cycles with gross IMEP below 0 % and 50 % of the mean value for the fast-idle conditions.

	Fraction of cycles				
Fast-idle	1250 rpm	1500 rpm	1750 rpm	2000 rpm	2250 rpm
IMEP < 0 %	1.0 %	0 %	0 %	0.17 %	0 %
IMEP < 50 %	2.3 %	0.17 %	0.67 %	1.0 %	1.3 %

at 200 bar for all conditions with 40 Nm load as well as the 20 Nm load conditions except at 1250 rpm, for which the injection pressure was 120 bar (see Figure 7.7c). The lowest injection pressure was 55 bar at fast-idle 1250 rpm. Among the other fast-idle conditions, the injection pressure was similar with a range of 123 bar to 130 bar. The combination of relatively late injection and low injection pressure could contribute to poorer mixing at the lower end of the test matrix and thus explain the elevated PN levels observed. High sensitivity on particulate emissions is usually attributed to the injection timing [213], with early injection risking increased fuel impingement and late injection causing insufficient mixing [214]. Elevated injection pressures can further aid the mixing process by dispersing the fuel in smaller droplets [57]. However, overall, there is again no apparent similarity between the SOI and injection pressure and the PN and GMD contour plots.

Of the six investigated engine metrics, the THC emissions provide the most convincing link to the measured particulate emissions, likely explaining the high emission levels towards the fast-idle condition at 1250 rpm. Other hypotheses could be developed based on the other metrics; however, the similarities between the respective contour plots are not unambiguous and provide little explanation of observed features such as the spike in emission levels without catalytic stripper at fast-idle 2000 rpm nor the trends in the GMD distribution.

7.5 Summary

Particulate emissions of a 1.0 l GDI engine were measured for a test matrix derived from a simulation of the WLTC, with a focus on city cycles. Measurements were conducted with a DMS that was operated with and without a catalytic stripper. Moreover, different digital filtering functions were applied to implement specified counting efficiencies, i.e. for SPN23 of the established PMP and SPN10 as per the latest regulatory proposals. The findings can be summarised as follows:

- An updated filtering function for SPN10 was applied to measurements acquired while using a catalytic stripper. The results showed an increase of up to 11.2 % compared to the closest previous sub-23 nm digital filtering function. However, this increase was highly dependent on the underlying PSD, with conditions of smaller GMD exhibiting a greater shift. These observations confirm the findings of a previous study in which the function was proposed based on DMS measurements without catalytic stripper.
- Directly comparing measurements with and without catalytic stripper revealed that the catalytic stripper noticeably reduced variability in sub-23 nm particle concentration measurements. A significant portion of particles in this size regime remained that can therefore be assumed to be non-volatile solid particles. The shift from SPN23 digital filtering without catalytic stripper to SPN10 digital filtering with catalytic stripper lead to a considerable difference in the resulting PSD.
- The measurements of the test matrix showed the highest PN emissions for fast-idle at 1250 rpm, regardless of using a catalytic stripper or the used digital filtering function. Specifically, the value doubled from SPN23 with $8.25 \cdot 10^7$ #/cm^3 to SPN10 of $1.93 \cdot 10^8$ #/cm^3. The number of particulates generally increased when comparing the SPN10 with the SPN23, from as low as 27 % at 1250 rpm with 40 Nm up to an almost four-fold 390 % at 1750 rpm with 20 Nm.

- Investigation of engine metrics revealed a similar trend between PN and THC emissions. The remaining included metrics, exhaust gas temperature, spark timing, 50 % MFB position, injection timing and pressure, could not conclusively explain the observed patterns in the PN and GMD measurements. However, analysis of the LNV revealed poor combustion performance to some extent for the fast-idle conditions. The occurrence of occasional misfires in these conditions could contribute to the elevated PN emissions and might explain the observed irregularities in the associated plots. A reason for this poor performance could be suboptimal calibration mapping for the fast-idle conditions.

8 TEM Analysis of Exhaust-Sampled Soot

Particulate emissions have been comprehensively characterised by electrical mobility measurements in Chapter 7. However, this approach of using equivalent diameters comes with the caveat that the obtained sizes are precisely that: equivalents. How close these equivalent diameters match the actual physical sizes depends not only on the size of the particulate itself but also the degree to which the particle structure is fractal and the chemical composition of the particles. Both can influence the electrical charge transferred to the particle and the resulting electrical mobility.

For an additional perspective on the emitted soot, TEM imaging of particulates sampled onto TEM grids is conducted in this chapter. Samples are acquired from three different operating conditions with the aim of linking soot features to specific engine conditions. The investigation covers the qualitative assessment of particulates, measurements of agglomerate sizes and primary particle diameters, and fringe analysis of graphitic nanostructures. A particular focus lies on the identification of particulates below 23 nm.

Parts of this chapter have been included in a manuscript that was submitted for publication:

S.A. Pfau, A. La Rocca, E. Haffner-Staton, and M.W. Fay. TEM investigation of soot from a GDI engine: Influence of operating conditions on nanostructure and morphology. Manuscript submitted for publication, 2021.

8.1 TEM Imaging of Soot Agglomerates

Soot was initially sampled on TEM grids by using a hot dilution in an ejector diluter. The dilution gas and the diluter were both heated to prevent condensation of the exhaust gas and enable capturing of solid particles without artefacts. An extended sampling duration of 40 min was required to achieve sufficient particle concentrations on the grid for TEM analysis. However, the concentrations remained relatively low. The sampling was conducted for three engine operating conditions: 1500 rpm fast-idle, 1500 rpm with 40 Nm brake torque, and 1750 rpm with 20 Nm brake torque. Selections of TEM images for the respective conditions are presented in Figures 8.1 to 8.3.

For the fast-idle condition at 1500 rpm, some large soot agglomerates with maximum skeleton dimensions of 940 nm to 1220 nm and fractal shapes can be observed (see Figures 8.1a to 8.1c). Primary particles cannot be clearly identified in Figure 8.1a as the aggregate appears to be covered in an additional layer, concealing the underlying structure. For Figures 8.1b and 8.1c, the primary particles measured on average 32 nm and 40 nm, respectively. Other agglomerates appeared less fractal in the two-dimensional images and measured only 438 nm to 534 nm by 246 nm to 418 nm in skeleton dimensions (see Figures 8.1d to 8.1f). Primary particles in Figure 8.1d appear relatively large, ranging from 31 nm to 64 nm with a mean around 52 nm. The mean diameters for Figures 8.1e and 8.1f are 38 nm and 40 nm, respectively.

Agglomerates similar to this second group of particulates can also be observed for the condition at 1500 rpm with 40 Nm brake torque (see Figures 8.2a to 8.2c). The agglomerates measure 329 nm to 380 nm by 171 nm to 231 nm, and all exhibit similar primary particle sizes of ca. 40 nm. An additional type of agglomerates can be observed that is generally smaller (see Figures 8.2d and 8.2e) and can consist of only a single string of particles (see Figure 8.2f). The maximum skeleton length of these particulates ranges from 109 nm to 157 nm. The primary particles are comparatively smaller, with a mean

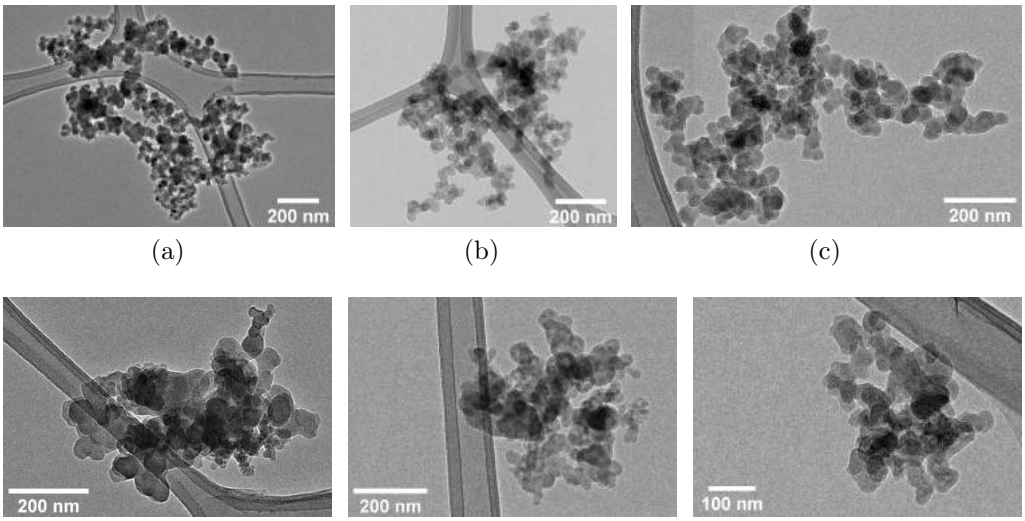

Figure 8.1: TEM images of thermophoretically collected soot after single-stage ejector dilution at 1500 rpm fast-idle.

diameter of around 21 nm for Figures 8.2d and 8.2e (range: 13 nm to 28 nm) and 32 nm for Figure 8.2f (range: 23 nm to 42 nm).

A group of particulates sampled at 1750 rpm with 20 Nm brake torque also exhibits maximum skeleton lengths of up to 360 nm (see Figures 8.3a to 8.3c). Contrary to similarly sized soot agglomerates of the other two conditions, the agglomerates here are less densely packed and exhibit single strings of primary particles. However, this observation could also be due to the two-dimensional projection of the TEM imaging that might not fully capture the three-dimensional shape of the particulates. The mean primary particle diameter for the three agglomerates shown in Figures 8.3a to 8.3c are 19 nm, 27 nm, and 26 nm, respectively. A second smaller group of particulates with maximum skeleton lengths of 205 nm to 212 nm can be observed (see Figures 8.3d to 8.3f). The primary particles in this second group exhibit mean diameters of 19 nm, 22 nm, and 24 nm, respectively.

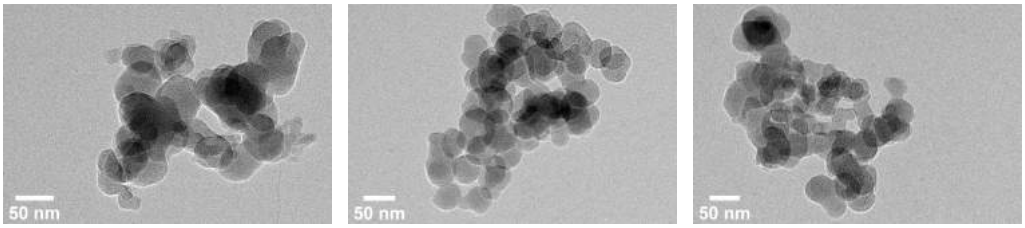

(a) (b) (c)

(d) (e) (f)

Figure 8.2: TEM images of thermophoretically collected soot after single-stage ejector dilution at 1500 rpm with 40 Nm brake torque.

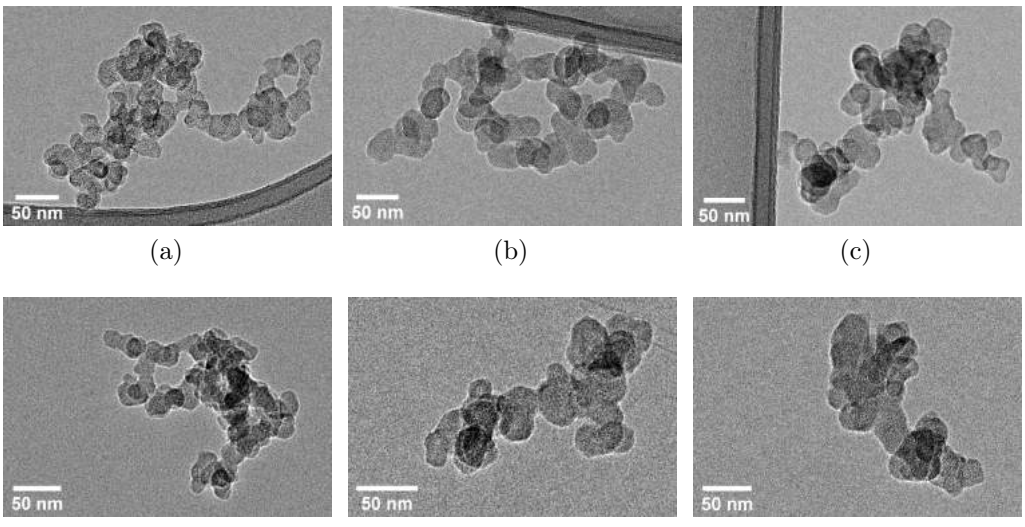

(a) (b) (c)

(d) (e) (f)

Figure 8.3: TEM images of thermophoretically collected soot after single-stage ejector dilution at 1750 rpm with 20 Nm brake torque.

Table 8.1: Summary of averaged primary particle sizes across the operating conditions.

Condition	Mean (nm)	Median (nm)	Number of particles
Fast-idle 1500 rpm	39.5	37.4	78
40 Nm @ 1500 rpm	34.6	36.1	76
20 Nm @ 1750 rpm	22.7	21.1	86

When comparing the three conditions, the soot particulates sampled at the 1500 rpm fast-idle condition exhibit the largest skeleton dimensions of agglomerates and the largest primary particle diameters. The type of agglomerates with the most extensive skeleton sizes above 1000 nm could not be observed for the grid sampled at 1500 rpm with 40 Nm brake torque. Moreover, the average primary particle diameter is almost 5 nm smaller (see Table 8.1). The soot sampled at 1750 rpm with 20 Nm brake torque comprises distinctly smaller agglomerates. Likewise, the average primary particle diameter is again lower by almost 12 nm compared to the 1500 rpm with 40 Nm brake torque condition. Only a limited number of comparable studies is available on primary particle sizes of exhaust sampled soot from GDI engines. Existing publications generally found a size range of 5 nm to 65 nm with modes from 10 nm to 22 nm [46, 47, 49]. Primary particles in the GDI soot-in-oil sample ranged from 20 nm to 90 nm with a mean at 36 nm [67]. The extracted soot aggregates from a comparable 1.0 l GDI engine analysed in Chapter 5 exhibited primary particles with sizes from 12 nm to 55 nm and a mean at 30 nm. For all primary particles measured here ($n = 240$), the sizes range from 13 nm to 65 nm, and the mean is 32 nm. The measurements for the exhaust soot match the findings for the soot-in-oil sample relatively closely. This confirms the findings of previous studies that the primary particle properties remain unaffected by the sample preparation.

The underlying data here is relatively small compared to more extensive studies such as [247]. However, as available studies linking operating con-

ditions and parameters of engines are scarce, an initial assessment of the engine metrics considering the discussion above is carried out. The primary particle sizes observed here decrease with increasing speed and load. While no comparable studies using GDI engines could be found, some works on diesel engines are available. Xu et al. [72] observed a reduction of 3 nm in primary particle diameter as the BMEP increased from 0.3 bar to 0.9 bar. This would correspond to a 5 Nm increase in brake torque for the GDI engine used here. Moreover, Lapuerta et al. [64] reported decreased primary particle size from ca. 26 nm to 15 nm as speed increased from 1400 rpm to 2400 rpm. It is interesting to note that the same trends can be observed, despite differences in values, across the different engine types.

To further investigate the mechanisms, the engine metrics as summarised in Table 8.2 can be considered. Of the few available studies that used GDI engines and assessed the influence of operating parameters, the injection timing is covered most frequently. Barone et al. [46] observed ca. 10 nm smaller primary particles if the fuel injection was delayed by 40 °CA. Seong et al. [276] reported a similar decrease in primary particle size by 9 nm for a more considerable fuel injection delay of 140 °CA. Here, the fuel was injected 9 °CA later for the fast-idle condition, compared to the other conditions, and the primary particles were the largest. However, this could be due to the changes in the other metrics. The fuel injection pressure was the lowest for the fast-idle condition too. Despite the fact that no comparable GDI studies were found, a study by Kook et al. [247] using a diesel engine found a ca. 6 nm decrease in primary particle size as the injection pressure increased from 70 bar to 160 bar. Another consideration could be the exhaust temperature.

A study by Lee and Zhu [277] on a diesel engine found a negatively parabolic correlation between exhaust gas temperature and primary particle size. For the sampling position between turbocharger and catalyst, a maximum diameter was observed at 300 °C, which decreased for deviations towards both lower and higher temperatures. Increased oxidation could, to some degree, explain the differences between the two conditions at 1500 rpm;

Table 8.2: Summary of engine metrics.

Parameter	Unit	Fast-idle 1500 rpm	40 Nm @ 1500 rpm	20 Nm @ 1750 rpm
CoV	%	11.1	0.8	1.1
Peak Temp.	°C	1507	1857	1758
Exh. Temp.	°C	282	443	397
CA50	°CA aTDC	12	7	6
SOI	°CA bTDC	253	262	262
Inj. Pressure	bar	123	200	200
Inj. Duration	µs	301	1117	547

however, it does not fully explain the considerable drop in primary particle size for the 1750 rpm as the respective exhaust gas temperature is below the higher load 1500 rpm condition.

The agglomerates size measurements can further be compared to the NTA data of the GDI soot-in-oil samples analysed in Chapter 5. The analysis there revealed a peak in the size distribution at ca. 100 nm, with a shoulder at 155 nm and another smaller shoulder 241 nm. The principal distribution ranged from 70 nm to 300 nm, with the bulk of particles from 80 nm to 200 nm. An additional smaller peak was observed at 426 nm. It is worth pointing out that these sizes are equivalent diameters as derived from light scattering and Brownian motion. Therefore, one could assume there to be an inherent offset or difference compared to the measurements from TEM images. However, direct comparisons of TEM and NTA data previously showed good agreement [116, 258].

Generally, the dimensions of the exhaust soot agglomerates from the TEM images appear to be shifted towards larger sizes, with many particulates measuring between 200 nm and 500 nm. However, due to the relatively small number of agglomerates analysed, no conclusive statement on the

concentrations of individual sizes can be made. The difference between the measurements could stem from the source of the samples. Consequently, a reason for the absence of the largest particles in the NTA data—i.e. aggregates around 1000 nm—could be shearing effects breaking particles once they transferred into the lubricating oil. However, this area has not yet been covered in the literature.

8.2 Identifying Sub-23 nm Particulates

A second approach to sampling soot was taken by inserting the sampling probe directly into the exhaust gas stream. Overall, the TEM grids for all conditions were sparsely loaded with typical soot agglomerates. Instead, large numbers of very small particulates could be observed. The predominance of larger particles on the grids sampled with the ejector diluter could, in part, be due to particle losses or sampling effects of the setup favouring the observed particle sizes [246]. Sampling on the grids by directly inserting these in the exhaust gas stream avoids additional sampling and dilution steps, thus preventing particle losses. However, the sampling duration is greatly limited by the hostile environment of the exhaust gas. The grids could only be placed in the exhaust pipe for 3 min before degradation of the substrate became pronounced.

The particles observed in some regions of the grid sampled at the 1500 rpm fast-idle condition are displayed in Figure 8.4a. These were equally distributed on some sections of the grid and appeared to be stable under the electron beam, i.e. no decomposition was noticeable. This beam-stability suggests a non-volatile nature of the observed particles [48, 67]. Previously, Seong et al. [276] observed sub-20 nm features at the edges of soot agglomerates. Separate sub-25 nm particulates were reported by Barone et al. [46]. The TEM images included in their work showed only few of these particles, which were considerably less densely distributed on the TEM grid compared to Figure 8.4. Lee et al. [278] reported that large numbers of

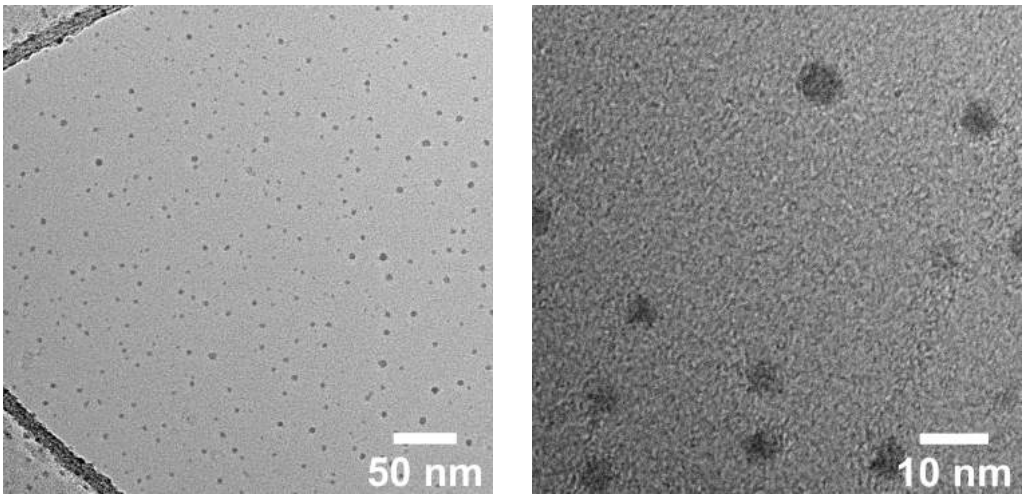

(a) (b)

Figure 8.4: TEM images of thermophoretically collected soot directly from the exhaust gas at 1500 rpm fast-idle.

sub-10 nm particulates had been observed on carbon only TEM grids but only rarely on the edges of lacey carbon grids; however, no images of these particles were included in their publication.

While some particulates exhibit a distinct border, the outline of others is challenging to be identified against the graphene oxide background (see Figure 8.4b). Nevertheless, HRTEM analysis was attempted on the particles to identify their nanostructure. Despite the challenging contrast, traces of crystalline pattern can be observed (see Figures 8.5a and 8.5d). FFTs have been used additionally to visualise the structural properties better. First, an FFT representation of the background area was obtained to determine the contribution of the substrate. Then the FFT of only the particle was processed. For the first particle in Figure 8.5a, the interference pattern is subtle, with a bright spot in the centre and two slightly darker spots above and below (see Figure 8.5c). The respective FFT of the second particle exhibits a more pronounced pattern (see Figure 8.5f); four spots can be observed surrounding the central interference point.

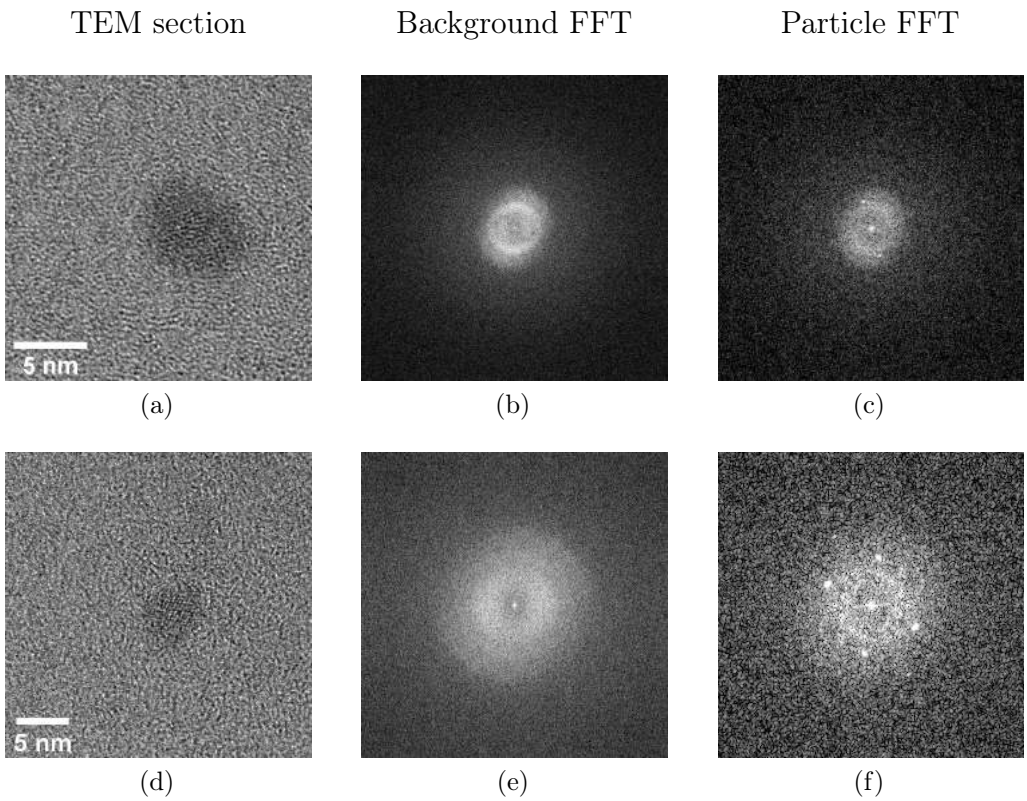

Figure 8.5: HRTEM images of two particles thermophoretically collected from the exhaust gas at 1500 rpm fast-idle (a,d). FFT images of the respective grid background area (b,e) and the particle area (c,f). Contrast and brightness of the FFT images were optimised linearly for better visualisation.

EDX analysis on both particles was not conclusive. A possibility could be that particles are sputtered from the copper grid of the mesh. In this case, EDX would not show a signal against the background of scatter from the grid. Although a relative lack of damage to the carbon film may suggest it is not copper, EELS analysis was attempted. This technique does not suffer from background scatter from nearby bulk structures. No signal from copper could be detected using EELS. However, the sensitivity threshold was quite poor, likely due to the relatively small volume of the particles and the overall significant amount of carbon overshadowing any measurements.

Thus, the sputter possibility could not conclusively be ruled out but remains somewhat unlikely as such particles have not been observed in previous works with the same types of grids, nor were these previously observed by the grid manufacturer.

A hypothesis as to where these particulates originate from the engine could be the lubricating oil film within the combustion chamber or the wear of the engine. Traces of elements likely from these two sources were identified on particulates of soot-in oil samples from a comparable engine in Chapter 5. Thus, this theory would suggest that the formation of crystalline regions already occurs in the combustion chamber and not just as the soot particulates interact with the lubricating oil chemistry.

The particulates in the TEM image shown in Figure 8.4a have been manually measured to provide further quantitative information. The resulting size distribution is shown in Figure 8.6 alongside DMS exhaust measurements. The average particle diameter from the TEM image is 4.7 nm for a total of 215 particles measured. The mode at ca. 4 nm is below the respective mode in the PSD of the DMS at around 6 nm. The additional DMS measurement with the catalytic stripper shows a mode at around 10 nm with a peak concentration of a fifth of the measurement without the catalytic stripper. This indicates a considerable level of sub-23 nm particulates but also the presence of some volatiles in the exhaust gas. The difference between the TEM and DMS size measurements should be interpreted in light of three considerations. First, the inherent differences of the measurement techniques. The TEM captures a visual representation of the particulates. In contrast, DMS measurements are based on electrical mobility diameters that can highly depend on the particulates' morphology, size, and composition [279]. As such, elements other than carbon in the observed sub-23 nm particulates—as apparent by the crystalline structures—could affect the particle charge model. Secondly, the DMS measures particles only after the transfer through the 5 m heated line, while the soot is sampled on TEM grids directly at the sampling port. Thus, artefacts from the sampling process are possible, and

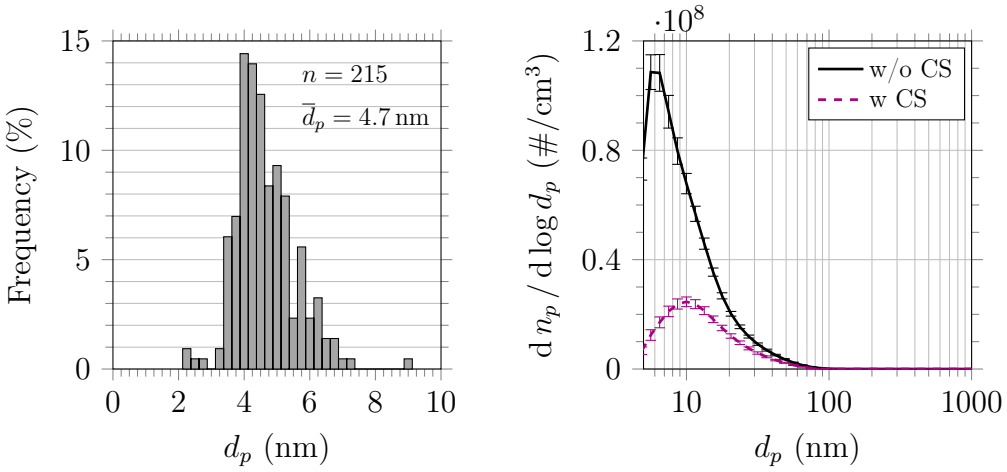

Figure 8.6: Size distribution of soot particle diameters in TEM image Figure 8.11a as sampled directly from the exhaust gas at 1500 rpm fast-idle (a), and corresponding DMS measurements with and without catalytic stripper (CS) at the same condition (b).

particle losses could occur along the line. Thirdly, the mode observed in TEM images is below the technical capability of the DMS instrument, i.e. below the lower detection size limit of the DMS (i.e. 5 nm).

Similar particulates could also be found on the grids onto which soot was sampled at the 1500 rpm with 40 Nm condition (see Figure 8.7). Although regions of these particles appeared to be less frequent on the grid, the concentration of particles within seemed similar. Likewise, the particulates were stable under electron beam and showed no signs of decomposition, again indicating a solid nature.

HRTEM imaging of the observed particles also found crystalline structures that were even more visible (see Figure 8.8a). Subsequent FFT for the background area shows a similar yet slightly different pattern. The additional dark ring stems from a marginally different focus point of the TEM compared to Figure 8.5. The importance of using the FFT to monitor

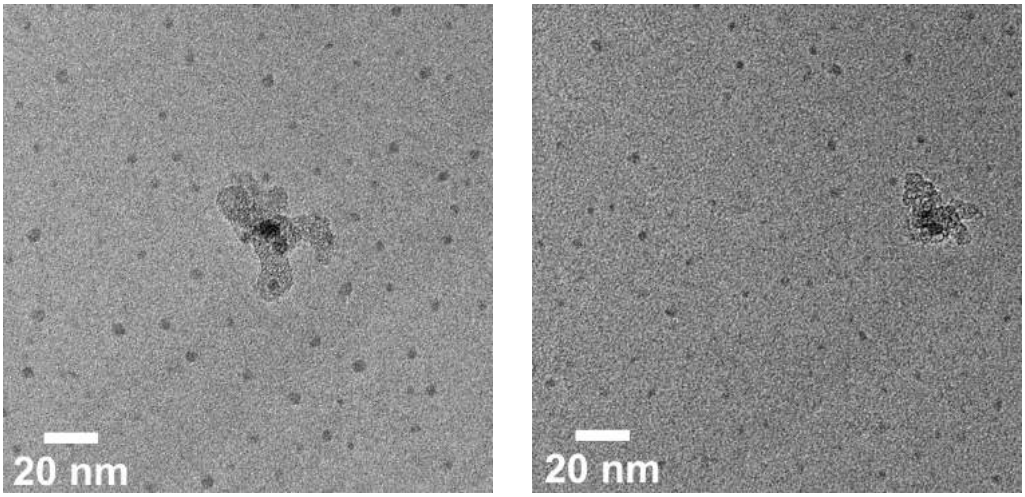

(a) (b)

Figure 8.7: TEM images of thermophoretically collected soot directly from the exhaust gas at 1500 rpm with 40 Nm brake torque.

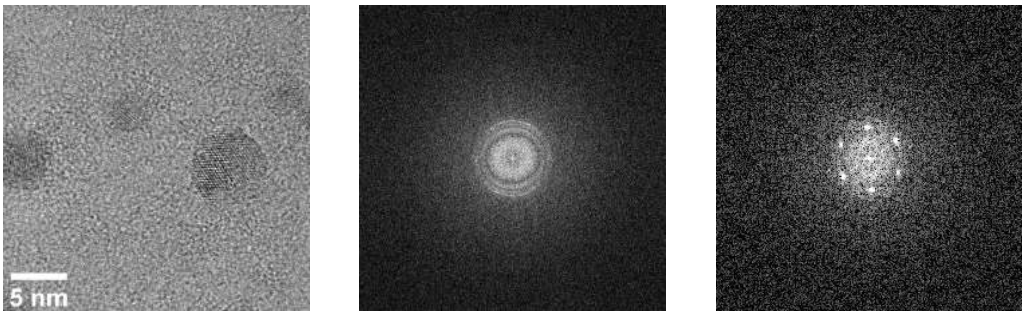

(a) (b) (c)

Figure 8.8: HRTEM image of particles thermophoretically collected from the exhaust gas at 1500 rpm with 40 Nm brake torque (a). FFT images of the grid background area (b) and the particle area (c). Contrast and brightness of the FFT images were optimised linearly for better visualisation.

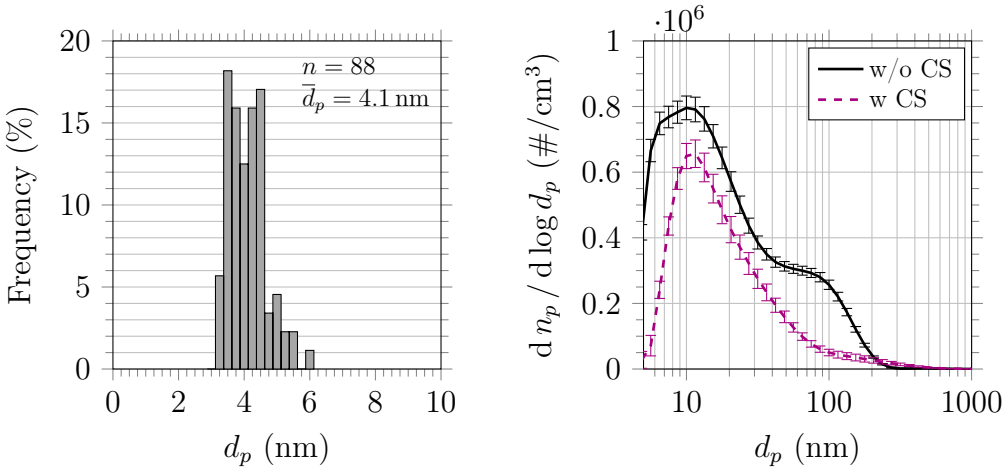

Figure 8.9: Size distribution of soot particle diameters in TEM images of Figure 8.7 as sampled directly from the exhaust gas at 1500 rpm with 40 Nm brake torque (a), and corresponding DMS measurements with and without catalytic stripper (CS) at the same condition (b).

the focus point for HRTEM of soot was demonstrated in Chapter 4. As expected from the distinct crystalline pattern in the TEM image, the FFT shows strong diffraction with a hexagonal array. The findings of EDX and EELS analysis were again not conclusive as for the particulates of the 1500 rpm fast-idle condition.

The observed sub-23 nm particles were measured (see Figure 8.9a), but only a smaller number of particles could be identified in the obtained TEM images compared to the fast-idle condition. The average diameter was found to be 4.1 nm, i.e. smaller by 0.6 nm for 40 Nm brake torque than for fast-idle at 1500 rpm. This difference is relatively small and could potentially change simply by measuring a greater number of particles. The mode in the PSD is just above 10 nm for both DMS measurements with and without catalytic stripper (see Figure 8.9b). The change in the concentration level is less drastic than the fast-idle condition; however, the distribution

shape changes noticeably. Thus, an appreciable level of volatiles could still be assumed. The 6 nm difference between the modes of TEM and DMS measurements should be seen under the same considerations mentioned above for the fast-idle condition.

As for the two conditions at 1500 rpm, sub-23 nm particulates could also be found on the grid sampled at 1750 rpm with 20 Nm brake torque (see Figure 8.10). Measurements of 143 particles identified a mean diameter of 3.7 nm. This value is smaller than for the two previous conditions but only by up to 1 nm. The DMS measurements cannot confirm this difference as the mode in the recorded PSDs is 10 nm and 11.6 nm with and without catalytic stripper, respectively (see Figure 8.11). The two DMS measurements exhibit a closer agreement than the previous conditions, as the PSD shape remains similar, and the concentration level is only slightly reduced with the catalytic stripper. Thus, the concentration of volatiles could be considered to be lower at this condition. The discrepancy between the measurements from the two techniques is again several nanometres, with the mean diameter of the particles in the TEM images below the lower detection size limit of the DMS. These interpretations should again be considered with the same caveats mentioned for the fast-idle condition above.

Sub-23 nm particulates were found for all three conditions, and subsequent measurements revealed mean diameters below 5 nm. The largest average size of 4.7 nm was observed at 1500 rpm fast-idle and the smallest of 3.7 nm at 1750 rpm with 20 Nm brake torque. The nanostructure of these particulates exhibited crystalline features that were identified both visually and by FFTs of particle sections. Moreover, the particulates can be considered non-volatile in nature as these were stable under the electron beam. This assumption is further supported by considerable concentrations of sub-23 nm particles detected by the DMS with the catalytic stripper. The reason for the difference in particle sizes observed between TEM and DMS measurements could be twofold. First, the average particle size as obtained by TEM images is below the lower detection size limit of the DMS (i.e. 5 nm). Secondly, the

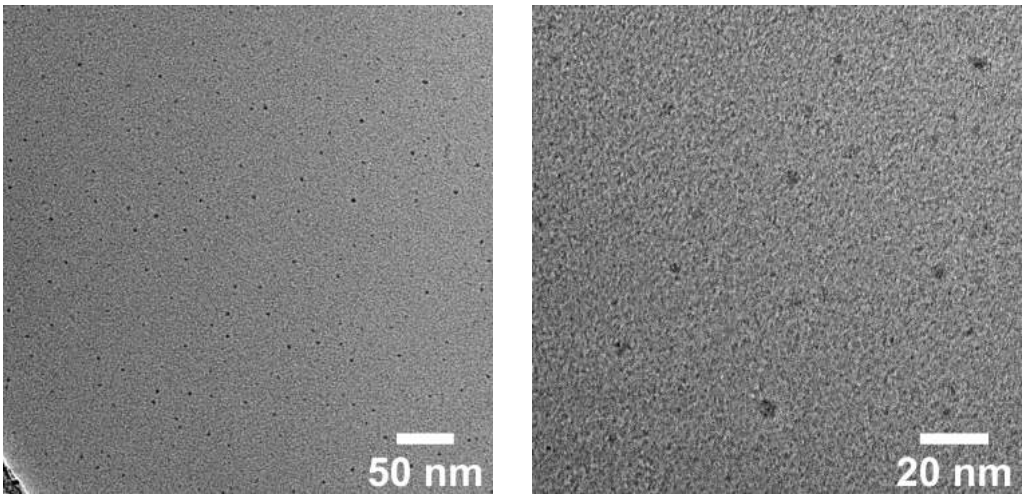

(a) (b)

Figure 8.10: TEM images of thermophoretically collected soot directly from the exhaust gas at 1750 rpm with 20 Nm brake torque.

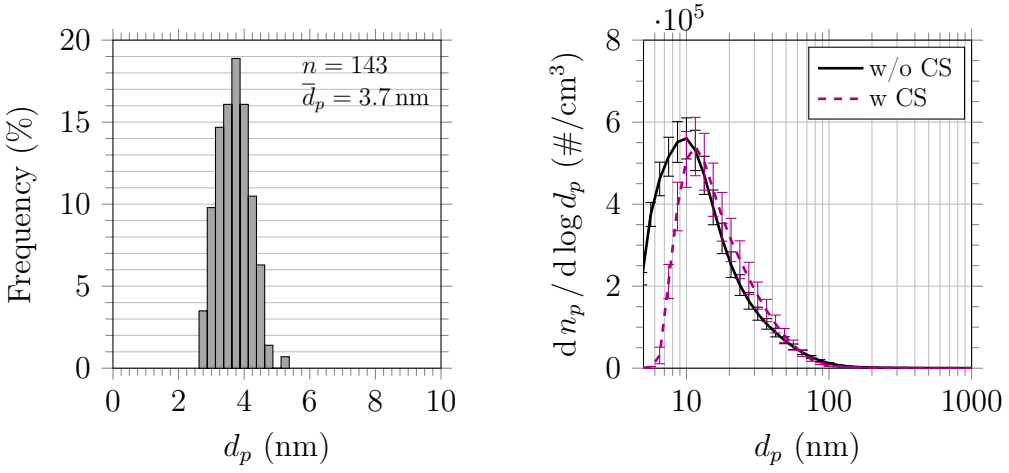

(a) (b)

Figure 8.11: Size distribution of soot particle diameters in TEM images of Figure 8.10a as sampled directly from the exhaust gas at 1750 rpm with 20 Nm brake torque (a), and corresponding DMS measurements with and without catalytic stripper (CS) at the same condition (b).

composition of the particulates with elements other than carbon—apparent by the crystalline structures—could affect the particle charge model of the DMS and thus skew the PSD. A considerable portion of these solid particles in the PSDs would be excluded if the proposed counting efficiency of 65 % at 10 nm for upcoming regulatory PN limits was applied [195]. Particles with a size of 5 nm would be excluded almost entirely, depending on the specific CPC calibration or filtering function (cf. Chapter 6). Consequently, counting efficiencies would have to be lowered to even smaller particle sizes to reflect the emitted particulates accurately.

8.3 Classifying Nanostructure Types

Further HRTEM analysis was conducted on the primary particles that constitute the agglomerates observed in Section 8.1. In contrast to the separate sub-23 nm particles, considerably better contrast could be achieved here, and nanostructures of primary particles were identified. The particles sampled at 1500 rpm fast-idle exhibit diverse nanostructure types (see Figure 8.12). The structure of some particles falls into the typical core-shell category, i.e. graphitic layers surrounding an amorphous core (see Figure 8.12a). While frequently only a single core was observed, other particles could be found that exhibit multiple cores and, as such, a higher degree of disorder (see Figure 8.12b). Nevertheless, graphitic fringes were still clearly visible.

Additional amorphous carbon features can be observed in particles with further nanostructure types. The particle shown in Figure 8.12c exhibits a relatively thin amorphous layer surrounding the particle. Beneath this superficial layer, traces of graphitic fringes are noticeable. The pattern is similar to Figure 8.12b, i.e. a semi-graphitic order with multiple cores. However, overall the fringes are less visible—possibly due to the higher material thickness of the larger particle. Traces of graphitic fringes are even fainter for the particle in Figure 8.12d, yet a considerably thicker

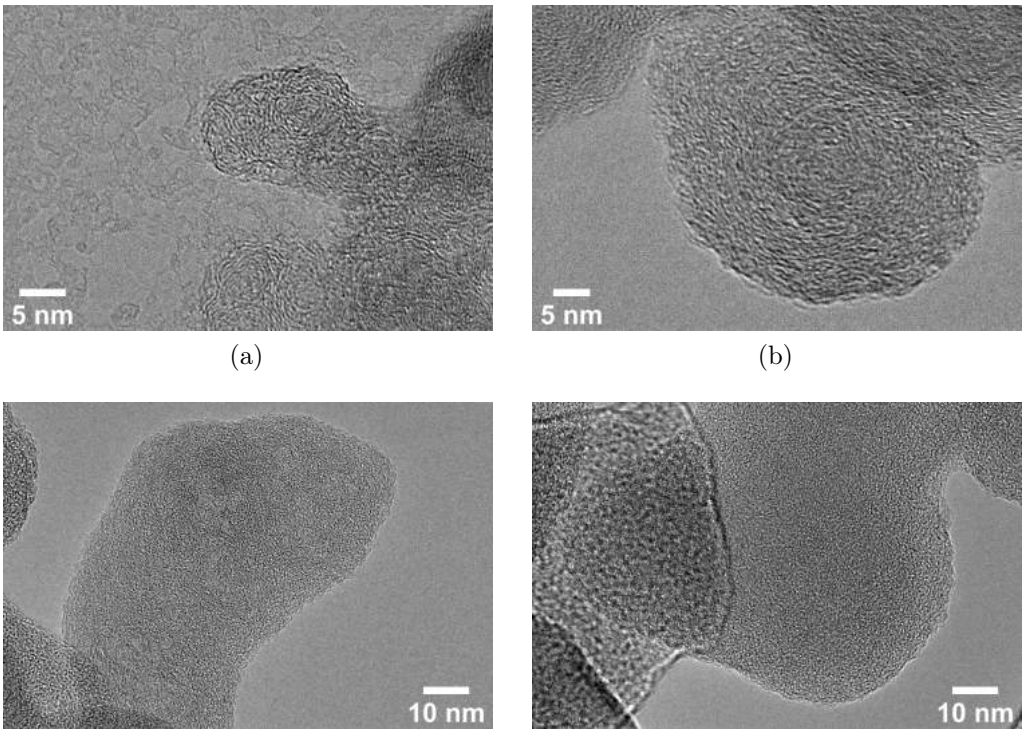

(a) (b)

(c) (d)

Figure 8.12: HRTEM images of soot particles sampled at 1500 rpm fast-idle, revealing various nanostructure types.

amorphous layer can be identified. The fringe traces suggest an underlying structure similar to Figure 8.12a.

Enlarged sections of Figures 8.12c and 8.12d are depicted for better visualisation in Figures 8.13a and 8.13b, respectively. The amorphous layer is annotated in both images, and its thickness measures on average 3.8 nm for Figure 8.13a and 13.7 nm for Figure 8.13b. The assumed core-shell structure is somewhat more apparent in Figure 8.13b; however, the level of detail is likely limited by the particle thickness. A similar observation was made in Chapter 5: The primary particle of a soot-in-oil aggregate exhibited a core-shell structure with an amorphous layer. However, the noticeable difference is the lower thickness of the surrounding layer of less than 5 nm.

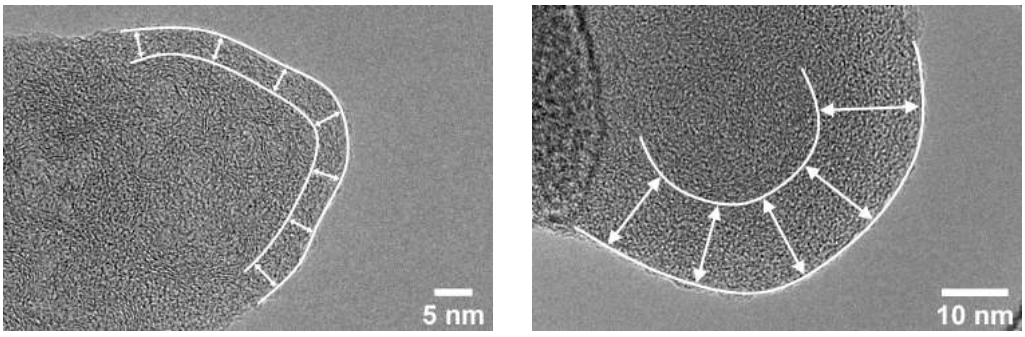

(a) (b)

Figure 8.13: Enlarged sections of Figure 8.12c (a) and Figure 8.12d (b) with annotated amorphous outer layer.

Primary particles in the agglomerates sampled at 1500 rpm with 40 Nm brake torque mostly exhibit core-shell structures with single-core (see Figure 8.14a) or multi-core (see Figure 8.14b) arrangements. The latter appears to be somewhat more ordered with more pronounced graphitic fringes compared to Figure 8.12b. However, this should be considered a qualitative observation rather than a quantitative finding due to the small number of particles investigated. A surrounding amorphous layer could not be observed on any of the imaged particles. Instead, crystalline regions within aggregates were identified (see Figure 8.14c). Moreover, particles were observed that lack any graphitic fringes and appear entirely crystalline (see Figure 8.14d).

As for the separate sub-23 nm particles, the FFT of images was used for additional confirmation. The crystalline area in Figure 8.14c is relatively small, with only just over 5 nm in diameter, and is not in a strongly diffracting orientation. Consequently, the resolution of the FFT is relatively poor; however, two interference marks can be observed left and right of the central point (see Figure 8.15c). This appearance is similar to the FFT of some sub-23 nm particles, e.g. Figure 8.5c. The dark ring in the background FFT of Figure 8.14d (see Figure 8.15e) is suspected to be a frequency artefact that was only noticed in post-acquisition analysis. The interference

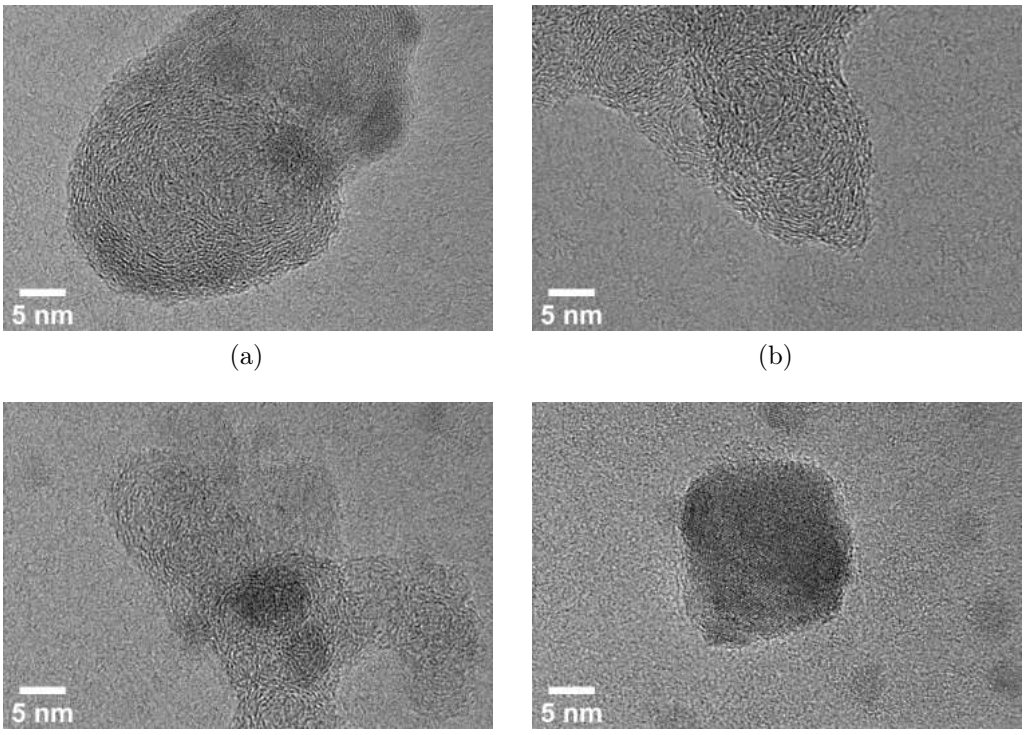

(a) (b)

(c) (d)

Figure 8.14: HRTEM images of soot particles sampled at 1500 rpm with 40 Nm brake torque, revealing various nanostructure types.

pattern in the particle FFT is considerably more pronounced, exhibiting an elongated hexagonal shape with two additional interference marks on the longer edges (see Figure 8.15f). This appearance is closer to other particles, such as Figure 8.8.

Primary particles in the agglomerates sampled at 1750 rpm with 20 Nm brake torque appear to be the least diverse. Most primary particles only exhibit a distinct core-shell structure (see Figures 8.16a to 8.16c). Despite the predominance of graphitic particles with a single core, some particulates exhibit less ordered nanostructures with potentially multiple cores (see Figure 8.16d). These are similar to some features observed in the previous two conditions, i.e. particles depicted in Figures 8.12b and 8.14b.

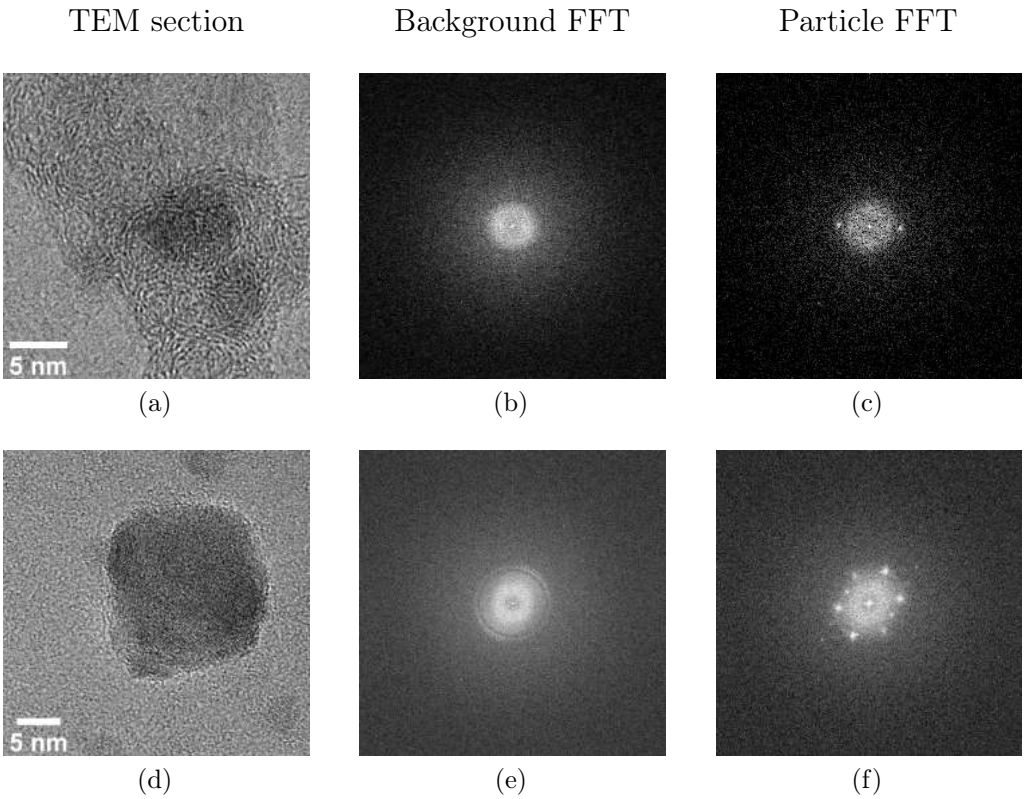

Figure 8.15: Cropped sections of Figure 8.14c (a) and Figure 8.14d (d) as sampled at 1500 rpm with 40 Nm brake torque. FFT images of the respective grid background area (b,e) and the particle area (c,f). Contrast and brightness of the FFT images were optimised linearly for better visualisation.

Primary particles with multiple cores were previously also observed for diesel engine soot [261]. In addition to core-shell particles with single or multiple cores, several studies on GDI engine soot also reported entirely amorphous particles that only exhibit a so-called turbostratic nanostructure [76, 78]. These observations were further confirmed for soot-in-oil samples in Chapter 5. Such particulates, as well as particles with an additional amorphous shell surrounding a core-shell structure, could only be observed for one condition here. The surrounding amorphous shell was also observed in Chapter 5. Another feature identified in some GDI soot-in-oil samples

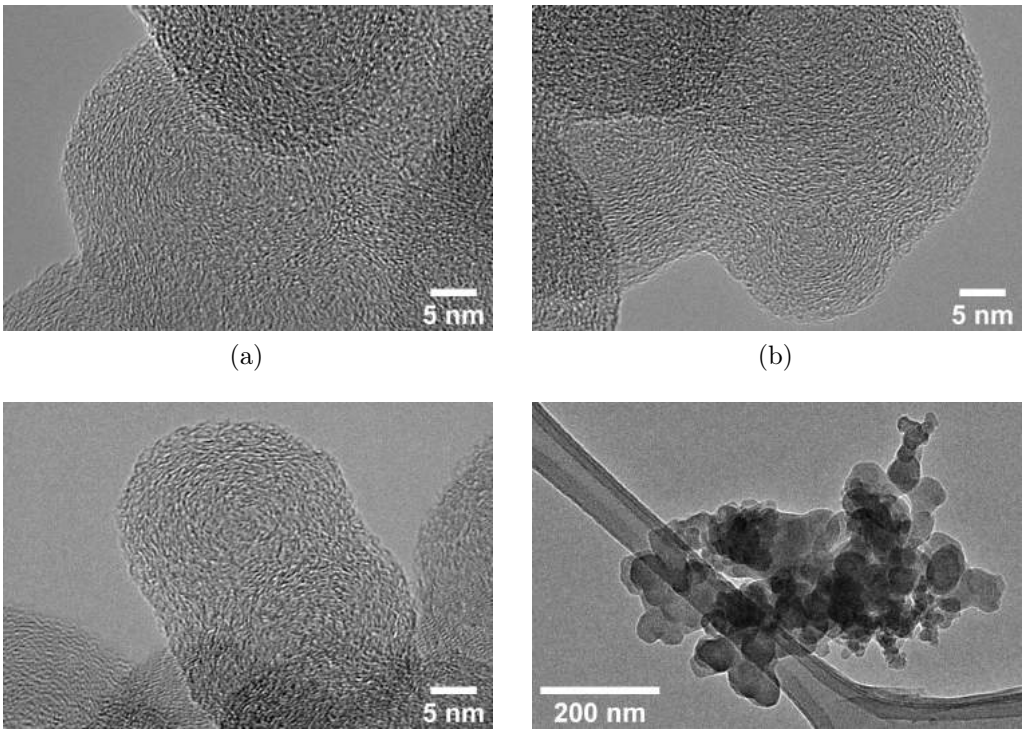

(a) (b)

(c) (d)

Figure 8.16: HRTEM images of soot particles sampled at 1750 rpm with 20 Nm brake torque, revealing various nanostructure types.

are "sludge-like" particles (cf. [48] and Chapter 5); however, these were not found here. Crystalline regions on the surface of soot agglomerates were also reported by La Rocca et al. [67]. In contrast to the findings here, the relevant particles in the work of La Rocca et al. decomposed under the electron beam, indicating volatile nature. Only one other study investigating the impact of engine speed and load on nanostructure types could be found. Seong et al. [276] reported no appreciable differences in nanostructure between engine speeds of 1500 rpm and 3000 rpm, or loads of 25 %, 50 %, and 75 %. While this finding contrasts the observations described here, the loads in the study by Seong et al. are considerably higher; the highest load of 40 Nm corresponds to ca. 23.5 % of the maximum load.

8.4 Fringe Analysis

Fringe analysis was performed to obtain quantitative information on the nanostructures and provide an additional angle to the particle description. Only those particles with distinct core-shell structures and thus clearly visible fringes were included. More disordered or multi-core particle types were excluded. This consideration is similar to how the region of interest itself is selected, i.e. if only the graphitic layers or also the amorphous core (i.e. the entire particle) are included. Here, only the graphitic shell region is considered. Consequently, the results need to be interpreted in the context of highly diverse nanostructure types. Moreover, only images acquired at 500 000 × magnification were considered, as the processing parameters were optimised for the spatial resolution of this specific magnification (cf. Chapter 4). The resulting total number of fringes falls somewhat short of the suggested threshold of 4000 fringes for the three conditions. This is a considerable limitation for the 1500 rpm fast-idle condition with only 571 extracted fringes. However, the values for the other two conditions are more meaningful due to higher total fringe numbers of 1896 and 1872 fringes for 1500 rpm with 40 Nm and 1750 rpm with 20 Nm brake torque, respectively. Nonetheless, additional imaging and analysis should be conducted to confirm these results.

Overall, the fringe length is similar for 1500 rpm with 40 Nm and 1750 rpm with 20 Nm brake torque, with 1.05 nm and 1.03 nm, respectively (see Figure 8.17a). The difference between the conditions is well within the 95 % confidence intervals of 0.031 nm and 0.028 nm, respectively. A decrease in fringe length with an increasing number of fringes can be observed, but the mean values remain within the range of the 95 % confidence intervals. Moreover, the metric remains relatively stable between 1000 and the maximum of just under 1900 total fringes. For fast-idle at 1500 rpm, longer fringes of 1.16 nm can be observed. However, this value is still within the boundaries of the 95 % confidence intervals at the respective total fringe number.

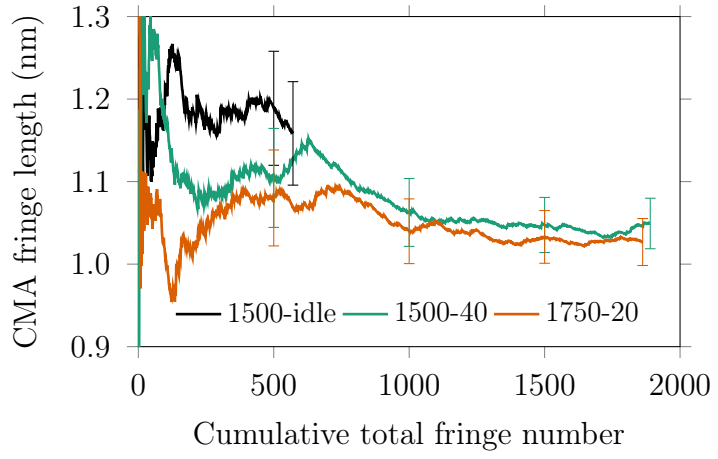

(a)

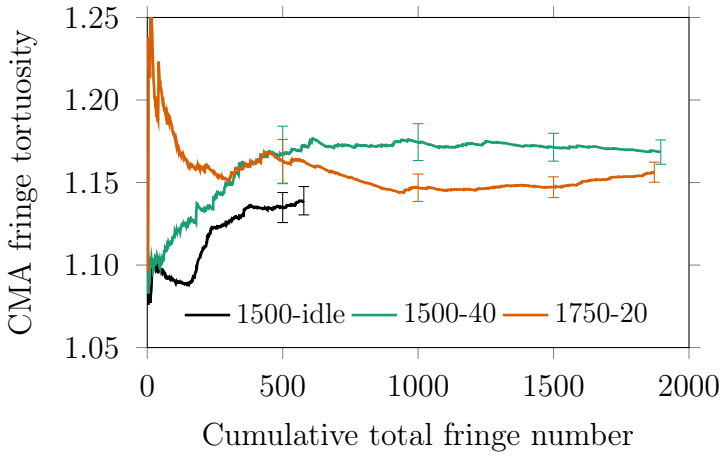

(b)

Figure 8.17: Cumulative moving average (CMA) of fringe length (a) and tortuosity (b) for the cumulative total fringe number for soot sampled at three operating conditions: 1500 rpm fast-idle, 1500 rpm with 40 Nm, and 1750 rpm with 20 Nm brake torque. The error bars are indicative of 95 % confidence intervals.

Observations for the fringe tortuosity exhibit a similar pattern as for the fringe length (see Figure 8.17b). Values for 1500 rpm with 40 Nm and 1750 rpm with 20 Nm brake torque—1.168 and 1.156, respectively—differ by less than their confidence interval ranges—0.0074 and 0.0061, respectively. The cumulative moving average exhibits no drastic changes with the increasing total fringe number, but the gap between the two conditions is gradually closing beyond 1000 fringes. The tortuosity is lower for fast-idle at 1500 rpm. The difference is beyond the 95 % confidence interval; however, an upward trend is noticeable, and the value could likely change with larger fringe numbers.

The findings can further be compared to the previous analysis of soot from a comparable 1.0 l in-vehicle GDI engine. The fringe length measurements here are similar to the initial results of the soot-in-oil GDI samples in Section 5.3.1 but shorter than the subsequent analysis with a larger number of fringes in Section 5.3.2, i.e. an average fringe length of ca. 1.21 nm for over 4000 measured fringes. In contrast, the tortuosity values here are also similar to the reported tortuosity of the latter, i.e. ca. 1.167. Other studies observed shorter fringes but similar tortuosity values. Gaddam and Vander Wal [47] reported a mean fringe length of 0.82 nm for a baseline condition of a GDI engine, with a reduction to 0.74 nm for a delayed injection timing by 60 °CA. The tortuosity increased from 1.175 to 1.19 for the same conditions. Wu et al. [76] observed a mean fringe length of 0.83 nm that increased by up to 0.08 nm for deviations from the stoichiometric air-fuel ratio, while the tortuosity decreased from 1.49 by up to 0.05.

8.5 Summary

Soot particulates from a 1.0 l GDI engine at three operating conditions were analysed by TEM imaging:

- Agglomerates for 1500 rpm fast-idle exhibited the largest skeleton dimensions, with some reaching above 1000 nm. A smaller type of particles with dimensions ranging from 171 nm to 534 nm was observed for all three conditions. The agglomerates for 1750 rpm with 20 Nm brake torque appeared less densely packed and exhibited single strings of primary particles. Moreover, a second smaller group of particulates with maximum lengths of up to 212 nm was observed for this condition.
- The largest primary particles with an average of 39.5 nm were observed for fast-idle at 1500 rpm. The mean diameter was smaller by almost 5 nm and 17 nm for 1500 rpm with 40 Nm and 1750 rpm with 20 Nm brake torque, respectively. The overall average primary particle size was 32 nm.
- Separate sub-10 nm particulates were found equally distributed on some sections of the grids for all three conditions, with average diameters between 3.7 nm to 4.7 nm. These were apparently stable under the electron beam, i.e. no decomposition was noticeable, suggesting a non-volatile nature. DMS measurements with and without catalytic stripper suggested the presence of volatiles to some degree but also indicated high levels of solid sub-23 nm particulates.
- Primary particles of all conditions exhibited mainly typical core-shell nanostructures. An additional surrounding amorphous layer of 3.8 nm to 13.7 nm could be observed for particles at 1500 rpm fast-idle. For 1500 rpm with 40 Nm brake torque, crystalline features within agglomerates and entirely amorphous/crystalline particulates could be found. No additional features could be observed for the particulates of 1750 rpm with 20 Nm brake torque.
- Fringe analysis was conducted for all three samples. Preliminary results were obtained, with just under 1900 fringes for 1500 rpm with 40 Nm and 1750 rpm with 20 Nm brake torque. The differences between the two conditions were below the 95 % confidence intervals, with fringe lengths of ca. 1.04 nm and tortuosity around 1.16.

9 Conclusions

The aim of this PhD project was to close the gap in knowledge between GDI and diesel soot. Understanding the intricacies of the generated particulates is important due to their harmful impact on human health and the environment. However, detailed soot characteristics are also crucial in preventing wear and improving the performance of engines by designing suitable lubricating oils and particulate filters, among other possible applications. Considering the increasing market share of vehicles with GDI engines in the European Union over recent years, these challenges will remain prevalent for years to come. Additional motivation for particulate research stems from upcoming regulations that are focusing on the smallest of emitted particles, with proposed counting efficiencies covering previously excluded sub-23 nm particles.

Consequently, two areas have been covered here. On the one hand, ex-situ analysis techniques have been used for an in-depth comparison of soot types, establishing similarities but also differences between samples from various sources. On the other hand, in-situ measurements of particulate emissions in the exhaust gas stream have been carried out. These investigations assessed the implications of updated counting efficiencies and the impact of using a catalytic stripper for exhaust gas conditioning. Finally, ex-situ techniques were used on exhaust-sampled soot to provide further insight and connect the findings of the two approaches.

9.1 Summary of Findings

The main part of the thesis starts with an investigation of a fringe analysis algorithm in Chapter 4. Variations in the chosen processing parameters were found to have a considerable influence on the number and shape of the extracted fringes. For best representation of the particle nanostructure, a set of parameters was recommended for the spatial resolution of 0.025 nm/px at the used magnification of 500 000 ×: Gaussian low-pass filter standard deviation between 2.0 and 3.0, white top-hat transformation disk size of 5 px or 7 px, and calculation of the binarisation threshold using the method proposed by Otsu [111]. The quality of the acquired images was assessed by using extended exposures through repeated images to improve the signal-to-noise ratio; however, only a minor effect was observed beyond the used image acquisition equipment. Similarly, the fringe metrics were not affected by the size of the selected ROI. However, the TEM focus point can affect the fringe length and the calculated binarisation threshold noticeably. Consequently, consistent focusing with the help of FFT is necessary across particles and samples.

Chapter 5 started with TGA measurements of GDI soot-in-oil samples with different oil mileages. The obtained results revealed a soot deposition rate of 0.96 wt% per 15 000 km with a standard deviation of 0.08 wt%. This trend is in agreement with linear deposition rate models for diesel engines, suggesting that soot in the lubricating oil is of similar importance for GDI engines. Subsequently, samples from two GDI and two diesel engines have been comprehensively characterised along with one carbon black sample using a range of techniques. HRTEM images showed a common core-shell nanostructure for some particles among all samples. While the diesel samples only diverged slightly from the highly ordered carbon black, the GDI samples showed a greater diversity in structure types. Entirely amorphous particles were observed, with some exhibiting crystalline regions. Subsequent EDX analysis suggested additives of lubricant oil and wear materials as the source

of these embedded phases. For a GDI sample, additional measurements were acquired. The primary particles exhibited a mean diameter of 30 nm in TEM images. Moreover, agglomerate sizes were obtained by NTA, revealing an asymmetric distribution with a primary mode at 100 nm, additional populations at 155 nm and 241 nm, and a minor mode at 426 nm.

Moreover, fringe analysis was conducted for primary particle nanostructures of all samples. GDI soot exhibiting the shortest fringes by 9.7 % and 15.1 % compared with the diesel soot and carbon black, respectively. The tortuosity of the fringes was observed to be higher for the engine soot samples over the carbon black by 3.3 %. The quantitative reliability of these metrics was additionally assessed with varying total numbers of fringes. The metrics stabilised when reaching 3000 fringes; however, a minimum of 4000 fringes was recommended to ensure a stabilised window of roughly 1000 fringes prior to the data point used. Furthermore, the observations made by the fringe analysis were confirmed by Raman spectroscopy. The A_{D1}:A_G values were 1.88 for carbon black, 2.37 for 2.0L Diesel soot and 3.85 for 1.0L GDI soot, suggesting 1.0L GDI soot was the most structurally disordered sample. A strong linear correlation was found between A_{D1}:A_G and the fringe length with R^2 value of 0.997, validating the fringe analysis. However, fringe tortuosity showed no linear correlation, but rather a difference between carbon black and soot from internal combustion engines could be identified.

Measurements of particulate emissions from a GDI engine were acquired with a DMS in Chapter 6. Four operating conditions were used as test cases, and different processing methods were applied to the obtained PSDs: discrete linear approximation, lognormal function fitting, and counting efficiency modelling by digital filtering functions. The results are highly dependent on the shape of the PSD in terms of the number and position of modes. Lognormal fitting for the accumulation mode can be closely matched with a digital filtering function. The approach is useful for the scope of the existing PMP with the exclusion of sub-23 nm particles. However, with proposed changes, particles of the corresponding nucleation type mode are included.

Thus, this approach is not viable any longer. A new filtering function was proposed based on the previously established method of filtering functions. The function was designed to match the proposed counting efficiencies for an updated PMP, covering sub-23 nm solid particulates. The new filters increased the TPN by 10 % to 17 % compared to a previous sub-23 nm filter. The PN levels were elevated even further—by 64 % to 452 %—if compared to a PMP-type filter. Similarly, the fraction of sub-23 nm particles increased by 2 % to 7 % with the new filter compared to a previous sub-23 nm filter. Compared to a PMP-type filter, the increase was found to be 38 % to 60 %.

The missing element for assessing the implications of future regulations—a catalytic stripper—was included in Chapter 7. Particulate emissions of a 1.0 l GDI engine were measured for a test matrix derived from a simulation of the WLTC, with a focus on city cycles. The measurements were again acquired with a DMS and were repeated with and without a catalytic stripper. The direct comparison between these data sets revealed that the catalytic stripper noticeably reduced the variability in sub-23 nm particle concentration measurements. A significant portion of particles in this size regime remained and can therefore assumed to be solid (non-volatile). Moreover, different digital filtering functions were applied to implement specified counting efficiencies. The measurements confirmed the previous observations regarding the newly proposed filtering function for sub-23 nm emissions: An increase of up to 11.2 % compared to the closest previous sub-23 nm digital filtering function was observed. However, this increase was highly dependent on the underlying PSD, with conditions of smaller GMD exhibiting a greater shift. The shift from SPN23 digital filtering without catalytic stripper to SPN10 digital filtering with catalytic stripper lead to a considerable difference in the resulting PSDs. Measurements across the test matrix exhibited the highest PN emissions for fast-idle at 1250 rpm, regardless of using a catalytic stripper or the used digital filtering function. The number of particulates generally increased when comparing the SPN10 with the SPN23, from as low as 27 % at 1250 rpm with 40 Nm up to an

almost four-fold 390 % at 1750 rpm with 20 Nm. Investigation of engine metrics revealed a similar trend between PN and THC emissions. The remaining included metrics, exhaust gas temperature, spark timing, 50 % MFB position, injection timing and pressure, could not conclusively explain the observed patterns in the PN and GMD measurements.

TEM analysis was conducted in Chapter 8 for exhaust-sampled soot to investigate the particulates from a different angle and apply the techniques previously used for the characterisation of soot-in-oil samples. Of the three operating conditions analysed, the largest primary particles and agglomerate skeleton dimensions were observed for 1500 rpm fast-idle. In contrast, the smallest agglomerates and primary particles were observed for 1750 rpm with 20 Nm brake torque. Moreover, the agglomerates of this 1750 rpm condition appeared less densely packed and exhibited single strings of primary particles. The overall primary particle size across the three conditions was similar to the previous study with 32 nm. Primary particles of all conditions exhibited mainly typical core-shell nanostructures. Fringe analysis of these structures provided preliminary results, with just under 1900 fringes for 1500 rpm with 40 Nm and 1750 rpm with 20 Nm brake torque. The differences between the two conditions were below the 95 % confidence intervals, with fringe lengths of ca. 1.04 nm and tortuosity around 1.16. An additional surrounding amorphous layer of 3.8 nm to 13.7 nm could be observed for particles at 1500 rpm fast-idle. For 1500 rpm with 40 Nm brake torque, crystalline features within agglomerates and entirely amorphous/crystalline particulates could be found. No additional features could be observed for the particulates of 1750 rpm with 20 Nm brake torque. Separate sub-10 nm particulates were found equally distributed on some sections of the grids for all three conditions, with average diameters between 3.7 nm to 4.7 nm. These were apparently stable under the electron beam, i.e. no decomposition was noticeable, suggesting a non-volatile nature. DMS measurements with and without catalytic stripper suggested the presence of volatiles to some degree but also indicated high levels of solid sub-23 nm particulates.

9.2 Contribution to Knowledge

The findings of the work contained in this thesis provide new insight into the characteristics of soot from GDI engines and improvements for some of the required analysis techniques.

The assessment of the fringe analysis method contrasts previous studies by demonstrating the importance of the processing parameters for comparable and robust nanostructure measurements. Since the publication of these findings, further research was conducted by other researchers. Botero et al. [280] underlined the need for high-quality imaging to obtain measurements that are free of artefacts. It was further highlighted that the processing parameters need to be optimised for different spatial resolutions, and that short exposure times of particles to the electron beam are crucial to avoid structural changes. Toth [281] extended the present work with an in-depth investigation of the fringe analysis method. The study assessed the impact of various magnifications, the fringe number, TEM focus point, and included a more rigorous statistical assessment of the processing parameters.

The investigation into the deposition rate of soot into the lubricating oil for a GDI engine was novel in that it revealed levels comparable to diesel engines, even though particulate emission levels in the exhaust gas are typically lower by one order of magnitude. This observation underlined that understanding the properties of soot is similarly important for GDI engines as for their diesel counterparts. To the knowledge of the author, the subsequent comparative investigation was the first study to include GDI soot along with diesel soot and carbon black for nanostructural quantification by fringe analysis, facilitating a consistent set of processing parameters and TEM imaging by the same TEM operator. Despite similarities in agglomerate and primary particle sizes, distinct differences in the nanostructures could be observed. Recently, Hagen et al. [282] assessed a more extensive number of samples of both GDI and diesel engines as well as several carbon blacks. A similar nanostructure quantification was conducted in the context of

investigating oxidative reactivity. The mean fringe length of the primary particles correlated well with the reactivity of the sample. In contrast, no correlation could be observed between the reactivity and the primary particle size or surface area.

A modified digital filtering function was proposed to match the proposed counting efficiencies of upcoming new regulations. This function is essential in progress towards obtaining the new SPN10 metric from electrical mobility size distributions. Thus, enabling comparisons with regulatory CPC measurements. Furthermore, the function could directly be implemented as a roll-off function for the DMS500 instrument. Applying this methodology to the measurement of particulate emissions from a GDI engine revealed considerable fractions of particulates below 23 nm. These fractions largely remained even for measurements with a catalytic stripper, indicating a non-volatile nature of these particulates. To the knowledge of the author, this is the first study to identify a significant number of sub-10 nm particulates with non-volatile nature in TEM images. These findings highlight the importance of including sub-23 nm particulates in regulatory measurements. Moreover, the observed mean diameter of below 5 nm for particulates in the TEM images would suggest moving towards sub-10 nm.

9.3 Future Work

Despite the progress made in the improvement of analysis techniques and the gained knowledge of GDI soot properties, there are several opportunities for further research activities.

The processing parameters for the fringe analysis script were optimised for the spatial resolution of 0.025 nm/px at 500 000 × magnification. As both Gaussian low-pass filter standard deviation and white top-hat transformation disk size are dependent on spatial resolution, similar investigations as in this study would need to be carried out for other spatial resolutions.

Currently, the analysis approach is semi-automatic as the region of interest within nanostructures has to be selected by the user. Further work could focus on automating this step, thus allowing for larger numbers of fringes to be measured more easily. This approach would also require either a fixed magnification for the TEM with optimised parameters or an underlying model for the correlation between spatial resolution and processing parameters to allow variable magnification.

Future work could further encompass the verification of the suggested soot deposition behaviour for GDI engines, with the potential scope of developing a universal deposition rate model. This investigation could be conducted as a large-scale study including a range of vehicles and mileages. The effects of both engine and vehicle specifications, as well as operating conditions, would therewith be averaged. The resulting understanding of soot deposition would enable the design of effective lubricating oils and technical guidelines. Moreover, engine dynamometer tests could be carried out to establish the effect of individual engine parameters on the soot deposition rate.

The engine tests in this thesis were limited to steady-state operation due to the available type of dynamometer. Additional investigations of dynamic conditions or entire driving cycles would be beneficial to cover transient effects. Moreover, detailed tests into the role of engine parameters would help to determine their individual contribution towards sub-23 nm emissions. With a view on challenges in the market, the influence of various fuel formulations and the lubricating oil chemistry would be of interest.

The methodology that was used here for the exhaust particulate measurements, i.e. DMS measurements with a catalytic stripper and applied digital filtering, could also be compared with measurements of a PMP SPN10 compliant system that uses a CPC. Such investigations would be required to validate the function for regulatory metrics. Likewise, electrical mobility diameters can help assess how well the measurements outlined by the regulations capture the distribution of emitted particulates. Characterising the crystalline structure and elemental composition of the sub-10 nm par-

ticulates could provide an insight into their origin and formation process. Additional HRTEM imaging of the primary particle graphitic nanostructures would be required to obtain more robust fringe analysis measurements and thus enable relating the operating conditions to the oxidative reactivity of the emitted soot.

Volatile species are excluded from both the existing and the upcoming particulate emissions regulations to ensure reliability and repeatability of results. Nonetheless, volatile species can be present in the exhaust gas and present a real concern for human health and the environment. Additional information could be obtained by chemical analysis of exhaust gas condensates, capturing all condensible volatiles species. This approach would bring the depth of studies on primary and secondary organic aerosols to the characterisation of engine exhaust.

Bibliography

[1] F. Zhao, M.C. Lai, and D.L. Harrington. Automotive spark-ignited direct-injection gasoline engines. Progress in Energy and Combustion Science, 25(5):437–562, 1999. DOI 10.1016/S0360-1285(99)00004-0.

[2] H. Zhao. Overview of gasoline direct injection engines. In: H. Zhao (Ed.). Advanced direct injection combustion engine technologies and development: Gasoline and gas engines, pages 1–19. Woodhead Publishing, Cambridge, 2010, DOI 10.1533/9781845697327.1.

[3] Y. Iwamoto, K. Noma, O. Nakayama, et al. Development of gasoline direct injection engine. SAE Technical Paper 970541, 1997. DOI 10.4271/970541.

[4] P. Leduc, B. Dubar, A. Ranini, and G. Monnier. Downsizing of gasoline engine: An efficient way to reduce CO2 emissions. Oil & Gas Science and Technology, 58(1):115–127, 2003. DOI 10.2516/ogst:2003008.

[5] J.W.G. Turner, A. Popplewell, S. Richardson, et al. Ultra boost for economy: Realizing a 60% downsized engine concept. In: Internal combustion engines: Performance, fuel economy and emissions, pages 3–17. Woodhead Publishing, Cambridge, 2013, DOI 10.1533/9781782421849.1.3.

[6] International Council on Clean Transportation Europe. European vehicle market statistics – Pocketbook 2019/20, 2019. URL `https://theicct.org/publications/european-vehicle-market-statistics-20192020`. Last accessed: 01 July 2021.

[7] M. Braisher, R. Stone, and P. Price. Particle number emissions from a range of European vehicles. SAE Technical Paper 2010-01-0786, 2010. DOI 10.4271/2010-01-0786.

[8] M. Borghi, E. Mattarelli, J. Muscoloni, et al. Design and experimental development of a compact and efficient range extender engine. Applied Energy, 202:507–526, 2017. DOI 10.1016/j.apenergy.2017.05.126.

[9] F. Catapano, S. Di Iorio, L. Luise, et al. In-cylinder soot formation and exhaust particle emissions in a small displacement spark ignition engine operating with ethanol mixed and dual fueled with gasoline. SAE Technical Paper 2017-01-0653, 2017. DOI 10.4271/2017-01-0653.

[10] B.M. Graves, C.R. Koch, and J.S. Olfert. Morphology and volatility of particulate matter emitted from a gasoline direct injection engine fuelled on gasoline and ethanol blends. Journal of Aerosol Science, 105:166–178, 2017. DOI 10.1016/j.jaerosci.2016.10.013.

[11] S. Di Iorio, F. Catapano, A. Magno, et al. Investigation on sub-23 nm particles and their volatile organic fraction (VOF) in PFI/DI spark ignition engine fueled with gasoline, ethanol and a 30 %v/v ethanol blend. Journal of Aerosol Science, 153:105723, 2021. DOI 10.1016/j.jaerosci.2020.105723.

[12] AQEG. Particulate matter in the UK: Summary. Defra, London, 2005. URL `https://uk-air.defra.gov.uk/assets/documents/reports/aqeg/pm-summary.pdf`. Last accessed: 01 July 2021.

[13] World Health Organization. WHO air quality guidelines for particulate matter, ozone, nitrogen dioxide and sulfur dioxide, 2005. URL `https://apps.who.int/iris/bitstream/handle/10665/69477/WHO_SDE_PHE_OEH_06.02_eng.pdf`. Last accessed: 01 July 2021.

[14] K.H. Kim, K. Sekiguchi, S. Kudo, and K. Sakamoto. Characteristics of atmospheric elemental carbon (char and soot) in ultrafine and fine particles in a roadside environment, Japan. Aerosol and Air Quality Research, 11(1):1–12, 2011. DOI 10.4209/aaqr.2010.07.0061.

[15] J.C. Huang. Carbon black filled conducting polymers and polymer blends. Advances in Polymer Technology, 21(4):299–313, 2002. DOI 10.1002/adv.10025.

[16] A.D.H. Clague, J.B. Donnet, T.K. Wang, and J.C.M. Peng. A comparison of diesel engine soot with carbon black. Carbon, 37(10):1553–1565, 1999. DOI 10.1016/S0008-6223(99)00035-4.

[17] Y. Cheng, K.B. He, F.K. Duan, et al. Ambient organic carbon to elemental carbon ratios: Influence of the thermal-optical temperature protocol and implications. Science of the Total Environment, 468-469: 1103–1111, 2014. DOI 10.1016/j.scitotenv.2013.08.084.

[18] D.B. Kittelson. Engines and nanoparticles: A review. Journal of Aerosol Science, 29(5–6):575–588, 1998. DOI 10.1016/S0021-8502(97)10037-4.

[19] World Health Organization. Ambient air pollution: A global assessment of exposure and burden of disease. Geneva, Switzerland, 2016. ISBN 9789241511353.

[20] European Environment Agency. The European environment — state and outlook 2020. Publications Office of the European Union, Luxembourg, 2019. URL `https://www.eea.europa.eu/publications/soer-2020/at_download/file`. Last accessed: 01 July 2021.

[21] European Environment Agency. Exceedance of air quality standards in Europe, 2020. URL `https://www.eea.europa.eu/ds_resolveuid/af962d7241d14729a2a4e402c9d01f5c`. Last accessed: 01 July 2021.

[22] Department for Environment Food and Rural Affairs (DEFRA). The air quality strategy for England, Scotland, Wales and Northern Ireland (Volume 1), 2007. URL `https://www.gov.uk/government/publications/the-air-quality-strategy-for-england-scotland-wales-and-northern-ireland-volume-1`. Last accessed: 01 July 2021.

[23] R.W. Baldauf, R.B. Devlin, P. Gehr, et al. Ultrafine particle metrics and research considerations: Review of the 2015 UFP workshop. International Journal of Environmental Research and Public Health, 13 (11):1054, 2016. DOI 10.3390/ijerph13111054.

[24] G. Oberdörster, Z. Sharp, V. Atudorei, et al. Translocation of inhaled ultrafine particles to the brain. Inhalation Toxicology, 16(6–7):437–445, 2004. DOI 10.1080/08958370490439597.

[25] K. Donaldson, L. Tran, L.A. Jimenez, et al. Combustion-derived nanoparticles: A review of their toxicology following inhalation exposure. Particle and Fibre Toxicology, 2(1):1–14, 2005. DOI 10.1186/1743-8977-2-10.

[26] D.M. Broday and R. Rosenzweig. Deposition of fractal-like soot aggregates in the human respiratory tract. Journal of Aerosol Science, 42(6):372–386, 2011. DOI 10.1016/j.jaerosci.2011.03.001.

[27] G. Oberdörster. Significance of particle parameters in the evaluation of exposure-dose response relationships of inhaled particles. Particulate Science and Technology, 14(2):135–151, 1996. DOI 10.1080/02726359608906690.

[28] B. Giechaskiel, U. Manfredi, and G. Martini. Engine exhaust solid sub-23 nm particles: I. Literature survey. SAE International Journal of Fuels and Lubricants, 7(3):950–964, 2014. DOI 10.4271/2014-01-2834.

[29] S. Heidari Nejad, R. Takechi, B.J. Mullins, et al. The effect of diesel exhaust exposure on blood-brain barrier integrity and function in a murine model. Journal of Applied Toxicology, 35(1):41–47, 2015. DOI 10.1002/jat.2985.

[30] T.C. Bond, S.J. Doherty, D.W. Fahey, et al. Bounding the role of black carbon in the climate system: A scientific assessment. Journal of Geophysical Research: Atmospheres, 118(11):5380–5552, 2013. DOI 10.1002/jgrd.50171.

[31] M.Z. Jacobson. Control of fossil-fuel particulate black carbon and organic matter, possibly the most effective method of slowing global warming. Journal of Geophysical Research, 107(D19):4410, 2002. DOI 10.1029/2001JD001376.

[32] J. Song, M. Alam, and A.L. Boehman. Impact of alternative fuels on soot properties and DPF regeneration. Combustion Science and Technology, 179(9):1991–2037, 2007. DOI 10.1080/00102200701386099.

[33] M. Lapuerta, F. Oliva, J.R. Agudelo, and A.L. Boehman. Effect of fuel on the soot nanostructure and consequences on loading and regeneration of diesel particulate filters. Combustion and Flame, 159 (2):844–853, 2012. DOI 10.1016/j.combustflame.2011.09.003.

[34] A. La Rocca, G. Di Liberto, P.J. Shayler, and M.W. Fay. The nanostructure of soot-in-oil particles and agglomerates from an automotive diesel engine. Tribology International, 61:80–87, 2013. DOI 10.1016/j.triboint.2012.12.002.

[35] C.K. Gaddam, C.H. Huang, and R.L. Vander Wal. Quantification of nano-scale carbon structure by HRTEM and lattice fringe analysis. Pattern Recognition Letters, 76:90–97, 2016. DOI 10.1016/j.patrec.2015.08.028.

[36] D.A. Green and R. Lewis. The effects of soot-contaminated engine oil on wear and friction: A review. Proceedings of the Institution of Mechanical Engineers, Part D: Journal of Automobile Engineering, 222(9):1669–1689, 2008. DOI 10.1243/09544070JAUTO468.

[37] M. Gautam, M. Durbha, K. Chitoor, et al. Contribution of soot contaminated oils to wear. SAE Technical Paper 981406, 1998. DOI 10.4271/981406.

[38] H. Sato, N. Tokuoka, H. Yamamoto, and M. Sasaki. Study on wear mechanism by soot contaminated in engine oil (First report: Relation between characteristics of used oil and wear). SAE Technical Paper 1999-01-3573, 1999. DOI 10.4271/1999-01-3573.

[39] S. Li, A.A. Csontos, B.M. Gable, et al. Wear in Cummins M-11 / EGR test engines. SAE Technical Paper 2002-01-1672, 2002. DOI 10.4271/2002-01-1672.

[40] I. Berbezier, J.M. Martin, and P. Kapsa. The role of carbon in lubricated mild wear. Tribology International, 19(3):115–122, 1986. DOI 10.1016/0301-679X(86)90016-2.

[41] R. Mainwaring. Soot and wear in heavy duty diesel engines. SAE Technical Paper 971631, 1997. DOI 10.4271/971631.

[42] D.J. Growney, O.O. Mykhaylyk, L. Middlemiss, et al. Is carbon black a suitable model colloidal substrate for diesel soot? Langmuir, 31(38): 10358–10369, 2015. DOI 10.1021/acs.langmuir.5b02017.

[43] S. Antusch, M. Dienwiebel, E. Nold, et al. On the tribochemical action of engine soot. Wear, 269(1–2):1–12, 2010. DOI 10.1016/j.wear.2010.02.028.

[44] C. Esangbedo, A.L. Boehman, and J.M. Perez. Characteristics of diesel engine soot that lead to excessive oil thickening. Tribology International, 47:194–203, 2012. DOI 10.1016/j.triboint.2011.11.003.

[45] D.M. Stehouwer, G. Shank, S.N. Herzog, et al. Sooted diesel engine oil pumpability studies as the basis of a new heavy duty diesel engine oil performance specification. SAE Technical Paper 2002-01-1671, 2002. DOI 10.4271/2002-01-1671.

[46] T.L. Barone, J.M.E. Storey, A.D. Youngquist, and J.P. Szybist. An analysis of direct-injection spark-ignition (DISI) soot morphology. Atmospheric Environment, 49:268–274, 2012. DOI 10.1016/j.atmosenv.2011.11.047.

[47] C.K. Gaddam and R.L. Vander Wal. Physical and chemical characterization of SIDI engine particulates. Combustion and Flame, 160(11): 2517–2528, 2013. DOI 10.1016/j.combustflame.2013.05.025.

[48] D. Uy, M.A. Ford, D.T. Jayne, et al. Characterization of gasoline soot and comparison to diesel soot: Morphology, chemistry, and wear. Tribology International, 80:198–209, 2014. DOI 10.1016/j.triboint.2014.06.009.

[49] A. Liati, D. Schreiber, P. Dimopoulos Eggenschwiler, et al. Electron microscopic characterization of soot particulate matter emitted by modern direct injection gasoline engines. Combustion and Flame, 166: 307–315, 2016. DOI 10.1016/j.combustflame.2016.01.031.

[50] Web of Science. URL `https://webofknowledge.com`. Last accessed: 01 July 2021.

[51] SAE Mobilus. URL `https://saemobilus.sae.org`. Last accessed: 01 July 2021.

[52] H. Richter and J.B. Howard. Formation of polycyclic aromatic hydrocarbons and their growth to soot – A review of chemical reaction pathways. Progress in Energy and Combustion Science, 26(4–6): 565–608, 2000. DOI 10.1016/S0360-1285(00)00009-5.

[53] I.M. Kennedy. Models of soot formation and oxidation. Progress in Energy and Combustion Science, 23(2):95–132, 1997. DOI 10.1016/S0360-1285(97)00007-5.

[54] M. Commodo, K. Kaiser, G. De Falco, et al. On the early stages of soot formation: Molecular structure elucidation by high-resolution atomic force microscopy. Combustion and Flame, 205:154–164, 2019. DOI 10.1016/j.combustflame.2019.03.042.

[55] D.R. Tree and K.I. Svensson. Soot processes in compression ignition engines. Progress in Energy and Combustion Science, 33(3):272–309, 2007. DOI 10.1016/j.pecs.2006.03.002.

[56] H. Omidvarborna, A. Kumar, and D.S. Kim. Recent studies on soot modeling for diesel combustion. Renewable and Sustainable Energy Reviews, 48:635–647, 2015. DOI 10.1016/j.rser.2015.04.019.

[57] Y. Qian, Z. Li, L. Yu, et al. Review of the state-of-the-art of particulate matter emissions from modern gasoline fueled engines. Applied Energy, 238:1269–1298, 2019. DOI 10.1016/j.apenergy.2019.01.179.

[58] M.R. Kholghy, A. Veshkini, and M.J. Thomson. The core-shell internal nanostructure of soot - A criterion to model soot maturity. Carbon, 100:508–536, 2016. DOI 10.1016/j.carbon.2016.01.022.

[59] P. Eastwood. Particulate emissions from vehicles. John Wiley & Sons, Chichester, 2008, DOI 10.1002/9780470986516.

[60] B. Giechaskiel, M. Cresnoverh, H. Jörgl, and A. Bergmann. Calibration and accuracy of a particle number measurement system. Measurement Science and Technology, 21(4):045102, 2010. DOI 10.1088/0957-0233/21/4/045102.

[61] K.O. Lee, R. Cole, R. Sekar, et al. Morphological investigation of the microstructure, dimensions, and fractal geometry of diesel particulates. Proceedings of the Combustion Institute, 29(1):647–653, 2002. DOI 10.1016/S1540-7489(02)80083-9.

[62] J. Zhu, K.O. Lee, A. Yozgatligil, and M.Y. Choi. Effects of engine operating conditions on morphology, microstructure, and fractal geometry of light-duty diesel engine particulates. Proceedings of the Combustion Institute, 30(2):2781–2789, 2005. DOI 10.1016/j.proci.2004.08.232.

[63] A. Neer and U.O. Köylü. Effect of operating conditions on the size, morphology, and concentration of submicrometer particulates emitted from a diesel engine. Combustion and Flame, 146(1–2):142–154, 2006. DOI 10.1016/j.combustflame.2006.04.003.

[64] M. Lapuerta, F.J. Martos, and J.M. Herreros. Effect of engine operating conditions on the size of primary particles composing diesel soot agglomerates. Journal of Aerosol Science, 38(4):455–466, 2007. DOI 10.1016/j.jaerosci.2007.02.001.

[65] A. Liati, P. Dimopoulos Eggenschwiler, D. Schreiber, et al. Variations in diesel soot reactivity along the exhaust after-treatment system, based on the morphology and nanostructure of primary soot particles. Combustion and Flame, 160(3):671–681, 2013. DOI 10.1016/j.combustflame.2012.10.024.

[66] G. Ferraro, E. Fratini, R. Rausa, et al. Multiscale characterization of some commercial carbon blacks and diesel engine soot. Energy & Fuels, 30(11):9859–9866, 2016. DOI 10.1021/acs.energyfuels.6b01740.

[67] A. La Rocca, F. Bonatesta, M.W. Fay, and F. Campanella. Characterisation of soot in oil from a gasoline direct injection engine using transmission electron microscopy. Tribology International, 86:77–84, 2015. DOI 10.1016/j.triboint.2015.01.025.

[68] P.A. Marsh, A. Voet, T.J. Mullens, and L.D. Price. Quantitative micrography of carbon black microstructure. Carbon, 9(6):797–805, 1971. DOI 10.1016/0008-6223(71)90013-3.

[69] A. Sharma, T. Kyotani, and A. Tomita. A new quantitative approach for microstructural analysis of coal char using HRTEM images. Fuel, 78(10):1203–1212, 1999. DOI 10.1016/S0016-2361(99)00046-0.

[70] K. Yehliu, R.L. Vander Wal, and A.L. Boehman. Development of an HRTEM image analysis method to quantify carbon nanostructure. Combustion and Flame, 158(9):1837–1851, 2011. DOI 10.1016/j.combustflame.2011.01.009.

[71] M. Sakai, H. Iguma, K. Kondo, and T. Aizawa. Nanostructure analysis of primary soot particles directly sampled in diesel spray flame via HRTEM. SAE Technical Paper 2012-01-1722, 2012. DOI 10.4271/2012-01-1722.

[72] Z. Xu, X. Li, C. Guan, and Z. Huang. Effects of injection timing on exhaust particle size and nanostructure on a diesel engine at different loads. Journal of Aerosol Science, 76:28–38, 2014. DOI 10.1016/j.jaerosci.2014.05.002.

[73] I.C. Jaramillo, C.K. Gaddam, R.L. Vander Wal, and J.S. Lighty. Effect of nanostructure, oxidative pressure and extent of oxidation on model carbon reactivity. Combustion and Flame, 162(5):1848–1856, 2015. DOI 10.1016/j.combustflame.2014.12.006.

[74] X. Li, C. Guan, Y. Luo, and Z. Huang. Effect of multiple-injection strategies on diesel engine exhaust particle size and nanostructure. Journal of Aerosol Science, 89:69–76, 2015. DOI 10.1016/j.jaerosci.2015.07.008.

[75] B. Rohani and C. Bae. Morphology and nano-structure of soot in diesel spray and in engine exhaust. Fuel, 203:47–56, 2017. DOI 10.1016/j.fuel.2017.04.093.

[76] Z. Wu, C. Song, G. Lv, et al. Morphology, fractal dimension, size and nanostructure of exhaust particles from a spark-ignition direct-injection engine operating at different air–fuel ratios. Fuel, 185(2016): 709–717, 2016. DOI 10.1016/j.fuel.2016.08.025.

[77] M. Bogarra, J.M. Herreros, A. Tsolakis, et al. Influence of on-board produced hydrogen and three way catalyst on soot nanostructure in gasoline direct injection engines. Carbon, 120:326–336, 2017. DOI 10.1016/j.carbon.2017.05.049.

[78] Y.Z. An, S.P. Teng, Y.Q. Pei, et al. An experimental study of polycyclic aromatic hydrocarbons and soot emissions from a GDI engine fueled with commercial gasoline. Fuel, 164:160–171, 2016. DOI 10.1016/j.fuel.2015.10.007.

[79] R. Zhang and S. Kook. Influence of fuel injection timing and pressure on in-flame soot particles in an automotive-size diesel engine. Environmental Science & Technology, 48(14):8243–8250, 2014. DOI 10.1021/es500661w.

[80] S. Key, A. La Rocca, M. Fay, et al. Morphological characterisation of diesel soot in oil and the associated extraction dependence. SAE Technical Paper 2018-01-0935, 2018. DOI 10.4271/2018-01-0935.

[81] F.J. Martos, M. Lapuerta, J.J. Expósito, and E. Sanmiguel-Rojas. Overestimation of the fractal dimension from projections of soot agglomerates. Powder Technology, 311:528–536, 2017. DOI 10.1016/j.powtec.2017.02.011.

[82] O. Orhan, E. Haffner-Staton, A. La Rocca, and M. Fay. Characterisation of flame-generated soot and soot-in-oil using electron tomography volume reconstructions and comparison with traditional 2D-TEM measurements. Tribology International, 104:272–284, 2016. DOI 10.1016/j.triboint.2016.09.015.

[83] A. La Rocca, J. Campbell, M.W. Fay, and O. Orhan. Soot-in-oil 3D volume reconstruction through the use of electron tomography: An introductory study. Tribology Letters, 61(1), 2016. DOI 10.1007/s11249-015-0625-z.

[84] E. Haffner-Staton. Development of high-throughput electron tomography for 3D morphological characterisation of soot nanoparticles. PhD thesis, University of Nottingham, Nottingham, 2019.

[85] D.B. Williams and C.B. Carter. Transmission electron microscopy. Springer, Boston, MA, USA, 2nd edition, 2009, DOI 10.1007/978-0-387-76501-3.

[86] M. Alfè, B. Apicella, R. Barbella, et al. Structure-property relationship in nanostructures of young and mature soot in premixed flames. Proceedings of the Combustion Institute, 32(1):697–704, 2009. DOI 10.1016/j.proci.2008.06.193.

[87] H. Bhowmick and S.K. Biswas. Relationship between physical structure and tribology of single soot particles generated by burning ethylene. Tribology Letters, 44(2):139–149, 2011. DOI 10.1007/s11249-011-9831-5.

[88] M. Schenk, S. Lieb, H. Vieker, et al. Morphology of nascent soot in ethylene flames. Proceedings of the Combustion Institute, 35(2): 1879–1886, 2015. DOI 10.1016/j.proci.2014.05.009.

[89] M. Lapuerta, J. Barba, A.D. Sediako, et al. Morphological analysis of soot agglomerates from biodiesel surrogates in a co-flow burner. Journal of Aerosol Science, 111:65–74, 2017. DOI 10.1016/j.jaerosci.2017.06.004.

[90] Z. Li, C. Song, J. Song, et al. Evolution of the nanostructure, fractal dimension and size of in-cylinder soot during diesel combustion process. Combustion and Flame, 158(8):1624–1630, 2011. DOI 10.1016/j.combustflame.2010.12.006.

[91] E. Haffner-Staton, A. La Rocca, and M.W. Fay. Progress towards a methodology for high throughput 3D reconstruction of soot nanoparticles via electron tomography. Journal of Microscopy, 270(3): 272–289, 2018. DOI 10.1111/jmi.12680.

[92] Á.B. Palotás, L.C. Rainey, C.J. Feldermann, et al. Soot morphology: An application of image analysis in high-resolution transmission electron microscopy. Microscopy Research and Technique, 33(3):266–278, 1996. DOI 10.1002/(SICI)1097-0029(19960215)33:3<266::AID-JEMT4>3.0.CO;2-O.

[93] H.S. Shim, R.H. Hurt, and N.Y.C. Yang. A methodology for analysis of 002 lattice fringe images and its application to combustion-derived carbons. Carbon, 38(1):29–45, 2000. DOI 10.1016/S0008-6223(99)00096-2.

[94] A. Galvez, N. Herlin-Boime, C. Reynaud, et al. Carbon nanoparticles from laser pyrolysis. Carbon, 40(15):2775–2789, 2002. DOI 10.1016/S0008-6223(02)00195-1.

[95] M.L. Botero, D. Chen, S. González-Calera, et al. HRTEM evaluation of soot particles produced by the non-premixed combustion of liquid fuels. Carbon, 96:459–473, 2016. DOI 10.1016/j.carbon.2015.09.077.

[96] P. Toth, D. Jacobsson, M. Ek, and H. Wiinikka. Real-time, in situ, atomic scale observation of soot oxidation. Carbon, 145:149–160, 2019. DOI 10.1016/j.carbon.2019.01.007.

[97] P. Toth, A.B. Palotas, E.G. Eddings, et al. A novel framework for the quantitative analysis of high resolution transmission electron micrographs of soot I. Improved measurement of interlayer spacing. Combustion and Flame, 160(5):909–919, 2013. DOI 10.1016/j.combustflame.2013.01.002.

[98] P. Toth, A.B. Palotas, E.G. Eddings, et al. A novel framework for the quantitative analysis of high resolution transmission electron micrographs of soot II. Robust multiscale nanostructure quantification. Combustion and Flame, 160(5):920–932, 2013. DOI 10.1016/j.combustflame.2013.01.003.

[99] C. Wang, T. Huddle, E.H. Lester, and J.P. Mathews. Quantifying curvature in high-resolution transmission electron microscopy lattice fringe micrographs of coals. Energy & Fuels, 30(4):2694–2704, 2016. DOI 10.1021/acs.energyfuels.5b02907.

[100] C. Wang, T. Huddle, C.H. Huang, et al. Improved quantification of curvature in high-resolution transmission electron microscopy lattice fringe micrographs of soots. Carbon, 117:174–181, 2017. DOI 10.1016/j.carbon.2017.02.059.

[101] P. Pré, G. Huchet, D. Jeulin, et al. A new approach to characterize the nanostructure of activated carbons from mathematical morphology applied to high resolution transmission electron microscopy images. Carbon, 52:239–258, 2013. DOI 10.1016/j.carbon.2012.09.026.

[102] P. Toth, Á.B. Palotás, J. Lighty, and C.A. Echavarria. Quantitative differentiation of poorly ordered soot nanostructures: A semi-empirical approach. Fuel, 99:1–8, 2012. DOI 10.1016/j.fuel.2012.04.013.

[103] J.O. Müller, D.S. Su, U. Wild, and R. Schlögl. Bulk and surface structural investigations of diesel engine soot and carbon black. Physical Chemistry Chemical Physics, 9(30):4018–4025, 2007. DOI 10.1039/b704850e.

[104] M.L. Botero, Y. Sheng, J. Akroyd, et al. Internal structure of soot particles in a diffusion flame. Carbon, 141:635–642, 2019. DOI 10.1016/j.carbon.2018.09.063.

[105] B. Apicella, P. Pré, M. Alfè, et al. Soot nanostructure evolution in premixed flames by high resolution electron transmission microscopy (HRTEM). Proceedings of the Combustion Institute, 35(2):1895–1902, 2015. DOI 10.1016/j.proci.2014.06.121.

[106] B. Apicella, P. Pré, J.N. Rouzaud, et al. Laser-induced structural modifications of differently aged soot investigated by HRTEM. Combustion and Flame, 204:13–22, 2019. DOI 10.1016/j.combustflame.2019.02.026.

[107] K. Yehliu, R.L. Vander Wal, and A.L. Boehman. A comparison of soot nanostructure obtained using two high resolution transmission electron microscopy image analysis algorithms. Carbon, 49(13):4256–4268, 2011. DOI 10.1016/j.carbon.2011.06.003.

[108] C. Russo and A. Ciajolo. Effect of the flame environment on soot nanostructure inferred by Raman spectroscopy at different excitation wavelengths. Combustion and Flame, 162(6):2431–2441, 2015. DOI 10.1016/j.combustflame.2015.02.011.

[109] A. Sadezky, H. Muckenhuber, H. Grothe, et al. Raman microspectroscopy of soot and related carbonaceous materials: Spectral analysis and structural information. Carbon, 43(8):1731–1742, 2005. DOI 10.1016/j.carbon.2005.02.018.

[110] H.J. Seong and A.L. Boehman. Evaluation of Raman parameters using visible Raman microscopy for soot oxidative reactivity. Energy & Fuels, 27(3):1613–1624, 2013. DOI 10.1021/ef301520y.

[111] N. Otsu. A threshold selection method from gray-level histograms. IEEE Transactions on Systems, Man, and Cybernetics, 9(1):62–66, 1979. DOI 10.1109/tsmc.1979.4310076.

[112] K. Wan, D. Chen, and H. Wang. On imaging nascent soot by transmission electron microscopy. Combustion and Flame, 198:260–266, 2018. DOI 10.1016/j.combustflame.2018.09.021.

[113] K. Kondo, T. Aizawa, S. Kook, and L. Pickett. Uncertainty in sampling and TEM analysis of soot particles in diesel spray flame. SAE Technical Paper 2013-01-0908, 2013. DOI 10.4271/2013-01-0908.

[114] R.L. Vander Wal, A.J. Tomasek, K. Street, et al. Carbon nanostructure examined by lattice fringe analysis of high-resolution transmission electron microscopy images. Applied Spectroscopy, 58(2):230–237, 2004. DOI 10.1366/000370204322842986.

[115] F.A. Ruiz, M. Cadrazco, A.F. López, et al. Impact of dual-fuel combustion with n-butanol or hydrous ethanol on the oxidation reactivity and nanostructure of diesel particulate matter. Fuel, 161:18–25, 2015. DOI 10.1016/j.fuel.2015.08.033.

[116] A. La Rocca, G. Di Liberto, P.J. Shayler, et al. Application of nanoparticle tracking analysis platform for the measurement of soot-in-oil agglomerates from automotive engines. Tribology International, 70:142–147, 2014. DOI 10.1016/j.triboint.2013.09.018.

[117] M. Salamanca, J.R. Agudelo, F. Mondragón, and A. Santamaría. Chemical characteristics of the soot produced in a high-speed direct injection engine operated with diesel/biodiesel blends. Combustion Science and Technology, 184(7):1179–1190, 2012. DOI 10.1080/00102202.2012.664007.

[118] A. Bredin, A.V. Larcher, and B.J. Mullins. Thermogravimetric analysis of carbon black and engine soot – Towards a more robust oil analysis method. Tribology International, 44(12):1642–1650, 2011. DOI 10.1016/j.triboint.2011.06.002.

[119] K. Yehliu, R.L. Vander Wal, O. Armas, and A.L. Boehman. Impact of fuel formulation on the nanostructure and reactivity of diesel soot. Combustion and Flame, 159(12):3597–3606, 2012. DOI 10.1016/j.combustflame.2012.07.004.

[120] G. Mullins and J. Truhan. Measurement of semi-volatiles in used natural gas engine oil using thermogravimetric analysis. International Journal of Engine Research, 8(5):439–448, 2007. DOI 10.1243/14680874JER00907.

[121] F.E. Lockwood, Z.G. Zhang, S.U.S. Choi, and W. Yu. Effect of soot loading on the thermal characteristics of diesel engine oils. SAE Technical Paper 2001-01-1714, 2001. DOI 10.4271/2001-01-1714.

[122] G. Di Liberto, A. La Rocca, and P. Shayler. Computational analysis of the influence of exhaust gas recirculation on the rate of soot transfer to lubricating engine oil. FISITA Technical Paper F2016-ESYG-020, 36th FISITA World Automotive Congress, Korea, September 26-30, 2016.

[123] V. Sharma, D. Uy, A. Gangopadhyay, et al. Structure and chemistry of crankcase and exhaust soot extracted from diesel engines. Carbon, 103:327–338, 2016. DOI 10.1016/j.carbon.2016.03.024.

[124] B. Giechaskiel, M. Maricq, L. Ntziachristos, et al. Review of motor vehicle particulate emissions sampling and measurement: From smoke and filter mass to particle number. Journal of Aerosol Science, 67: 48–86, 2014. DOI 10.1016/j.jaerosci.2013.09.003.

[125] J.S. MacDonald, S.L. Plee, J.B. D'Arcy, and R.M. Schreck. Experimental measurements of the independent effects of dilution ratio and filter temperature on diesel exhaust particulate samples. SAE Technical Paper 800185, 1980. DOI 10.4271/800185.

[126] I.A. Khalek, T.L. Ullman, S.A. Shimpi, et al. Performance of partial flow sampling systems relative to full flow CVS for determination of particulate emissions under steady-state and transient diesel engine operation. SAE Technical Paper 2002-01-1718, 2002. DOI 10.4271/2002-01-1718.

[127] I. Abdul-Khalek, D. Kittelson, and F. Brear. The influence of dilution conditions on diesel exhaust particle size distribution measurements. SAE Technical Paper 1999-01-1142, 1999. DOI 10.4271/1999-01-1142.

[128] P. Mikkanen, M. Moisio, J. Keskinen, et al. Sampling method for particle measurements of vehicle exhaust. SAE Technical Paper 2001-01-0219, 2001. DOI 10.4271/2001-01-0219.

[129] L. Ntziachristos, B. Giechaskiel, P. Pistikopoulos, et al. Performance evaluation of a novel sampling and measurement system for exhaust particle characterization. SAE Technical Paper 2004-01-1439, 2004. DOI 10.4271/2004-01-1439.

[130] M. Bergmann, R. Vogt, J. Szente, et al. Using ejector diluters to sample vehicle exhaust at elevated pressures and temperatures. SAE International Journal of Engines, 1(1):1167–1178, 2009. DOI 10.4271/2008-01-2434.

[131] B. Giechaskiel, L. Ntziachristos, and Z. Samaras. Effect of ejector dilutors on measurements of automotive exhaust gas aerosol size distributions. Measurement Science and Technology, 20(4):045703, 2009. DOI 10.1088/0957-0233/20/4/045703.

[132] B. Giechaskiel and Y. Drossinos. Theoretical investigation of volatile removal efficiency of particle number measurement systems. SAE International Journal of Engines, 3(1):1140–1151, 2010. DOI 10.4271/2010-01-1304.

[133] A.C. Mayer, A. Ulrich, J. Czerwinski, and J.J. Mooney. Metal-oxide particles in combustion engine exhaust. SAE Technical Paper 2010-01-0792, 2010. DOI 10.4271/2010-01-0792.

[134] Y.M. Kuo, C.W. Lin, S.H. Huang, et al. Effect of aerosol loading on breakthrough characteristics of activated charcoal cartridges. Journal of Aerosol Science, 55:57–65, 2013. DOI 10.1016/j.jaerosci.2012.08.002.

[135] J. Swanson and D. Kittelson. Evaluation of thermal denuder and catalytic stripper methods for solid particle measurements. Journal of Aerosol Science, 41(12):1113–1122, 2010. DOI 10.1016/j.jaerosci.2010.09.003.

[136] P. Kulkarni, P.A. Baron, and K. Willeke (Eds.). Aerosol measurement: Principles, techniques, and applications. John Wiley & Sons, Hoboken, NJ, USA, 3rd edition, 2011, DOI 10.1002/9781118001684.

[137] R.W. Welker. Size analysis and identification of particles. In: R. Kohli and K.L. Mittal (Eds.). Developments in surface contamination and cleaning: Detection, characterization, and analysis of contaminants, pages 179–213. William Andrew, Oxford, 2012, DOI 10.1016/B978-1-4377-7883-0.00004-3.

[138] S.V. Hering and M.R. Stolzenburg. A method for particle size amplification by water condensation in a laminar, thermally diffusive flow. Aerosol Science and Technology, 39(5):428–436, 2005. DOI 10.1080/027868290953416.

[139] R.C. Flagan. History of electrical aerosol measurements. Aerosol Science and Technology, 28(4):301–380, 1998. DOI 10.1080/02786829808965530.

[140] K. Siegmann and H.C. Siegmann. Fast and reliable "in situ" evaluation of particles and their surfaces with special reference to diesel exhaust. SAE Technical Paper 2000-01-1995, 2000. DOI 10.4271/2000-01-1995.

[141] F.X. Ouf and P. Sillon. Charging efficiency of the electrical low pressure impactor's corona charger: Influence of the fractal morphology of nanoparticle aggregates and uncertainty analysis of experimental results. Aerosol Science and Technology, 43(7):685–698, 2009. DOI 10.1080/02786820902878245.

[142] H. Jung and D.B. Kittelson. Characterization of aerosol surface instruments in transition regime. Aerosol Science and Technology, 39 (9):902–911, 2005. DOI 10.1080/02786820500295701.

[143] C. Qi, C. Asbach, W.G. Shin, et al. The effect of particle pre-existing charge on unipolar charging and its implication on electrical aerosol measurements. Aerosol Science and Technology, 43(3):232–240, 2009. DOI 10.1080/02786820802587912.

[144] M.M. Maricq. On the electrical charge of motor vehicle exhaust particles. Journal of Aerosol Science, 37(7):858–874, 2006. DOI 10.1016/j.jaerosci.2005.08.003.

[145] L. Ntziachristos, B. Giechaskiel, J. Ristimäki, and J. Keskinen. Use of a corona charger for the characterisation of automotive exhaust aerosol. Journal of Aerosol Science, 35(8):943–963, 2004. DOI 10.1016/j.jaerosci.2004.02.005.

[146] D.R. Collins, R.C. Flagan, and J.H. Seinfeld. Improved inversion of scanning DMA data. Aerosol Science and Technology, 36(1):1–9, 2002. DOI 10.1080/027868202753339032.

[147] L.M. Russell, R.C. Flagan, and J.H. Seinfeld. Asymmetric instrument response resulting from mixing effects in accelerated DMA-CPC measurements. Aerosol Science and Technology, 23(4):491–509, 1995. DOI 10.1080/02786829508965332.

[148] J. Wang, V.F. McNeill, D.R. Collins, and R.C. Flagan. Fast mixing condensation nucleus counter: Application to rapid scanning differential mobility analyzer measurements. Aerosol Science and Technology, 36(6):678–689, 2002. DOI 10.1080/02786820290038366.

[149] A. Wiedensohler, W. Birmili, A. Nowak, et al. Mobility particle size spectrometers: Harmonization of technical standards and data structure to facilitate high quality long-term observations of atmospheric particle number size distributions. Atmospheric Measurement Techniques, 5(3):657–685, 2012. DOI 10.5194/amt-5-657-2012.

[150] H. Holmgren. On the formation and physical behaviour of exhaled particles. PhD thesis, Chalmers University of Technology, Göteborg, Sweden, 2011.

[151] H. Kaminski, T.A.J. Kuhlbusch, S. Rath, et al. Comparability of mobility particle sizers and diffusion chargers. Journal of Aerosol Science, 57:156–178, 2013. DOI 10.1016/j.jaerosci.2012.10.008.

[152] J.P.R. Symonds, K.S.J. Reavell, J.S. Olfert, et al. Diesel soot mass calculation in real-time with a differential mobility spectrometer. Journal of Aerosol Science, 38(1):52–68, 2007. DOI 10.1016/j.jaerosci.2006.10.001.

[153] B. Giechaskiel, A. Mamakos, J. Andersson, et al. Measurement of automotive nonvolatile particle number emissions within the European legislative framework: A review. Aerosol Science and Technology, 46 (7):719–749, 2012. DOI 10.1080/02786826.2012.661103.

[154] B. Giechaskiel, T. Lähde, and Y. Drossinos. Regulating particle number measurements from the tailpipe of light-duty vehicles: The next step? Environmental Research, 172:1–9, 2019. DOI 10.1016/j.envres.2019.02.006.

[155] B. Giechaskiel, P. Dilara, and J. Andersson. Particle measurement programme (PMP) light-duty inter-laboratory exercise: Repeatability and reproducibility of the particle number method. Aerosol Science and Technology, 42(7):528–543, 2008. DOI 10.1080/02786820802220241.

[156] B. Giechaskiel, M. Arndt, W. Schindler, et al. Sampling of non-volatile vehicle exhaust particles: A simplified guide. SAE International Journal of Engines, 5(2):379–399, 2012. DOI 10.4271/2012-01-0443.

[157] L. Isella, B. Giechaskiel, and Y. Drossinos. Diesel-exhaust aerosol dynamics from the tailpipe to the dilution tunnel. Journal of Aerosol Science, 39(9):737–758, 2008. DOI 10.1016/j.jaerosci.2008.04.006.

[158] I.A. Khalek. 2007 diesel particulate measurement research, CRC report no. E-66-3. Technical report, Coordinating Research Council, Alpharetta, GA, USA, 2007.

[159] B. Giechaskiel, L. Ntziachristos, and Z. Samaras. Calibration and modelling of ejector dilutors for automotive exhaust sampling. Measurement Science and Technology, 15(11):2199–2206, 2004. DOI 10.1088/0957-0233/15/11/004.

[160] Council Directive 70/220/EEC of 20 March 1970 on the approximation of the laws of the Member States relating to measures to be taken against air pollution by gases from positive-ignition engines of motor vehicles. Official Journal of the European Communities, L76:171–191, 1970. URL `https://eur-lex.europa.eu/eli/dir/1970/220/oj`. Last accessed: 01 July 2021.

[161] M. Shelef and R.W. McCabe. Twenty-five years after introduction of automotive catalysts: What next? Catalysis Today, 62(1):35–50, 2000. DOI 10.1016/S0920-5861(00)00407-7.

[162] B. Giechaskiel, A. Joshi, L. Ntziachristos, and P. Dilara. European regulatory framework and particulate matter emissions of gasoline light-duty vehicles: A review. Catalysts, 9(7):586, 2019. DOI 10.3390/catal9070586.

[163] Council Directive 91/441/EEC of 26 June 1991 amending Directive 70/220/EEC on the approximation of the laws of the Member States relating to measures to be taken against air pollution by emissions from motor vehicles. Official Journal of the European Communities, L242:1–106, 1991. URL `https://eur-lex.europa.eu/eli/dir/1991/441/oj`. Last accessed: 01 July 2021.

[164] Directive 94/12/EC of the European Parliament and the Council of 23 March 1994 relating to measures to be taken against air pollution by emissions from motor vehicles and amending Directive 70/220/EEC. Official Journal of the European Communities, L100:42–52, 1994. URL `https://eur-lex.europa.eu/eli/dir/1994/12/oj`. Last accessed: 01 July 2021.

[165] Directive 98/69/EC of the European Parliament and of the Council of 13 October 1998 relating to measures to be taken against air pollution by emissions from motor vehicles and amending Council Directive 70/220/EEC. Official Journal of the European Communities, L350:1–57, 1998. URL `https://eur-lex.europa.eu/eli/dir/1998/69/oj`. Last accessed: 01 July 2021.

[166] Regulation (EC) No 715/2007 of the European Parliament and of the Council of 20 June 2007 on type approval of motor vehicles with respect to emissions from light passenger and commercial vehicles (Euro 5 and Euro 6) [...]. Official Journal of the European Union, L171:1–16, 2007. URL `https://eur-lex.europa.eu/eli/reg/2007/715/oj`. Last accessed: 01 July 2021.

[167] Commission Regulation (EC) No 692/2008 of 18 July 2008 implementing and amending Regulation (EC) No 715/2007 of the European Parliament and of the Council on type-approval of motor vehicles with respect to emissions [...]. Official Journal of the European Union, L199:1–136, 2008. URL https://eur-lex.europa.eu/eli/reg/2008/692/oj. Last accessed: 01 July 2021.

[168] E. Zervas, P. Dorlhène, L. Forti, et al. Interlaboratory test of exhaust PM using ELPI. Aerosol Science and Technology, 39(4):333–346, 2005. DOI 10.1080/027868290930222.

[169] Commission Regulation (EU) No 459/2012 of 29 May 2012 amending Regulation (EC) No 715/2007 of the European Parliament and of the Council and Commission Regulation (EC) No 692/2008 as regards emissions from light passenger and commercial vehicles (Euro 6). Official Journal of the European Union, L142:16–24, 2012. URL https://eur-lex.europa.eu/legal-content/EN/TXT/?uri=CELEX:32012R0459. Last accessed: 01 July 2021.

[170] Commission Regulation (EU) 2016/646 of 20 April 2016 amending Regulation (EC) No 692/2008 as regards emissions from light passenger and commercial vehicles (Euro 6). Official Journal of the European Union, L109:1–22, 2016. URL https://eur-lex.europa.eu/legal-content/EN/TXT/?uri=CELEX:32016R0646. Last accessed: 01 July 2021.

[171] Commission Regulation (EU) 2016/427 of 10 March 2016 amending Regulation (EC) No 692/2008 as regards emissions from light passenger and commercial vehicles (Euro 6). Official Journal of the European Union, L82:1–98, 2016. URL https://eur-lex.europa.eu/legal-content/EN/TXT/?uri=CELEX:32016R0427. Last accessed: 01 July 2021.

[172] Commission Regulation (EU) 2017/1151 of 1 June 2017 supplementing Regulation (EC) No 715/2007 of the European Parliament and of the Council [...]. Official Journal of the European Union, L175:1–643, 2017. URL https://eur-lex.europa.eu/legal-content/EN/TXT/?uri=CELEX:32017R1151. Last accessed: 01 July 2021.

[173] Commission Regulation (EU) 2017/1154 of 7 June 2017 amending Regulation (EU) 2017/1151 supplementing Regulation (EC) No 715/2007 of the European Parliament and of the Council on type-approval of motor vehicles. Official Journal of the European Union, L175:708–732, 2017. URL https://eur-lex.europa.eu/legal-content/EN/TXT/?uri=CELEX:32017R1154. Last accessed: 01 July 2021.

[174] B. Giechaskiel, M. Clairotte, V. Valverde-Morales, et al. Framework for the assessment of PEMS (portable emissions measurement systems) uncertainty. Environmental Research, 166:251–260, 2018. DOI 10.1016/j.envres.2018.06.012.

[175] Commission Regulation (EU) 2018/1832 of 5 November 2018 amending Directive 2007/46/EC of the European Parliament and of the Council, Commission Regulation (EC) No 692/2008 and Commission Regulation (EU) 2017/1151. Official Journal of the European Union, L301:1–314, 2018. URL https://eur-lex.europa.eu/legal-content/EN/TXT/?uri=CELEX:32018R1832. Last accessed: 01 July 2021.

[176] Judgement of 13 December 2018, T-339/16 Ville de Paris v Commission, T-352/16 Ville de Bruxelles v Commission, T-391/16 Ville de Madrid v Commission, EU:T:2018:927. URL https://eur-lex.europa.eu/legal-content/EN/TXT/?uri=CELEX:62016TJ0339. Last accessed: 01 July 2021.

[177] General Court of the European Union. Press release No 198/18, 2018. URL https://curia.europa.eu/jcms/upload/docs/application/pdf/2018-12/cp180198en.pdf. Last accessed: 01 July 2021.

[178] G. Martini, B. Giechaskiel, and P. Dilara. Future European emission standards for vehicles: The importance of the UN-ECE particle measurement programme. Biomarkers, 14(sup1):29–33, 2009. DOI 10.1080/13547500902965393.

[179] M.M. Maricq, R.E. Chase, D.H. Podsiadlik, and R. Vogt. Vehicle exhaust particle size distributions: A comparison of tailpipe and dilution tunnel measurements. SAE Technical Paper 1999-01-1461, 1999. DOI 10.4271/1999-01-1461.

[180] Regulation No 83 of the Economic Commission for Europe of the United Nations (UN/ECE) – Uniform provisions concerning the approval of vehicles with regard to the emission of pollutants according to engine fuel requirements. Official Journal of the European Union, L42:1–207, 2012. URL `https://eur-lex.europa.eu/legal-content/EN/TXT/?uri=CELEX:42012X0215(01)`. Last accessed: 01 July 2021.

[181] B. Giechaskiel, R. Chirico, P.F. DeCarlo, et al. Evaluation of the particle measurement programme (PMP) protocol to remove the vehicles' exhaust aerosol volatile phase. Science of the Total Environment, 408(21):5106–5116, 2010. DOI 10.1016/j.scitotenv.2010.07.010.

[182] M.R. Stolzenburg and P.H. McMurry. An ultrafine aerosol condensation nucleus counter. Aerosol Science and Technology, 14(1):48–65, 1991. DOI 10.1080/02786829108959470.

[183] W. Liu, B.L. Osmondson, O.F. Bischof, and G.J. Sem. Calibration of condensation particle counters. SAE Technical Paper 2005-01-0189, 2005. DOI 10.4271/2005-01-0189.

[184] B. Giechaskiel, T. Lähde, R. Suarez-Bertoa, et al. Particle number measurements in the European legislation and future JRC activities. Combustion Engines, 174(3):3–16, 2018. DOI 10.19206/CE-2018-301.

[185] Y. Otsuki, K. Takeda, K. Haruta, and N. Mori. A solid particle number measurement system including nanoparticles smaller than 23 nanometers. SAE Technical Paper 2014-01-1604, 2014. DOI 10.4271/2014-01-1604.

[186] Z. Zheng, T.D. Durbin, G. Karavalakis, et al. Nature of sub-23-nm particles downstream of the european particle measurement programme (PMP)-compliant system: A real-time data perspective. Aerosol Science and Technology, 46(8):886–896, 2012. DOI 10.1080/02786826.2012.679167.

[187] H. Yamada, K. Funato, and H. Sakurai. Application of the PMP methodology to the measurement of sub-23nm solid particles: Calibration procedures, experimental uncertainties, and data correction methods. Journal of Aerosol Science, 88:58–71, 2015. DOI 10.1016/j.jaerosci.2015.06.002.

[188] B. Giechaskiel and G. Martini. Engine exhaust solid sub-23 nm particles: II. Feasibility study for particle number measurement systems. SAE International Journal of Fuels and Lubricants, 7(3):935–949, 2014. DOI 10.4271/2014-01-2832.

[189] H.G. Horn. PEMs4Nano Report: Calibrated CPC with D50 <= 10 nm for laboratory use – Together with the documented calibration procedure, 2017. URL https://www.pems4nano.eu/download/public_reports/reports_of_project_results_deliverables/PEMs4Nano-D2.05-Calibrated-CPC-with-D50-10nm-for-PEMS-use-PU-2018-03-30.pdf. Last accessed: 01 July 2021.

[190] L. Chasapidis, A.D. Melas, A. Tsakis, et al. A sampling and conditioning particle system for solid particle measurements down to 10 nm. SAE Technical Paper 2019-24-0154, 2019. DOI 10.4271/2019-24-0154.

[191] A.D. Melas, V. Koidi, D. Deloglou, et al. Development and evaluation of a catalytic stripper for the measurement of solid ultrafine particle emissions from internal combustion engines. Aerosol Science and Technology, 54(6):704–717, 2020. DOI 10.1080/02786826.2020.1718061.

[192] P. Kreutziger. PEMs4Nano Report: Report on particle losses in the instruments, 2019. URL https://pems4nano.eu/wp-content/uploads/2020/01/PEMs4Nano_D2-10_Report-on-particles-losses-in-the-instruments_PU_2019-12-20.pdf. Last accessed: 01 July 2021.

[193] United Nations Economic Commission for Europe. PMP 52th session [sic], 2020. URL https://wiki.unece.org/display/trans/PMP+52th+Session. Last accessed: 01 July 2021.

[194] United Nations Economic Commission for Europe. PMP web conference 11.05.2020, 2020. URL https://wiki.unece.org/display/trans/PMP+Web+Conference+11.05.2020. Last accessed: 01 July 2021.

[195] United Nations Economic Commission for Europe. Final report on the development of Amendment 6 to global technical regulation No. 15 on worldwide harmonized light vehicles test procedures (WLTP), Informal document GRPE-81-15, 2020. URL https://unece.org/DAM/trans/doc/2020/wp29grpe/GRPE-81-15e.pdf. Last accessed: 01 July 2021.

[196] B. Giechaskiel, J. Woodburn, A. Szczotka, and P. Bielaczyc. Particulate matter (PM) emissions of Euro 5 and Euro 6 vehicles using systems with evaporation tube or catalytic stripper and 23 nm or 10 nm counters. SAE Technical Paper 2020-01-2203, 2020. DOI 10.4271/2020-01-2203.

[197] B. Giechaskiel, A.D. Melas, T. Lähde, and G. Martini. Non-volatile particle number emission measurements with catalytic strippers: A review. Vehicles, 2(2):342–364, 2020. DOI 10.3390/vehicles2020019.

[198] X. He, M.A. Ratcliff, and B.T. Zigler. Effects of gasoline direct injection engine operating parameters on particle number emissions. Energy & Fuels, 26(4):2014–2027, 2012. DOI 10.1021/ef201917p.

[199] M. Raza, L. Chen, F. Leach, and S. Ding. A review of particulate number (PN) emissions from gasoline direct injection (GDI) engines and their control techniques. Energies, 11(6):1417, 2018. DOI 10.3390/en11061417.

[200] Y.Q. Pei, J. Qin, and S.Z. Pan. Experimental study on the particulate matter emission characteristics for a direct-injection gasoline engine. Proceedings of the Institution of Mechanical Engineers, Part D: Journal of Automobile Engineering, 228(6):604–616, 2014. DOI 10.1177/0954407013493899.

[201] C. Park, S. Lee, and U. Yi. Effects of engine operating conditions on particle emissions of lean-burn gasoline direct-injection engine. Energy, 115:1148–1155, 2016. DOI 10.1016/j.energy.2016.09.051.

[202] D. Kayes and S. Hochgreb. Mechanisms of particulate matter formation in spark-ignition engines. 1. Effect of engine operating conditions. Environmental Science & Technology, 33(22):3957–3967, 1999. DOI 10.1021/es9810991.

[203] P. Price, B. Twiney, R. Stone, et al. Particulate and hydrocarbon emissions from a spray guided direct injection spark ignition engine with oxygenate fuel blends. SAE Technical Paper 2007-01-0472, 2007. DOI 10.4271/2007-01-0472.

[204] A. Velji, M. Lüft, and S. Merkel. Mixture formation, combustion and pollutant emissions in high-speed direct-injection diesel engines. In: H. Zhao (Ed.). Advanced direct injection combustion engine technologies and development: Diesel engines, pages 105–154. Woodhead Publishing, Cambridge, 2009, DOI 10.1533/9781845697457.1.105.

[205] A. Cairns, H. Blaxill, and N. Fraser. Exhaust gas recirculation boosted direct injection gasoline engines. In: H. Zhao (Ed.). Advanced direct injection combustion engine technologies and development: Gasoline and gas engines, pages 105–132. Woodhead Publishing, Cambridge, 2010, DOI 10.1533/9781845697327.105.

[206] M.D. Hageman and D.A. Rothamer. Impacts of combustion phasing, load, and speed on soot formation in spark-ignition engines. International Journal of Engine Research, 2019. DOI 10.1177/1468087419836584.

[207] M.M. Maricq, D.H. Podsiadlik, D.D. Brehob, and M. Haghgooie. Particulate emissions from a direct-injection spark-ignition (DISI) engine. SAE Technical Paper 1999-01-1530, 1999. DOI 10.4271/1999-01-1530.

[208] M. Zhang, W. Hong, F. Xie, et al. Experimental investigation of impacts of injection timing and pressure on combustion and particulate matter emission in a spray-guided GDI engine. International Journal of Automotive Technology, 19(3):393–404, 2013. DOI 10.1007/s12239-018-0038-8.

[209] F. Bonatesta, E. Chiappetta, and A. La Rocca. Part-load particulate matter from a GDI engine and the connection with combustion characteristics. Applied Energy, 124:366–376, 2014. DOI 10.1016/j.apenergy.2014.03.030.

[210] F. Leach, R. Stone, D. Richardson, et al. Particulate emissions from a highly boosted gasoline direct injection engine. International Journal of Engine Research, 19(3):347–359, 2018. DOI 10.1177/1468087417710583.

[211] N. Bock, J. Jeon, D. Kittelson, and W.F. Northrop. Solid particle number and mass emissions from lean and stoichiometric gasoline direct injection engine operation. SAE Technical Paper 2018-01-0359, 2018. DOI 10.4271/2018-01-0359.

[212] K. Kim, J. Kim, S. Oh, et al. Evaluation of injection and ignition schemes for the ultra-lean combustion direct-injection LPG engine to control particulate emissions. Applied Energy, 194:123–135, 2017. DOI 10.1016/j.apenergy.2017.03.012.

[213] K. Choi, J. Kim, A. Ko, et al. Evaluation of time-resolved nano-particle and THC emissions of wall-guided GDI engine. SAE Technical Paper 2011-28-0022, 2011. DOI 10.4271/2011-28-0022.

[214] J. Cho, W. Si, W. Jang, et al. Impact of intermediate ethanol blends on particulate matter emission from a spark ignition direct injection (SIDI) engine. Applied Energy, 160:592–602, 2015. DOI 10.1016/j.apenergy.2015.08.010.

[215] Z. Ming, Z. Jun, C. Stefano, and L. Luigi. Particulate matter emission suppression strategies in a turbocharged gasoline direct-injection engine. Journal of Engineering for Gas Turbines and Power, 139(10): 102801, 2017. DOI 10.1115/1.4036301.

[216] P. Price, R. Stone, T. Collier, and M. Davies. Particulate matter and hydrocarbon emissions measurements: Comparing first and second generation DISI with PFI in single cylinder optical engines. SAE Technical Paper 2006-01-1263, 2006. DOI 10.4271/2006-01-1263.

[217] S. Di Iorio, M. Lazzaro, P. Sementa, et al. Particle size distributions from a DI high performance SI engine fuelled with gasoline-ethanol blended fuels. SAE Technical Paper 2011-24-0211, 2011. DOI 10.4271/2011-24-0211.

[218] A.N. Johansson, S. Hemdal, and P. Dahlander. Experimental investigation of soot in a spray-guided single cylinder GDI engine operating in a stratified mode. SAE Technical Paper 2013-24-0052, 2013. DOI 10.4271/2013-24-0052.

[219] J. Su, M. Xu, P. Yin, et al. Particle number emissions reduction using multiple injection strategies in a boosted spark-ignition direct-injection (SIDI) gasoline engine. SAE International Journal of Engines, 8(1): 20–29, 2015. DOI 10.4271/2014-01-2845.

[220] A. Berndorfer, S. Breuer, W. Piock, and P. Von Bacho. Diffusion combustion phenomena in GDI engines caused by injection process. SAE Technical Paper 2013-01-0261, 2013. DOI 10.4271/2013-01-0261.

[221] J. Chung, N. Kim, H. Choi, and K. Min. Study on the effect of injection strategies on particulate emission characteristics under cold start using in-cylinder visualization. SAE Technical Paper 2016-01-0822, 2016. DOI 10.4271/2016-01-0822.

[222] B. Wang, S. Mosbach, S. Schmutzhard, et al. Modelling soot formation from wall films in a gasoline direct injection engine using a detailed population balance model. Applied Energy, 163:154–166, 2016. DOI 10.1016/j.apenergy.2015.11.011.

[223] C. Farron, N. Matthias, D. Foster, et al. Particulate characteristics for varying engine operation in a gasoline spark ignited, direct injection engine. SAE Technical Paper 2011-01-1220, 2011. DOI 10.4271/2011-01-1220.

[224] D. Kayes and S. Hochgreb. Mechanisms of particulate matter formation in spark-ignition engines. 3. Model of PM formation. Environmental Science & Technology, 33(22):3978–3992, 1999. DOI 10.1021/es981101o.

[225] L. de Francquevilla and G.L. Pilla. Investigation of particle formation processes in a GDI engine in catalyst heating operation. In: 10th International Symposium on Combustion Diagnostics, pages 129–137, 2012. ISBN 9783000326691.

[226] F. Xie, W. Hong, Y. Su, et al. Effect of external hot EGR dilution on combustion, performance and particulate emissions of a GDI engine. Energy Conversion and Management, 142:69–81, 2017. DOI 10.1016/j.enconman.2017.03.045.

[227] R. Stone. Introduction to internal combustion engines. Macmillan, Basingstoke, 3rd edition, 1999, DOI 10.1007/978-1-349-14916-2.

[228] L. Chen, R. Stone, and D. Richardson. Effect of the valve timing and the coolant temperature on particulate emissions from a gasoline direct-injection engine fuelled with gasoline and with a gasoline–ethanol blend. Proceedings of the Institution of Mechanical Engineers, Part D: Journal of Automobile Engineering, 226(10):1419–1430, 2012. DOI 10.1177/0954407012444966.

[229] J.F. Rodriguez and W.K. Cheng. Reduction of cold-start emissions through valve timing in a GDI engine. SAE International Journal of Engines, 9(2):1220–1229, 2016. DOI 10.4271/2016-01-0827.

[230] C. Tan, H. Xu, H. Ma, and A. Ghafourian. Investigation of VVT and spark timing on combustion and particle emission from a GDI Engine during transient operation. SAE Technical Paper 2014-01-13702, 2014. DOI 10.4271/2014-01-1370.

[231] T.W. Chan, E. Meloche, J. Kubsh, et al. Impact of ambient temperature on gaseous and particle emissions from a direct injection gasoline vehicle and its implications on particle filtration. SAE International Journal of Fuels and Lubricants, 6(2):350–371, 2013. DOI 10.4271/2013-01-0527.

[232] D.S. Cardoso, P.O. Fael, and A. Espírito-Santo. A review of micro and mild hybrid systems. Energy Reports, 6:385–390, 2020. DOI 10.1016/j.egyr.2019.08.077.

[233] Y. Sun, W. Dong, and X. Yu. Effects of coolant temperature coupled with controlling strategies on particulate number emissions in GDI engine under idle stage. Fuel, 225:1–9, 2018. DOI 10.1016/j.fuel.2018.03.075.

[234] L. Chen, Z. Liang, X. Zhang, and S. Shuai. Characterizing particulate matter emissions from GDI and PFI vehicles under transient and cold start conditions. Fuel, 189:131–140, 2017. DOI 10.1016/j.fuel.2016.10.055.

[235] H. Yamamoto. Investigation on relationship between thermal efficiency and NOx formation in ultra-lean combustion. SAE Technical Paper 1999-01-3328, 1999. DOI 10.4271/1999-01-3328.

[236] M.M. Ojapah, Y. Zhang, and H. Zhao. Analysis of gaseous and PM emissions of 4-stroke CAI/HCCI and SI combustion in a DI gasoline engine. SAE Technical Paper 2013-01-1549, 2013. DOI 10.4271/2013-01-1549.

[237] J.E. Dec. Advanced compression-ignition combustion for high efficiency and ultra-low NOx and soot. In: D. Crolla, D.E. Foster, T. Kobayashi, and N. Vaughan (Eds.). Encyclopedia of automotive engineering. John Wiley & Sons, 2014, DOI 10.1002/9781118354179.auto121.

[238] M. Bunce, A. Cairns, and H. Blaxill. The use of active jet ignition to overcome traditional challenges of pre-chamber combustors under low load conditions. International Journal of Engine Research, 2020. DOI 10.1177/1468087420972555.

[239] A. Qiao and X. Wu. Research on the new ignition control system of lean-and fast-burn SI engines. SAE Technical Paper 2008-01-1721, 2008. DOI 10.4271/2008-01-1721.

[240] M. Bunce, H. Blaxill, W. Kulatilaka, and N. Jiang. The effects of turbulent jet characteristics on engine performance using a pre-chamber combustor. SAE Technical Paper 2014-01-1195, 2014. DOI 10.4271/2014-01-1195.

[241] W.P. Attard, N. Fraser, P. Parsons, and E. Toulson. A turbulent jet ignition pre-chamber combustion system for large fuel economy improvements in a modern vehicle powertrain. SAE Technical Paper 2010-01-1457, 2010. DOI 10.4271/2010-01-1457.

[242] M. Bunce and H. Blaxill. Sub-200 g/kWh BSFC on a light duty gasoline engine. SAE Technical Paper 2016-01-0709, 2016. DOI 10.4271/2016-01-0709.

[243] A.L. Randolph. Methods of processing cylinder-pressure transducer signals to maximize data accuracy. SAE Technical Paper 900170, 1990. DOI 10.4271/900170.

[244] E. Rosseel, R. Sierens, and R.S.G. Baert. Evaluating piezo-electric transducer response to thermal shock from in-cylinder pressure data. SAE Technical Paper 1999-01-0935, 1999. DOI 10.4271/1999-01-0935.

[245] J.P.R. Symonds. Calibration of fast response differential mobility spectrometers. In: Metrology of Airborne Nanoparticles, Standardisation and Applications (MANSA), London, 2010. DOI 10.13140/2.1.2095.1046.

[246] P. Kumar, P. Fennell, J. Symonds, and R. Britter. Treatment of losses of ultrafine aerosol particles in long sampling tubes during ambient measurements. Atmospheric Environment, 42(38):8819–8826, 2008. DOI 10.1016/j.atmosenv.2008.09.003.

[247] S. Kook, R. Zhang, K. Szeto, et al. In-flame soot sampling and particle analysis in a diesel engine. SAE International Journal of Fuels and Lubricants, 6(1):80–97, 2013. DOI 10.4271/2013-01-0912.

[248] J.B. Heywood. Internal combustion engine fundamentals. McGraw-Hill, New York, NY, USA, 1988. ISBN 007028637X.

[249] M.F.J. Brunt, H. Rai, and A.L. Emtage. The calculation of heat release energy from engine cylinder pressure data. SAE Technical Paper 981052, 1998. DOI 10.4271/981052.

[250] G. Woschni. A universally applicable equation for the instantaneous heat transfer coefficient in the internal combustion engine. SAE Technical Paper 670931, 1967. DOI 10.4271/670931.

[251] G.F. Hohenberg. Advanced approaches for heat transfer calculations. SAE Technical Paper 790825, 1979. DOI 10.4271/790825.

[252] P. Huegel, H. Kubach, T. Koch, and A. Velji. Investigations on the heat transfer in a single cylinder research SI engine with gasoline direct injection. SAE Technical Paper 2015-01-0782, 2015. DOI 10.4271/2015-01-0782.

[253] United Nations. UN GTR No. 15 Amendment 4 – United Nations Global Technical Regulation on worldwide harmonized light vehicles test procedures (WLTP), 2018. URL `https://unece.org/fileadmin/DAM/trans/main/wp29/wp29wgs/wp29gen/wp29registry/ECE-TRANS-180a15am4e.pdf`. Last accessed: 01 July 2021.

[254] K. Zuiderveld. Contrast limited adaptive histogram equalization. In: P.S. Heckbert (Ed.). Graphics gems IV, pages 474–485. Academic Press, 1994, DOI 10.1016/B978-0-12-336156-1.50061-6.

[255] M.L. Botero, E.M. Adkins, S. González-Calera, et al. PAH structure analysis of soot in a non-premixed flame using high-resolution transmission electron microscopy and optical band gap analysis. Combustion and Flame, 164:250–258, 2016. DOI 10.1016/j.combustflame.2015.11.022.

[256] R.L. Vander Wal. Soot nanostructure: Definition, quantification and implications. SAE Technical Paper 2005-01-0964, 2005. DOI 10.4271/2005-01-0964.

[257] M. Lapuerta, F. Oliva, J.R. Agudelo, and J.P. Stitt. Optimization of Raman spectroscopy parameters for characterizing soot from different diesel fuels. Combustion Science and Technology, 183(11):1203–1220, 2011. DOI 10.1080/00102202.2011.587484.

[258] A. La Rocca, G. Di Liberto, P. Shayler, et al. A novel diagnostics tool for measuring soot agglomerates size distribution in used automotive lubricant oils. SAE International Journal of Fuels and Lubricants, 7 (1):301–306, 2014. DOI 10.4271/2014-01-1479.

[259] R.L. Vander Wal and A.J. Tomasek. Soot oxidation: Dependence upon initial nanostructure. Combustion and Flame, 134(1–2):1–9, 2003. DOI 10.1016/S0010-2180(03)00084-1.

[260] P. Thévenaz, U.E. Ruttimann, and M. Unser. A pyramid approach to sub-pixel registration based on intensity mailing address. IEEE Transactions on Image Processing, 7(1):27–41, 1998. DOI 10.1109/83.650848.

[261] Y. Zhang, R. Zhang, and S. Kook. Nanostructure analysis of in-flame soot particles under the influence of jet-jet interactions in a light-duty diesel engine. SAE International Journal of Engines, 8(5):2213–2226, 2015. DOI 10.4271/2015-24-2444.

[262] W.M.F. Wan Mahmood, A. La Rocca, P.J. Shayler, et al. Predicted paths of soot particles in the cylinders of a direct injection diesel engine. SAE Technical Paper 2012-01-0148, 2012. DOI 10.4271/2012-01-0148.

[263] M. Patel and P.B. Aswath. Structure and chemistry of crankcase and cylinder soot and tribofilms on piston rings from a Mack T-12 dynamometer engine test. Tribology International, 77:111–121, 2014. DOI 10.1016/j.triboint.2014.04.004.

[264] M. Patel, C.L. Azanza Ricardo, P. Scardi, and P.B. Aswath. Morphology, structure and chemistry of extracted diesel soot – Part I: Transmission electron microscopy, Raman spectroscopy, X-ray photoelectron spectroscopy and synchrotron X-ray diffraction study. Tribology International, 52:29–39, 2012. DOI 10.1016/j.triboint.2012.03.004.

[265] V. Sharma, S. Bagi, M. Patel, et al. Influence of engine age on morphology and chemistry of diesel soot extracted from crankcase oil. Energy & Fuels, 30(3):2276–2284, 2016. DOI 10.1021/acs.energyfuels.5b02512.

[266] C. Kim, C.A. Passut, and D.M. Zang. Relationships among oil composition, combustion-generated soot, and diesel engine valve train wear. SAE Technical Paper 922199, 1992. DOI 10.4271/922199.

[267] C. Liu, S. Nemoto, and S. Ogano. Effect of soot properties in diesel engine oils on frictional characteristics. Tribology Transactions, 46(1): 12–18, 2003. DOI 10.1080/10402000308982593.

[268] B. Rohani and C. Bae. Effect of exhaust gas recirculation (EGR) and multiple injections on diesel soot nano-structure and reactivity. Applied Thermal Engineering, 116:160–169, 2017. DOI 10.1016/j.applthermaleng.2016.11.116.

[269] K. Al-Qurashi and A.L. Boehman. Impact of exhaust gas recirculation (EGR) on the oxidative reactivity of diesel engine soot. Combustion and Flame, 155(4):675–695, 2008. DOI 10.1016/j.combustflame.2008.06.002.

[270] J. Hoard and L. Rehagen. Relating subjective idle quality to engine combustion. SAE Technical Paper 970035, 1997. DOI 10.4271/970035.

[271] S. Zinola, M. Leblanc, L. Rouleau, et al. Measurement of sub-23 nm particles emitted by gasoline direct injection engine with new advanced instrumentation. SAE Technical Paper 2019-01-2195, 2019. DOI 10.4271/2019-01-2195.

[272] F.C.P. Leach. Particulate emissions from gasoline direct injection engines. PhD thesis, University of Oxford, Oxford, 2014.

[273] F.C.P. Leach, R. Stone, D. Richardson, et al. The effect of oxygenate fuels on PN emissions from a highly boosted GDI engine. Fuel, 225: 277–286, 2018. DOI 10.1016/j.fuel.2018.03.148.

[274] F.C.P. Leach, R. Stone, D. Richardson, et al. The effect of fuel composition on particulate emissions from a highly boosted GDI engine – An evaluation of three particulate indices. Fuel, 252:598–611, 2019. DOI 10.1016/j.fuel.2019.04.115.

[275] F. Leach, A. Lewis, S. Akehurst, et al. Sub-23 nm particulate emissions from a highly boosted GDI engine. SAE Technical Paper 2019-24-0153, 2019. DOI 10.4271/2019-24-0153.

[276] H. Seong, K. Lee, and S. Choi. Effects of engine operating parameters on morphology of particulates from a gasoline direct injection (GDI) engine. SAE Technical Paper 2013-01-2574, 2013. DOI 10.4271/2013-01-2574.

[277] K.O. Lee and J. Zhu. Effects of exhaust system components on particulate morphology in a light-duty diesel engine. SAE Technical Paper 2005-01-0184, 2005. DOI 10.4271/2005-01-0184.

[278] K.O. Lee, H. Seong, S. Sakai, et al. Detailed morphological properties of nanoparticles from gasoline direct injection engine combustion of ethanol blends. SAE Technical Paper 2013-24-0185, 2013. DOI 10.4271/2013-24-0185.

[279] S. Dhaniyala, M. Fierz, J. Keskinen, and M. Marjamäki. Instruments based on electrical detection of aerosols. In: P. Kulkarni, P.A. Baron, and K. Willeke (Eds.). Aerosol measurement: Principles, techniques, and applications, pages 393–416. John Wiley & Sons, Hoboken, NJ, USA, 3rd edition, 2011, DOI 10.1002/9781118001684.ch18.

[280] M.L. Botero, J. Akroyd, D. Chen, et al. On the thermophoretic sampling and TEM-based characterisation of soot particles in flames. Carbon, 171:711–722, 2021. DOI 10.1016/j.carbon.2020.09.074.

[281] P. Toth. Nanostructure quantification of turbostratic carbon by HRTEM image analysis: State of the art, biases, sensitivity and best practices. Carbon, 178:688–707, 2021. DOI 10.1016/j.carbon.2021.03.043.

[282] F. Hagen, F. Hardock, S. Koch, et al. Why soot is not alike soot: A molecular/nanostructural approach to low temperature soot oxidation. Flow, Turbulence and Combustion, 106(2):295–329, 2021. DOI 10.1007/s10494-020-00205-2.